EXPLORING CORRELATION BETWEEN LOCAL STRUCTURE, MAGNETIC AND TRANSPORT PROPERTIES OF MULTIFUNCTIONAL Cr-BASED CHALCOSPINELS

Ph.D. Thesis

By

PRIYADARSHINI SUCHISMITA BEHERA

DISCIPLINE OF PHYSICS

INDIAN INSTITUTE OF TECHNOLOGY INDORE

JULY 2017

EXPLORING CORRELATION BETWEEN LOCAL STRUCTURE, MAGNETIC AND TRANSPORT PROPERTIES OF MULTIFUNCTIONAL Cr-BASED CHALCOSPINELS

A THESIS

Submitted in partial fulfillment of the
requirements for the award of the degree
of
DOCTOR OF PHILOSOPHY

by

PRIYADARSHINI SUCHISMITA BEHERA

DISCIPLINE OF PHYSICS
INDIAN INSTITUTE OF TECHNOLOGY INDORE
JULY 2017

INDIAN INSTITUTE OF TECHNOLOGY INDORE

CANDIDATE'S DECLARATION

I hereby certify that the work which is being presented in the thesis entitled **EXPLORING CORRELATION BETWEEN LOCAL STRUCTURE, MAGNETIC AND TRANSPORT PROPERTIES OF MULTIFUNCTIONAL Cr-BASED CHALCOSPINELS** in the partial fulfillment of the requirements for the award of the degree of **DOCTOR OF PHILOSOPHY** and submitted in the **DISCIPLINE OF PHYSICS, Indian Institute of Technology Indore**, is an authentic record of my own work carried out during the time period from July, 2012 to July, 2017 under the supervision of Dr. Preeti A. Bhobe, Associate Professor, Discipline of Physics, Indian Institute of Technology Indore.

The matter presented in this thesis has not been submitted by me for the award of any other degree of this or any other institute.

Signature of the student with date
(PRIYADARSHINI SUCHISMITA BEHERA)

This is to certify that the above statement made by the candidate is correct to the best of my knowledge.

Signature of Thesis Supervisor with date
(Dr. PREETI A. BHOBE)

PRIYADARSHINI SUCHISMITA BEHERA has successfully given her Ph.D. Oral Examination held on _____.

Signature of Chairperson (OEB)
Date:

Signature of External Examiner
Date:

Signature(s) of Thesis Supervisor(s)
Date:

Signature of PSPC Member #1
Date:

Signature of PSPC Member #2
Date:

Signature of Convener, DPGC
Date:

Signature of Head of Discipline
Date:

ACKNOWLEDGMENTS

First and foremost, I express my heartfelt gratitude to the Almighty for giving me the wisdom, strength, courage and ample blessings throughout my research work. I would like to pay special thankfulness, warmth and sincere appreciation to those who have made this thesis successful and supported me in one way or the other during this amazing journey.

At this moment of accomplishment, I am greatly indebted to my research mentor, **Dr. Preeti A. Bhobe**, who accepted me as her first PhD student and offered me her mentorship, motherly love and care. This research work would not have been possible without her sustained guidance and involvement, her support and persistent encouragement on daily basis from the start of this research work to till date. Under her supervision, I successfully overcame many difficulties and learnt a lot, not only in conducting research, but also in being an integrated person. Her own zeal for perfection, unflinching courage, enormous passion for high-quality scientific research and rigorous work ethic have had a remarkable influence on me and hopefully my entire career.

My sincere gramercy goes out as well to the doctoral committee members: **Dr. Krushna Mavani** and **Dr. Satya Bulusu** for their time, valuable suggestions and reinforcement during my annual research progress seminar, sharing their expertise and knowledge in reviewing this thesis. Also, I am very much thankful to Dr. Krushna Mavani for providing me experimental facilities in her laboratory.

I gratefully acknowledge **Ministry of Human Research Development, Govt of India,** for providing me the teaching assistant fellowship and **Director**, **Prof. Pradeep Mathur**, Indian Institute of Technology (IIT) Indore to allow me to peruse my PhD degree in this esteemed Institution. I would like to acknowledge Council for Scientific and Industrial Research (**CSIR**), India (Grant No. 03(1298)/13/ EMR-II) and Department of Science and Technology (**DST**), New Delhi (Grant No. SR/S2/CMP-0109/2012) for providing financial support.

I take this opportunity to profoundly thankful to **Dr. Manvendra Mahato,** Head of the department and **all the faculty members and** non-teaching staff **Mr. Ujjwal Kulkarni** of the department of Physics at IIT Indor**e** for their help and support provided for the completion of this research work in various ways.

I would like to offer my sincere gratefulness to **Prof. A. K. Nigam, Department of Condensed Matter Physics and Material Science, Tata Institute of Fundamental Research Centre, Mumbai,** for extending the facility for magnetic properties measurement and thankful to **Mr. Devendra Buddhikot** for his technical help regarding the magnetic measurements.

I am extremely grateful to **Prof. K.R. Priolkar,** Department of Physics, Goa University, India for providing me the facility to carry out the sample preparation. Again, I am thankful to his students; **Kapil**, **Eillen** and **Nilima** for their helpfulness made me to stay at Goa university happily.

I would like to express my sincere appreciation to **Dr. V.G. Sathe**, UGC-DAE Consortium for Scientific Research (CSR), Indore, India for allowing me to perform the Raman Spectroscopy measurement. I want to thank **Mr. Ajay Rathod** for all support in carrying out the Raman experiment.

I extend my gratitude towards **Dr. Mukul Gupta** from UGC-DAE CSR Indore, for providing facility to record synchrotron source soft X-ray absorption spectroscopy data in beamline BL01, Indus-2 located at Raja Raman Centre for Advance Research, Indore, India.

I would like to thank the DST, India for the financial support and Saha Institute of Nuclear Physics, India for facilitating the high resolution, temperature dependent X-Ray Diffraction (XRD) experiments at the Indian Beamline, Photon Factory, KEK, Japan.

I must thank **Mr. P. K. Parthiban**, Glassblower at IIT Indore, for sealing of evacuated quartz ampoules during my sample preparation process. I wish to thank Sophisticated Instrument Centre (SIC) at IIT Indore, specifically **Mr. Kinny Pandey** and **Mr. Nitin Upadhyay** for helping me to take Energy Dispersive X-Ray Spectroscopy and Powder XRD measurement.

My sincere thanks to **Dr. Somaditya Sen,** Department of physics, IIT Indore for providing one month training on experimental technique of Field Emission Scanning Electron Microscopy. He also allowed me in his laboratory for table top XRD measurement, furthermore I also thank to his student, **Arun Yadav**, who helped me in this regard.

I am highly obliged to my M. Phil supervisor **Dr. D. Bharathimohan,** Department of Physics, Pondicherry University, Puducherry; Co-supervisor **Prof. C.S. Sunandana,** School of Physics, Hyderabad Central University, Hyderabad; and My Project guide **Dr. K. Jayasankar,** Advanced Material Technology Department, CSIR-Institute of Mineral and Materials Technology, Bhubaneswar, for motivated me to join PhD programme.

I sincerely thank to **Dr. Raghunath Sahoo**, Department of Physics, IIT Indore, **Dr. Gayatri Sahoo** and their daughter **Ananya** for all their love, care and support during my stay at Indore.

I also want to extend my gratitude to **Ms. Monika Gupta** and **Ms. Sarita Batra**, IIT Indore for their encouragement, help and moral support.

My heartfelt thanks to my senior labmates **Dr. Dhirendra Kumar**, **Dr. Mehedi Hassan** for their guidance and valuable suggestions. They always helped me out when I got any difficulties or queries regarding my experimental disscussions. Also, my deepest and heartiest thanks to all my junior labmates; **Mithun**, **Sayan**, **Gowtham**, **Tamalika**, **Rajib**, **Piyush** and **Sania** for their help, cheerful cooperation, encouragement, sisterly affection and enjoyment during this course of time. My special appreciation goes to **Mithun (M!TH)** for all the brotherly love, care and fight that he has showered on me.

A special mention of profound thanks to my PhD. class mates from department of physics at IIT Indore; **Shailendra (Shailu)** and **Harimohan (Khali)**, **Ravikiran Late**, **Ravi Kancharla**, who have been a source of moral support to me and have extended their helping hands without fail, their valuable discussions and suggestions, and friendship shall always be remembered. I also acknowledge my other PhD fellows; **Aditya**, **Sudeep**, **Nazeem**, **Pritpal**, **Ankita di** for their constant support and cooperation during my stay. I warmly thank to my PhD seniors, **Dr.**

Fozia Aziz, **Dr. Mahesh Bhat** and **Dr. Ajay Panwar** and my juniors; **Vikash Mishra**, **Surjendu**, **Kamal**, **Tulika**, **Priyanka**, **Kavita**, **Ankit**, **Kushal**, **Prateek** and **Saptarshee** for their love, affection and help.

I will forever be grateful to my roommate **Pragati** for keeping a healthy atmosphere and bearing with me all these days and my flat mates **Camelia**, **Deepika**, **Aparna** and **Madhurima**, for their fundamental support towards me during the stressful moments. Again, a big thank you to all my dearies for their sisterly love, various handmade yummy food, all kinds of fun we have had in the last four years and most importantly, sharing a wonderful relationship as compassionate friends, which made my stay very memorable. Thanks to the cutest and tiniest **Coco**, who has given numerous happening moments throughout.

Friends have helped me find a home away from home. I would never forget all the chats and beautiful moments I shared with some of my amazing friends. My heartfelt thanks to all such friends; **Smrutipriya**, **Shanu**, **Pooja**, **Deblina**, **Smriti**, **Anuradha** and **Tanu** for their immeasurable kindness, love, and support. I would like to extent my unfeigned thanks to some of my other nice friends at IIT Indore from school of engineering; **Krishna (KD)**, **Tejendra (TD)**, **Shivendra (Pandey)**, **Yogesh** and **Nishant** for their continuous support, friendly atmosphere and always ready to give their timely help whenever required. Also, their companionship has made this last five years of my PhD exceptionally memorable.

I also deeply acknowledge to the odia group at IIT indore, faculty, seniors, friends and juniors, **Dr. Amarjit Nayak, Dr. Swadesh Sahoo**, **Dr. Manas Ranjan**, **Dr. Sarita Agrawal**, **Dr. Sreelekha Dash**, **Dr. Sanjay Lenka**, **Dr. Bijay Sethi**, **Sidheswar**, **Debasis**, **Basanta**, **Alfa**, **Sushant**, **Dhananjay**, **Arvind**, **Sarthak**, **Abhiram**, **Yogi**, **Rajesh**, **Sushree** for providing the homely environment and delicious odia food.

In this occasion, I would like to mention some of my magnetic school friends **Mukshi**, **Nitika**, **Priyanka**, **Anu**, **Simarjit**, **Saptashree**, **Vikram**, **Durgesh, Aditya and Saroj**, I will never forget the time we spent together with very fruitful discussions. I cherish to acknowledge my best buddies forever; **Smrutirekha Swain**, **Dr. Rajesh Desapogu**, **Dhiraj**, **Anil pal**, **Bikash**, **Manas**,

Melee, **Swati**, **Sharmistha**, **Chinu**, **Sushree**, **Pankajini**, **Viswarupa** for their support, encouragement and careness.

I feel a deep sense of gratitude for the people who mean a lot to me, my grandfathers **(Jeje and Aja)**, My parents **(Bou and Bapa)** and my only brother **(Dulu)** for showing faith in me and giving me liberty to choose what I desired. I salute you all for the blessings, selfless love, care, encouragement, pain and sacrifice you did to shape my life. Although you people hardly understood what I researched on, you all were always willing to support any decision I made. Really, I am feeling so overwhelmed towards my beloved parents and sweet brother for their endless co-operation during the entire course of study.

I owe my deepest gratitude towards a very special person, my better half **(Puchu)** for his eternal support and understanding of my goals and aspirations. His infallible love, patience and sacrifice will remain my inspiration throughout my life. Without his help, I would not have been able to complete much of what I have done and become who I am. Again, my heart felt regard goes to all my in-law's family, special thankful to **Papa** (father in law), **Mummy** (mother in law), **Keval Kamani** (brother in law), **Neha Kamani** (sister in law), **Bhavik Doshi** (jiju) and her family for their unconditional love, moral support and constant reassurance.

I express my heartfelt thanks to all my uncle (**Mr. Sukanta Ku. Muduli**, **Mr. Bibhudatta Mahapatra**, **Mr. Debadatta Mahapatra**), all my aunties (**Mrs. Shantilata Muduli**, **Mrs. Jayanti Behera**, **Mrs. Basanti Sahoo**, **Mrs. Anita Rana**, **Mrs. Geeta Rani Sahoo**, **Mrs. Kabita Behera**, **Mrs. Bharati Mohapatra**) and my lovely sisters **Shibani** and **Bhabani** for their unflinching love, care, continuous support, and valuable prayers. A special note of gratitude to all my cousins and rest of my relatives.

I want to express my gratitude towards **Dr. Shilpa** and **Dr. P. Matkar** and other staff members of IIT Indore dispensary who kept me physically fit and healthy.

Last but not least, I wish to thank all the staff members of IIT Indore for giving all comfort, convenience and cooperation throughout my journey in the last five years.

Dedicated

To

My Beloved Grandparents:

Jema Dei and Khetrabasi Behera,

Jagganath Behera,

My Adorable Parents and In-laws:

Sabita Behera and Kailash Nath Behera

Jyoti Kamani and Mahesh Kamani,

My Dearest Husband: Rahul Kamani

&

My lovely Brother

Kamalesh Behera

SYNOPSIS

Introduction

The coexistence of magnetic and ferroelectric phases in a material has been one of the attractive issues in fundamental and applied research in recent years. Such materials-termed as the multiferroics – are potential candidates for applications in electronic devices which are operational both by magnetic field and by electric field. To make technological advances in this field, a complete understanding of the interaction mechanism existing among the magnetic moments, the electric dipole, and the lattice responsible for the uncommon behavior should be well understood.

Relaxor ferroelectricity and colossal magneto-capacitance has recently been observed in Cr-based spinel chalcogenides like $CdCr_2S_4$, $HgCr_2S_4$ and $CdCr_2Se_4$. Further, $CdCr_2S_4$ also exhibits colossal electrocapacitive, electro-resistive, and magneto-resistive effects. Owing to its wide variety of magnetic ground states and range of magnetic exchange strengths, one can find that magnetic spinel systems of the type ACr_2X_4 (A= Zn, Cd, Hg, Fe, Cu; X= O, S, Se) are the most studied materials for more than half a century. The ease of integrating different elements (at A & X sites) in the spinel structure leading to different lattice constant, is what provides the flexibility to various magnetic ground states and ordering temperatures (T_C). For example, the Cr spins in oxide spinels forms a pyrochlore lattice structure where a strong geometrical frustration exists between magnetic spin directions. On the other hand, sulphur spinels order ferromagnetically (FM), and in fact, simultaneously exhibit colossal magnetocapacitive (CMC ~ 500%), colossal electrocapacitive (CEC ~ 200%), colossal electroresistive (CER ~ 80%), and colossal magnetoresistive (CMR ~ 50%) effects in a single composition, $CdCr_2S_4$.

On the other hand, Se-based materials though less explored, show a wide range of electrical and magnetic properties due to increased covalency and stronger hybridization of Cr *d* and Se *p* orbitals. For example, $CuCr_2Se_4$ is an FM metal with highest $T_C \approx 430$ K in its class of compounds, while $CdCr_2Se_4$ is a semiconductor with $T_C \approx 130$ K. Further, $CdCr_2Se_4$ exhibits substantial magneto-caloric property

making it a promising magnetic refrigerant material. Another similar composition, $ZnCr_2Se_4$, is a canonical incommensurate simple helical magnet that orders in a complex antiferromagnetic (AFM) order below Neel temperature (T_N) = 21 K despite strong FM exchange reflected in a significant positive value of the Curie-Weiss temperature θ_{CW} = 115 K. Moreover, it is a *p*-type semiconductor with a band gap of E_g = 0.3 eV.

An easily noticed difference between ACr_2Se_4 compounds is that the A-site cations (Cd & Zn) are divalent, whereas it is not clear whether Cu is divalent or monovalent in $CuCr_2Se_4$. Therefore, the origin of magnetism for all such compositions has been in controversy for many years. Three models have been proposed and famously discussed in the context of $CuCr_2Se_4$:

(a) Lotgering model, that assumes valence distribution to be $Cu^{1+}(Cr^{3+}Cr^{4+})\ Se^{2-}$ with FM and metallicity attributed to double-exchange (DE) mechanism between Cr^{3+} and Cr^{4+};

(b) Goodenough model, that proposed a divalent state of Cu^{2+} with moment antiparallel to Cr^{3+} via 90º superexchange mediated through the filled Se *4p* states and;

(c) Lotgering and van Stapele, who modified the second model to accommodate experimental results, which shows that the DE is not relevant to the magnetism of $CuCr_2Se_4$. They presumed that the spinel $CuCr_2Se_4$ contained Cu^+ ($3d^{10}$) ions as in their original model. But the chromium ions were all trivalent Cr^{3+} ($3d^3$) so that the monovalent Cu induces one hole in a ligand *p* orbital and these holes are responsible for the electrical conduction and also for the strong ferromagnetic exchange between the Cr^{3+} ions. Besides, band structure calculations for this compound predict a highly spin-polarized DOS with half-metallic properties for suitably doped compositions.

In a general way, the dominating exchange interactions in ACr_2Se_4 systems are governed by the interatomic distances. For small Cr-Cr distances, a strong direct AFM exchange dominates. An increase in Cr-Cr bond distance strengthens the underlying 90° FM (Cr-Se-Cr) superexchange. Further, a complex (Cr-Se-A-Se-Cr) antiferromagnetic superexchange (SE), although very weak, has been argued to be quite important.

Present study

Motivated from above background, we attempted to explore the correlations in crystal structure – magnetic –electronic properties of ACr_2Se_4 spinels, with A = Cd, Cu and Zn. As slight lattice distortions and cation valence/site disorder play an important role in determining the properties of this class of materials, substitutions of different elements at various tetrahedral (Cd/Cu/Zn) site, octahedral Cr-site and anion sites were carried out. All samples were prepared by solid state reaction method. The crystal structure of the prepared compositions was thoroughly studied using experimental probes like powder X-ray diffraction (XRD), Extended X-ray Absorption Fine Structure spectroscopy (EXAFS), and Raman spectroscopy. Magnetic properties were measured using a SQUID magnetometer. Transport measurements were carried out using standard four-probe resistivity technique.

The influence of Cr-Cr and Cr-Se bond distances in governing the magnetic ground state of the materials was clearly established. Tweaking the physical properties with suitable substitutions gives rise to emergent properties that are technologically relevant, like magneto-resistance, spin-phonon coupling and possible half-metallic ground state. These possibilities were explored for the studied samples. In particular, the exact compositions studies here are:

i. **$CdCr_2Se_4$**
   a) $Cd_{1-x}M_xCr_2Se_4$ with M = Sb, In, Sn and $0 \leq x \leq 0.1$
   b) $CdCr_2Se_{3.8}S_{0.2}$ and $CdCr_2Se_{3.6}S_{0.4}$

ii. **$CuCr_2Se_4$**
   a) $Cu_{1-x}M_xCr_2Se_4$ with M = Mn, Fe, Co, Ni and $x = 0.1$
   b) $CuCr_{2-x}Ti_xSe_4$ with $0 \leq x \leq 1$

iii. **$Cd_{0.9}Cu_{0.1}Cr_2Se_4$, $Zn_{0.9}Cu_{0.1}Cr_2Se_4$, and $Zn_{0.1}Cu_{0.9}Cr_2Se_4$**

Chapter wise organization of the thesis

The organization of this thesis is as follows:

Chapter 1: The first chapter provides a brief review of existing literature related to various Cr – based spinel chalcogenides. This includes studies on the crystal structure, magnetic, vibrational and electronic -transport properties relevant to spinel chalcogenides. This chapter also defines the objective of the thesis.

Chapter 2: This chapter contains details about the method of sample synthesis and a brief description of various characterization techniques employed in the present study. Experimental probes such as X-ray diffraction (XRD), energy dispersive X-ray analysis (EDAX), extended X-ray absorption spectroscopy (EXAFS), soft X-ray absorption spectroscopy (XAS), Raman spectroscopy, magnetic properties measurement, four-probe resistivity measurement and heat capacity measurement are described here. A brief mention of the working principles of various instruments like SQUID – based magnetic properties measurement system (MPMS) and physical property measurement system (PPMS), vibrating sample magnetometer (VSM), EXAFS spectrometer and Raman spectrometer has also been made.

Chapter 3: This chapter summarizes the investigation carried out on the A-site substituted chalcospinels, *viz.* $Cd_{1-x}M_xCr_2Se_4$ (M = Sb, In, Sn). $CdCr_2Se_4$ orders magnetically below T_C ~130K. Partial substitution of Cd^{2+} by a small percentage (≤ 10%) of non-magnetic In^{3+}, Sb^{3+}, or Sn^{4+} results in same cubic symmetry in spite of the differences between the cationic radii and ionic charge. However, manifestation of local lattice distortion and charge-imbalance effect is seen on the structural and magnetic properties of the studied compositions. While Sb and In substituted samples reflect expected trends in its lattice parameters and magnetic properties, the Sn-substituted compositions show interesting deviations and correlation in lattice constant and T_C. With increasing Sn content, the T_C (~ 130 K for $CdCr_2Se_4$) drops down to 116 K (for 5% Sn) and slowly regains the value of 124 K for 10% of Sn. Overall the magnetic properties of all the studied compositions display the manifestation of competition between Cr-Se-Cr ferromagnetic and Cr-Cr antiferromagnetic interactions. EXAFS measured at Cr K-edge shows an enhancement in the thermal displacement parameters associated with Cr-Se bonds, that signal presence of local disorder while maintaining the overall cubic structure. Also, an apparent change in the feature related to Cr-Cr interaction occurs with changing concentration of substituted ions. Certain features in magnetic properties hint towards a low-spin transition of Cr^{2+}. XANES recorded at the Cr K-edge provides final evidence of the presence of Cr mixed valence (Cr^{3+}/Cr^{2+}) state.

Chapter 4: This chapter presents evidence of local lattice distortion and its effect on the spin-phonon coupling in $CdCr_2Se_{4-x}S_x$ and $Cd_{1-x}Sn_xCr_2Se_4$ for ($0 \leq x \leq 0.1$).

Our earlier attempt at understanding crystal structure–magnetic properties correlation in leads to the inference that, both, local lattice distortion and formation of mixed valence of chromium ions influence the Cr-Cr and Cr-Se-Cr interactions. In this work, we attempt to isolate the role of local lattice distortions in controlling the magnetic superexchange interactions.

Slight substitution of isovalent S in place of Se indicates that S-doping leads to the decrease in the unit cell parameters without affecting the valence state of Cr ions. From EXAFS analysis, we obtain two different bond distances for Cr-Se and Cr-S, indicating structural distortion of the Cr-Se octahedra at a local level within the overall cubic unit cell. The interesting fact is that despite the sizable lattice distortions, neither the T_c nor the magnetic moment seems to be much affected by S-substitution. Apart from EXAFS analysis, room temperature Raman spectra also provide evidence for local structure distortion. Temperature dependent Raman spectra further reveal anomalous variation in the peak position of vibrational modes across the magnetic transition temperature, suggesting an existence of spin-phonon coupling in the system.

As discussed in Chapter 3, Sn-substituted compositions show influence of both, charge and lattice distortion on its magnetic properties. The slight increase in lattice constants causes a considerable difference in the overlap of *d*-orbitals. This result in wider separation of bands, triggering a low-spin transition of Cr^{2+} ions that are formed due to charge imbalance created by Sn^{4+} substitution at Cd^{2+} site. Hence a detailed investigation into the changing local crystal structure and its effect on spin-phonon coupling in $Cd_{1-x}Sn_xCr_2Se_4$ for ($0 \leq x \leq 0.1$) were carried out using Cr-Kedge EXAFS and Raman spectroscopy technique. EXAFS revealed that considerable change in the Cr-Cr bond distance as compared to Cr-Se. From the Raman data analysis, it is clear that the lattice is involved in modulating the lifetime of phonon, but its coupling with spin is not sufficiently strong to modulate the frequency.

Chapter 5: Electronic structure calculations present in literature, indicate the possibility of inducing half-metallic ground state in $CuCr_2Se_4$ spinel system, by a careful choice of chemical substituent. From chapter 3 and chapter 4, our study on $CdCr_2Se_4$ tells us that substitutions at A-site provide an effective way to control the magneto-structural properties of these materials than substitutions at Se-site. Hence, with an intention to change the *3d* density of states at Fermi level we carried out the investigation of $Cu_{1-x}M_xCr_2Se_4$ (M= Mn, Fe, Co, Ni and x = 0.1) and $CuCr_{2-x}Ti_xSe_4$ for its structure, magnetic and transport properties. In this chapter, we discuss the results of $Cu_{1-x}M_xCr_2Se_4$ (M= Mn, Fe, Co, Ni and x = 0.1). The next chapter elaborates on properties of $CuCr_{2-x}Ti_xSe_4$.

With the 10% magnetic ion substitution at Cu site, the T_C in $CuCr_2Se_4$ is reduced from 430 K to 390 K, but the saturation magnetic moment does not change much. But fascinatingly, 10% of Mn substitution causes a sufficient - reduction of T_C from 430 K to 350 K and significant increase of the saturation magnetic moment of 5.5 μ_B/f.u. XANES confirms the monovalent state of Cu and divalent state of Mn, Fe, Co and Ni. Introducing a small amount of Fe^{2+} /Co^{2+}/Ni^{2+} at Cu^{+} site leads to a formation of the mixed valence of Cr ions (Cr^{3+}/ Cr^{4+}) at octahedral sites and a strong FM order originates due to the double exchange mechanism. Electrical measurement of all these samples shows the metallic-type conductivity with strong electron correlations present in the low temperature region.

Chapter 6: As stated above, this chapter is dedicated to the study of $CuCr_{2-x}Ti_xSe_4$ spinels.

We carried out the investigation of magnetic, electrical and crystal structure properties of polycrystalline $Cu[Cr_{2-x}Ti_x]Se_4$ spinel with x = 0, 0.3, 0.4, 0.5, 0.75 and 1.0 respectively. The gradual increase of Ti substitution at Cr-site in $CuCr_2Se_4$ compound causes a progressive increase in lattice parameters. The predominant ferromagnetic state appears in the range of $0 < x < 0.75$. However, a strong re-entrant spin glass type of state observed in $CuCrTiSe_4$ sample at 14 K. The electrical transport behavior is also quite interesting, with all composition from $CuCr_2Se_4$ up to $CuCr_{1.5}Ti_{0.5}Se_4$ showing metallic conductivity, whereas $CuCr_{1.6}Ti_{0.4}Se_4$ shows the semiconducting rise with fall in temperature. Further increase in Ti concentration changes the electrical conductivity back to metal – like. From

preliminary studies, it appears that $CuCr_{1.6}Ti_{0.4}Se_4$ might indeed qualify to be a half-metal.

Chapter 7: This chapter deals with the unusual magnetic behavior and local structure of $Cd_{0.9}Cu_{0.1}Cr_2Se_4$, $Zn_{0.9}Cu_{0.1}Cr_2Se_4$ and $Cu_{0.9}Zn_{0.1}Cr_2Se_4$ systems.

Introducing a small amount of Cu at Cd /Zn site causes multiple valences of Cr ions (Cr^{3+}/ Cr^{4+}) at octahedral sites in the otherwise stable Cr^{3+} compositions of $CdCr_2Se_4$ and $ZnCr_2Se_4$. This is confirmed from Cr K-edge XANES measurement. The magnetic ground state thus becomes quite rich and competing magnetic interactions results, as evidenced from inverse dc susceptibility curve above T_C. Electronic transport behaviour of both $A_{0.9}Cu_{0.1}Cr_2Se_4$ (A = Cd/Zn) compounds follows Mott variable range hopping process (semiconducting nature). $Cd_{0.9}Cu_{0.1}Cr_2Se_4$ shows ferromagnetic nature whereas $Zn_{0.9}Cu_{0.1}Cr_2Se_4$ compound displays complex AFM and FM behaviour.

In the case of higher Cu^+ substitution at Zn site, i.e. $Cu_{0.9}Zn_{0.1}Cr_2Se_4$ the complex magnetic AFM-FM nature changes completely to strong FM behaviour and electronic conductance changes from semiconducting to metallic nature. This complexity in magnetism is discussed in this chapter. Cr K-edge EXAFS of $Cd_{0.1}Cu_{0.9}Cr_2Se_4$ and $Zn_{0.1}Cu_{0.9}Cr_2Se_4$ shows considerable changes at its first nearest-neighbor shell ($CrSe_6$ octahedra) in terms of (Cr-Se) and second nearest neighbor (Cr-Cr) bond length.

Chapter 8: This is the last chapter of the present thesis. It concludes the present study by summarizing all the obtained results and also describes the possible future scope of the research work that can be undertaken in this area.

LIST OF PUBLICATION

A. From Peer reviewed journals

[1] **P. Suchismita Behera**, P. A. Bhobe; 'Crystal structure and magnetic property correlation in $Cd_{1-x}M_xCr_2Se_4$ (M=Sb, Sn, In)', J. Magn. Magn. Mater, 394 (2015) 200-206. (DOI: 10.1016/j.jmmm.2015.06.064)

[2] **P. Suchismita Behera**, P. A. Bhobe, V. G. Sathe, A. K. Nigam; 'Local lattice distortions and magnetic properties of $CdCr_2Se_{4-x}S_x$', **J. Appl. Phys.** 120 (2016) 045107-1 - 045107-6. (DOI: 10.1063/1.4959878)

[3] **P. Suchismita Behera**, Dhirendra Kumar, V. G. Sathe, P. A. Bhobe; 'Influence of local structural distortions on magnetism and spin-phonon coupling of $Cd_{1-x}Sn_xCr_2Se_4$', **J. Appl. Phys.** 121 (2017) 243905. (DOI: 10.1063/1.4990292)

[4] **P. Suchismita Behera,** P. A. Bhobe, V. G. Sathe, A. K. Nigam; 'Understanding Magnetic Properties of $Cd_{1-x}Sb_xCr_2Se_4$ using EXAFS' Material Research Express (Communicated)

[5] **P. Suchismita Behera**, P.A. Bhobe, A.K. Nigam, 'Influence of Ti substitution on magnetic properties of $CuCr_2Se_4$' (Manuscript under Preparation)

[6] **P. Suchismita Behera,** P.A. Bhobe, A.K. Nigam, 'Magnetic and transport properties of transition-metal-doped $CuCr_2Se_4$ spinel' (Manuscript under Preparation)

B. From Conference

[1] **P. Suchismita Behera,** P. A. Bhobe and A. K. Nigam; 'Structural and magnetic effects of $Cd_{1-x}In_xCr_2Se_4$' AIP Conf. Proc., AIP Publishing, 1665, (2015) p**.** 130026. (DOI: 10.1063/1.4918174)

[2] **P. Suchismita Behera,** A. K. Nigam, and P. A. Bhobe; 'Magnetic properties of $CuCr_2Se_4$ and $CuCr_{1.5}Ti_{0.5}Se_4$' AIP Conf. Proc.**,** AIP Publishing, 1731, (2016) p**.**130009. (DOI: 10.1063/1.4948115)

[3] **P. Suchismita Behera**, V.G. Sathe, and P. A. Bhobe; 'Local structure distortion and mix valence effect on Magnetic property of Cd-substituted $CdCr_2Se_4$', AIP Conf. Proc.**,** AIP Publishing, 1832, (2017) p**.**130029. (DOI: 10.1063/1.4980749)

Presentations at International/ National Conference

[1] **P. Suchismita Behera**, P. A. Bhobe and A. K. Nigam;
"Magnetic properties of S-doped $CdCr_2Se_4$"
Presented (ORAL) at International Conference on Magnetic Materials and Applications Dec 2-4, 2015, VIT University, Vellore.

[2] **P. Suchismita Behera,** P. A. Bhobe and A. K. Nigam;
"Investigation of Local Structure and Magnetic Properties of $CdCr_2Se_4$"
Presented (ORAL) at -International Conference on Electronic Materials (ICEM-2016), July 4-8, 2016, Suntech City, Singapore.

[3] **P. Suchismita Behera**, P. A. Bhobe and A. K. Nigam;
"Crystal Structure-Magnetic Property Correlation in $CdCr_2Se_4$"
Presented (POSTER) at International Conference on Magnetic Materials and Applications, Sep 15-17, 2014, Pondicherry University, Puducherry.
[Received Best Poster Award]

[4] **P. Suchismita Behera,** P. A. Bhobe and A. K. Nigam;
"Structural and magnetic effects of $Cd_{0.9}Cu_{0.1}Cr_2Se_4$"
Presented (POSTER) at DAE-Solid State Physics Symposium, Dec 16-20 2014, VIT University, Vellore, Tamilnadu.

[5] **P. A. Bhobe** and P. Suchismita Behera;
"Exploring crystal structure – magnetic properties correlation in $CdCr_2Se_4$"
Presented (POSTER) at Donostia International Workshop on Energy, Materials and Nanotechnology, Sept 1 – 4 2015, San Sebastian-Donostia, Spain.

[6] **P. Suchismita Behera,** P. A. Bhobe and A. K. Nigam;
"Magnetic properties of $CuCr_2Se_4$ and $CuCr_{1.5}Ti_{0.5}Se_4$"
Presented (POSTER) at DAE-Solid State Physics Symposium, Dec 21-25, 2015, Amity University, Noida, U.P.

[7] **P. Suchismita Behera**, V.G. Sathe and P. A. Bhobe;
"Local structure distortion and mix valence effect on Magnetic property of Cd-substituted $CdCr_2Se_4$", Presented (POSTER) at DAE-Solid State Physics Symposium, Dec 26-30, 2016, KIIT University, Bhubaneswar, Odisha. ***[Received Best Poster Award]***

[8] **P. Suchismita Behera,** P. A. Bhobe and A. K. Nigam;
"Unusual Magnetic Behavior of the Spinel Compound $Cd_{0.9}Cu_{0.1}Cr_2Se_4$"
Presented (POSTER) at International Conference on Magnetic Materials and Applications, Feb 1-3, 2017, Hyderabad.

Conference/School/Seminar/ Participated

- Indo-UK joint seminar on "Functional and Energy Materials Manufacturing and Structures" (FAEMMS-2013) at University of Hyderabad, Gachibowli, Hyderabad during March 25-26, 2013.
- "Frontier Lecture Series in Chemistry (FLSC-2014)" Indian Institute of Technology Indore, M.P., Jan 30-31, 2014.
- DST-SERC sponsored school on "Advanced Functional Magnetic Materials" held at Goa University, Taleigao Plateau, Goa from February 3 - 21, 2014.

TABLE OF CONTENTS

Chapter 2: Synthesis Method and Experimental Techniques

Chapter 3: Crystal Structure and Magnetic Property Correlation in $Cd_{1-x}M_xCr_2Se_4$ (M = Sb, Sn, In)

LIST OF FIGURES

LIST OF TABLES

NOMENCLATURE

α	Alpha
β	Beta
Γ	Gamma
θ	Theta
$\AA$	Angstrom
λ	Wavelength
μ	Micro
m	Mili
Σ	Sigma
Π	Pi
H	Eta
Ω	Omega
Φ	Phi
Δ	Delta
σ	Sigma
~	Tilde
χ	Chi
h	Planck's Constant
J	Exchange integral
Hz	Hertz
MHz	Mega hertz
K	Kelvin
kJ	KiloJoules
cm	Centimetre
nm	Nanometre
°	Degree
$°C$	Degree centigrade
μ_{eff}	Effective paramagnetic moment
a. u.	Arbitrary Unit
emu	Electromagnetic Unit

amu	Atomic Mass Unit
Min	Minute
Sec	Second
hr	Hour
θ_{CW}	Curie-Weiss Temperature
T_M	Magnetic Transition Temperature
μ_B	Bohr-Magnetron
eV	Electron Volt
T_N	Neel Temperature
T_C	Curie Temperature
Oe	Oersted
T	Tesla
M_S	Saturation Magnetization
a	Lattice Constant
h k l	Miller indices
$\mathcal{H}_{ex}$	Heisenberg Hamiltonian
$\hat{S}$	Spin Operator
$\sum$	Summation
N	Nu
E_a	Activation Energy
E_F	Fermi Energy
k_B	Boltzmann Constant
ρ	Rho
N_A	Avogadro's Number

ACRONYMS

FM	Ferromagnetic
AFM	Antiferromagnetic
PM	Paramagnetic
SE	Super-exchange
DE	Double-exchange
MO	Magnetic Order
MCE	Magneto Caloric Effect
XRD	X-Ray Diffraction
EDX	Energy-Dispersive X-Ray Analysis Spectroscopy
FESEM	Field Emission Scanning Electron Microscope
XAS	X-Ray Absorption Spectroscopy
EXAFS	Extended X-Ray Absorption Fine Structure Spectroscopy
XANES	X-Ray Absorption Near Edge Spectroscopy
XMCD	X-ray magnetic circular dichroism
NTE	Negative Thermal Expansion
RT	Room Temperature
PXRD	Powder X-Ray Diffraction
CIF	Crystallographic Information File
JCPDS	Joint Committee on Powder Diffraction Standards
SXAS	Soft X-Ray Absorption Spectroscopy
FWHM	Full Width Half Maximum
MPMS	Magnetic Properties Measurement System
PPMS	Physical Properties Measurement System
SQUID	Superconducting Quantum Interference Device
VSM	Vibrating Sample Magnetometer
EMF	Electromotive Force
AC	Alternating Current
DC	Direct Current
ZFC	Zero Field Cooling
FCC	Field Cooled Cooling

FCH	Field Cooled Heating
IR	Infra-Red
FT	Fourier Transform
MR	Magnetoresistance
CMR	Colossal Magnetoresistance
CF	Crystal Field
DOS	Density of States
MIT	Metal Insulator Transition

Chapter 1

Introduction

1.1 General Perspectives on Cr-based Chalcospinels

Multifunctional materials are those designed and fabricated to meet specific needs and applications through the tailoring of their properties. Many of these materials are designed to mimic nature, but with improved performances and durability. In present day, materials science is now capable of producing materials built from molecules to complete structures, presenting a specific desirable electronic, magnetic, optical, thermal, or a combination of properties to satisfy previously unattainable performance metrics [1].

Spin-based transport in semiconductor systems has been proposed as the foundation of a new class of devices. For the practical realization of such devices it is important to identify new magnetic systems operating at room temperature that can be readily integrated with standard semiconductors. A promising class of materials for this purpose are the ferromagnetic (FM) chromium-based chalcogenides (ACr_2X_4: A = Cd, Hg, Cu, Zn etc; X=S, Se, Te) that have spinel structure (Chalcospinels) with non-magnetic A elements, show a wide range of electrical and magnetic properties compared to oxides due to increased *d-p* covalency or hybridization of *Cr d* and chalcogen *p* orbitals. Additionally, they serve as important model systems for the fundamental studies of the interaction between charge carriers and magnetic ions.

For normal chromium based spinel structure configuration, the Cr ions ($3d^3$) occupy the B-sites (octahedral environment). However, a splitting of the *d* level into a lower t_{2g} triplet (single occupation in each orbital) and an excited empty e_g doublet is observed due to the influence of the octahedral crystal field. This results in an almost spherical charge distribution and minimal spin-orbit coupling. In the

cases, where A= Cd or Hg, the A^{2+} have filled d^{10} orbitals and therefore do not contribute to the magnetic or orbital degrees of freedom. However, because of the relatively large size of the A-ions, these systems show a tendency to ionic off-center distortions [2].

In some of these Cr-based spinel systems, the competing magnetic exchange interactions and geometric frustration of the magnetic pyrochlore lattice [3] gave origin to interesting phenomena like complex magnetic ground states [4], strong metamagnetism [5,6], and multiferroic behavior [7,8]. Spin-phonon coupling [9] in systems with strong electronic correlations has also been under the attention of researchers.

The following features of Cr-based chalcospinels were of interest in many future technologies.

- Strong flexibility of the structure in hosting various metal ions, differently distributed between the A-site and Cr-site sub-lattices [10].
- Not only a unique combination of magnetic, electrical, and optical properties but also a strong correlation between these properties, associated with the participation of current carriers in exchange interaction [11].
- Magnetic chalcogenide spinels possessing semiconducting properties comprise the most representative group of magnetic semiconductors, promising materials for magneto-optic memory applications [12].
- Exhibit attractive physical properties; such as high optical activity, a sizeable photo-ferromagnetic effect [13], spin-glass state [14].
- Illustrate anomalous behaviour of their magnetoresistance and photoconductivity near the Curie temperature [15], make them candidate materials for many electronic applications.

1. 2 Physical properties of Cr-based Chalcospinels

1.2.1 Crystal Structure

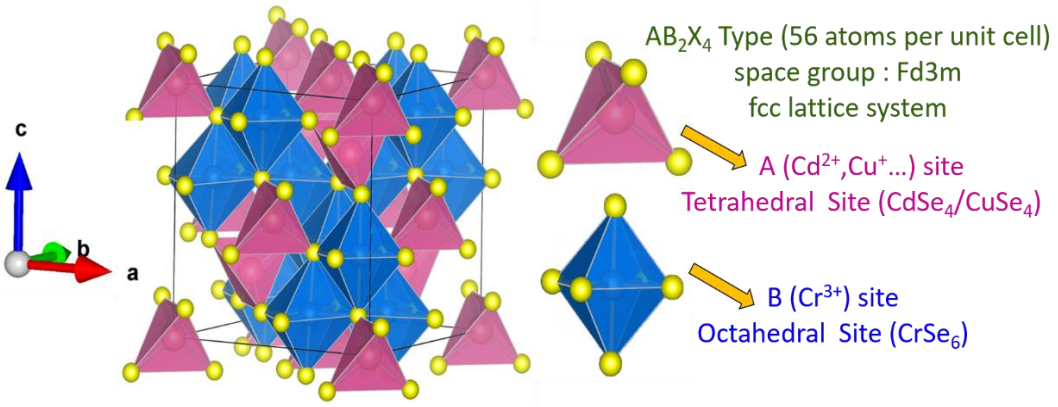

Figure 1.1: Crystal structure of spinel ACr_2X_4, where A sites are the tetrahedrally coordinated ions and are indicated by pink spheres. Octahedrally coordinated Cr^{3+} ions are shown as small blue spheres and anions (O^{2-}, S^{2-}, Se^{2-}, Te^{2-} ions) as large yellow spheres.

Chromium spinels have the composition ACr_2X_4 where A represents a divalent cation such as Cd, Cu, Zn, Hg, Mn, Fe, Co, Ni and X^{2-} represents O^{2-}, S^{2-}, Se^{2-} or Te^{2-} ions. The crystal structure is characterized by a face centred cubic (fcc) arrangement with a large unit cell, containing eight formula units (8 A-cations, 16 B-cations and 32-anions) [16], in a cubic close-packed arrangement of the anions, with the cations located in the interstitial positions. In the spinel crystal two different interstitial positions are present, one called the A-site position where the anions are in the vertices of a tetrahedron having the divalent cation (A^{2+}) at the center and a B-site with the divalent anions in the vertices, of an octahedron having the trivalent cation (Cr^{3+}) in the center. B^{3+} forms a pyrochlore lattice which occupies 1⁄2 of the octahedral voids. A diamond lattice is formed by A^{2+} and includes 1⁄8 of the tetrahedral voids [16]. Fig. 1.1 represents the normal spinel structure, where one can recognize that the A site is tetrahedrally surrounded by four X^{2-} anions (AX_4) and B-site is octahedrally occupied by six X^{2-} anions (CrX_6).

Another related structure is the so-called inversed spinel. Here the tetrahedral sites are occupied by trivalent cations whereas the octahedral sites by divalent cations [17]. A random distribution of the divalent and trivalent cations, in the octahedral B-site is also possible to be formed in the inverse structure. Usually the distribution of cations among the A and B sites can be deduced from their ionic radius. Additionally, different type of spinels can also appear because they are very sensitive to the stoichiometry of the reactant elements in their synthesis and to heating and cooling rates [17]. In this thesis only the normal spinel structure has been considered. The normal spinel structure crystallizes in the cubic *Fd*-3*m* space group [16].

1.2.2 Magnetic Properties

Chromium spinels have been studied for more than half a century because they present an enormous range of magnetic exchange strengths and different magnetic ground states [18-20]. This is mostly due to the different elements in the A and X sites that can integrate into the structure, leading to different lattice constants and thus different Cr – Cr distances. Thus, these compounds to exhibit Curie-Weiss (CW) temperatures (θ_{CW}) ranging from – 400 to 200 K, and low temperature antiferro or ferromagnetic order [18,19].

The magnetic exchange interactions of these compounds can be divided into nearest-neighbor (*nn*) and distant-nearest-neighbor (*nnn*) interactions as shown in Fig.1.2. In a general way, the dominating exchange interaction in these systems are governed by the nearest-neighbour interatomic distances. For small Cr – Cr distances a strong direct antiferromagnetic (AFM) exchange dominates while increasing the distance, the 90° FM Cr – X – Cr indirect superexchange becomes important [21].

Apart from these interactions, Rudolf et al. suggested that in all of these spinels and for all the different interatomic spacings, a weak and complex Cr – X – A – X – Cr antiferromagnetic super exchange (SE) is active [21]. Some

characteristic parameters of chromium spinel compounds (oxides, sulphides and selenides) are summarized in Table 1.1.

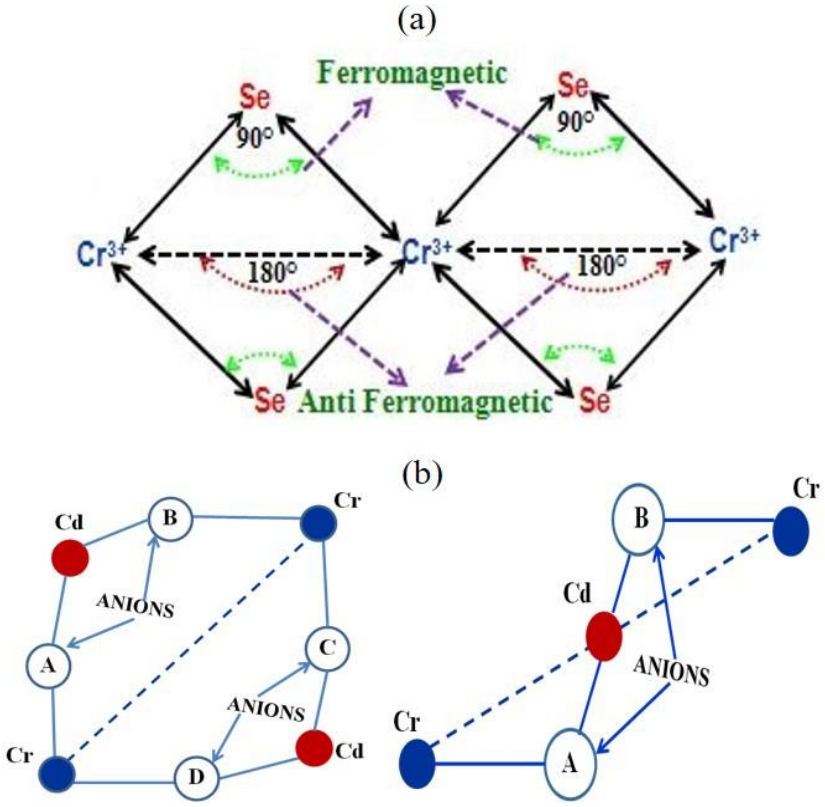

Figure 1.2: Schematic magnetic exchange interactions of (a) nearest neighbour (b) distant neighbour interaction.

Following the Table 1.1, it comes into notice that an increase of the lattice constant leads to an increase of the CW temperatures, going from strongly negative AFM exchange in the oxides to moderately FM exchange in the selenides. In case of oxide spinels, due to the small Cr – Cr distances a strong direct AFM exchange dominates. Increasing the Cr – Cr distance, the AFM interaction becomes weaker and compete with the 90° FM Cr – X – Cr exchange that starts dominating in the selenides. In fact, the Hg, Cd and Cu selenides show high FM ordering temperatures as compared to the small ordering temperatures of the AFM oxides as shown in the Table 1.1. The later exhibit also strong geometrical frustration. In chromium spinel, where chromium is the only magnetic ion, the lack of spin-orbit coupling is verified by the almost spin-only values (S = 3/2), yielding 3.87 μ_B for the paramagnetic (PM) moment of the Cr moments.

Compound	***a (Å)***	μ_{eff} (μ_B)	θ_{CW} ***(K)***	T_M ***(K)***	***Magnetic Order (MO)***
$ZnCr_2O_4$	8.328(2)	3.85	-398	~15	AFM
$MgCr_2O_4$	8.319(3)	3.71	-346	12.7	AFM
$CdCr_2O_4$	8.596(2)	4.03	-71	8.2	AFM
$HgCr_2O_4$	8.658(1)	3.72	-32	5.8	AFM
$CuCr_2S_4$	9.814(3)	3.10	390	377	FM
$ZnCr_2S_4$	9.983(2)	3.86	7.9	~12	AFM
$MgCr_2S_4$	10.108(2)	1.27	-12	80	FM
$CdCr_2S_4$	10.239(2)	3.88	155	85	FM
$HgCr_2S_4$	10.244(1)	3.90	140	22	AFM
$CuCr_2Se_4$	10.348(9)	3.20	465	430	FM
$ZnCr_2Se_4$	10.498(1)	4.04	90	21	AFM
$CdCr_2Se_4$	10.743(9)	3.89	200	106	FM
$HgCr_2Se_4$	10.745(3)	3.82	184	130	FM

Table 1.1: Summary of parameters of some chromium spinels. Lattice constants, effective, PM moment, CW temperature, magnetic ordering temperature and magnetic order. Data taken from Ref. No [3], [5], [8] and [22].

1.2.2.1 A Brief description of the Magnetic Exchange Interactions

The exchange interaction is the largest magnetic interaction in solids (≈ 1 eV) and is responsible for the spontaneous allignment of the spins (either in parallel or antiparallel fashion) below a certain transition temperature (T_C). The exchange interaction might be mediated by different mechanisms depending on the material system under consideration. Here, the most important mechanisms present in spinel systems are described below.

1.2.2.1.1 Direct exchange

The direct exchange arises from a direct overlap of electronic wave functions of the neighbouring atoms and the Pauli exclusion principle, which requires different symmetry properties from the spatial and spin parts of the

electronic wave function. In a two-spin system, the exchange energy is defined as the energy difference between the parallel and antiparallel spin configuration. For a many-electron system, the exchange energy is given by the expectation value of the Heisenberg Hamiltonian

$$\mathcal{H}_{ex} = -2J \sum_{i,j} S_i S_j \qquad (1.1)$$

Where J_{ij} is the exchange integral describing the coupling between two spins or magnetic moments represented by the spin operators $\hat{S}_i$ and $\hat{S}_j$. Depending on the interatomic distances (i.e. orbital overlap) the values of J_{ij} might have positive or negative sign, resulting in the parallel or antiparallel ground state configuration of spins, respectively. The direct exchange is a short-range interaction. If the interatomic distance is too large (i.e. wave function overlap too small) the direct exchange coupling is not strong enough to overcome thermal excitations, giving rise to paramagnetism [23].

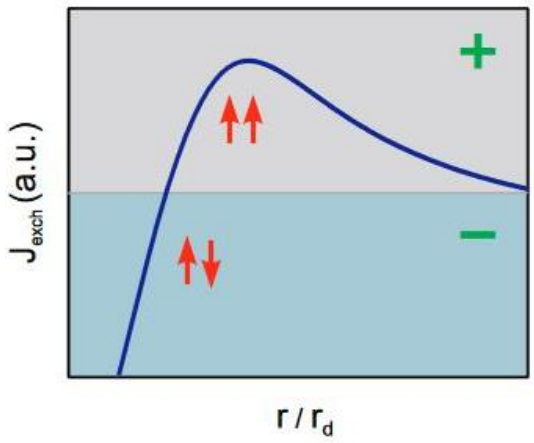

Figure 1.3: Direct exchange energy as a function of the interatomic distance '*r*' divided by the radius of the '*d*' orbital r_d (Ref.). A negative value of the exchange energy results in an antiferromagnetic ground state alignment of spins, whereas a positive value leads to a ferromagnetic ground state coupling. This is illustrated by red arrows. The curve is also known as the Bethe-Slater curve.

1.2.2.1.2 Superexchange

The overall coupling between the cations depends on a combination of direct exchange, excitation and intra-atomic (Hund's Rule) coupling, and is known as super exchange. Superexchange is another kind of indirect exchange interaction and is important in Cr-based spinel chalcogenides. The interaction between the

magnetic Cr atoms is mediated by the diamagnetic selenium though the overlap of the metal's 3*d* and selenium's 4*p* orbitals, and a partial delocalization of the involved electrons (Fig. 1.4). In the case of a parallel orientation (180°)of the magnetic moments located at the metal centers, no delocalization occurs, which makes the antiferromagnetic alignment energetically favourable and a perpendicular orientation (90°) of the magnetic moments makes ferromagnetic allignment. Generally, the size of the superexchange depends on the magnitude of the magnetic moments on the metal atom, the orbital overlap between the metal, and the non-metallic element and the bond angle [24].

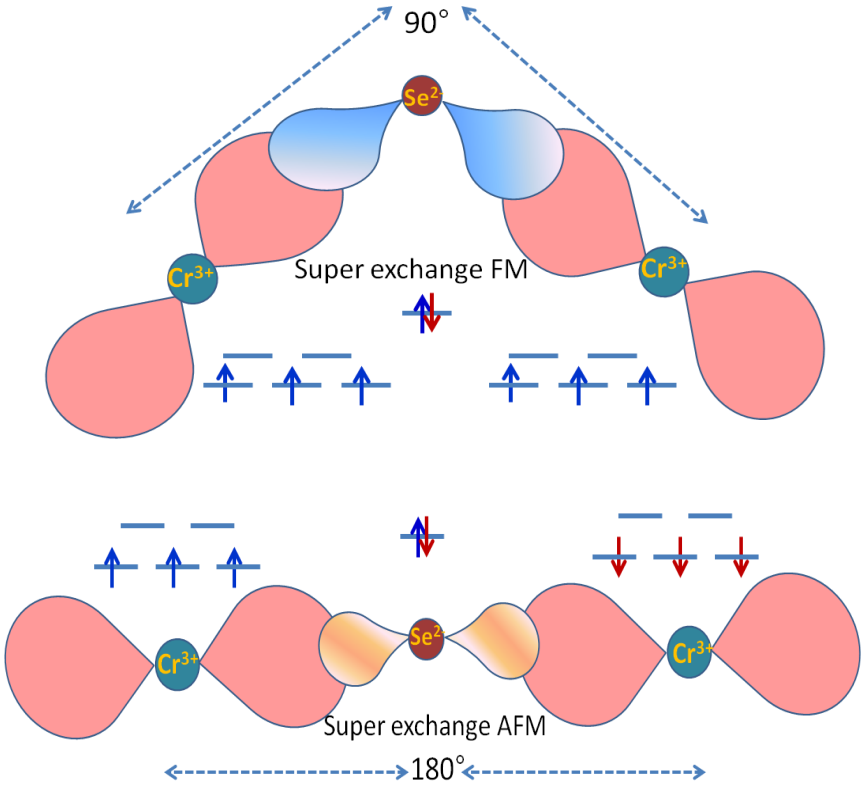

Figure 1.4: A schematic picture showing (a) super exchange interaction favoring FM and AFM coupling between the Cr ions, which is mediated via the Se ion lying in between. The blue dotted line shows the Cr-Se interatomic distance in both cases. Pink lobes around Cr atoms in both the figures and around Se is presenting the spin-polarized charge density, whereas the blue and very light orange lobes around Cr in above figure represent spin-unpolarized charge density. The blue and red arrows present the positive and negative spin densities, respectively.

1.2.2.1.3 Double exchange

Double exchange model proposed by Zener [ref] in 1960s and also known as Zener model, occurs in two magnetic ions separated by non-magnetic atom. The magnetic ions involved in this interaction usually have different oxidation states [25]. The electron can be transferred from a magnetic ion through nonmagnetic ion to the nearest neighboring magnetic ion. The mechanism of this exchange interaction is the hopping of electron from one magnetic ion to the adjacent ion. Spin in magnetic ions that are involved in such exchange interactions need to be in the same state (spin up or spin down) in order to favor or increase the hopping probability. This state corresponds to the more favorable and stable in term of kinetic energy of the system. An illustration of double exchange interaction of Cr^{3+}-Se^{2-}-Cr^{4+} in $CuCr_2Se_4$ chalcospinel is presented in the above Fig. 1.5, where ferromagnetism and metallicity usually come together. The Zener's model was developed to explain the magnetism in the metal. The ferromagnetic critical temperature in double exchange model is proportional to the density of the carriers and bandwidth, with very small values in the low density limit appropriate to diluted magnetic oxides. This model failed to explain the high Curie temperature of diluted magnetic oxides and other diluted magnetic semiconductors.

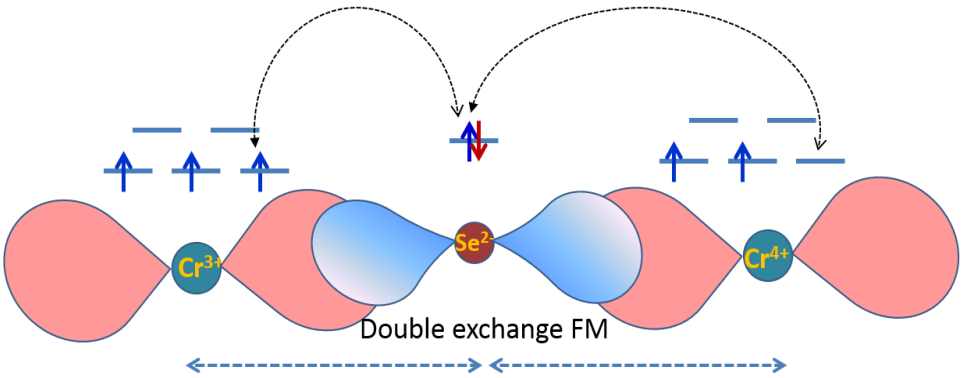

Figure 1.5: A schematic picture showing double exchange interaction favoring FM coupling between the Cr^{3+} and Cr^{4+} ions, which is mediated via the Se ion lying in between. The blue dotted line shows the Cr-Se interatomic distance in both cases. Pink lobes around Cr atoms and blue lobes around Se is presenting the spin-polarized charge density. The black connecting curved dotted line shows the simultaneous charge transfer between Cr and Se atoms. The blue and red arrows present the positive and negative spin densities, respectively.

1.2.3 Vibrational Properties

Raman spectroscopy is also a powerful probe to reveal the structural and vibrational properties in terms of non-stoichiometry, the presence of vacancies, interstitial cations, and defects that may result in activation of phonon modes of spinel Chalcogenides. Optical measurements [26] have revealed the strong coupling between spin system and electronic state which may act as intermediate states in various Raman scattering process. Vibrations of mainly spinel sulfides and selenides with A being Cd, Fe, Mn, and Zn, were calculated by Gupta et al. [Ref] who find the B-X interaction to dominate the A-X interaction. Recently, the Raman measurement explained the origin of large magnetocapacitive effects in stoichiometric single crystals of $CdCr_2S_4$ prepared by Br transport reactions show pronounced phonon anomalies that are evidence for a symmetry reduction and Cr off-centering in the cubic unit cell. [27].

Group theory provides a mathematical tool for studying vibrational properties of crystal structures. As we know for spinel structure, although 56 atoms are present within the spinel's unit cell, only 14 atoms are necessary to construct the simplest primitive cell. The analysis presented first by White and DeAngelis [28] shows that the 42 normal modes of spinel, 3 acoustic modes and 39 optical modes, belong to the symmetry species;

$$A_{1g}(R) + E_g(R) + T_{1g} + 3T_{2g}(R) + 2A_{2u} + 2Eu + 5T_{1u}(IR) + 2T_{2u}. \quad (1.2)$$

The (R) and (IR) identify Raman- and infrared-active vibrational species, respectively. The E_g and T_{2g} modes are doubly and triply degenerate, respectively. The three acoustic modes belong to a single F_{1u} species. A common notation exists in most of the literature to distinguish between the Raman and IR modes belonging to the same representation, and will be used in the present work. The three Raman-active T_{2g} modes are labelled T_{2g} *(1)*, T_{2g} *(2)*, and T_{2g} *(3)*, where T_{2g} *(1)* is the lowest-frequency T_{2g} mode and T_{2g} *(3)* is the highest-frequency mode of this vibrational species. Conversely, the four IR-active F_{1u} modes are labelled v_1, v_2, v_3, and v_4 in descending value of frequency. v_1 is the highest-frequency T_{1u} mode, whereas *v4* is the lowest-frequency mode [28]. Because the spinel structure has an inversion

symmetry element, the active modes are mutually exclusive. Thus, the vibrational modes are either infrared or Raman active, but not both.

The atomic positions within a crystal can be defined as a fraction of the lattice parameter of the unit cell, *a*. The ideal spinel lattice assumes that the (X = O, S and Se) atoms are arranged as a cubic close-packed array. However, the anionic position of many spinels deviates slightly from this ideal geometry, and instead are displaced along a direction perpendicular to the diagonal of the cube, and an anionic parameter, u, is defined, where $u = 3/8$ for the ideal structure. Hill et al. list the mathematical expressions for calculating distances between neighbouring atoms within the spinel lattice. The A-X and B-X bond distances are given by:

$$\text{A-X: } a\sqrt{3}(u - 0.125) \tag{1.3}$$

$$\text{B-X: } a\sqrt{3}u2 - 2u + 0.375, \tag{1.4}$$

where a is the lattice parameter, and u is the anionic (O/S/Se) parameter [29].

1.2.4 Electronic-Transport Properties

Cr-based spinel chalcogenides are attractive for its versatile electric applications as they Exhibit a wide range of electronic properties – from metals to semiconductors (See Table 1.2). Precise, heavy doping of the semiconductor is critical to obtain optimal power factor for both n- and p-type materials. Some of the examples are given as follows; $Cu_{0.5}Co_{0.5}Cr_2Se_4$ for example, are metals having room temperature resistivity (ρ) from about 10^{-4} to 10^{-3} Ω cm. Others, such as the alloys $Cu_{0.5}In_{0.5}Cr_2Se_4$ and $Cu_{0.5}Al_{0.5}Cr_2Se_4$, are semimetals or very low band gap semiconductors with high carrier concentrations.

Spinels having a stable +2 A-site atoms, are usually insulators or high band gap (~1 eV optical gap) semiconductors. These semiconductors can then be doped n- or p-type [30-34]. Exchange split of Cr^{+3} in octahedral coordination will have 3 electrons to completely fill the majority spin T_{2g} orbital (or subsequent band); thus Cr^{+3} may not provide metallic carriers. This is certainly the case for the insulating chromium spinels as shown in Table 1.2. The doping or alloying on the A- site can produce doped semiconductors or metals. However, significant alloying on the A site may result in a polaron semiconductor instead of a metal due to the localization

effects of the distant dopant atoms. Such behavior is more clearly demonstrated in the related defect NiAs-type ACr_2Se_4 chromium selenides [35].

Compound	***Resistivity mΩcm***	$\Delta E_{resistivity}$ ***(eV)***	***Mobility*** (cm^2/Vs)
$FeCr_2S_4$	Insulating (I) (2×10^4)	0.02-0.2	0.3
$CoCr_2S_4$	I	0.01-0.3	0.2
$MnCr_2S_4$	I	0.01-0.3	-
$ZnCr_2S_4$	I	0.6	-
$CdCr_2S_4$	I	0.2-0.6	-
$HgCr_2S_4$	I	0.4-2.0	-
$CuCr_2S_4$	0.9	-	-
$ZnCr_2Se_4$	I	0.3	<2
$HgCr_2Se_4$	I	0.4-2.0	30
$CdCr_2Se_4$	I	0.2-0.6	50
$CuCr_2Se_4$	0.28	-	<10
$Cu_{0.5}Al_{0.5}Cr_2Se_4$	30	-	6
$Cu_{0.5}Co_{0.5}Cr_2Se_4$	30	-	16
$Cu_{0.5}In_{0.5}Cr_2Se_4$	30	-	10

Table 1.2: Room temperature electric properties of some spinel compounds [36].

As mentioned above, among ACr_2X_4 compounds $CdCr_2Se_4$ (with divalent A atoms) show ferromagnetic order below 100 K. In these, the Cr^{3+} ions have integral valency and semiconducting nature. In contrast to this, $CuCr_2X_4$ compounds with monovalent copper are ferromagnetic metals above room temperature. The reasons for the high T_c in these compounds have been in dispute since the beginning of their discovery in 1956 by Hahn et al [37]. The low value of saturation magnetization $5\mu_B$ per molecule as compared to $6\mu_B$ per molecule for Cr^{3+} (d^3) configuration, along with metallic conduction has been the main subject of discussion for these compounds. Three different models for the electronic

structure of $CuCr_2X_4$ have been proposed to explain properties like p-type metallic conductivity, saturation magnetization of about $5\mu_B$ per molecule, high Curie temperatures well above room temperature and the absence of magnetic moment at the copper sites [38-40].

Three different proposed models are as follows:

1. In the Lotgering model, the formal valence state of atoms has been suggested as $Cu^{+}[Cr^{3+}Cr^{4+}]X_4$ [38]. Here it is assumed that the diamagnetic Cu^{+} ion in d^{10} configuration occupies the tetrahedral sites and that the ferromagnetic moment arises from a parallel alignment of the spins of Cr^{3+} and Cr^{4+} present at the octahedral sites. The metallic conduction and ferromagnetic interaction are attributed due to double exchange between Cr^{3+} and Cr^{4+} (transfer of electrons between Cr^{3+} - Cr^{4+} without the change of spin).
2. The Lotgering and van Stapele model, is the improved version of Lotgering model $Cu^{+}[Cr^{3+}Cr^{4+}]X_4$ [39]. The Cu ions are monovalent and diamagnetic in the d^{10} configuration. The t_{2g} orbitals of Cr^{3+} and Cr^{4+} ions form a narrow unfilled t_{2g} band. Since this band lies below the top of the valence band constructed mainly of the *p* orbitals of the chalcogen ions X, there exist spin polarised holes in the valence band which are responsible for conduction as well as the strong ferromagnetic exchange interaction between Cr ions. The observed total magnetization of $5\mu_B$ per molecule results from a moment between $5\mu_B$ and $6\mu_B$ localized on the Cr ions and a corresponding negative polarization of the holes.
3. The Goodenough model, $Cu^{2+}[Cr^{3+}\ Cr^{3+}]X_4$ suggests that the Cu ions are divalent in the d^9 configuration and all of the Cr ions are trivalent [40]. There exist delocalized holes in the Cu *3d* band which are responsible for the metallic conduction. The ferromagnetic coupling between the Cr^{3+} moments is enhanced by superexchange like indirect interaction via the collective Cu *d* holes, giving rise to a moment $6\mu_B$ per molecule. There is also an antiparallel spin density due to Cu *d* holes, having a net moment of $-1\mu_B$ per molecule. This gives total magnetic moment of $5\mu_B$ per molecule.

1.3.4.1 Conduction Mechanism in Metallic Spinels

In metallic Cr-based chalcospinels, temperature dependence of the of the resistivity ρ in general described by the Bloch–Grüneisen formula:

$$\rho(T) = \rho_0 + A\left(\frac{T}{\Theta_R}\right)^n \int_0^{\theta_R} \frac{x^n}{(e^x-1)(1-e^{-x})}\,dx \quad (1.5)$$

where ρ_0 is the residual resistivity due to defect scattering, A is a constant that depends on the velocity of electrons at the Fermi surface, the Debye radius and the number density of electrons in the metal. Θ_R is the Debye temperature as obtained from resistivity measurements and matches very closely with the values of Debye temperature obtained from specific heat measurements. n is an integer that depends upon the nature of interaction [41]:

- n = 5 implies that the resistance is due to scattering of electrons by phonons
- n = 3 implies that the resistance is due to s-d electron scattering
- n = 2 implies that the resistance is due to electron–electron interaction or electron magnon single scattering
- n = 1 implies that resistance is due to electron-phonon interaction.

1.3.4.2 Conduction Mechanism in Semiconductor

In Cr-based chalcospinels, semiconduction in general described by Arrhenius equation $\rho = \rho_0 e^{(E_a/k_B T)}$, Where, k is Boltzmann constant, E_a activation energy of conduction, ρ_0 is a pre-exponential factor [42] and also can be explained on the basis of small polaron hopping mechanism [36]. The small polaron are trapped carriers which exhibits thermally activated phonon assisted hopping from one site to other. The atomic displacement generally produces a potential well for the excess carriers, if this carrier induced potential well is sufficiently deep, the carrier occupies a bound state as it is unable to move without alteration of the position of the surrounding atoms. This unit comprising of trapped carriers and its induced lattice deformation is the polarons and since it is confined to a small region it is termed as small polaron. The temperature dependence of electrical resistivity is given by the relationship (modified version of Arrhenius equation), $\rho = \rho_0 T^n e^{(E_a/k_B T)}$ Where, k_B is Boltzmann constant, E_a activation energy of conduction, ρ_0 is a constant which is the energy required for the hopping of the electron or hole [36].

In case of some doped Cr-based chalcospinels, the conduction of electricity can be described by localized electrons, involves a mechanism very different from the conduction mechanism in a metallic system. Since the average velocity of the electron in a localized state is zero it cannot, by itself, carry current through the system. In order to carry current, the electron in a localized state has to move to another localized state which can accommodate it, at some other spatial position. These electron transitions are brought about by some other agent, which are usually phonons for disordered semiconductors at low temperature. Such a method of charge transport is called Mott type variable range hopping (VRH) transport. An important difference between metallic conduction and variable range hopping transport in disordered systems, is in the role of the phonons. Whereas in metals, phonons (lattice vibrations) are a factor which restrict the mobility of the electrons through scattering, in the systems of electrons in localized states, it is the electron-phonon interaction which makes charge conduction at all possible. Mott type of VRH model described by $\rho = \rho_{\infty}T^{n}\exp(T_0/T)^{p}$, where $p = 1/(d+1)$, 'd' being the dimensionality of the system [43] and the value of characteristic temperature (T_0) in Mott VRH model is given by $24/\pi L^{d}k_{B}N(E_F)$, where L is localization length of trapped charge carriers, $N(E_F)$ is density of the localized states at Fermi level and 'd' is the dimensionality of the system.

1.3 Motivation

Among all the spinel structured-magnetic material, Cr-based chalcospinels $CdCr_2S_4$, $CdCr_2Se_4$, $CuCr_2S_4$, $CuCr_2Se_4$, $ZnCr_2S_4$, $ZnCr_2Se_4$ are very well known for their diverse magnetic and electronic transport properties.

1.3.1 $CdCr_2S_4$ and $CdCr_2Se_4$ Systems

Since its discovery in the 1960s, $CdCr_2S_4$ and $CdCr_2Se_4$ has been the focus of many studies from fundamental properties to applications, *e.g.* already in 1965, its magnetic properties were investigated by *Baltzer et al.* [20], who found a ferromagnetic insulator state below 97 K and 130 K respectively. Since then, many other studies have been performed searching for an explanation for the unusual nature of some experimental results, like an abnormal negative thermal expansion

at low temperatures [44] with a simultaneous broadening of the diffraction lines [45], which was found to correspond to a mode softening in both the spinel structure. Furthermore, a strong blue shift of the absorption edge [46], accompanied by an abnormally large phonon shift and damping effects were observed near the magnetic transition temperature T_C [47].

However, a very recent discovery of CMR in single crystalline $CdCr_2S_4$ spinel by Sun et al [48], once again, regenerated the interest on many of these type of chalcospinels. Moreover, $CdCr_2S_4$ that exhibits four colossal effects (the magnetocapacitive, electrocapacitive, electroresistive, and magnetoresistive effects) [48]. Since then $CdCr_2S_4$ spinel has been exhaustively studied due to the mutual coupling between magnetic and electric properties and for being potential candidate for semiconductor spintronic devices.

The coexistence of ferromagnetism and relaxor-like ferroelectricity together with colossal magnetocapacitance claimed in a seminal paper by J. Hemberger [7] has revived the attention on $CdCr_2S_4$. Later, the discovery of dielectric relaxational dynamics above the Curie temperature (T_C), responsible for the strongly increased dielectric permittivity of $CdCr_2S_4$ [49,50], has driven an intense debate in the research community [7,51].

The debate started with Hemberger et al [7] description of $CdCr_2S_4$ as a multiferroic relaxor, due to the observed relaxor-like dielectric properties and colossal magnetocapacitance (surpassing 500%). However, *Catalan et al* [50] argued that these results could originate from a conductive artefact. They went further, arguing that the polarization hysteresis loops published by Hemberger et al [7] had an uncharacteristic ferroelectric shape and that in fact it resembled more those of a lossy dielectric, like in the case of some semiconducting thiospinels.

Sun et al observation of a glassy dipolar state near T_C ~85 K and a ferroelectric ordering near ~56 K for single crystalline $CdCr_2S_4$ [52]. *Ramirez et al* [53] had already suggested that in naturally occurring magnetic spinels, geometric frustration within a room temperature highly symmetric cubic lattice could drive the relaxor-like freezing observed at low temperatures.

Gnezdilov et al [27] observed pronounced phonon anomalies by Raman scattering experiments, indicating a possible symmetry reduction and Cr off-Centering in the cubic unit cell of single crystal $CdCr_2S_4$. Interestingly, the

discovery of phonon anomalies at temperature below 130 K by means of Raman light scattering suggests that the electronic polarizability was enhanced by the Cr-S distance and respective bond hybridization [27]. Still undisclosed is the origin of the strong coupling of magnetization and dielectric permittivity in this compound. A coupling via exchange-striction, *i.e.*, volume changes arising from the magnetic exchange energy was suggested [51].

Similarly, $CdCr_2Se_4$ is also an exceptional magnetic material where large magneto caloric effects (MCE) have been investigated theoretically and experimentally and looked upon as a promising magnetic refrigerant material [54]. These materials allow strong interactions between the mobile carriers and the degree of order of the localized spins resulting in fundamental interesting properties like Seebeck and Hall effect [55], Spin-glass state [56] & high optical activity [57].

On the other hand, Se-based materials though less explored, show a wide range of electrical and magnetic properties due to increased covalency and stronger hybridization of Cr *d* and Se *p* orbitals. Moreover, the doped Cd-chromium chalcogenides have been revisited in recent years for wide technological application because of their unusual transport properties characterized by a large, temperature dependent magneto-resistance [48].

Though much scientific effort has been dedicated to unveil different phenomena and to settle multiferroism in $CdCr_2Se_4$ system, the understanding of these phenomena still needs to be explored clearly, which requires an adequate description of the structural, magnetic and charge degrees of freedom. Our interest in $CdCr_2Se_4$ and its substitutional variants, grew from this fact. Detailed local structural characterization using technique like EXAFS and Raman spectroscopy presents a good opportunity to shed some light onto this material and that on the future our findings can be conveyed onto other ferromagnetic semiconductor materials.

1.3.2 $CuCr_2Se_4$ System

It is well established that $CdCr_2Se_4$ is a ferromagnetic semiconductor while $CuCr_2Se_4$ is a ferromagnetic metal with relatively high Curie temperature ($T_C \approx 430$

K) [58]. It possess a pronounced magneto-optical Kerr effect near-infrared photon energy at room temperature [59].

An easily noticed difference between them is that all of the A site cations are definitely divalent for the $CdCr_2Se_4$, whereas it is not clear whether the Cu ion is divalent or monovalent in the metallic spinels. Therefore, the origin of magnetism for $CuCr_2Se_4$ has been in controversy for many years. Three proposed models have been famously discussed in this contest: (a) by Lotgering, that assumes the valence distribution to be $Cu^{1+}(Cr^{3+}Cr^{4+})Se^{2-}$ with ferromagnetism and metallicity attributed to double-exchange (DE) mechanism between Cr^{3+} and Cr^{4+} [38],(b) by Goodenough, who proposed a divalent state of Cu^{2+} with moment antiparallel to Cr^{3+} via 90º superexchange mediated through the completely filled Se *4p* states [40], (c) by Lotgering and van Stapele, who modified the second model to accommodate accumulated experimental results, which shows that the DE is not relevant to the magnetism of $CuCr_2Se_4$ [39]. They presumed that the spinel $CuCr_2Se_4$ contained Cu^+ ($3d^{10}$) ions as in their original model, but that the chromium ions were all trivalent Cr^{3+} ($3d^3$) ions, so that the monovalent Cu induces one hole in a ligand *p* orbital and these holes are responsible for the electrical conduction and also for the strong ferromagnetic exchange between the Cr^{3+} ions.

Among these three models, the main difference resides in the valence states, which determine the conduction carriers and magnetic contributions of the Cr and Cu ions. The seemingly simple issue, however, turns out to be very difficult to settle. Studies with various spectroscopic tools have suggested monovalency in the Cu ion [60-64] while magnetic studies do not exclude the possibility that divalent Cu ions exist [65,66]. The XMCD result also shows that the double exchange is not relevant in $CuCr_2Se_4$ and suggests that Cu *d* holes could play a crucial role in the intriguing magnetic and electrical transport properties of $CuCr_2Se_4$ [67].

Band structure calculations for this compound predict a highly spin-polarized DOS with half-metallic properties for suitably doped compositions [68]. In case of $CuCr_2Se_4$, the chromium d band is split by the cubic crystal field into a t_{2g} and an e_g band. In the majority spin channel, the hybridization between the Se 4*p* and Cr 3*d* splits the selenium band and induces a gap just below the Fermi energy. Consequently, one hole appears in the upper branch of the selenium band

for majority spins. Complete spin polarization of the charge carriers can be achieved by tiny electron doping [68].

1.3.3 $ZnCr_2Se_4$ System

Another similar composition is $ZnCr_2Se_4$, where FM and AFM interactions exist in almost equivalent strength giving rise to a strong magnetic frustration. Eventually the system orders antiferromagnetically at T_N = 21 K [69]. Despite strong FM exchange reflected in a large positive value of the Curie-Weiss temperature θ_{CW} =115 K [69]. The magnetic phase transition is of first order, as evidenced by sharp anomalies in the specific heat and thermal expansion [5].

The magnetic phase transition can be suppressed by an external magnetic field. $ZnCr_2Se_4$ reveals negative thermal expansion (NTE) below 75 K down to T_N and extremely large magnetostriction [5]. The magnetic transition is accompanied by small structural distortions with a lowering of the symmetry from cubic Fd-3m to tetragonal I41 /amd [70] or orthorhombic Fddd [71]. The magnetic origin of the structural distortions is most clearly evidenced in the phonon spectra of $ZnCr_2Se_4$. IR spectroscopy revealed a pronounced splitting of the IR-active phonon modes at T_N that can be completely suppressed by the application of an external magnetic field [72].

1.4 Selection of Samples for present study

The exotic intercorrelated structural, magnetic and electronic-transport phenomena invoked for describing the Cr -based chalcospinels, not only make these materials as promising candidates for technological advances, but also present the fertile grounds to understand the fundamental physics aspects in design of new smart materials.

In this present work, substitutions of different kind of elements with varying ionic radii, charge valence and magnetic or non-magnetic nature have been performed at various tetrahedral (Cd/Cu/Zn site), octahedral Cr-site and anion site of $CdCr_2Se_4$, $CuCr_2Se_4$ and $ZnCr_2Se_4$ chalcospinels. All the substituted polycrystalline samples were prepared by standard solid-state reaction method.

1.5 Objectives of the present study

- Identify the change in the valency of Cr ions by doping or deviation from stoichiometry in the all the substituted $CdCr_2Se_4$, $CuCr_2Se_4$ and $ZnCr_2Se_4$ compositions and its effect on its magneto-structural properties.
- Substitution of the different elements (in the A, Cr and X sites), leading to different lattice constants and thus different Cr – Cr and Cr-Se distances may cause lattice distortion at their local environment. So, at first our aim is to explore the origin of local lattice distortions and what extent does these distortions impact the magnetic properties of these chalcospinel compounds.
- To change the *3d* density of states at Fermi level and affect the double-exchange pairs impacting magnetism in substituted $CuCr_2Se_4$ chalcospinels, in order to obtained modification in the magneto-transport properties.
- To determine the influence of nonmagnetic Ti substitution on the crystal structure, electronic, magnetic and transport properties of $CuCr_{2-x}Ti_xSe_4$ compounds.
- To understand the uncommon magnetic behavior in $Cd_{1-x}Cu_xCr_2Se_4$ and $Zn_{1-x}Cu_xCr_2Se_4$ spinels through Extended X-ray absorption spectroscopy (EXAFS) and X-ray absorption near edge spectroscopy XANES analysis.

1.6 Outline of the thesis

The above study with systematic elaboration will be compiled in the form of a thesis. The organization of this thesis is as follows;

Chapter 1: This chapter provides background and motivation to the fundamental and application of Cr-based spinel chalcogenide systems with inclusion of the detailed information on the crystal structure, magnetic, vibrational and electronic-transport properties. It also defines the objective of the study/thesis.

Chapter 2: This chapter delivers about the synthesis method of sample preparation by solid state technique. It also includes a small note on each characterization techniques employed in this work.

Chapter 3: This chapter systematically explained the crystal structure and magnetic property correlation in $Cd_{1-x}M_xCr_2Se_4$ (M = Sb, In, Sn) chalcospinels.

Chapter 4: This chapters presents evidence and origin of local lattice distortion and spin phonon coupling in $CdCr_2Se_{4-x}S_x$ spinel chalcogenides.

Chapter 5: This chapter gives the detailed study on magnetic and transport properties of transition metal doped $CuCr_2Se_4$ spinel system.

Chapter 6: This chapter briefly discourses about the influence of non-magnetic Ti substitution on magnetic and transport properties of $CuCr_2Se_4$ and also establish the valence state of each atom at their local environment for $CuCr_{2-x}Ti_xSe_4$ selenospinels.

Chapter 7: This chapter deals with the unusual magnetic behavior and valence state of $Cd_{0.9}Cu_{0.1}Cr_2Se_4$ and contrasting magnetic and transport properties of $Zn_{1-x}Cu_xCr_2Se_4$ chalcogenide spinel systems.

Chapter 8: Last chapter concludes the present study by summarizing all the obtained results and the possible future scope of this current research work

Chapter 2

Synthesis Method and Experimental Techniques

2.1. Introduction

Before any kind of analysis is taken up, it is important to obtain single phase and well characterized samples. The complete characterization of any material consists of phase analysis, chemical composition, structural, transport, electrical and magnetic studies, which have strong bearings on the physical properties of materials. In this chapter, method used for the synthesis of Cr-based spinel chalcogenides has been described in great detail. Also, different instruments and analytical techniques used to characterize these Cr-based spinel chalcogenides are briefly described.

2.2. Synthesis Method

Most widely used method for synthesizing the polycrystalline solids (powders) is the direct reaction of a mixture of starting materials.

In this dissertation, the steps involved in solid state reaction method for synthesizing single phase polycrystalline Cr-based spinel (ACr_2X_4) type metal chalcogenide samples are described below:

1. All starting materials in elemental form, having 99.999% purity were taken in (1:2:4) stoichiometric ratios, weighed for desired composition using high precision electronic weighing balance (Make: Mettler Toledo).
2. In order to avoid oxide formation in the chalcogenides, all the weighed elements were placed in a glove box with controlled Nitrogen gas atmosphere.
3. This mixture of solids was thoroughly ground using agate mortar and pestle for approx. 5-6 hrs. to form homogeneous fine powder.
4. The mixed powder was pressed into a pellet using uniaxial hydraulic press with pressure of about 3.0-5.0 Ton.

5. Afterwards, the mixture was kept in a clean quartz ampoule and sealed under vacuum at a pressure of 10^{-5} mbar created using a diffusion pump based vacuum pumping system (Make: Hind Hi. Vac.).
6. This evacuated quartz ampoule was kept in a programmable box furnace for heat treatment.
7. In order to obtain single phase composition, repeated grinding, vacuum sealing and annealing were required.

Once the final heat treatment was over, the sample is taken out of the quartz ampoule, ready for further characterization. The schematic of entire synthesis process is illustrated in Fig. 2.1. This above mentioned solid state reaction route has proved to be the most suitable method for synthesizing reproducible samples of Cr-based spinel chalcogenides. The exact synthesis process for all the samples are given in the section below.

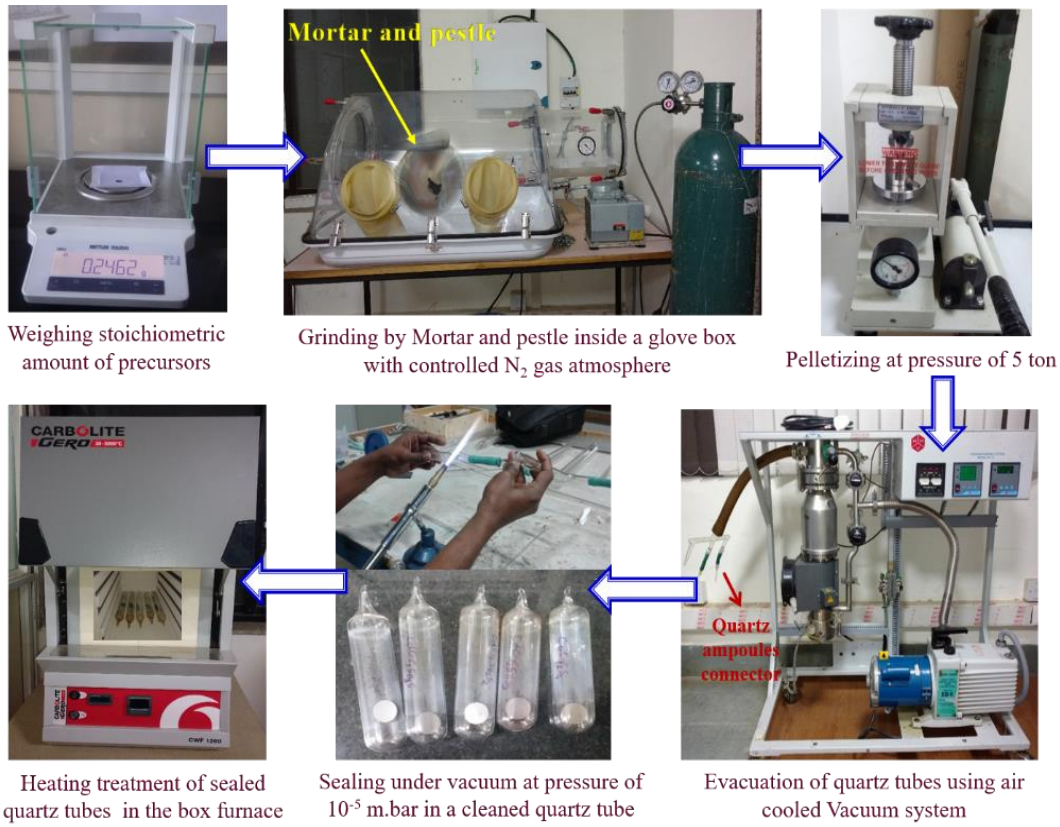

Figure 2.1: Steps involved in the solid-state synthesis of the polycrystalline Cr-based spinel chalcogenides.

2.2.1 Synthesis of Cd- and Se-site substituted compositions

For synthesis of $[Cd_{1-x}M_x]Cr_2Se_4$ (M = Sb, In, Sn), $CdCr_2Se_{4-x}S_x$ and $Cd_{0.9}Cu_{0.1}Cr_2Se_4$ samples, two times vacuum sealing and different annealing process is required to get exact composition.

a) **Heating**

28˚C (RT) $\xrightarrow{5\ K\ /min}$ 650˚C

Dwelling at 650˚C for 48 hr

Cooling

650˚C (RT) $\xrightarrow{5\ K\ /min}$ 28˚C (RT)

b) **Heating**

28˚C (RT) $\xrightarrow{5\ K\ /min}$ 800˚C

Dwelling at 800˚C for 96 hr

Cooling

800˚C (RT) $\xrightarrow{5\ K\ /min}$ 28˚C (RT)

2.2.2 Synthesis of $Cu_{1-x}M_xCr_2Se_4$ with (M = Mn, Fe, Co, Ni, Zn) and (x = 0 and 0.1)

Heating

28˚C (RT) $\xrightarrow{1˚C\ /min}$ 200˚C

Dwelling at 200˚C for 21 hr 10 min.

200˚C $\xrightarrow{1˚C\ /min}$ 400˚C

Dwelling at 400˚C for 20 hr 40 min.

400˚C $\xrightarrow{1˚C\ /min}$ 600˚C

Dwelling at 600˚C for 20 hr 40 min.

600˚C $\xrightarrow{1˚C\ /min}$ 800˚C

Dwelling at 800˚C for 44 hr 40 min.

800˚C $\xrightarrow{1˚C\ /min}$ 900˚C

Dwelling at 900˚C for 23 hr.

Cooling

900˚C $\xrightarrow{1˚C\ /min}$ 28˚C (RT)

A complete homogenization could be obtained by following this above heat treatment two times. After being slowly cooled down, the synthesized powder was homogenized by grinding in agate mortar & pestle for minimum 2 hrs.

2.2.3 Synthesis of $CuCr_{2-x}Ti_xSe_4$ with $0 \leq x \leq 1$

Heating

28°C (RT) $\xrightarrow{1°C/min}$ 850°C

Dwelling at 850°C for 144 hr (6 days)

Cooling

850°C (RT) $\xrightarrow{1°C/min}$ 28°C (RT)

A complete homogenization could be obtained by following this above heat treatment two times. After being slowly cooled down, the synthesized powder was homogenized by grinding in agate mortar & pestle for minimum 1 hrs.

2.2.4 Synthesis of $Zn_{0.9}Cu_{0.1}Cr_2Se_4$

a) **Heating**

28°C (RT) $\xrightarrow{1°C/min}$ 850°C

Dwelling at 850°C for 168 hr (7 days)

Cooling

850°C (RT) $\xrightarrow{1°C/min}$ 28°C (RT)

b) **Heating**

28°C (RT) $\xrightarrow{1°C/min}$ 850°C

Dwelling at 850°C for 72 hr (3 days)

Cooling

850°C (RT) $\xrightarrow{1°C/min}$ 28°C (RT)

2.3. Structural Characterization Techniques

2.3.1. Powder X-Ray Diffraction Technique (PXRD)

X-ray diffraction (XRD) is an extremely useful and non - destructive analytical technique for determining the crystal structure chemical analysis, stress measurements, phase equilibria and particle size [73]. We used powder XRD

method for confirming the phase of a sample. For a thorough discussion of X-ray diffraction method, the standard textbook by Cullity [74] and Guinebretiere [75] may be consulted. In an X-ray diffraction experiment, the X-ray is produced by an X-ray tube. The beam is then monochromatized to select only the radiation with a specific wavelength which is then directed towards a crystalline sample. The sample reflects the X-ray when the incident beam is at a specific angle with respect to the face of the crystal.

The incoming X-ray beam is reflected by the electrons bound to the atoms in the lattice. Consider the incoming X-ray beam reflected to the detector with paths A-B-C and D-E-F in Fig. 2.2. At a certain angle θ, the difference in the path length between path A-B-C and D-E-F is an integral multiple of the X-ray wavelength. This results in a constructive interference because the radiation from both paths are in phase. Therefore, the detector will show a significant increase in intensity at this particular angle, hence a peak. The condition for a peak to occur is;

$$2dsin\theta = n\lambda \tag{2.1}$$

where 'd' is, the plane spacing and 'λ' is the wavelength of the X-ray. Equation (2.1) is known as the Bragg's law. In the picture, only one set of planes of the lattice is considered, but there are other sets of planes of the lattice which are indexed using the Miller indices *hkl*. Accordingly, the interplanar distance d should be written as d_{hkl}. The data obtained from a powder X-ray experiment are the intensity as a function of 2θ. Therefore, knowing the position of the peak in (2θ) and the Miller indices (*hkl)* of the peak, the interplanar distance of the set of planes with a specific *hkl* can be obtained.

For cubic lattice, the interplanar spacing, d_{hkl} can be related to the lattice parameter 'a_0' and Miller indices, (*hkl*), by an equation (2.2).

$$d_{hkl} = \frac{a_0}{\sqrt{h^2 + k^2 + l^2}} \tag{2.2}$$

From the d-spacing, phases can be identified in a sample using the standard reference files from the JCPDS database or PDF (Powder Diffraction File database) published by the International Centre for Diffraction Data, ICDD.

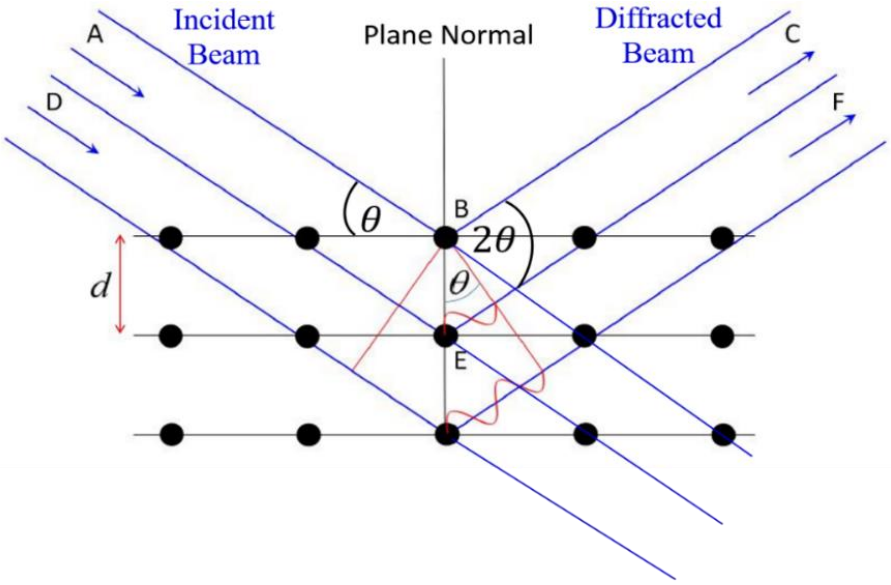

Figure 2.2: Illustration of x-ray diffraction, showing the incoming x-ray beam, which is reflected by the planes of the crystal. At a certain angle θ, the difference in the length of the path of the incoming and outgoing beams between the planes is integral multiples of the wavelength, resulting in a constructive interference.

Instrument specifications for Laboratory XRD [76]:

Make: RIGAKU; Model: Smart Lab; Max Power: 3 kW

X-Ray generator / Target: Cu anode (K_α=1.544Å)

Optics: Bragg Brentano, Parallel beam

Diffractometer with laboratory X-ray source was used to study all of the samples in this dissertation, but for the samples in the $Cd_{1-x}M_xCr_2Se_4$, where M = Sb, Sn and x = 0.05, 0.1 series, temperature dependent X-ray diffraction was carried out using the synchrotron source (λ = 0.7948 Å). As will be discussed in the following chapter, resolution provided by synchrotron radiation was required to check the possibility of phase transition in these samples. The measurement has been performed at the Indian beamline at KEK, Photon factory, Japan (as displayed in the Fig. 2.3).

A synchrotron is a particle accelerator that uses bending magnets to radially accelerate charged particles causing them to emit electromagnetic radiation at a specific wavelength. Synchrotron radiation is far more intense than laboratory X-ray source with excellent signal to noise ratio for even small samples.

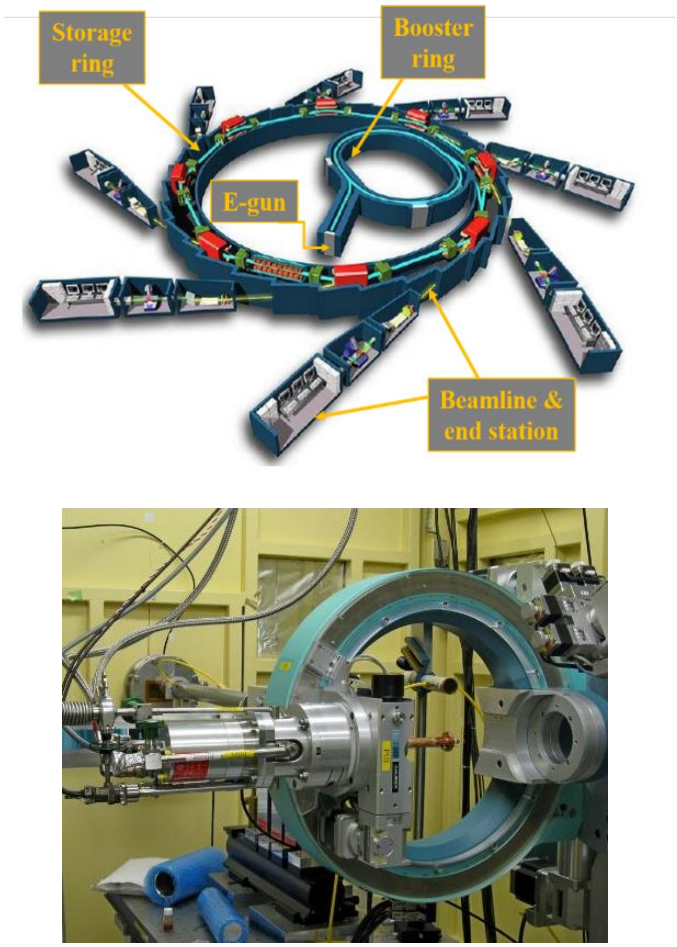

Figure 2.3: Image of the low temperature high resolution XRD system at Indian beamline, BL18B, KEK, Photon Factory, Japan [77].

Instrument specifications of synchrotron XRD [77]:

- The four-circle goniometer with a cryostat for low temperature measurement, Aluminized Mylar window as the radiation shield and Be window for the vacuum shield.
- Low Temperature Range: 4.2 K – 250 K
- Usable range of synchrotron energy: 7 to 20 keV
- Detector: point detector or 100 K 2D Pilatus detector for data collection

2.3.1.1 Rietveld Refinement

The Rietveld refinement method, named for Hugo Rietveld who developed the method, incorporates all of the variables that affect diffraction peaks, and involves

a least square fit to refine structural information of the sample [78]. In the Rietveld method, diffraction patterns are simulated on the basis of an initial crystal structure model, and then a number of parameters are refined by a regression algorithm to minimize the difference between the simulated and experimental patterns. In this method, one builds a simulated model of the lattice which consists of atoms of specific elements and their positions in the lattice, the symmetry of the lattice, and the size of the lattice. In addition, instrument-specific parameters are also considered, which include the width of the peaks, polarization factor, peak asymmetry factor, and zero correction. The instrument-specific parameters are obtained by performing an XRD experiment and a Rietveld refinement on a standard calibration sample. Once obtained, the instrumental parameters are fixed in the refinement. In the Rietveld refinement, one tunes the sample parameters to obtain the best fit to the experimental data. Parameters used for the Rietveld refinement are categorized on the instrument and sample based factors as mentioned in the Tab. 2.1.

	Instrumental Factors	**Sample Based Factors**
Peak Position	Wavelength, Zero-point error, Sample Height	Unit cell dimensions
Peak Shape	Diffractometer geometry, slit sizes, Type of detectors, X-ray source	Size of crystallites, Strain, Defects
Intensity	Amount of sample, Lorentz- polarization and other diffractometer factors	Atomic coordinates, Temperature factors, Absorption, Site Occupancies
Background	Air scatter, Detector noise, Sample holder	Fluorescence, Disorder

Table 2.1: The parameters used for the simulation of the powder X-ray pattern.

The indication of good fit is measured in terms of *R* values. The weighted profile *R* value is termed as R_{wp} and is given as

$$R_{wp} = \left[\frac{\sum_i w_i[y_i\,(observed) - y_i(calculated)]^2}{\sum_i w_i[y_i(observed)]^2}\right]^{\frac{1}{2}} \quad (2.3)$$

where, y_i (observed) is the observed intensity with step size *i*, y_i (calculated) is the calculated intensity and w_i is the weighting factor. The quantity R_{wp} should actually minimize during a Rietveld refinement. For the best fit the R_{wp} value should tend to R_{exp}.

$$R_{exp} = \left[\frac{(N-P)^2}{\sum_i^N w_i[y_i(observed)]^2}\right]^{\frac{1}{2}} \quad (2.4)$$

where, *N* is the number of observations and *P* is the number of parameters. R_{exp} reflects the quality of the statistics expected *R* value. The goodness of fitting is ratio of R_{wp}/ R_{exp} and given as χ^2;

$$\chi = \frac{R_{wp}}{R_{exp}} \quad (2.5)$$

If the R_{wp} is approaching the R_{exp} then χ^2 should approach unity which depends on the scan period. The most important R factor considered for the structural studies is the Bragg *R* factor, R_{Bragg};

$$R_{Bragg} = \frac{\sum_{hkl}|I_{hkl}(observed) - I_{hkl}(calculated)|}{\sum_{hkl}|I_{hkl}(observed)|} \quad (2.6)$$

where $I_{hkl} = mF_{hkl}^2$, I_{hkl} being the intensity of pattern and '*m*' the multiplicity factor. The smaller the R_{Bragg} value better is the fitting with the observed data.

In this work, the Rietveld refinement of XRD pattern was performed by using software FULLPROF suite [79].

2.3.2 Energy dispersive X-ray Spectroscopy (EDX)

Energy dispersive X-ray analysis spectroscopy is commonly known as EDXS or EDS or EDX. It is a technique used for identifying the elemental composition of the unknown sample. The EDX analysis system works as an integrated feature of field emission scanning electron microscope (FESEM). The schematic of an energy dispersive spectrometer is shown in Fig. 2.4, where the EDX detector is a solid-state device, consisting of a semiconductor.

The working principle of EDX is shown in Fig. 2.5. the electron beam is bombarded to the sample specimen that knocks out electrons from the inner shell.

A position vacated by an ejected inner shell electron is eventually occupied by a higher-energy electron from an outer shell. In this process, the transferring outer electron gives up some of its energy by emitting a photon. the atom of every element releases X-rays with unique wavelength. one can identify the element from the position of the peak in the EDX spectrum, while the intensity of the peak is related to the concentration of that element. Thus, the composition of sample can be known [80].

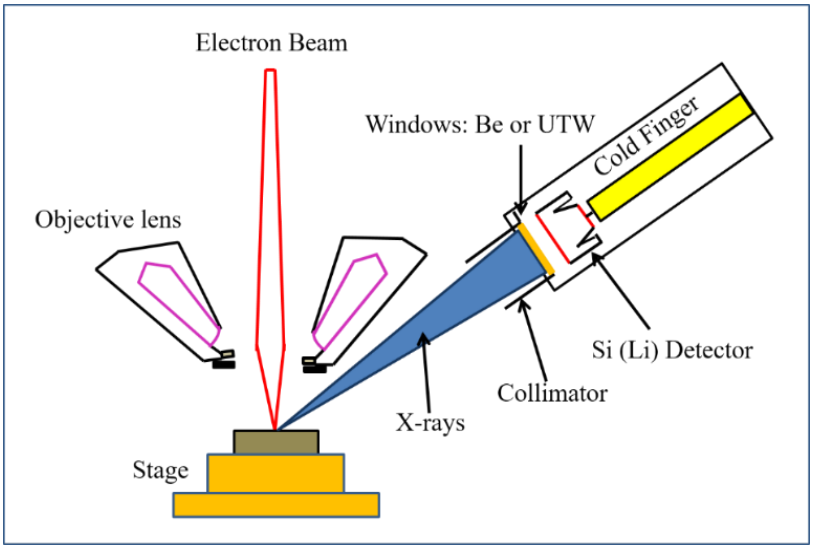

Figure 2.4: Schematic of an Energy Dispersive Spectrometer.

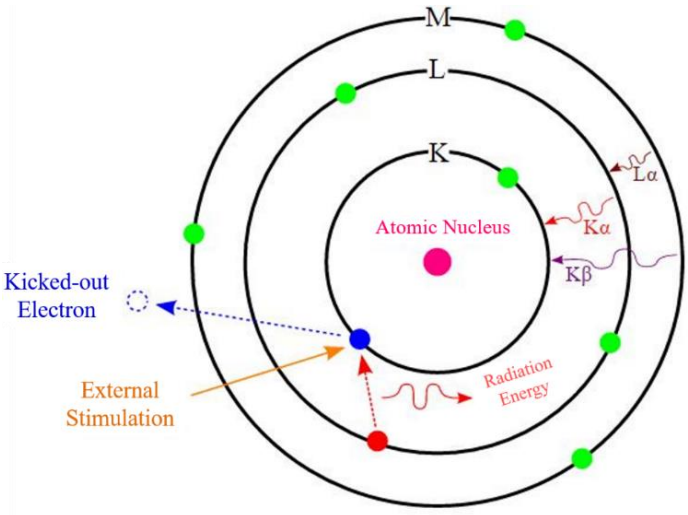

Figure 2.5: Electron shell model with different type of radiation emitted when an electron from the inner shell is removed.

Instrument Specifications [81]:

Make: Zeiss; Model: Supra 55; Max Power: 3 kW

2.3.3 X-ray Absorption Spectroscopy (XAS)

XAS is based on the measurement of the absorption coefficient $\mu(E)$ of the material, as a function of the energy of the incoming radiation on the material under study. According to the Beer- Lambert law for transmission process:

$$\mu\,(E)x = log\left(\frac{I_0}{I_t}\right) \tag{2.7}$$

and in X-ray fluorescence is

$$\mu\,(E)x \propto \left(\frac{I_f}{I_0}\right) \tag{2.8}$$

where I_t and I_0 are the intensities of the transmitted and incident radiations respectively, x is the thickness of the absorber and I_f is the monitored intensity of a fluorescence line (or, again, electron emission) associated with the absorption process.

The X-ray absorption coefficient is a smooth function of energy that is dependent on the sample density ρ (g/cm^3), the atomic number Z, the atomic mass A, and the energy of the X-ray E as

$$\mu \approx \frac{\rho z^4}{AE^3} \tag{2.9}$$

The absorbing process is illustrated in Fig. 2.6(a). As the energy of the incident X-rays approaches the binding energy of a core level electron there is a sharp rise in the absorption coefficient as the cross section of the X-ray increases. This gives rise to experimentally observed absorption edges when an X-ray has sufficient energy to promote a core level electron into unoccupied bound states, quasi bound states, or the continuum (photoelectric effect) as indicated in Fig. 2.6(b). The schematic view of X-ray absorption coefficient as a function of incident photon energy is shown in Fig. 2.7. The appearance of several absorption edges, labelled L_3, L_2, L_1, and K respectively, corresponding to core level electrons at different energy levels is observed. The K-edge refers to the excitation of 1s electrons, the L_1-edge refers to excitation of $2s$ electrons, and the L_3 and L_2-edges refer to the

excitation $2p_{3/2}$ and $2p_{1/2}$ electrons respectively. Due to the high degree of sensitivity of μ to the atomic number Z each element has characteristic absorption edges at different X-ray energies.

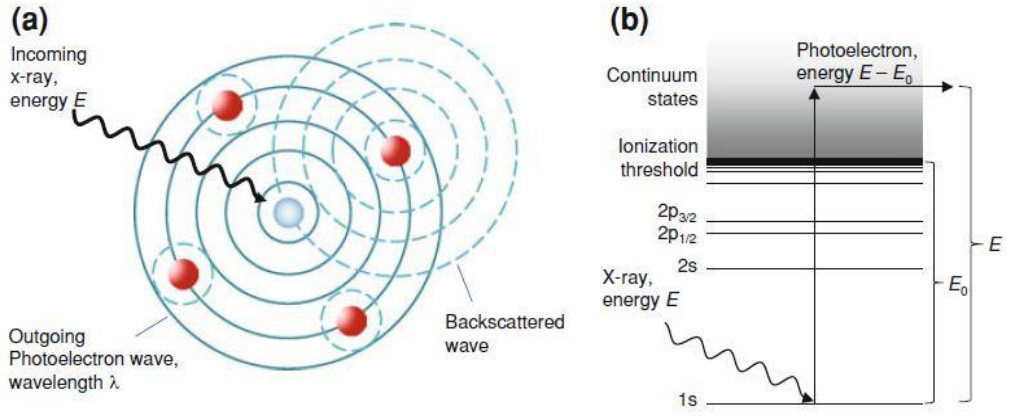

Figure 2.6: Schematics of the X-ray absorption process. (**a)** An absorbing atom (blue) is shown here surrounded by several other atoms (red). Whenever the energy of an X-ray is greater than the binding energy of one of the absorbing atom's core electrons, a photoelectron is liberated. (**b)** Energy-level diagram of an absorbing atom showing the atom's first few core-electron orbitals: *1s*, *2s*, $2p_{1/2}$, and $2p_{3/2}$. The ionization potential energy is denoted by E_0. With the absorption of a photon of energy E, the electron undergoes a transition to an unbound state in the continuum and, by conservation of energy, acquires a kinetic energy ($E - E_0$) [82].

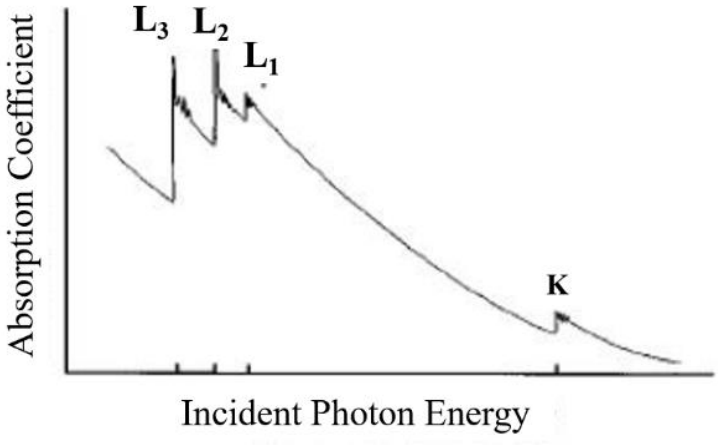

Figure 2.7: Schematic view of the x-ray absorption coefficient as a function of incident photon energy. The figure is taken from [83].

2.3.3.1 X-ray Absorption Fine Structure

When core level electrons in an atom are excited with X-ray energies at the binding energy, or absorption threshold (E_0), there is a sharp rise in the absorption probability (μ), followed by a monotonic decrease until the next core level is excited (Figure 2.8 (a)). The wavelength of the outgoing photoelectron can be expressed as;

$$\lambda \sim \frac{1}{\sqrt{(E-E_0)}} \tag{2.10}$$

In a diatomic system, however, fine structures are observed in μ when outgoing photoelectrons of the absorbing atom interact with neighbouring atoms resulting in scattering and subsequent constructive and destructive interference of the outgoing and scattered wavefunctions (Fig. 2.8 (b)). The modulation of the absorption coefficient as a function of X-ray excitation energy when the absorbing atom is in a chemical environment is known as X-ray absorption fine structure (XAFS). Traditionally, XAFS is further divided into two regions; (1) the near-edge region within 50 eV of the main absorption edge is referred to as X-ray absorption near edge structure (XANES), and (2) the extended region which extends from ~ 50 eV to 1000 eV above the absorption edge is referred to as extended X-ray absorption fine structure (EXAFS). This division is due to the difference in scattering behaviour of the electron as a function of its kinetic energy. In the near-edge region electronic transitions into bound and quasi-bound states and multiple scattering off of neighbouring atoms all contribute to the modulation of the absorption coefficient μ.

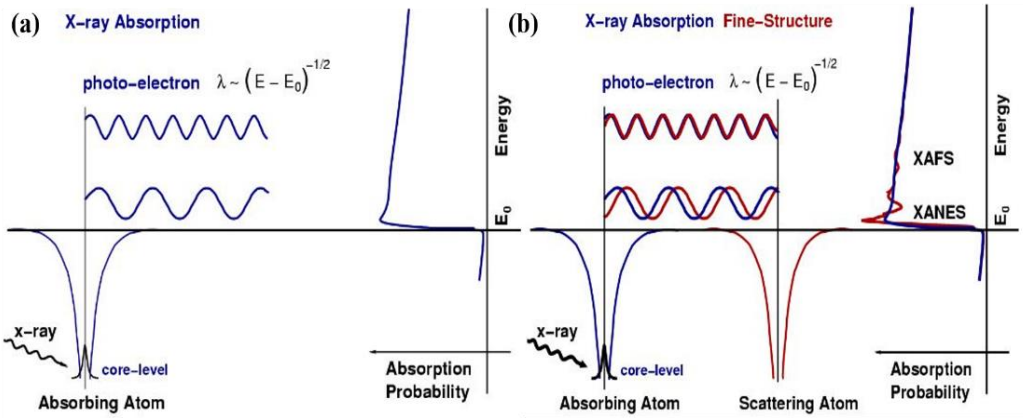

Figure 2.8: (a) X-ray absorption in a single atom system, and (b) X-ray absorption fine structure (XAFS) in a multi-atom system [84]

Thus, XANES is a very sensitive probe of the local chemical environment (oxidation state, unoccupied density of states, and local symmetry) of the absorbing atom. While in EXAFS, single scattering dominates the modulation of μ which makes it a local probe (within ~5 Å or the first two or three atomic shells) of bond length and short-range order. Therefore, XAFS is a powerful tool for the study of both the chemical environment and local structure of an absorbing atom. In this thesis, EXAFS study of samples has been taken up and the results are discussed in chapter 3, chapter 4 and chapter 7. The work presented in chapter 5 and chapter 6 is focused on the XANES region.

The EXAFS fine-structure function $\chi(E)$ can be defined as:

$$\chi(E) = \frac{\mu(E)-\mu_0(E)}{\Delta\mu_0(E)} \tag{2.11}$$

where $\mu(E)$ is the experimentally measured absorption coefficient, $\mu_0(E)$ is a smooth background function representing the absorption of the X-ray by an isolated atom, and $\Delta\mu_0(E)$ is the measured jump in absorption at the threshold energy (the binding energy of the core-level electron) E_0 [83]. Since, EXAFS is best explained by the wave nature of the photoelectron produced in the X-ray absorption process it is common to convert the X-ray energy to 'k' which is the wave number of the photoelectron in dimensions of $Å^{-1}$ which is demarcated as:

$$k = \sqrt{\frac{2m_e(E-E_0)}{\hbar^2}} \tag{2.12}$$

where m_e is the electron mass. So, the main quantity for EXAFS is $\chi(k)$ which is a measure of the oscillations in the absorption coefficient as a function of the photoelectron wave number 'k.

The equation for the EXAFS is given as [82]

$$\chi(k) = \sum_j \frac{N_j S_0^2 e^{-2k^2{\sigma_j}^2} e^{-2R_j/\lambda(k)} f_j(k)}{k{R_j}^2} \sin\left[2kR_j + \delta_j(k)\right] \tag{2.13}$$

where N *is* the coordination number of the absorbing atom and σ^2 ($Å^2$) is the thermal mean square displacement (also known as the Debye-Waller factor) in the bond distance R, λ is the mean-free-path of the photoelectron (typically ~5 to 30 Å) [81,82]. In most of the real systems, there is usually more than one type of neighbouring atom and thus the EXAFS will be a sum of the contributions from each scattering atom type (or coordination shell) and 'j' represents the individual

coordination shell of identical scattering atoms which are at approximately the same distance 'R_j' from the absorbing atom [84].

From equation 2.13, we can see that scattering factors depend on the atomic number, *Z*, of the neighbouring atom, hence sensitive to the atomic species of the neighbourhood. The EXAFS $\chi(k)$ is usually Fourier transformed into a radial structure function $\chi(R)$ that represents the data in terms of distances from the absorber. Peak positions in this radial structure function roughly correspond to the radii of the scattering shells.

The Fourier Transform (FT) is a useful way of judging qualitatively what shells may be present in a system and for comparing a fit to the data. However, it is important to remember that Fourier transforms are subject to several potential artefacts. In many cases, multiple shells of scatters do not give rise to multiple peaks in the FT [85]. Similarly, interference between two different peaks in the FT may give rise to a spurious third peak. Typically, however, only the modulus of the FT is plotted. This is useful for visualizing the major contributions to the EXAFS spectrum.

A schematic diagram of a laboratory source based XAFS system used for the measurement in present thesis, is shown in Fig. 2.9. This system configuration is based on Rowland geometry. The X-ray source 'S', the crystal center 'M' and the receiving slit 'F' are placed along Rowland circle with a radius 'R'. They are each mounted at one end of a bar of 'R' in length. The end of bars is linked. Two stepping motors are installed to make translational motion keeping the X-ray source to crystal and crystal to the receiving slit distances the same so that the incident angle and the exit angle are kept the same. During an energy scan, the X-ray source (S) and the crystal center (M) are moved, and distances SM and MF are kept the same. The full spectrum of X-ray light passes through an entrance slit, which helps collimate the radiation before entering into a crystal monochromator. The X-rays diffract off the crystals' lattice planes, which are aligned at an angle 'θ' with respect to the incoming beam. Different X-ray energies can be selected by changing the angle θ of the crystals. The monochromatic beam passes through a single-photon counter (S-PC) that monitors the beam intensity 'I_0' by absorbing part of it. The beam then passes through the sample, and the intensity of the transmitted X-ray 'I' is measured by a scintillation counter (SC). Taking the log of the ratio of 'I/I_0'

yields the absorption. We can also determine the sample's absorption by measuring the intensity of its X-ray fluorescence, I_f by moving the SC detector at 45° with respect to the sample.

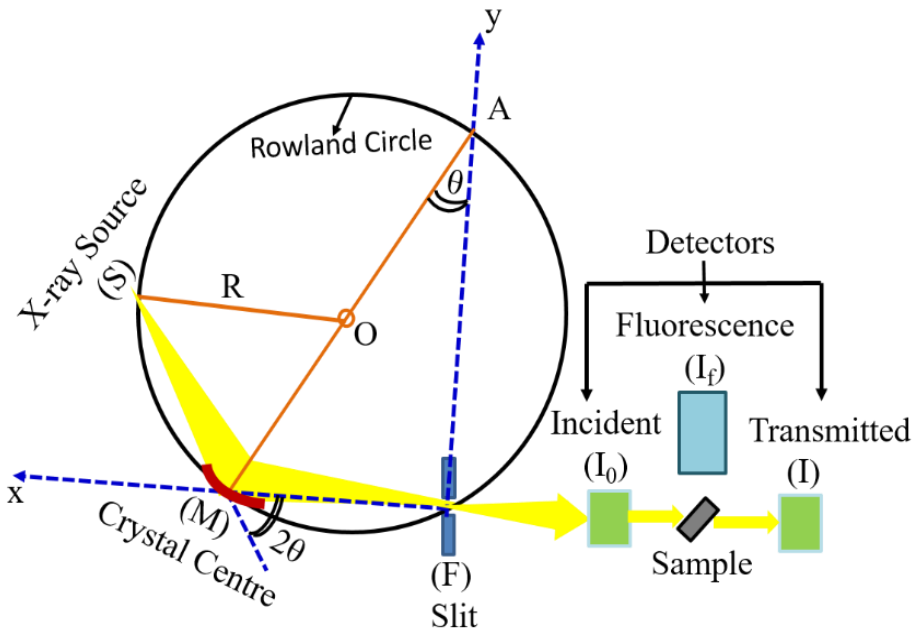

Figure 2.9: Schematic of the basic components of a Laboratory XAS Spectroscopy system.

Instrument specifications of laboratory XAS [86]:

Make: RIGAKU

Model: R-XAS looper

Maximum power: 3 kW

X-ray target: Mo, W

Filaments: W,

Measurements: transmission / fluorescence

Monochromating crystals: Ge(220), Ge(111),

Detectors: I_0 = S-PC, I = Scintillation SC

2.3.3.2 EXAFS Analysis

Extracting the values of the parameters in the EXAFS equation which determine the structural characteristics of the material is the main goal in EXAFS analysis. *R*, determines the interatomic separation and must be refined from an initial value that

is not too distant from that of the true value. EXAFS gives a fairly accurate value of *R*, usually reported to two decimal places, from accurate calculations of the phase shifts for different backscattering atoms. In this thesis work firstly, all the EXAFS raw spectra have been treated in ATHENA software for background removal and normalization before fitting. Then the EXAFS data is extracted in a suitable k-range. To extract the detailed information such as coordination number and radial distance, the Fourier transformed, $\chi(k)$ data is weighted by suitable power of *k* such functions are Fourier transformed in *R* space to generate the $\chi(R)$ versus *R* spectra in terms of the real distances from the absorbing atom. The FFT data is then fitted using Artemis program [87,88] with proper model to deliver local atomic structure information.

- **Artemis**

Artemis is part of the IFFEFIT suite of programs and uses the FEFF code for calculation of *ab initio* self-consistent real space multiple-scattering which yields the scattering amplitudes and phase shifts required for EXAFS analysis. the crystal structural model is based upon a crystallographic information file (CIF). Using the CIF, a FEFF calculation is performed up to a radial distance from the absorber, termed "cluster size". This FEFF calculation generates all single scattering and multiple scattering paths at distances up to the specified cluster size.

In terms of parameters, Artemis permits the deviation from the theoretical bond distance in the FEFF calculation After the fit Artemis produces a statistical analysis of each fit and the fitting parameters for each path are evaluated.

2.3.3.3 Soft X-ray Absorption Spectroscopy (SXAS)

X-ray absorption spectroscopy in the soft X-ray energy range (50 eV to 1200 eV), is a powerful technique and probes information about anisotropy (molecular orientation, lattice anisotropy: using linearly polarized X-rays), and probes magnetic materials (using circularly polarized X-rays).

In this thesis, we have also used polarized light at SXAS beamline (BL-1), at INDUS-II synchrotron source, Indore, for measurement of Cu, Cr and Ti L-edges in $CuCr_{2-x}Ti_xSe_4$ compounds which is represented in chapter-6.

A schematic of the basic setup for synchrotron based polarized light SXAS experiments in the BL01 beamline is shown in Fig. 2.10. According to the Fig.

2.10, the synchrotron radiation (SR) beams, coming from the centre of bending magnet, is linearly polarized, then fall on the water cooled toroidal pre-mirror(M1) to focus SR beam vertically on entrance slit (S1). Then the polarized X-ray beams pass through the three-different spherical grating monochromators according to the required element specific absorption energy edge [89].

In this present work, we have used 1500 gr/mm monochromator for Cu L-edge and 660 gr/mm for both Cr and Ti L-edge respectively. After the monochromatization, the polarized monochromatic beams fall horizontally on an exit slit (S2) to again refocus by a post mirror (M2). Then the monochromatized X-rays are directed on the sample. The detection of the X-rays after passing through the sample may be performed by fluorescence yield (FY) or total electron yield (TEY). We have used TEY mode in our measurement. All the spectra were recorded at room temperature in this study.

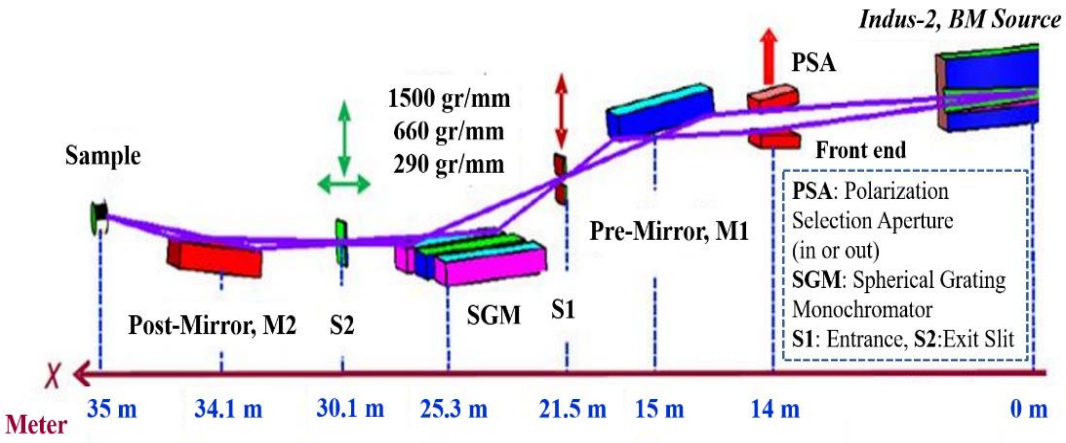

Figure 2.10: Schematic diagram of polarized light soft X-ray absorption spectroscopy beamline BL01 at Indus-2 [89].

Instrument specifications:

System Details: Beamline (BL01), Indus-2 Indore, India.

X-ray source: Bending Magnet source

Energy range: 100 eV – 1200 eV

2.3.4 Micro Raman Spectroscopy

Raman spectroscopy is established on the Raman effect, which was named after the Indian physicist Sir C.V. Raman in 1928 [90]. "Raman Effect" in solids arises due to an inelastic scattering of the incident light caused by the bond vibration also known as phonons. In Raman scattering, an incident optical photon of frequency (ω_i) and wavevector (k_i) interacts with the lattice through exchange of a quantum of energy and creates an electron-hole pair in the process. By measuring the shift of the energy of the scattered light relative to the incident laser light, the characteristic value of the vibrational energy of a given solid (Raman spectrum) is obtained [91]. Raman scattering is also sensitive to the change in the polarizability of the molecule or crystal with respect to its vibrational motion. The interaction of the polarizability with the incoming radiation creates an induced dipole moment in the molecule, and the radiation emitted by this induced dipole moment contains the observed Raman scattering.

A Raman spectrum is generally composed of several sharp peaks, related to different vibrational frequencies plotted between scatted intensity vs. energy. Each peak corresponds to a given Raman shift from the incident light energy '$h\nu_0$'. [92]. only those transitions involving $\Delta l = \pm 1$ are allowed (with l – atomic energy level). The Raman-active modes corresponding to different symmetries can be calculated using the factor group analysis [93].

During the analyses, all the characteristics of Raman spectra, *i.e*. the peak position, the peak intensity (I_{max}), and the full width at half maximum (FWHM), peak frequency shift can be used to gain information on different properties of materials. The schematic diagram of working principle of Raman spectra is given in Fig. 2.11.

In the present work room temperature and temperature dependent Raman scattering measurement were performed in the backscattering geometry on Cr-based chalcogenides as shown in chapter 3 and chapter 4. Raman spectra are acquired, when a sample is illuminated with a powerful laser light. Electromagnetic radiation from the illuminated spot is collected with a lens and sent through a monochromator. Elastic scattered radiation at the wavelength corresponding to the laser line (Rayleigh scattering) is filtered out by a notch filter. The filtered

Raman scattered light is then dispersed by diffraction grating and collected in the detector.

The schematic of a Micro Raman spectrometer is represented in Fig. 2.12 (a). The acquisition of spectra at low temperature was carried out using the THMS600 system consists of a sample stage, a T95 System Controller and LNP95 liquid nitrogen cooling pump. (as shown in Fig. 2.12(b)) [94].

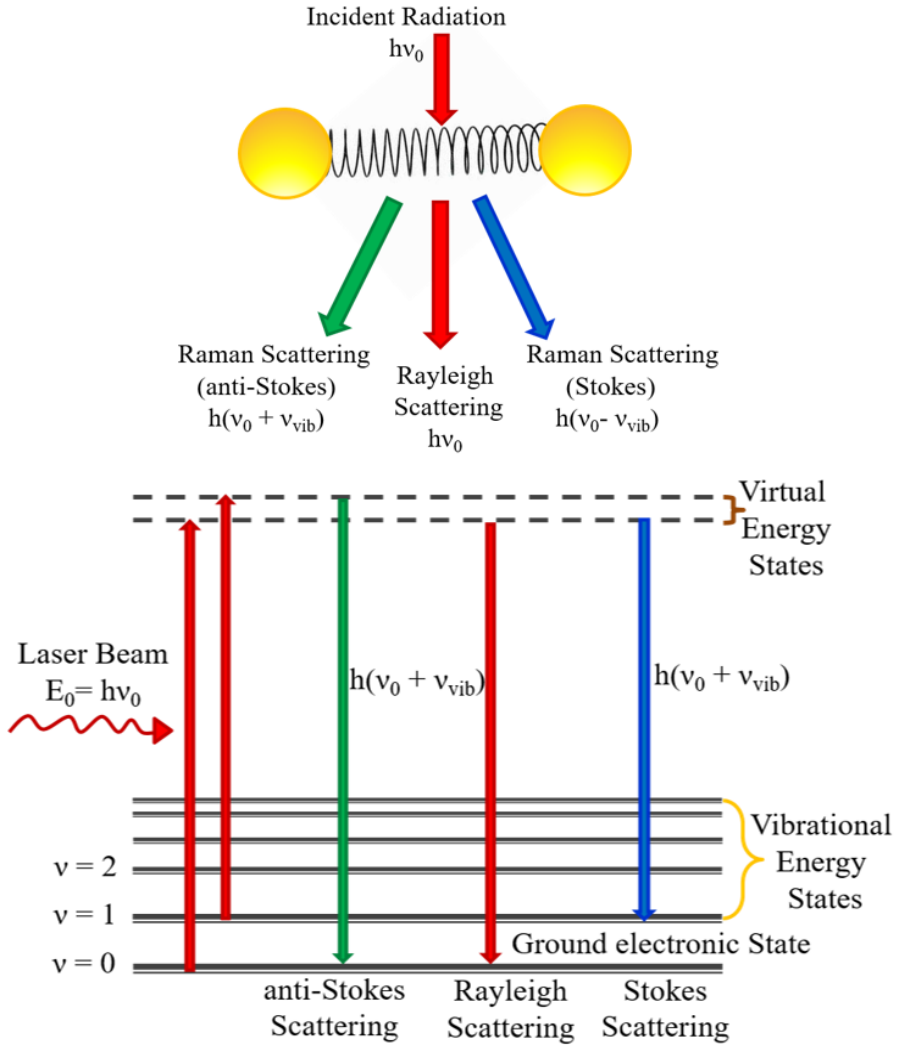

Figure 2.11: Working Principle of Raman Scattering process

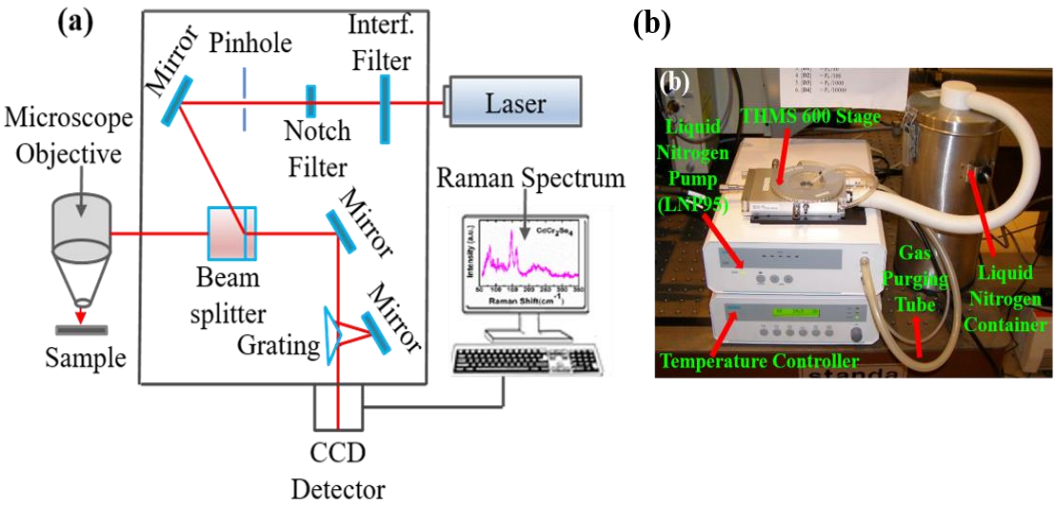

Figure 2.12: (a) Schematic of a Micro Raman spectrometer and (b) Image of a Low temperature attachment of THMS600 System.

Instrument specifications:

Make: Jobin Yvon Horibra

Model: LABRAM-HR visible (400 - 1100 nm)

Spectral Range: 50 cm^{-1} to 4000 cm^{-1} (Raman Shift)

Excitation Laser Sources: He-Ne 632.8 nm and Argon 488 nm

Optics: high stability confocal Microscope

2.4 Characterization of Magnetic properties

In this dissertation, the magnetic properties of the Cr-based spinel chalcogenides were measured using Quantum Design's Magnetic Properties Measurement System (MPMS) and Physical Property Measurement System configured with vibrating sample magnetometer (PPMS–VSM).

2.4.1 Magnetic Properties Measurement System (MPMS)

At the heart of a MPMS lies the superconducting quantum interference device (SQUID) which is an extremely sensitive current-to-voltage convertor, With SQUID-based magnetometer, magnetic moments of the order of 10^{-7} emu can be measured. An image of the MPMS-XL system, is shown in Figure 2.13 (a). A schematic of the measurement process of this equipment is displayed in Figure

2.13(b) [95]. In a MPMS, a measurement is performed by moving a sample through a system of superconducting pick-up coils spaced symmetrically outside the sample chamber at the centre of the superconducting magnet, as shown in Fig. 2.13 (b). When the sample moves through the coils, the magnetic moment of the sample induces an electric current in the detection coils. The detection coils, the connecting wires, and the SQUID input coil form a closed superconducting loop. So, any change of magnetic flux in the detection coils generates a change in the persistent current in the detection circuit, which is proportional to the change in magnetic flux. Since the SQUID is a highly linear current-to-voltage convertor, the variation in the current in the detection coils produces corresponding variations in the SQUID output voltage. Based on this profile of voltage (and thus flux) versus position of the sample the magnetic moment can be determined.

MPMS allows measuring magnetization as a function of magnetic fields and temperature.

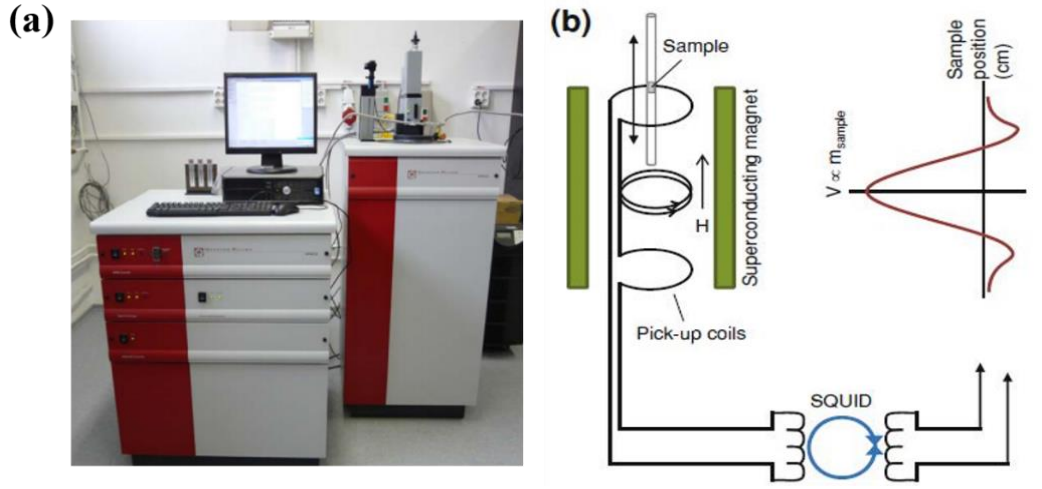

Figure 2.13: (a) Quantum Design MPMS-XL magnetometer [95]. (b) Schematic of the SQUID—based measurement system.

2.4.2 Physical Property Measurement System (PPMS)

PPMS is a versatile instrument offering the options for measuring a large variety of physical properties. Basic setup consists of dewar with the superconducting magnet and a universal 12-pin platform that can house different experimental measurement options like electrical resistivity, ac susceptibility, heat capacity etc. The typical schematic setup of a Quantum design PPMS is shown in Fig. 2.14 [96].

Figure 2.14: Quantum Design Physical Property Measurement System.

2.4.2.1 PPMS-VSM

The VSM option of PPMS utilizes a quartz mounting stick attached to a carbon fiber rod to which the sample is mounted using rubber cement. A linear motor is used to oscillate the sample between the pickup coils placed inside the evacuated sample chamber (see Fig.2.15). The magnetic moment is measured via the electromotive force (EMF), where a current will be induced in a pickup coil whenever there is a magnetic flux change within the pickup coil. The induced current will have an associated EMF voltage which can be measured and used to calculate the magnetic moment of the sample. The Quantum Design PPMS-VSM setup provides very fast measurement of the DC magnetization of the sample with very good sensitivity down to 10^{-6} emu.

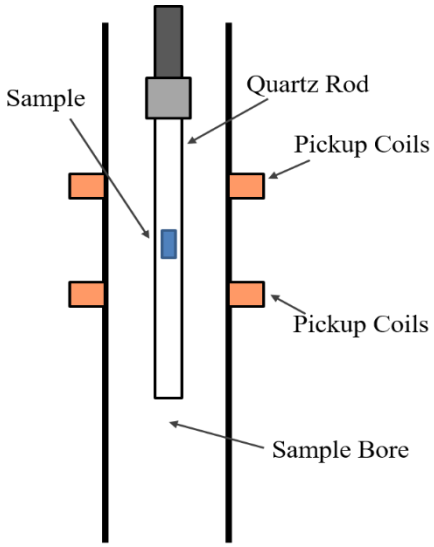

Figure 2.15: Schematic of the VSM Pickup Coil.

In this dissertation, temperature dependence of magnetisation, *M(T)*, and field dependence of magnetization, *M(H)*, hysteresis loop measurement was carried out. In the M(T) measurement, zero field cooled (ZFC), field cooled (FCC) and field cooled warming (FCH) protocols were followed. For this, the sample was cooled down to 5 K in the absence of a magnetic field and a constant magnetic field was applied. The magnetization was recorded at different temperature intervals as the sample warmed up to desired temperature, giving a ZFC profile. In the FCC measurement, the same sample was cooled from high temperature down to 5K in the presence of the same constant magnetic field and data was recorded simultaneously. One more cycle of recording the data during subsequent warm up in the same magnetic field gave the FCH profile. See Fig. 2.16 below for an example of a ZFC/FCC/FCH plot.

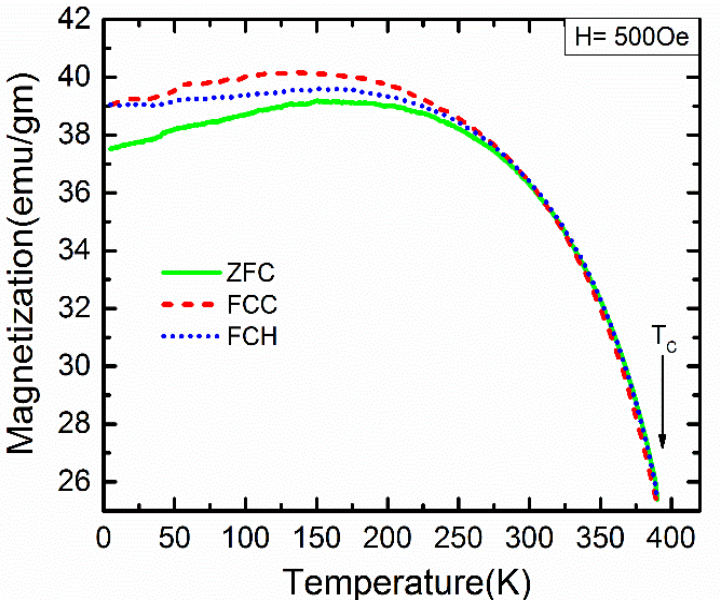

Figure 2.16: ZFC/FCC/FCH curve of a Ferromagnetic sample.

For hysteresis loop measurement *M (H)*, a DC magnetic field is slowly ramped up until the field is strong enough to saturate the sample (H_{max}). Subsequently, the field is decreased in steps down to $-H_{max}$. At each step, the magnetic moment is measured. By plotting the magnetization (*M*) versus the applied magnetic field (*H*), a hysteresis loop (*M-H* loop) is obtained. A typical hysteresis loop is shown in Fig. 2.17. From the hysteresis loop, the following magnetic properties can be obtained: the saturation magnetization M_s (the

magnetization when the applied field is large enough to saturate the sample), remanent magnetization M_r (the magnetization when the applied field is removed), and coercivity 'H_c' (the negative magnetic field at which magnetization reaches zero after saturating the sample in the positive field). In this work, for the hysteretic loop, *M(H)* measurements, the samples were subjected to a magnetic field cycling between +5 Tesla and -5 Tesla and magnetisation was measured at a particular temperature of 5 K.

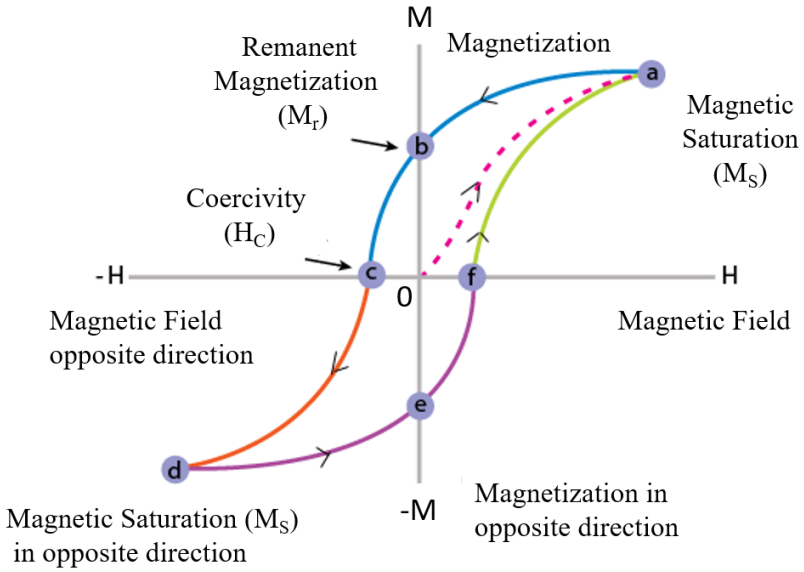

Figure 2.17: A typical magnetic hysteresis loop of a ferromagnetic material.

2.4.2.2 PPMS-ACMS

In AC magnetic measurements, a small AC drive magnetic field is superimposed on the DC field, causing a time-dependent moment in the sample. The field of the time-dependent moment induces a current in the pickup coils, allowing measurement without sample motion. The detection circuitry is configured to detect only in a narrow frequency band, normally at the fundamental frequency (that of the AC drive field).

In order to understand what is measured in AC magnetometry, first consider very low frequencies, where the measurement is most similar to DC magnetometry. In this case, the magnetic moment of the sample follows the *M(H)* curve that would be measured in a DC experiment. As long as the AC field is small, the induced AC moment is $M_{AC} = (dM/dH).\ H_{AC}\ sin(\omega t)$ where H_{AC} is the amplitude of the driving field, ω is the driving frequency, and $\chi = dM/dH$ is the slope of the M(H) curve,

called the susceptibility. Second, at higher frequencies, the AC moment of the sample does not follow along the DC magnetization curve due to dynamic effects in the sample. In this higher frequency case, the magnetization of the sample may lag behind the drive field, an effect that is detected by the magnetometer circuitry. Thus, the AC magnetic susceptibility measurement yields two quantities: the magnitude of the susceptibility, χ, and the phase shift, ϕ (relative to the drive signal). Alternately, one can think of the susceptibility as having an in-phase, or real, component χ' and an out-of-phase, or imaginary, component χ'' [97].

AC susceptibility measurements were carried out using the ACMS option of PPMS. In the AC susceptibility measurement, a small alternating field is applied to the large applied field from the PPMS superconducting magnet and measures a sample's magnetic moment response.

The origin of the magnetic moments arises from the orbital motion and spin of unpaired electrons. The way atomic magnetic moments order in a material can be inferred by the behaviour of the magnetic susceptibility of the sample, see Fig. 2.18. Materials can be paramagnetic so that when a magnetic field is applied a magnetization appears which aligns parallel with it (unpaired electrons are present), and diamagnetic when a magnetic field induces a magnetic moment which opposes the applied magnetic field that cause it (all electrons are paired) [98].

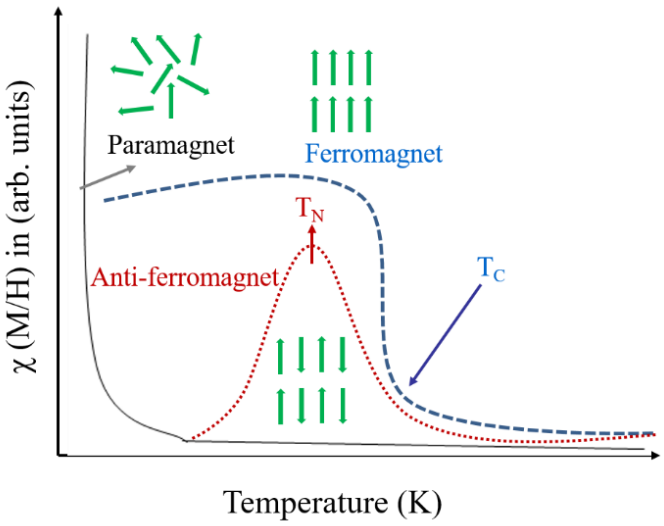

Figure 2.18: Generalized magnetic susceptibility response of a paramagnet, ferromagnet and antiferromagnet. The latter two are paramagnetic above their ordering temperatures, T_C and T_N respectively.

Ferromagnetic materials possess spontaneous magnetization when they are below a certain critical temperature, called the Curie temperature (T_C). On the other hand, the antiferromagnetic materials, have the spins of neighbour magnetic atoms aligned in opposite directions. The temperature below which an antiferromagnetic material order occurs is called the Neel temperature (T_N). In the paramagnetic phase of a FM or AFM material, the temperature dependence of the susceptibility is given by the well-known Curie-Weiss law:

$$\chi = \frac{C}{T-\theta_P} \tag{2.14}$$

where 'θ_P' is the Curie-Weiss temperature and is related with the exchange interaction between atomic magnetic moments, *'T'* is absolute temperature measured in Kelvin and '*C'* is a material-specific Curie constant. The Curie-Weiss temperature can adopt positive as well as negative values. θ_{CW} has a positive sign, when the low temperature alignment is ferromagnetic and negative sign when its antiferromagnetic. Notice that Curie's law is only valid in the low field regime and does not apply in the high field regime where saturation of magnetization occurs and the magnetic moments are aligned with the external applied field. For a paramagnetic ion with spin quantum number *S* (and quenched angular momentum, $<L> = 0$), the Curie constant can be related to the individual ions magnetic moment:

$$C = \frac{N_A}{3k_B}\mu_{eff}^2 \qquad where,\ \mu_{eff} = 2\sqrt{S(S+1)}\mu_B \tag{2.15}$$

where k_B is the Boltzmann constant and 'N_A' is the Avogadro's number.

2.5 Electrical Transport and Magneto-transport properties

The electrical resistance and magneto-resistance and heat capacity were measured from 400 K down to 5 K, using AC Transport Measurement option of the PPMS.

2.5.1 PPMS-ACT

The AC transport option incorporates a precision current source and a precision voltmeter in a package configured with the PPMS platform and supports four-probe alternating current resistivity measurements.

To measure the resistivity using this technique, the samples were cut in a rectangular bar shape using a diamond saw. For the electrical contacts of the probes with the sample, silver paint has been used. as shown in Fig. 2.19. As shown in the figure, current is passed through the outer probes (+I & -I) and resultant potential difference developed between two points is measured using the inner probes (+V & -V). The resistance can be calculated using the ohm's law V = IR, where 'I' is the current passed and 'V' is the voltage developed. It is crucial to keep the voltage probes between the current probes in a linear way. Using dimensions, shown in figure, the exact resistivity (ρ) of the sample can be calculated using the relation;

$$\rho = \frac{RA}{l} \tag{2.16}$$

where *R* is the resistance, *A* is the cross-sectional area of the sample. The samples are cooled down using liquefied He and then heated in a controlled way by using a heater and resistance is measured with slow increase of temperature [99].

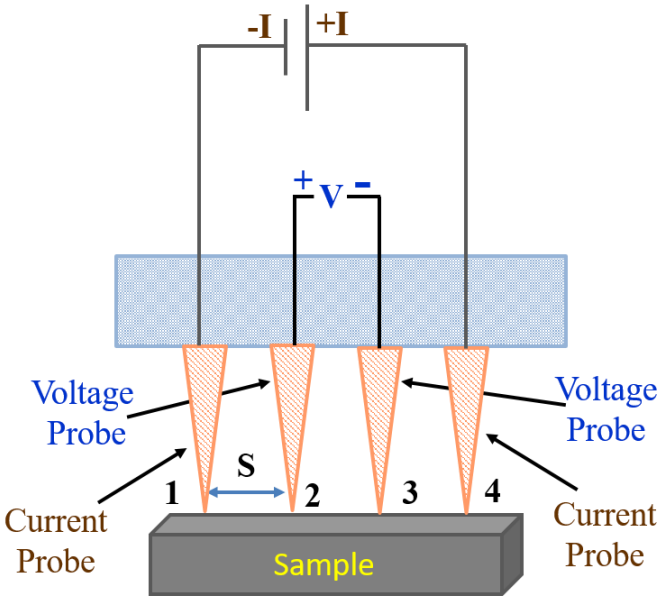

Figure 2.19: Four probe contacts of current and voltage supplies to the sample during the resistivity measurements.

The temperature dependent resistivity of the material in the presence and absence of constant applied magnetic field as well as resistivity isotherms by

ramping the magnetic field can be measured to observe the magnetoresistance (MR) properties of the material.

In this dissertation, $Cu_{0.9}M_{0.1}Cr_2Se_4$ (M = Mn, Fe, Co) pollycrystaline samples were mounted in four probe configuration and temperature dependence of the electrical resistance in the range 5 K - 400 K were measured under fields H = 0, 10 kOe and 50 kOe. Resistance isotherms R(H) at various temperatures (5 K, 50 K, 100 K, 200 K and 300 K) were also measured as discussed in chapter 5.

2.5.2 Heat Capacity measurement

The measurement of the heat capacity of solids can provide considerable information about the lattice, electronic, and even magnetic properties of materials. We performed heat capacity measurements to probe magnetic and structural transitions as discussed in chapters 3 and chapter 4. The heat capacity at constant pressure is defined as;

$$C_P = \left(\frac{dQ}{dT}\right)_P \tag{2.16}$$

Therefore, a phase transformation where the temperature change is very small despite the heat given to the material will be marked by a large heat capacity.

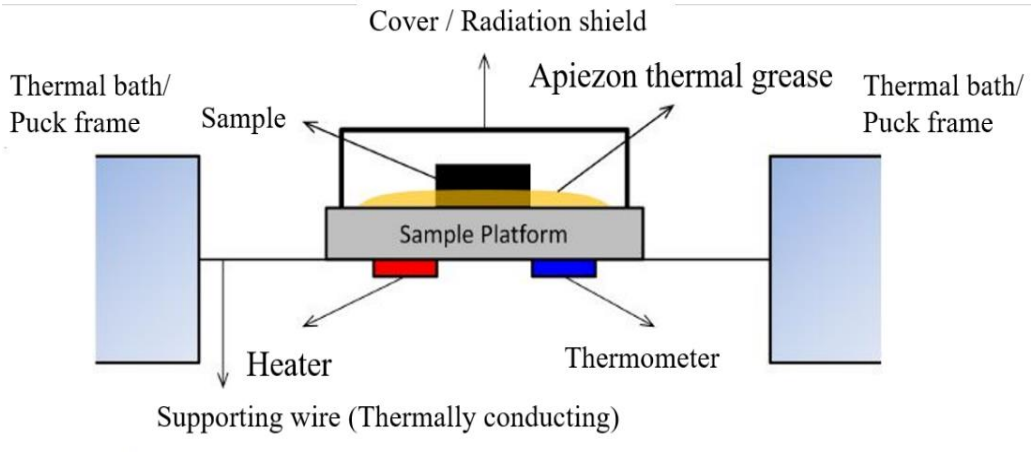

Figure 2.20: The schematic configuration of a sample stage for a heat capacity measurement using a Quantum Design PPMS (adapted from Ref. [100]).

The specific heat measurements on $Cd_{1-x}M_xCr_2Se_4$ (M=Sb, Sn and x = 0, 0.05, 0.1) were performed in the temperature range of 10 to 200 K using the heat

capacity option of PPMS that uses the thermal relaxation method to measure C_P [101]. The schematic of the experiment is shown in Fig. 2.20. The sample is mounted on a platform, which is suspended by thin wires. A thermal grease is used to mount the sample on this platform and to enhance the thermal contact between the sample and the platform. The experiment is done in vacuum. The initial temperature of the whole assembly is T_0. A pulsed current is sent through the heater to raise the temperature of the sample to a final temperature T_1. Because the thermal conduction to the platform occurs only through the thin wires, the temperature slowly decays from T_1 back to T_0. The time it takes to reach T_1 and back to T_0 are t and t' respectively. Due to the minimal thermal contribution from the surroundings, both t and t' should reflect the heat capacity of the sample and platform assembly. If the mass of the sample, the heat capacity of any non-sample components, thermal conductivity of the wires, and the heat applied to the sample are all known, then the heat capacity of the sample can be extracted from fitting the time dependence of the sample temperature.

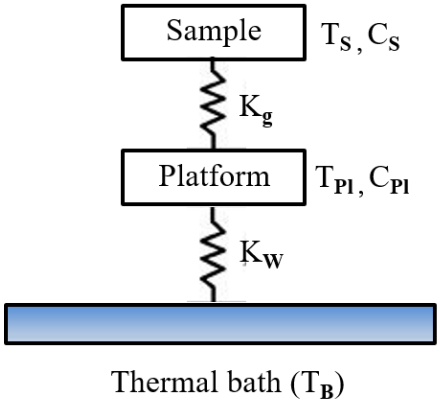

Figure 2.21: The diagram of the thermal connection of the platform and the corresponding parameters that has to be considered in equation 2.37.

In practice, a measurement that involves only the sample is impossible because the sample has to be mounted on a sample platform. Therefore, the heat capacity of the platform and any other non-sample component has to be measured first. This is done by measuring the heat capacity of the platform and the thermal grease, without the presence of the sample to create an addendum. Then after the heat capacity of the non-sample components has been measured, the sample is

mounted on the platform without adding or removing the grease. The heat capacity of the sample is then given by $C_P = C_{total} - C_{addenda}$. In the thermal relaxation, the heat-balance condition of the measurement is modelled by the relation [101]:

$$C_P \frac{dT_{Pl}}{dt} = P(t) + K_g(T_S - T_{Pl}) - K_w(T_{PL} - T_B), \quad (2.17)$$

$$, C_S \frac{dT_S}{dt} = -K_g(T_S - T_{Pl})$$

where *C*, *T*, *P(t)* and *K* are the heat capacity, temperature, power applied to the sample, and conductance, respectively and the indices *Pl*, *S*, *g*, *w*, *b* refers to the platform, sample, grease, wires, and thermal bath, respectively (see Fig. 2.21).

Chapter 3

Crystal Structure and Magnetic Property Correlation in $Cd_{1-x}M_xCr_2Se_4$ (M = Sb, Sn, In)

3.1 Overview

$CdCr_2Se_4$ spinel system have been an interesting avenue for studying magnetic, resistive, and thermoelectric properties since they are strongly correlated to the crystal structure that is tunable by selection of charges and sizes of the A-site ions. This compound orders magnetically below $T_C \sim 130K$ [30]. The magnetic ordering is believed to result from strong competition between the direct Cr–Cr spin couplings and the Cr-Se-Cr exchange interactions [18]. Partial substitution of Cd^{2+} by small percentage of non-magnetic In, Sb, or Sn is expected to bring about local lattice distortion and changes in the electronic charge redistribution that subtly affects the Cr-Cr and Cr-Se-Cr interactions. Our results on the measurement of magnetic properties of $Cd_{1-x}M_xCr_2Se_4$ (M = Sb, In, Sn) reflects this premise. We investigate compositions with upto 10% substitution of Cd^{2+} with Sb, In, and Sn ions so as to maintain the Fd3m symmetry of $CdCr_2Se_4$. The X-ray diffraction analysis using Rietveld refinement technique confirms the symmetry of the lattice and provides the various lattice parameters. Measurement of magnetic properties indicates change in the ordering temperatures and total magnetic moment. Cr K-edge EXAFS and Raman studies confirm the manifestation of mix valence state of Cr atom to maintain the charge balance in the substituted compounds. Heat capacity measurements further support the inference drawn from the magnetic studies. Moreover, the synchrotron x-ray diffraction results in Sb and Sn-substituted compounds with respect to parent display no structural phase transition occurs as shown in the investigated temperature range. Our results highlight the significance of direct exchange coupling between 180° Cr-Cr ions and indirect exchange interactions between 90° (Cr-Se-Cr) in the magnetic sub-lattice that drives the magnetic ground state in $Cd_{1-x}M_xCr_2Se_4$ (M = Sb, In and Sn).

It is known from previous studies [102-104] that high concentration of dopants leads to the formation of spin clusters in the low temperature ordered state, and structural phase transition may also occur at low temperatures. We have therefore restricted to small percentage (upto 10%) of substitutions as we aimed at maintaining the Fd3m symmetry of $CdCr_2Se_4$ whilst change in stoichiometry. The substitutions (M = In, Sb, Sn) bring about two effects: local lattice distortion and change in the electronic charge [103,105]. In tetrahedral environment the ionic radii of Sb, In and Sn decreases systematically as 0.76 Å > 0.62 Å > 0.55 Å, with only Sb-ions matching in size with the Cd (0.78 Å) ions. Whereas the electronic charge is expected to be 3+ for Sb, In, and 4+ for Sn. Thus, the magnetic properties for In-substituted samples, when contrasted with Sb-substituted samples are a manifestation of local lattice distortion. The Sn-substituted samples are affected by both lattice and charge effects. Our results on the measurement of magnetic properties indeed reflect this premise.

3.3 Results and Discussions

3.3.1 Compositional Analysis

	Atomic percentage (error ~ ± 3%)					
Composition	**Cd**	**Sb**	**In**	**Sn**	**Cr**	**Se**
$CdCr_2Se_4$	13.40	-	-	-	31.59	55.00
$Cd_{0.95}Sb_{0.05}Cr_2Se_4$	12.80	0.65	-	-	25.75	52.78
$Cd_{0.9}Sb_{0.1}Cr_2Se_4$	12.15	1.28	-	-	25.34	49.10
$Cd_{0.95}In_{0.05}Cr_2Se_4$	12.52	-	0.63	-	24.91	50.42
$Cd_{0.9}In_{0.1}Cr_2Se_4$	11.97	-	1.30	-	23.04	48.59
$Cd_{0.97}Sn_{0.03}Cr_2Se_4$	13.46	-	-	0.42	27.10	53.91
$Cd_{0.95}Sn_{0.05}Cr_2Se_4$	14.17	-	-	0.71	28.85	55.95
$Cd_{0.93}Sn_{0.07}Cr_2Se_4$	12.70	-	-	0.85	25.52	50.99
$Cd_{0.9}Sn_{0.1}Cr_2Se_4$	12.92	-	-	1.34	25.86	51.68

Table 3.1: Elemental ratio obtained by EDX for $[Cd_{1-x}M_x]Cr_2Se_4$ with M= In, Sb, Sn and $0 \leq x \leq 0.1$

The ratio of elemental compositions of cadmium (Cd), antimony (Sb), indium (In), tin (Sn), chromium (Cr) and selenium (Se) in all the prepared samples as obtained

from EDX, are presented in above Tab. 3.1. These numbers match well with the ratio of starting compositions.

3.3.2 Crystal Structure Characterization

3.3.2.1 XRD

The Reitveld refined room temperature XRD patterns for parent $CdCr_2Se_4$ and $[Cd_{1-x}M_x]Cr_2Se_4$ (M = Sb, In, Sn) series are shown in Fig. 3.1, Fig. 3.2, Fig. 3.3 and Fig. 3.4 respectively. All the observed peaks could be indexed to a face centered cubic cell, space group *Fd3m*. In the crystal structural model for normal spinels, the atomic positions of Cd, Cr, Se are set to tetrahedral 8*a* (A-Site), octahedral 16*d* (B-site) and 32*e*-site, respectively. Rietveld refinement was carried out for such a normal spinel with substituted atoms (i.e. M = In, Sb, Sn) at the Cd-site. Analysis was carried out by refining the thermal displacement parameters and site occupancy factors for both Cd-site and Cr-site. Referring to the parameters listed in Tab. 3.2, The ionic radii of Cd and Sb ions being similar (0.78 Å and 0.76 Å) we find no change in the lattice constants for Sb-substituted samples from that of $CdCr_2Se_4$. In- and Sn-substituted samples show a systematic increase in 'a', inspite of the fact that both these ions have a smaller ionic radius (0.62Å & 0.55 A) in comparison to Cd. Further, Sn samples show an initial increase in a for x = 0.03, 0.05 and starts to decrease as x increases further to 0.07 and 0.1.

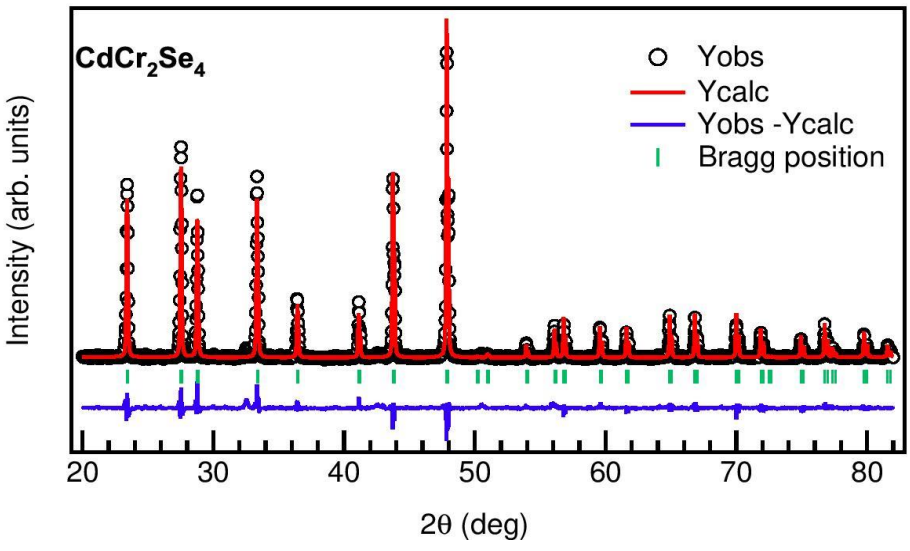

Figure 3.1: Rietveld refinement fit for the parent compound, $CdCr_2Se_4$.

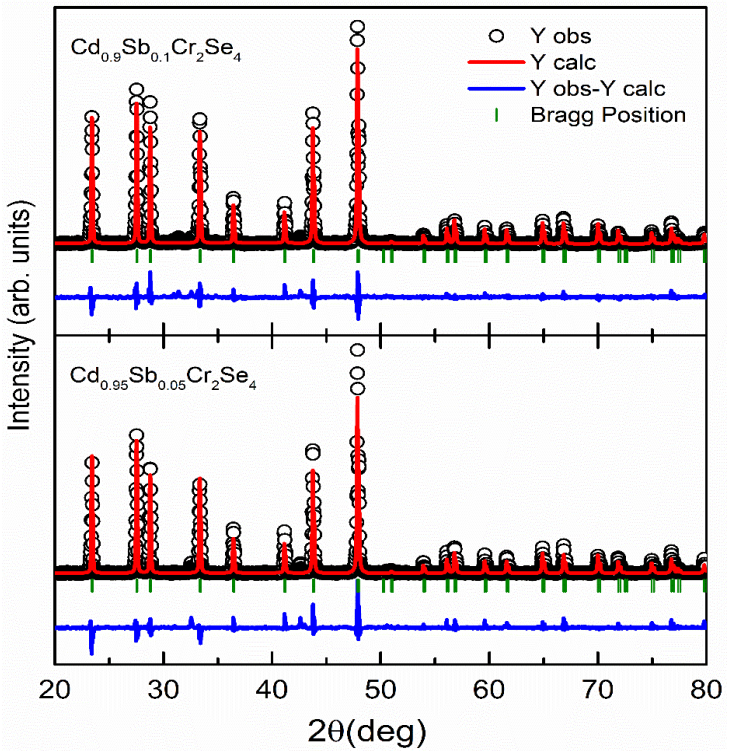

Figure 3.2: Rietveld refinement fit for $[Cd_{1-x}Sb_x]Cr_2Se_4$ series recorded at room temperature.

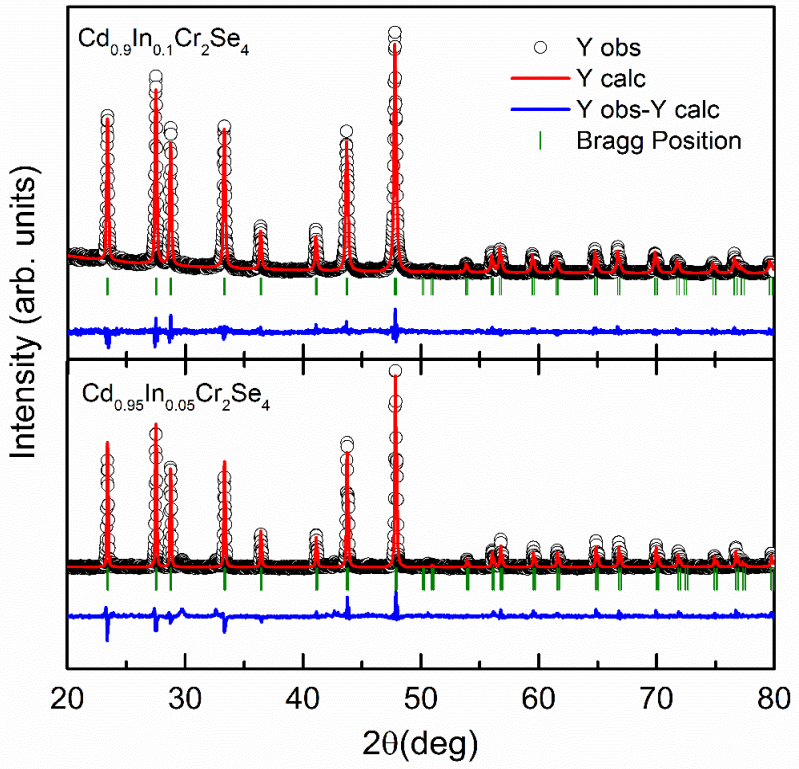

Figure 3.3: Rietveld refinement fit for $[Cd_{1-x}In_x]Cr_2Se_4$ series recorded at room temperature.

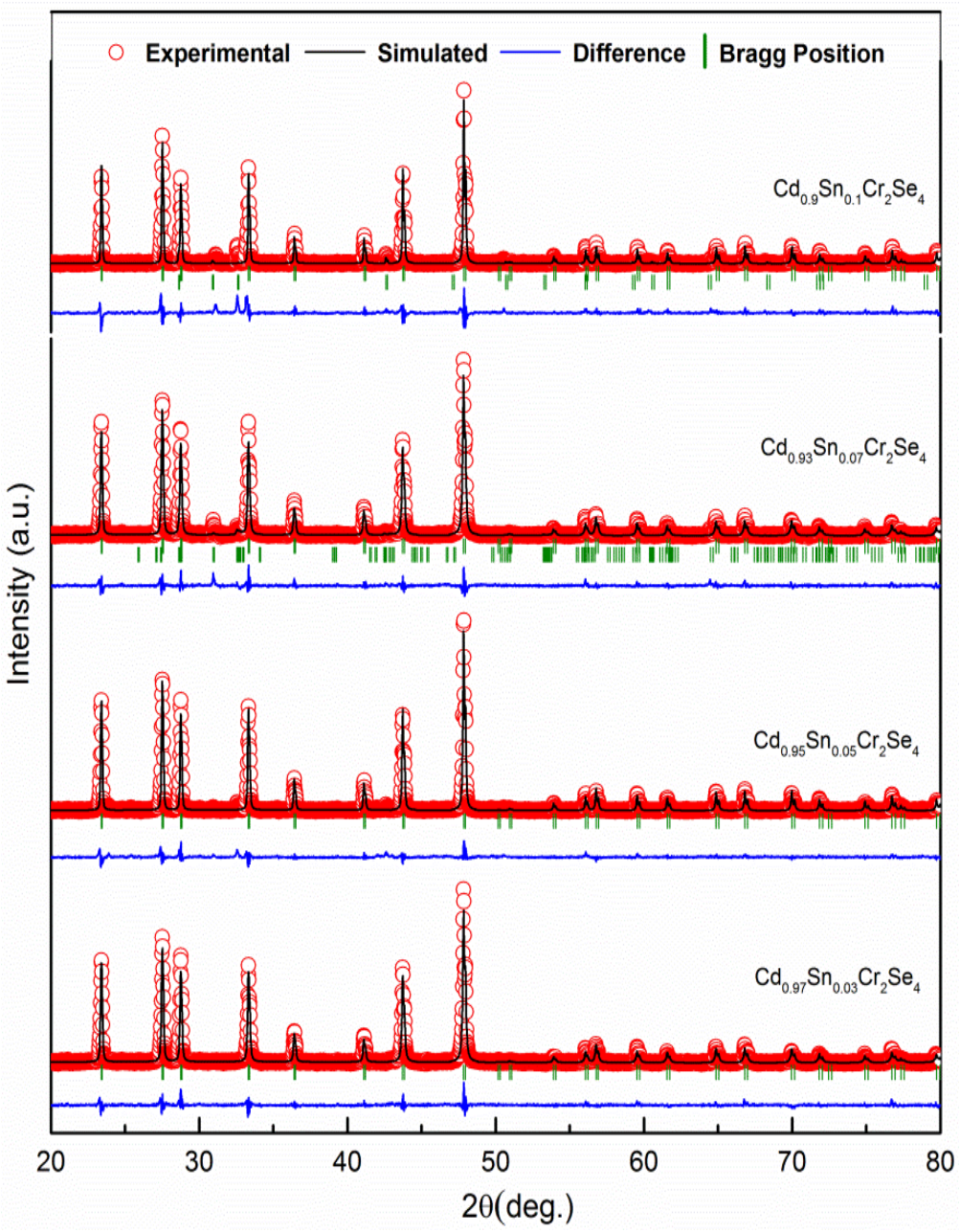

Figure 3.4: Rietveld refinement fit of the powder XRD pattern recorded at room temperature for $Cd_{1-x}Sn_xCr_2Se_4$ (x = 0.03, 0.05, 0.07 and 0.1).

In the below Fig. 3.5, where a single main peak is shown for different compositions, where a systematic shift in the peak positions with respect to the parent $CdCr_2Se_4$, reflecting change in the unit cell parameters (see Tab. 3.2).

Chemical Composition	*a (Å)*
$CdCr_2Se_4$	10.7444 ± 0.0001
$Cd_{0.95}Sb_{0.05}Cr_2Se_4$	10.7442 ± 0.0003
$Cd_{0.9}Sb_{0.1}Cr_2Se_4$	10.7440 ± 0.0003
$Cd_{0.95}In_{0.05}Cr_2Se_4$	10.7539 ± 0.0002
$Cd_{0.9}In_{0.1}Cr_2Se_4$	10.7568 ± 0.0002
$Cd_{0.97}Sn_{0.03}Cr_2Se_4$	10.7487 ± 0.0004
$Cd_{0.95}Sn_{0.05}Cr_2Se_4$	10.7525 ± 0.0004
$Cd_{0.93}Sn_{0.07}Cr_2Se_4$	10.7527 ± 0.0004
$Cd_{0.9}Sn_{0.1}Cr_2Se_4$	10.7471 ± 0.0004

Table 3.2: Lattice constants calculated from Rietveld refined XRD patterns of $Cd_{1-x}M_xCr_2Se_4$ (M = Sb, In, Sn).

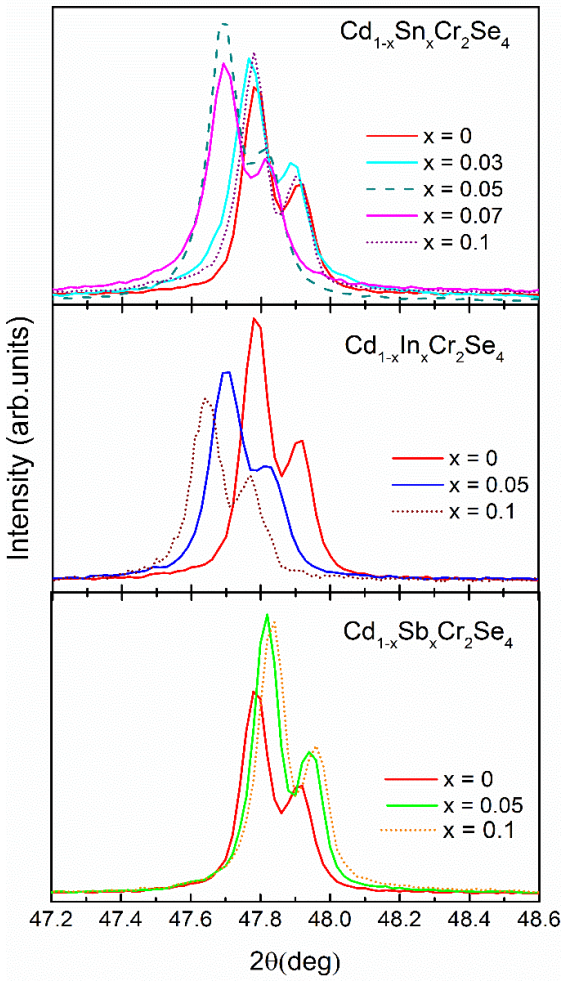

Figure 3.5: Single main peaks of all the substituted compounds display the shift in *2θ* value with respect to different composition as compared to parent one.

3.3.2.2 Raman Studies

Room temperature Raman spectra for the Sb, In and Sn substituted compositions, recorded using two different laser excitation sources, are shown in Fig. 3.6 to Fig. 3.8 respectively. Group theory predicts five Raman active modes for cubic spinel chalcogenides identified as (A_{1g} + E_g + $3T_{2g}$) [106]. As it follows from Fig. 3.6 to Fig. 3.8, all the five Raman active modes appear with 488nm (2.54 eV) excitation, whereas, first translational (T) mode at T_{2g} is absent in 633 nm (1.96 eV) excitation, matching with literature [107]. All samples reflect same crystal structure as that of the parent compound, no modes or extra spectral signatures as seen from both the excitation sources. This Raman study once again confirming the XRD results that the spinel crystal symmetry is maintained.

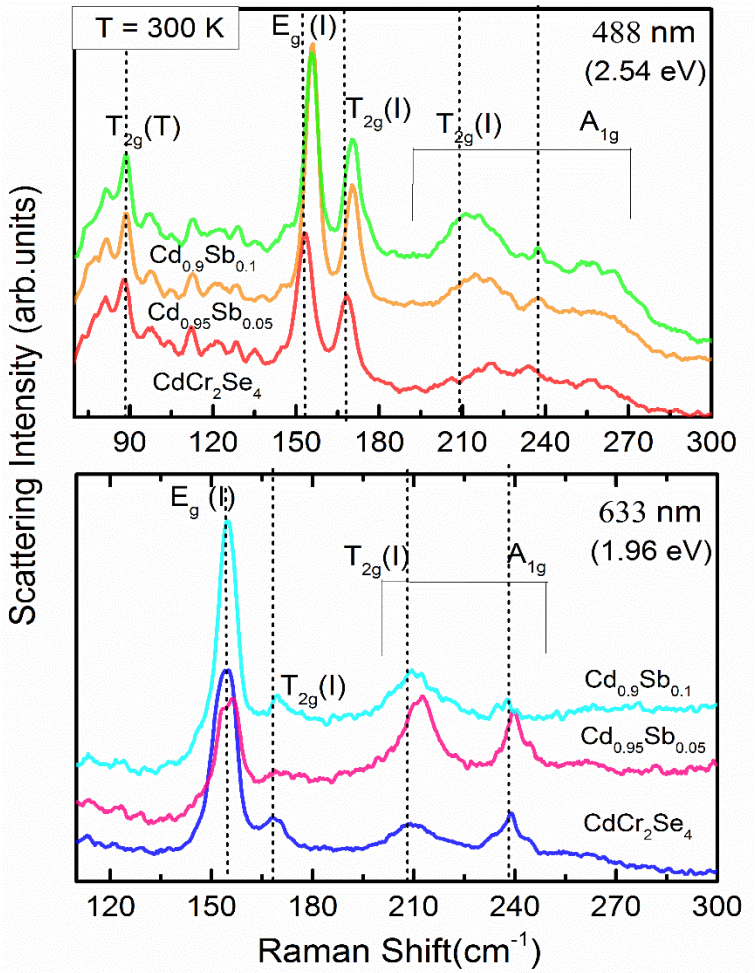

Figure 3.6: Room temperature Raman spectra measured with excitation wavelength of 488 nm (top panel) and 633 nm (bottom panel) for $Cd_{1-x}Sb_xCr_2Se_4$ (x = 0, 0.05, 0.1).

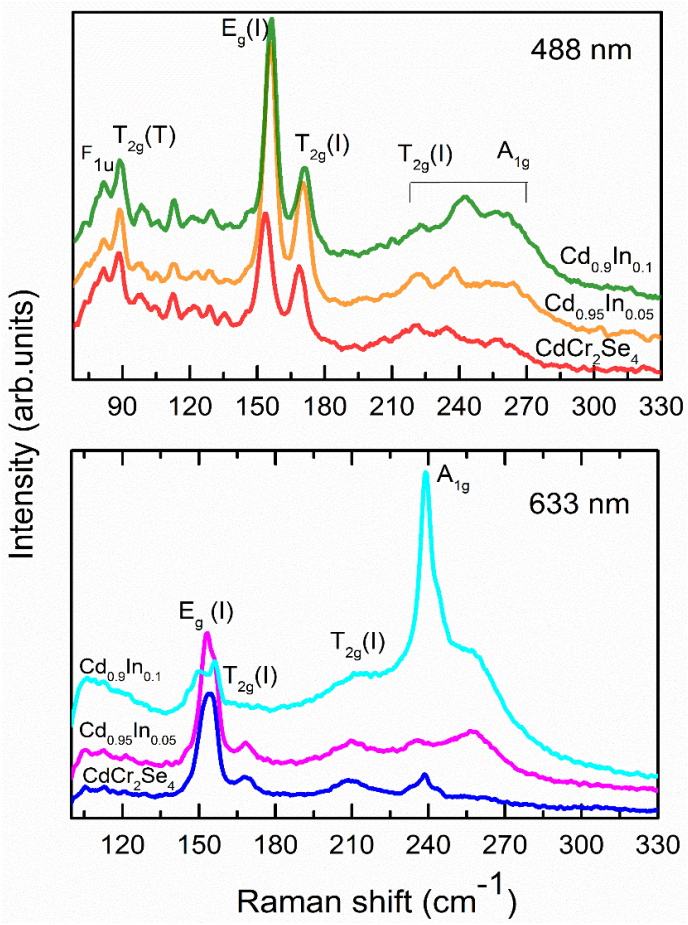

Figure 3.7: Room temperature Raman spectra measured with excitation wavelength of 488 nm (top panel) and 633 nm (bottom panel) for $Cd_{1-x}In_xCr_2Se_4$ (x = 0, 0.05, 0.1).

Accordingly, the first mode appearing at 82 cm^{-1} is the T_{2g} translational (T) mode, associated with complete translation of the $CdSe_4$ unit within the spinel lattice. The next and most intense mode is the E_g mode at ~154 cm^{-1}, associated with tangential displacement of the Se anions with respect to the Cd-Se bonds. The enhancement in intensity of these two modes for the substituted samples confirms the distribution of Sb, In and Sn at the targeted tetrahedral site. Next is the T_{2g} (I) mode at ~166 cm^{-1}, which is the only mode that directly involves the vibration of (Cr-Se-Cr) bonds. This indirect 90° bond interaction is one of strong magnetic interactions responsible for ferromagnetic ground state in spinel chalcogenides. In case of Raman spectra obtained using 488nm (2.54 eV) excitation, we can notice that the higher frequency modes *viz.* T_{2g} (I) and A_{1g} (I) observed in the region 200 – 270 cm^{-1}, originate from asymmetric bending, symmetric breathing and

stretching mode of the Se bonded to Cd in the $CdSe_4$ tetrahedra. Since Sb, In and Sn are incorporated at tetrahedral site, broadening and shift in peak positions of these two peaks is observed with increasing concentration.

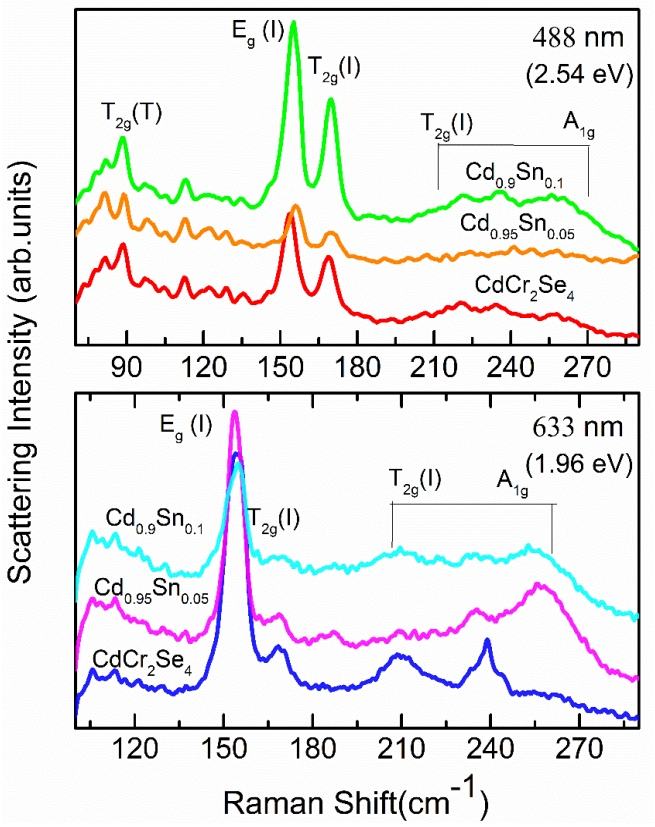

Figure 3.8: Room temperature Raman spectra measured with excitation wavelength of 488 nm (top panel) and 633 nm (bottom panel) for $Cd_{1-x}Sn_xCr_2Se_4$ (x = 0, 0.05, 0.1).

3.3.2.3 High-resolution Synchrotron XRD

Synchrotron XRD patterns recorded at temperatures below and above the magnetic ordering temperature (T_C) of $[Cd_{1-x}M_x]Cr_2Se_4$ compositions are depicted in Fig.3.9, Fig. 3.10 and Fig. 3.11. The extra reflections at ~17°, which is denoted as '*' in Sb and Sn substituted is due to the presence of a small impurity peak of Cr_2Se_3 and the intensity of peak reflection at ~26° for 5% Sb-doped sample at 120 K is derived from a spike/ spurious signal in the detector, not related to the sample. The XRD patterns presented in the thesis is as recorded, without correcting such glitch in the patterns. Apart from this, we did not find appearance of any extra peak, or

deformation, illustrating that the structure remains cubic across T_C within the investigated temperature range.

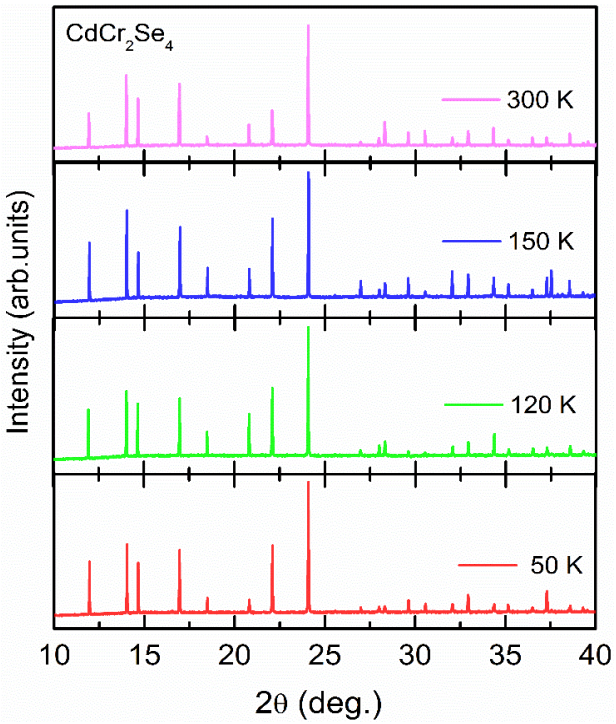

Figure 3.9: Synchrotron XRD patterns obtained for parent, $CdCr_2Se_4$ compound at different temperatures.

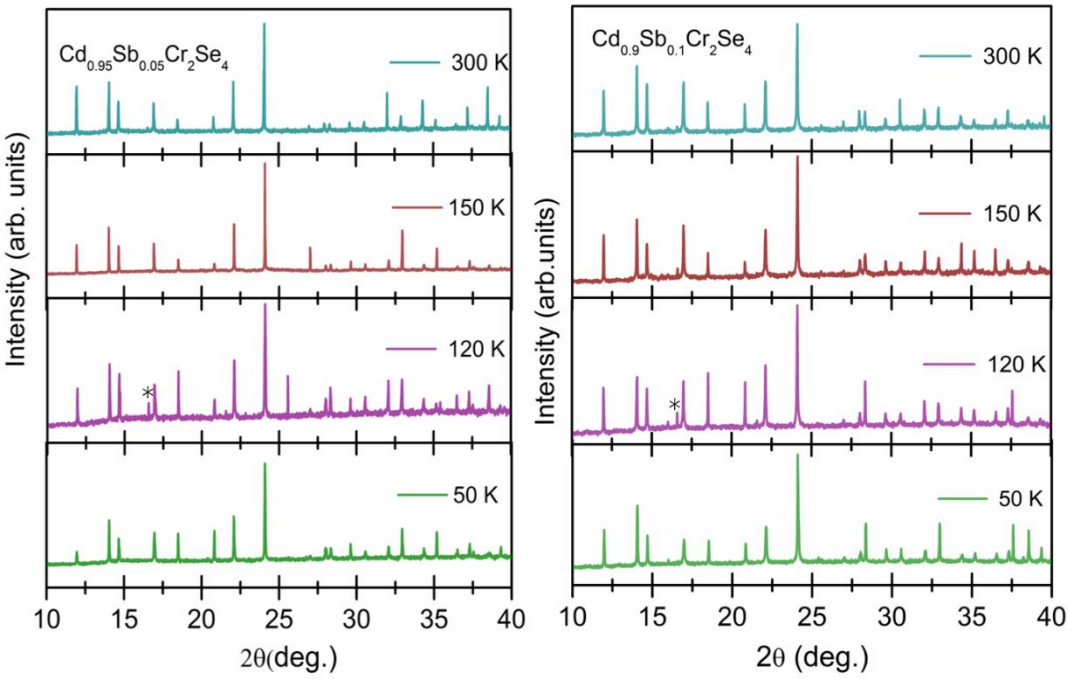

Figure 3.10: Synchrotron XRD patterns obtained for $Cd_{1-x}Sb_xCr_2Se_4$ series at different temperatures

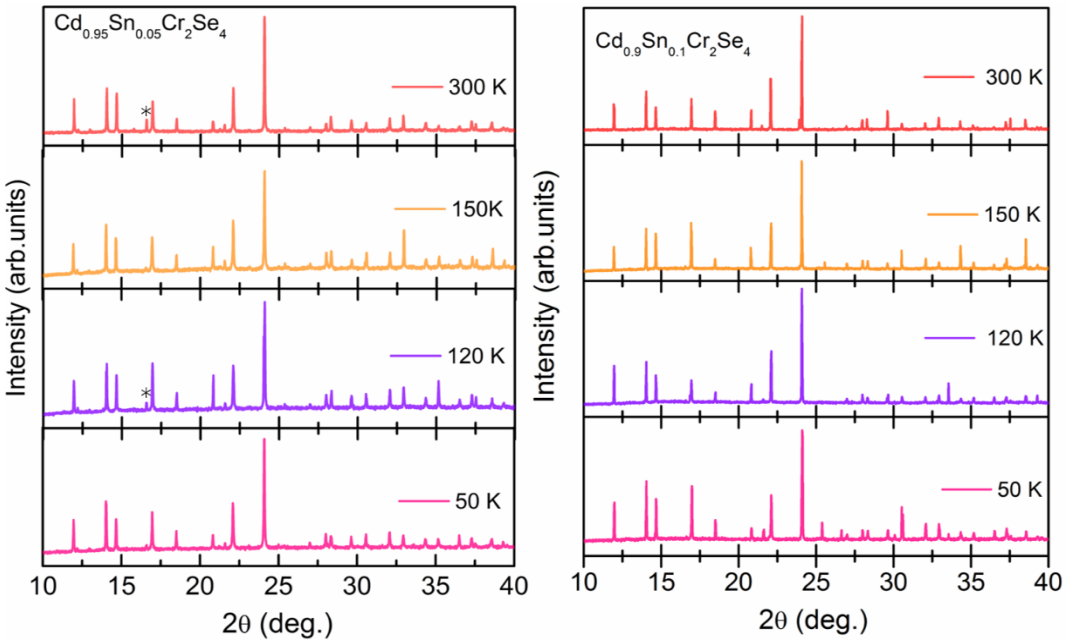

Figure 3.11: Synchrotron XRD patterns obtained for $Cd_{1-x}Sn_xCr_2Se_4$ series at different temperatures

3.3.3 Heat Capacity Measurements

As we know from the literature, that the overall magnetic order in $CdCr_2Se_4$ is a result of competition between indirect Cr^{3+}-Se-Cr^{3+} exchange interaction and direct Cr-Cr interaction. Thus, Cr ion mainly controls and contributes to magnetism in this compound. Partial replacement of non-magnetic Cd by Sb should not affect its magnetic properties as the lattice is seen to remain unaffected. Indeed, the magnetic ordering temperature (T_C) remains unchanged with rising Sb content. This is well depicted from the heat capacity (C_P) measurements performed across its ferromagnetic ordering temperature. Fig. 3.12 presents the plots of temperature dependence of C_P measured in all three compositions. A λ-type signature is found at T_C ~130 K in $CdCr_2Se_4$, matching with the reports present in literature [108]. The x = 0.05 and 0.1 compositions also show similar λ-type signature at the same temperature indicating no change in T_C with increasing Sb – content. Further, owing to its large molecular mass, a large value of C_P is generally observed in the chalcogenide spinels compared to its oxide counterparts. With x changing from 0 to 0.1, not much change in C_P takes place over the entire temperature range as the molecular mass changes very little from

one composition to other. This is also an indication that no phase transformation takes place in the low temperature region.

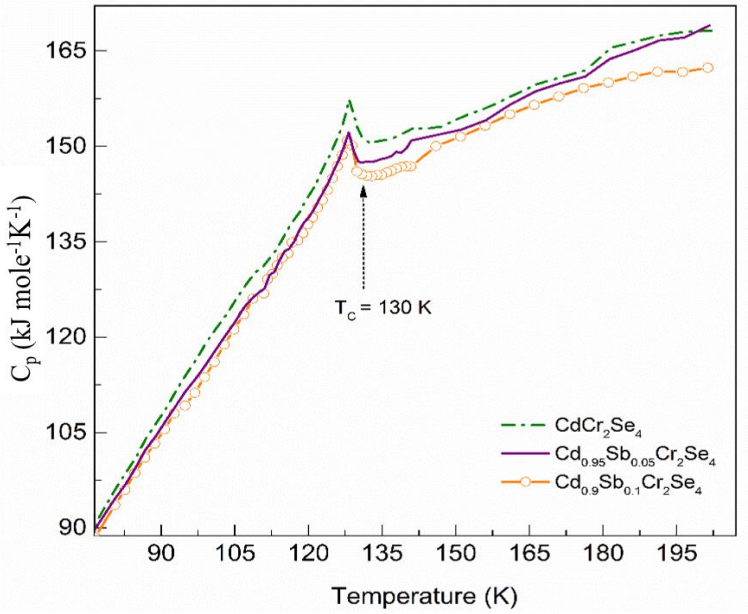

Figure 3.12: Temperature dependence of heat capacity recorded for $[Cd_{1-x}Sb_x]Cr_2Se_4$ (x = 0, 0.05, 0.1).

3.3.4 Magnetic Properties

The temperature-dependent and field-dependent magnetization for the parent compound is presented in Fig. 3.13 (a) and (c). The sharp rise in *M(T)* below the critical temperature of $T_C \sim 130$ K is seen, which matches with reports in literature. The magnetic moment *($M_S(\mu_B/f.u.)$)* was obtained from the saturation magnetization value of *M(H)* recorded at 5 K (see Fig. 3.13 (c)). It gives the value 5.38 μ_B/f.u. The *M(T)* curves for Sb, In and Sn substituted compositions show ferromagnetic ordering as depicted in Fig. 3.14, Fig. 3.15 and Fig. 3.16 respectively, the corresponding T_C values are listed in Tab. 3.3. Fig. 3.13 (b), Fig. 3.17 and Fig. 1.8 display the inverse *dc* susceptibility plotted as a function of temperature for all the substituted compounds along with parent one. By fitting the high temperature region with the Curie–Weiss law, $\frac{1}{\chi} = \frac{T-\theta}{C}$, we obtain the Curie-temperature θ and effective paramagnetic moment (μ_{eff}^{Cal}) from the relation, $C = \frac{N_A \mu_B^2 \left(\mu_{eff}^{cal}\right)^2}{3k_B\ Mole.\ wt.}$, where N_A is the Avogadro's number, k_B is the Boltzmann constant, and

μ_B is the value of Bohr magneton. The values of Curie temperature θ and μ_{eff}^{Cal} obtained from Curie constant *C* are listed in Tab. 3.3 alongside the magnetic moments calculated from the saturation magnetization obtained from *M(H)* plots measured at 5 K and depicted in Fig. 3.19.

Although substitution is carried out at the non-magnetic Cd site, altering the composition of parent compound is seen to impact its magnetic properties. Generally, the underlying complexities in magnetic ordering of a system get reflected through the ZFC and FC protocols followed during *M(T)* measurements. In the present case, the Sb-substituted samples show small splitting of the ZFC–FC plots similar to $CdCr_2Se_4$, and can be attributed to the variation in the particles grain-sizes. In the case of In-substituted samples the splitting is less prominent for $x = 0.05$ but increases considerably, immediately below T_C for $x = 0.1$. On the other hand, besides showing considerable splitting of the ZFC–FC curves, the $x = 0.05$ Sn-substituted sample shows a drop in the magnetization below ∼15 K. This signature of antiferromagnetic-like transition below T_C is not observed in other Sn-substituted samples. Hence, to further investigate the low temperature magnetic behavior in In-0.1 and Sn-0.05 samples, *M(T)* was recorded under a slightly higher applied field of 500 Oe. As evident from Fig. 3.20, the ZFC–FC splitting gets completely suppressed at this value of applied field. Moreover, the magnetic hysteresis plot for In-0.1 and Sn-0.05 shown in Fig. 3.21 displays characteristics of a soft ferromagnetic phase with very small coercivity and strong saturation magnetization at moderate field value. Presence of any spontaneous magnetization for weakly ordering magnetic systems can usually be confirmed from its Arrott plot recorded around the transition region, for example see Ref. [109]. Such an analysis for the current two samples at low temperature is presented in the left panel of Fig. 3.21. All the M^2 versus H/M curves measured across the low temperature feature (17–7 K) show positive slopes and curvature indicating second-order ferromagnetic phase. However, to completely rule out the possibility of spin cluster phase, ac magnetic susceptibility (χ *(T)*) at two different frequencies was measured and the plots are presented in the lower panel of Fig. 3.20. No drift with respect to frequency is observed at the low temperature antiferromagnetic-like feature.

Chemical Composition	T_C *(K)*	M_S *(μ_B/f.u.)*	θ *(K)*	$\mu_{eff}^{cal}(\mu_B)$
$CdCr_2Se_4$	130	5.38	158	6.47
$Cd_{0.95}Sb_{0.05}Cr_2Se_4$	130	5.83	146	6.78
$Cd_{0.9}Sb_{0.1}Cr_2Se_4$	130	5.82	143	6.96
$Cd_{0.95}In_{0.05}Cr_2Se_4$	123	5.71	147	6.56
$Cd_{0.9}In_{0.1}Cr_2Se_4$	117	4.84	144	6.50
$Cd_{0.97}Sn_{0.03}Cr_2Se_4$	122	5.68	147	6.35
$Cd_{0.95}Sn_{0.05}Cr_2Se_4$	116	3.79	139	5.93
$Cd_{0.93}Sn_{0.07}Cr_2Se_4$	120	5.77	151	6.68
$Cd_{0.9}Sn_{0.1}Cr_2Se_4$	124	5.23	176	6.49

Table 3.3: Magnetic ordering temperature (T_C), saturation magnetic moment, Curie temperature θ, and paramagnetic moment calculated from Curie constant C, for $Cd_{1-x}M_xCr_2Se_4$ (M = Sb, In, Sn).

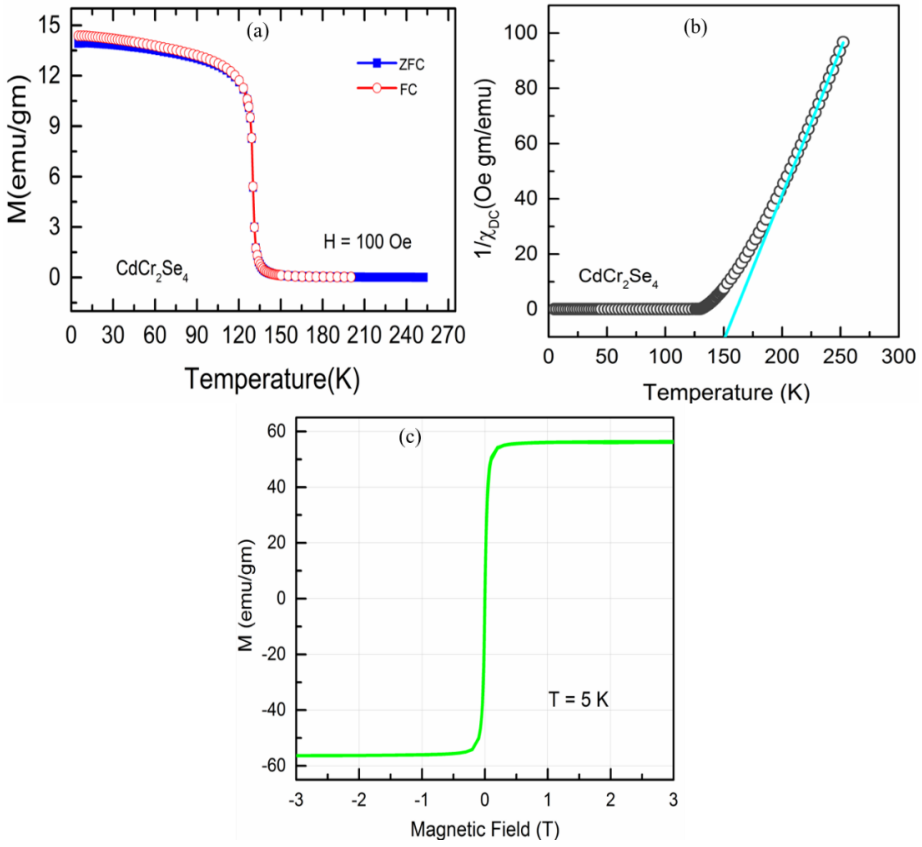

Figure 3.13: (a) Magnetization obtained for $CdCr_2Se_4$ as (a) function of temperature between 5 and 250 K (b) Curie– Weiss fit to the $1/\chi$ versus T plot and (c) function of applied field between 75 T (data upto 3 T is presented here for clarity of figure). The magnetic transition temperature (T_C) was determined from the differential of M with respect to T for ZFC curve.

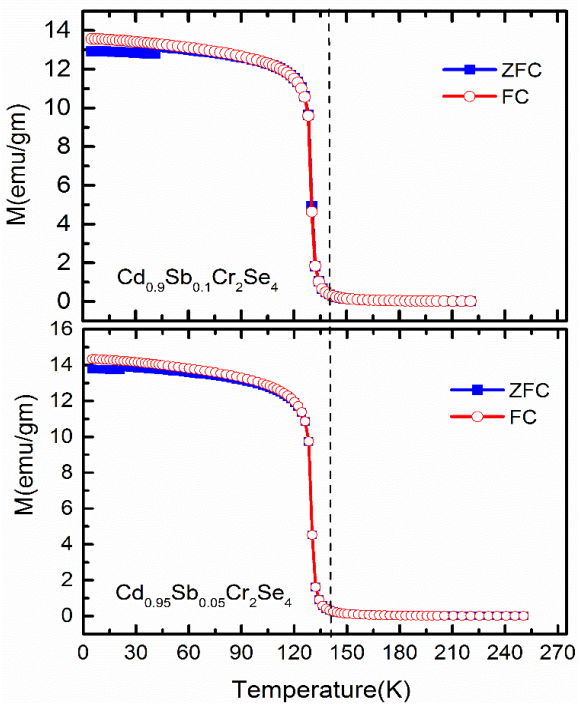

Figure 3.14: *M(T)* plots measured in the ZFC–FC mode under an applied field of 100 Oe for $Cd_{1-x}Sb_xCr_2Se_4$.The dotted line indicates the paramagnetic to ferromagnetic ordering temperature (T_C)

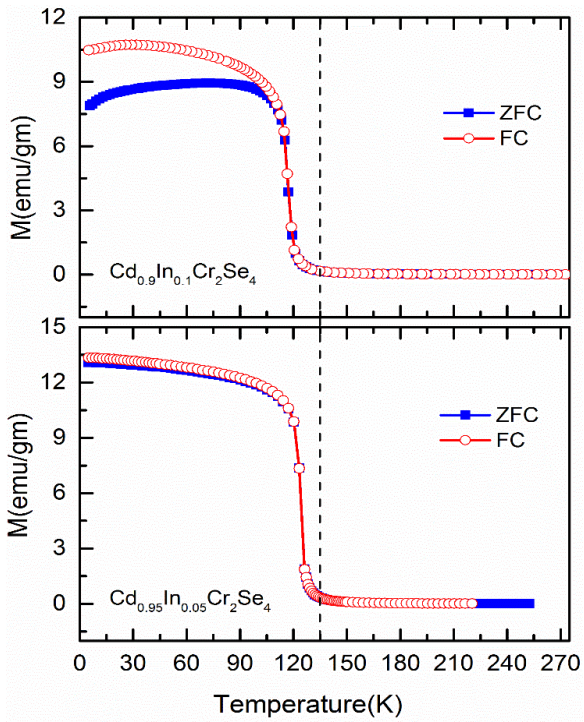

Figure 3.15: *M(T)* plots measured in the ZFC–FC mode under an applied field of 100 Oe for $Cd_{1-x}In_xCr_2Se_4$. The dotted line indicates the paramagnetic to ferromagnetic ordering temperature (T_C).

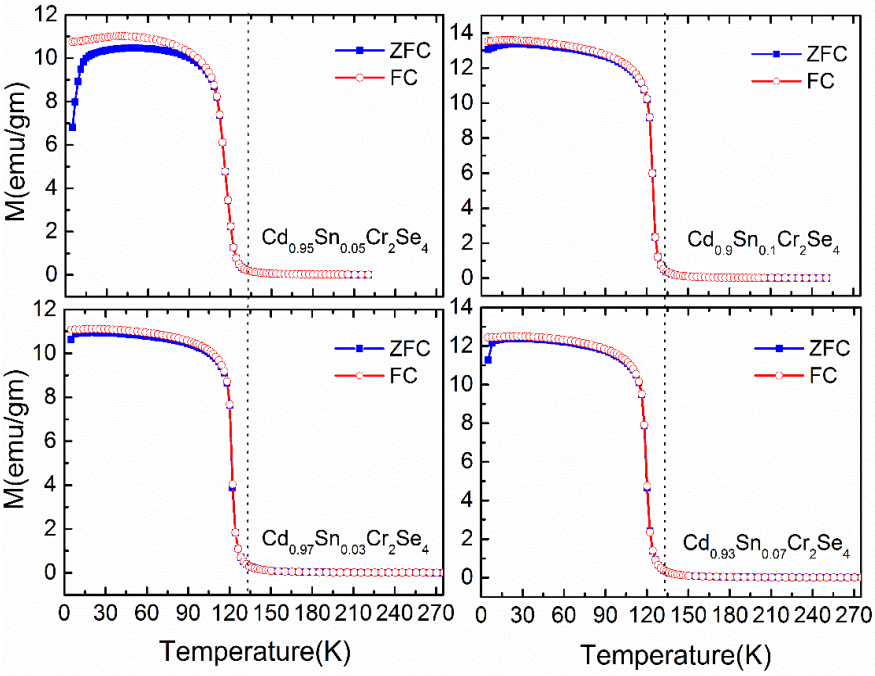

Figure 3.16: *M(T)* plots measured in the ZFC–FC mode under an applied field of 100 Oe for $Cd_{1-x}Sn_xCr_2Se_4$. The dotted line indicates the paramagnetic to ferromagnetic ordering temperature (T_C)

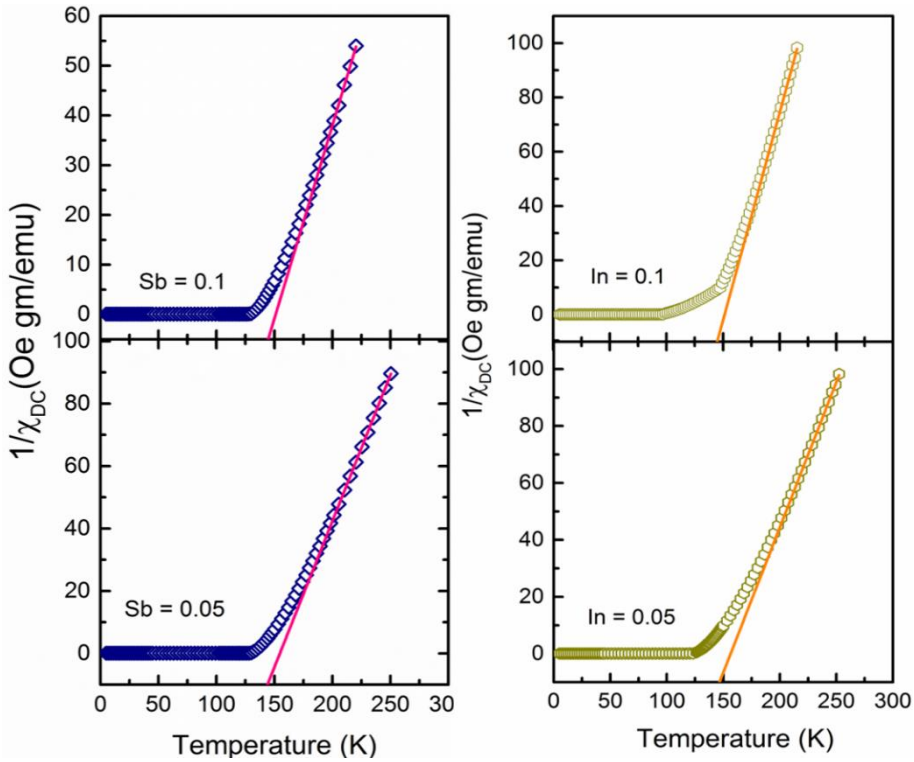

Figure 3.17: The above left and right panels display inverse dc magnetization and the solid line is the fit to Curie–Weiss law for $Cd_{1-x}Sb_xCr_2Se_4$ and $Cd_{1-x}In_xCr_2Se_4$ compounds respectively.

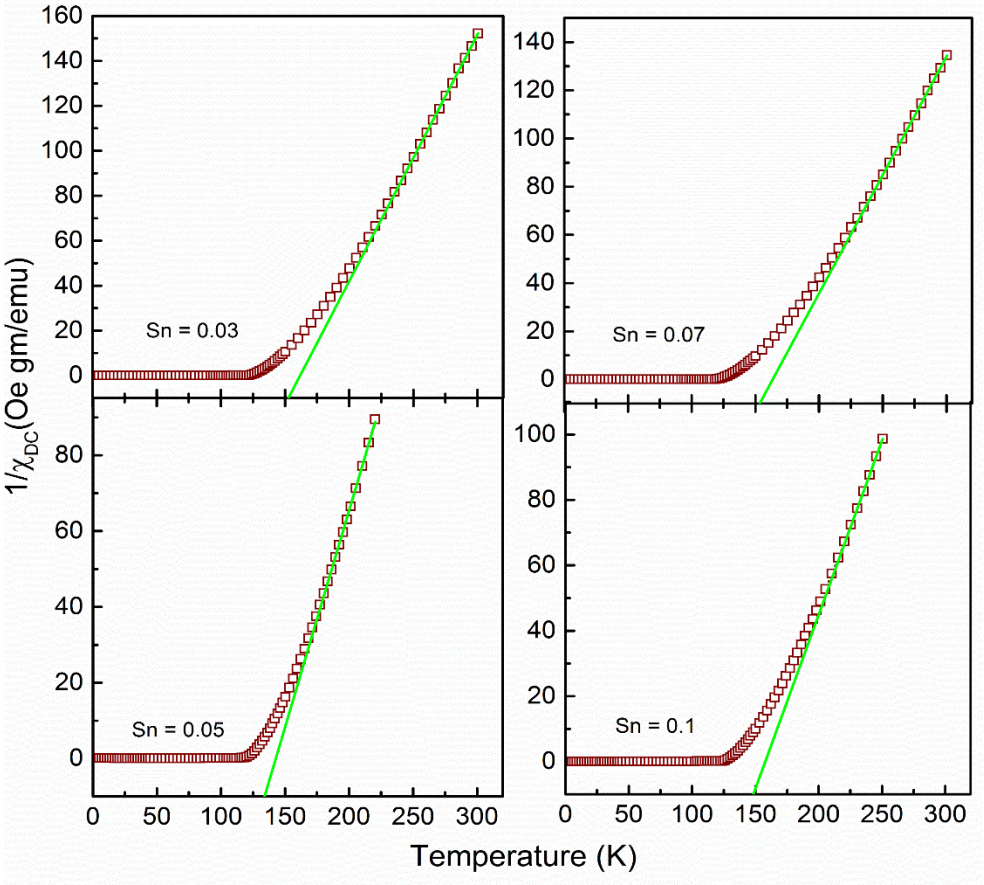

Figure 3.18: The above panels display inverse dc magnetization and the solid line is the fit to Curie–Weiss law for $Cd_{1-x}Sn_xCr_2Se_4$ series

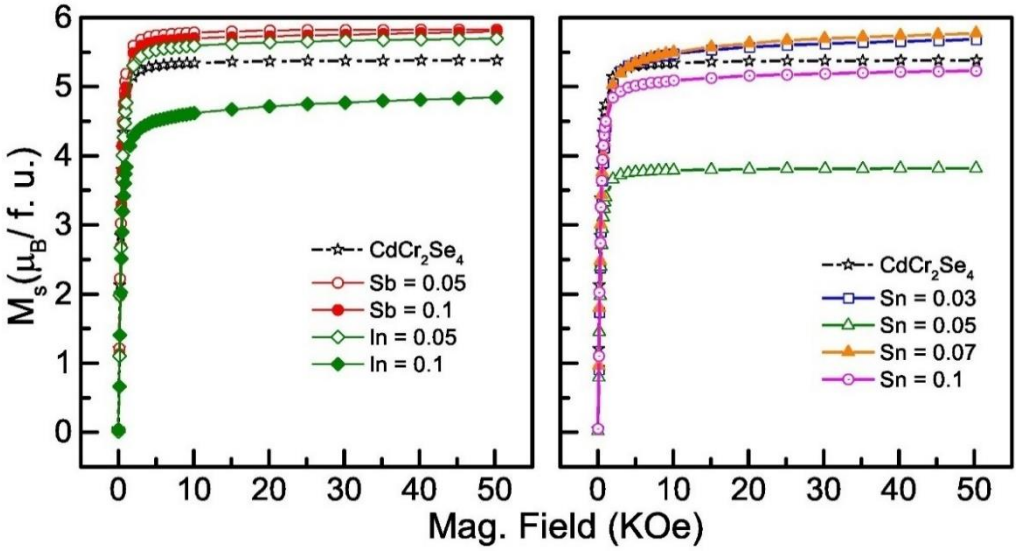

Figure 3.19: Magnetization as a function of field with maximum applied field upto 5 T, and temperature of 5 K.

The magnetic ground state in $CdCr_2Se_4$ results from competition between ferromagnetic Cr-Se-Cr interactions and antiferromagnetic Cr-Cr interactions. The large ZFC–FC splitting that disappears with higher applied field can be a manifestation of this competition but this alone cannot explain the low-temperature down turn in ac χ. For this we need to focus on the crystal structure parameters of this series. We begin with the trends seen in magnetic properties of all compositions. For Sb-substituted compositions, T_C remains same as that of $CdCr_2Se_4$, while the In-substituted samples show a linear fall in T_C with increasing concentration. On the other hand, Sn-substituted compositions deviate from such a trend; the T_C initially decreases upto x = 0.05 and then increases for x = 0.07 and 0.1. The overall behavior of the samples is well depicted in Fig. 3.22, where values of T_C are plotted as a function of concentration x. It is interesting to compare this trend in T_C with the changing lattice constants plotted in the upper panel of the same figure.

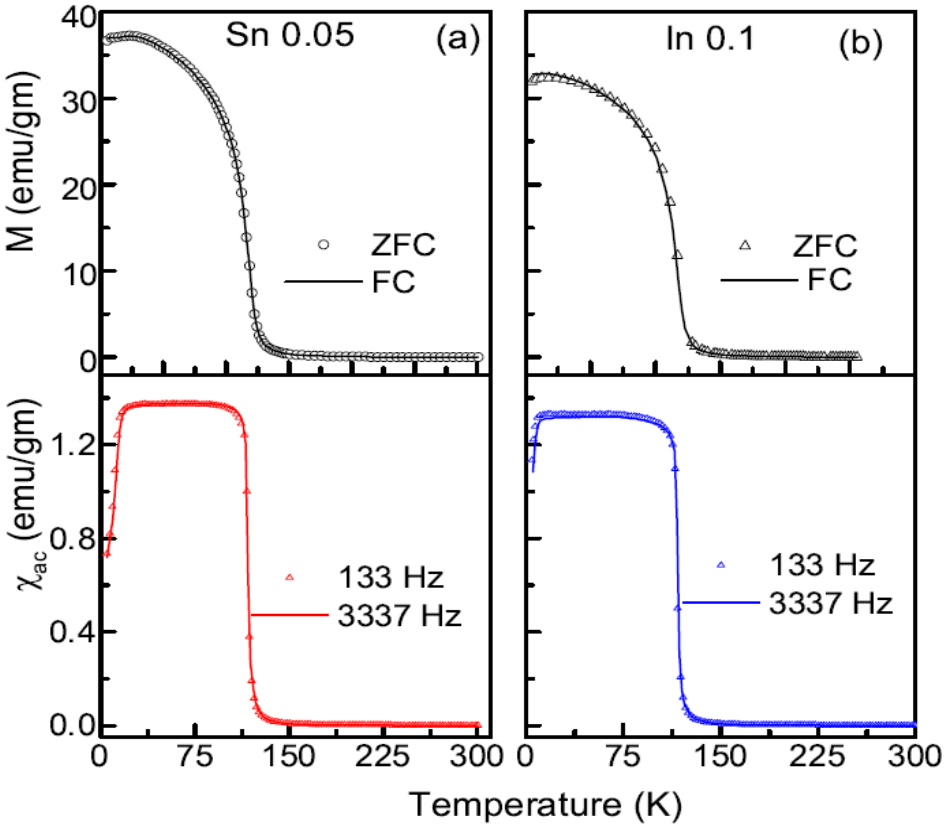

Figure 3.20: *M(T)* measured under an applied field of 500 Oe and ac χ*(T)* measured at two different frequencies for (a) $Cd_{0.95}Sn_{0.05}Cr_2Se_4$ and (b) $Cd_{0.9}In_{0.1}Cr_2Se_4$.

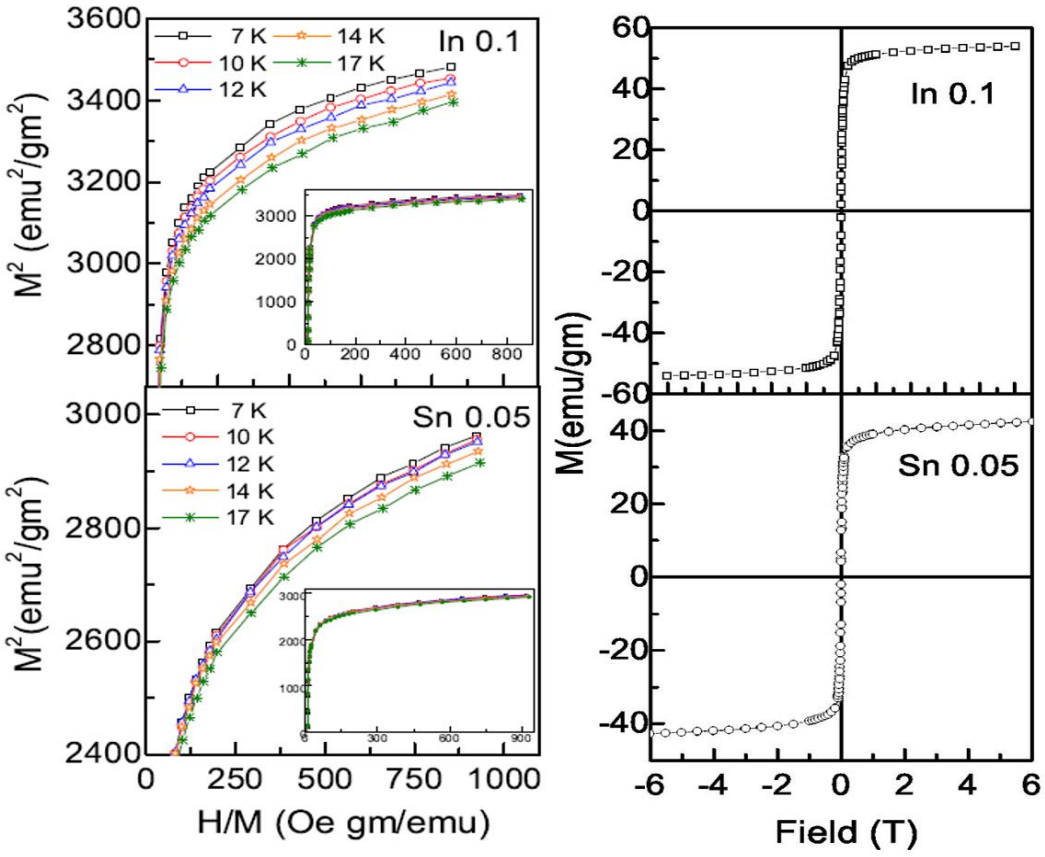

Figure 3.21: Left panel: Arrott plot at different temperatures close to the low temperature feature seen in $Cd_{0.9}In_{0.1}Cr_2Se_4$ and $Cd_{0.95}Sn_{0.05}Cr_2Se_4$, confirming the ferromagnetic nature of these two samples. Inset shows the entire plots while the main panel is shown on the expanded scale for clarity. Right panel: *M(H)* plots measured at ± 5 T for the same samples.

For the Sb-substituted compositions, since the lattice constant does not change with increasing concentration the tetrahedral location of Cd^{2+} occupied by Sb^{3+} has less impact on Cr-Cr or Cr-Se-Cr exchange interactions within the magnetic sub-lattice. This reflects through the observation of same ordering temperatures and only slight splitting of ZFC-FC plots. However, change in the valence at tetrahedral-site from 2+ to 3+ implies an appearance of Cr^{2+} state at Cr-sites in order to form a charge balanced composition. The spin magnetic moment of Cr^{2+} in the high spin configuration is 4.9 μ_B/mol, which is higher than that of Cr^{3+} (3.88 μ_B/mol). Since the paramagnetic moment of Sb-substituted samples (see Table 1) is observed to be higher than that of the parent composition, it is confirmed

that presence of Sb^{3+} ions leads to appearance of small amount of Cr^{2+} state at Cr-sites. Similar argument is extended to understand the magnetic moment value of In^{3+}-substituted composition with x = 0.05. The reduced T_C however relates to the increase in its lattice constant, which weakens the Cr-Se-Cr and Cr-Cr overlaps and hence the ordering temperature. The x = 0.1 sample of In shows further increase in lattice constant and corresponding decrease in T_C. However, slightly lower values of magnetic moment (M_S *(μ_B/f.u.)* as well as the paramagnetic moment) is observed in this case.

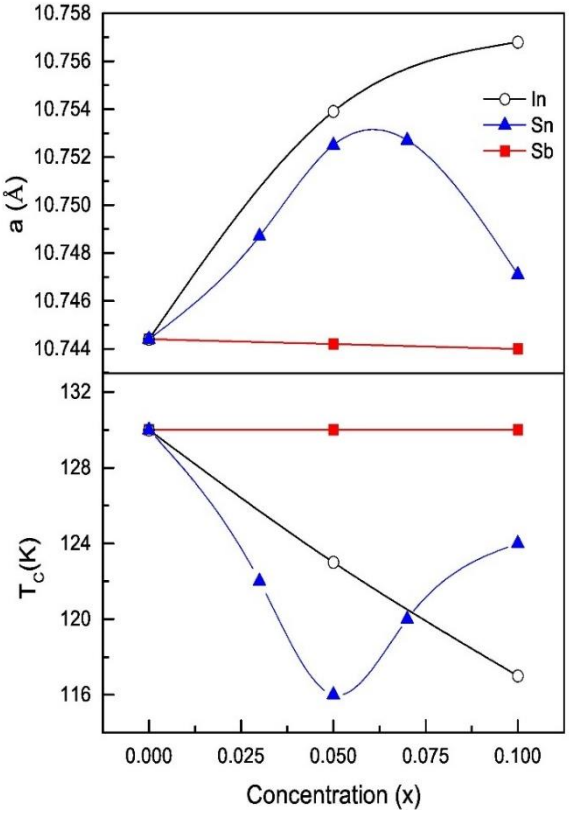

Figure 3.22: Variation in the (a) Lattice constant 'a' and (b) magnetic transition temperature (T_C) as a function of M concentration *(x)* for $[Cd_{1-x}M_x]Cr_2Se_4$ (M = Sb, In, Sn) series.

In line with argument applied to Sb and In compositions, the substitution of Sn^{4+} ions at Cd^{2+} site gives rise to the formation of Cr^{2+}. Moreover, we observe that lattice constants for Sn concentration of x = 0.05 and 0.07 are nearly equal while its paramagnetic moment, saturation magnetic moment, and the T_C are not same.

Rather x = 0.05 sample shows properties matching with In-0.1 composition. It is plausible that Sn-0.05 and In-0.1 samples undergo a low-spin transition in Jahn Teller active Cr^{2+} ions, signature of which is the low temperature anti-ferromagnetic like feature seen in its *M(T)* and ac χ measurements and reduced magnetic moments. Increase in lattice constants causes considerable difference in the overlap of *d*-orbitals, that could result in wider separation of bands, triggering a low-spin transition. However, such transition being an outcome of very critical balance between charge and lattice effects, slight variation of composition to Sn-0.07 and thereafter leads to convergence of crystal and magnetic properties towards that of the parent $CdCr_2Se_4$ composition. These higher concentrations of Sn, viz. x = 0.07 and 0.1 show magnetic moments, T_C, and lattice constants similar to the rest of series. Considerable difference between the cation radii and electronic charge of Sn^{4+} and Cd^{2+} impacts its electronic structure more strongly resulting in the rapid change in the magnetic properties.

3.3.5 Local Structure Analysis

3.3.5.1 XANES Results

In Cr – based spinel compounds like $CdCr_2Se_4$, the stability of Cd^{2+} valence state allows Cr ion to be present in $3d^3$ configuration. The octahedral site occupancy of Cr leads to lifting of degeneracy of the *d* orbitals such that the electrons redistribute in the low energy t_{2g} orbitals with quenched orbital degeneracy and negligible spin-orbit interaction [110]. Accordingly, the paramagnetic moment, extracted from susceptibility measurements of $CdCr_2Se_4$ used in the present study was ~ 6.47 μ_B/f.u., for In-substituted compositions, the μ_{eff}^{cal} value were observed to be slightly increased, moreover similar like parent one; 6.56 μ_B/f.u. and 6.50 μ_B/f.u. for x = 0.05 and 0.1 samples respectively. However, the values extracted for Sb – substituted compositions were found to be increased to 6.78 μ_B/f.u. and 6.96 μ_B/f.u. for x = 0.05 and 0.1 samples, respectively. It was suggested that the rise in the magnetic moment can be understood by considering a mixed valence configuration of Cr ions that develops upon Sb and In substitution, in order to maintain the overall charge balance in the compositions. It

was conjectured that, since partial replacement of Cd^{2+} takes place by Sb and In ions in its 3+ state, it causes an equivalent quantity of Cr^{2+} to appear at Cr – site.

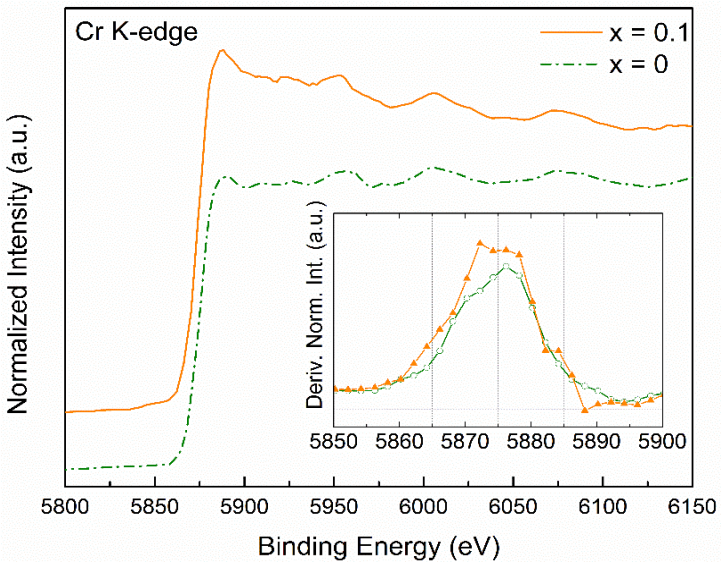

Figure 3.23: Cr K-edge XANES spectra for $Cd_{1-x}Sb_xCr_2Se_4$ (x = 0 and 0.1) compositions. The spectra have been displayed with some y-offset for better clarity. Inset shows the shift in absorption edge energy as evident from derivative plot of the absorption spectra.

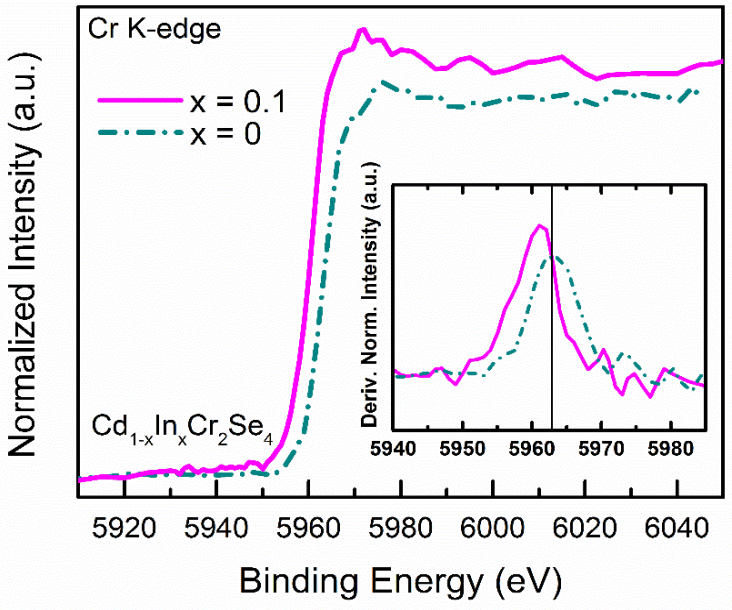

Figure 3.24: Cr K-edge XANES spectra for $Cd_{1-x}In_xCr_2Se_4$ (x = 0 and 0.1) compositions. The spectra have been displayed with some y-offset for better clarity. Inset shows the shift in absorption edge energy as evident from derivative plot of the absorption spectra.

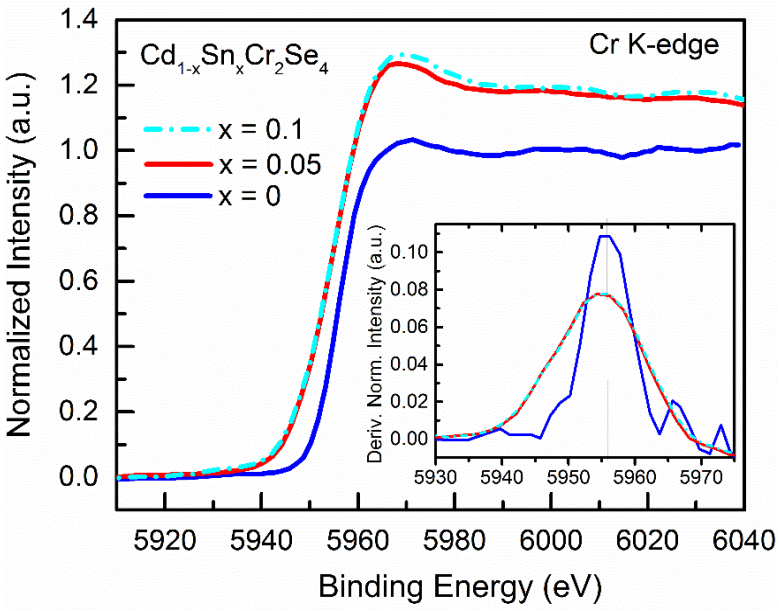

Figure 3.25: Cr K-edge XANES spectra for $Cd_{1-x}Sn_xCr_2Se_4$ (x = 0, 0.05 and 0.1) compositions. The spectra have been displayed with some y-offset for better clarity. Inset shows the shift in absorption edge energy as evident from derivative plot of the absorption spectra.

In this present work, we confirm such mixed valence configuration of Cr ions in both $Cd_{1-x}Sb_xCr_2Se_4$, $Cd_{1-x}In_xCr_2Se_4$ and $Cd_{1-x}Sn_xCr_2Se_4$ samples from purely local crystal structure tools of investigation. The evidence for Cr mix valence comes from the XANES recorded at the Cr K-edge for the above samples. The XANES spectra for parent and x = 0.1 samples for both Sb and In-substituted compositions and parent, x = 0.05 and x = 0.1 for Sn-substituted compositions are shown in Fig. 3.23, Fig. 3.24 and Fig. 3.25 respectively. The striking observation that can be made from the spectra presented here, is the clear shift towards lower binding energy of the absorption edge observed in the both x = 0.1 samples as compared to the parent $CdCr_2Se_4$. A shift towards lower binding energy signals an overall decrease in the valence state of Cr ions. Thus, it supports our argument of the formation of mixed valence of Cr ions (Cr^{3+} and Cr^{2+}) in the Sb, In and Sn substituted samples as opposed to pure Cr^{3+} state in $CdCr_2Se_4$. Also, it corroborates with the observation of rise and fall in magnetic moment of substituted compositions due to the presence of high spin and low spin state of Cr^{2+} ion. The shift in energy of Sn-substituted compositions is not that clear, with observation of

a broad peak. This is due to the disorder present in the compositions, as will be demonstrated through EXAFS analysis, presented later in the text.

3.3.5.2 EXAFS Results

As can be surmised from a simple chemical charge balance in the parent $CdCr_2Se_4$ composition, the Cr ions are in 3+ valence state giving a total magnetic moment of 5.38 (μ_B/f.u.) whereas, the moment increases to 5.83 (μ_B/f.u.) in the Sb containing samples. This rise in the magnetic moment can be understood due to the formation of mixed valence of Cr ions as confirmed from above XANES results, in order to balance the charge imbalance formed in the compositions owing to partial replacement of Cd^{2+} by Sb^{3+} ions. In fact, simple mathematics with respect to changing magnetic moments and amount of Cr^{3+} ions present in each formula unit provides us with an estimate of the amount of mixed valence of Cr. For example, the 10% Sb-substituted composition indicates the presence of nearly 13% of high spin Cr^{2+} ions, increasing its saturation magnetic moment as compared to parent compound. Similar arguments can be extended for In-substituted sample as well; the total magnetic moment of 10% In-substituted sample being smaller than the parent composition, it can be argued that Cr^{2+} ion is in the low spin state as demonstrated by the schematic present in the Fig. 3.26.

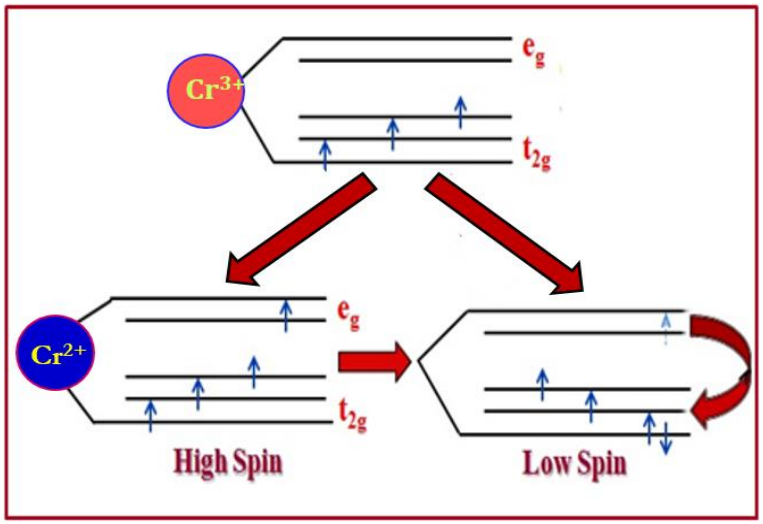

Figure 3.26: Schematic of distribution of electrons over 3d orbitals in low-spin state and high-spin state, for Cr^{2+} ion.

In support of such an argument we present the yet another result from local structural investigation of $Cd_{1-x}Sb_xCr_2Se_4$ and $Cd_{1-x}In_xCr_2Se_4$ compounds were carried out using EXAFS measurements at Cr K-edge. A fit to the data was modelled using the normal spinel structure with lattice parameter inputs obtained from XRD analysis. The fitting was carried out upto 3Å in *R* – space and *k* – range of (2 - 10) $Å^{-1}$. Similar argument of local structure investigation for $Cd_{1-x}Sn_xCr_2Se_4$ composition will be further discussed in the next chapter.

Chemical Composition	***a (Å)***	***u***	$d_{Cr\text{-}Se}$ ***(Å)***	$d_{(Cr\text{-}Se)\ expt.}$ ***(Å)***	σ^2
$CdCr_2Se_4$	10.744	0.2643	2.542	2.6108(86)	0.0053(1)
$Cd_{0.95}Sb_{0.05}Cr_2Se_4$	10.744	0.2643	2.542	2.6148(88)	0.0087(2)
$Cd_{0.9}Sb_{0.1}Cr_2Se_4$	10.744	0.2643	2.542	2.6224(84)	0.0092(4)
$Cd_{0.95}In_{0.05}Cr_2Se_4$	10.754	0.2646	2.541	2.6112(78)	0.0085(3)
$Cd_{0.9}In_{0.1}Cr_2Se_4$	10.757	0.2640	2.547	2.6217(75)	0.0087(1)

.

Table 3.4: Structural parameters as obtained from room temperature XRD and EXAFS analysis for $Cd_{1-x}Sb_xCr_2Se_4$ and $Cd_{1-x}In_xCr_2Se_4$. σ^2 refers to the thermal mean square parameter corresponding to bond-distance.

Parameters such as Cr-Se bond-length and the associated thermal mean square variation were refined until a good fit was obtained, as shown in Fig. 3.27 for parent and Fig. 3.28 and Fig. 3.29 for both Sb and In substituted compounds respectively. The final parameters extracted from the fit are listed in Tab. 3.3. Firstly, we find that the bond distance values obtained from EXAFS show considerable deviation from those calculated from the XRD profile. This is expected as XRD provides an average distribution of Cr-Se bond distances that are calculated from the statistically obtained lattice constant. On the other hand, EXAFS technique is based on interference of outgoing and back scattered photoelectron waves resulting from absorption of an x-ray photon. As a result, it probes at much local level around the absorbing atom and hence captures the bond-distances and distortions therein, with much better accuracy. However, the central point brought forward from EXAFS analysis is the steady increase in Cr-Se distance with rising Sb and In content. This observation is in stark contrast with the

XRD results wherein the unit cell parameter and hence the Cr-Se bond distance remains unchanged for all the prepared samples of $Cd_{1-x}Sb_xCr_2Se_4$ (x = 0, 0.05 and 0.1). But in case of $Cd_{1-x}In_xCr_2Se_4$ (x = 0, 0.05 and 0.1) samples, from XRD results, the unit cell parameters were slightly changes with respect to In substitution, wherein Cr-Se bond distance obtained from EXAFS analysis has changed considerably. Therefore, the EXAFS results should be understood in terms of inherent disorder present in Cr-Se bond. Such disorder is expected to arise from subtle difference in hybridization of Se ions with mixed valent Cr ions. A clear indication of presence of disorder comes from higher values of the thermal mean square vibration (σ^2), associated with the Cr–Se bond.

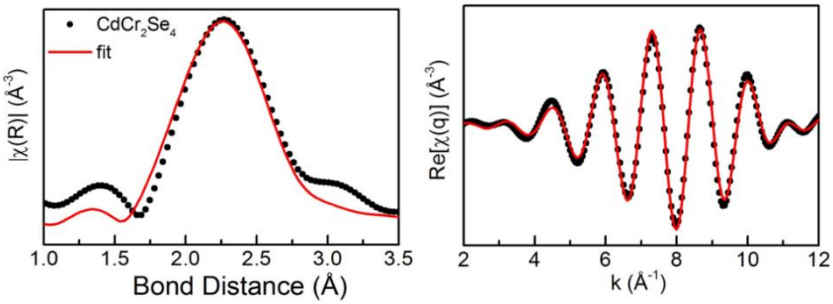

Figure 3.27: Fitting of the magnitude (left panel) and real component (right panel) of Fourier transform of Cr K-edge EXAFS spectra in $CdCr_2Se_4$ compound.

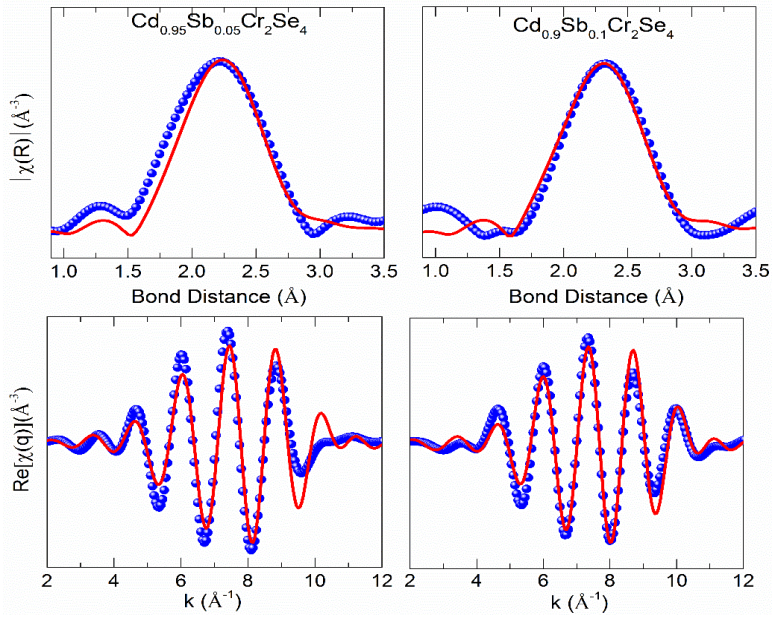

Figure 3.28: Fitting of the magnitude (top panel) and real component (bottom panel) of Fourier transform of Cr K-edge EXAFS spectra in $Cd_{1-x}Sb_xCr_2Se_4$ compounds.

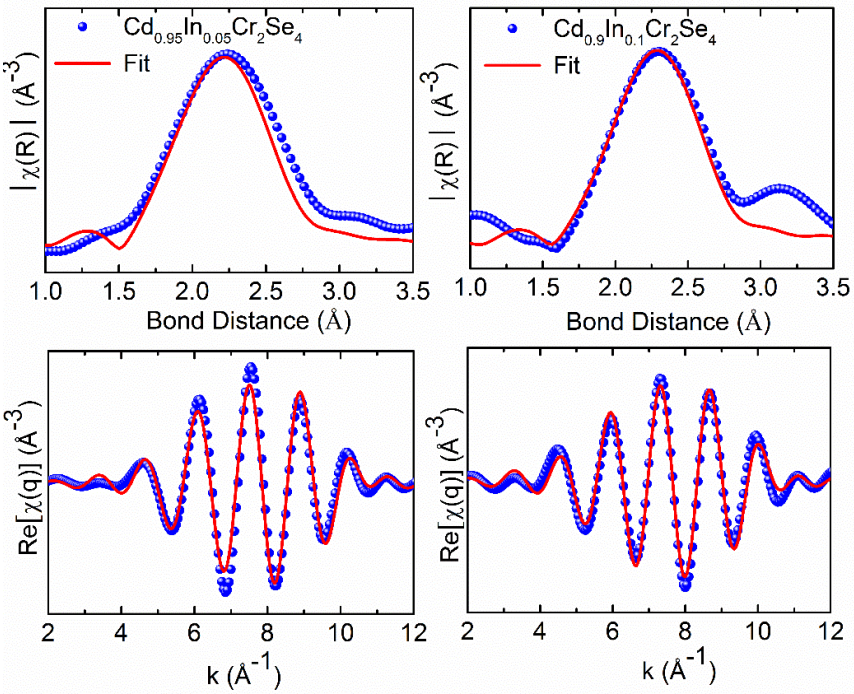

Figure 3.29: Fitting of the magnitude (top panel) and real component (bottom panel) of Fourier transform of Cr K-edge EXAFS spectra in $Cd_{1-x}In_xCr_2Se_4$ compounds.

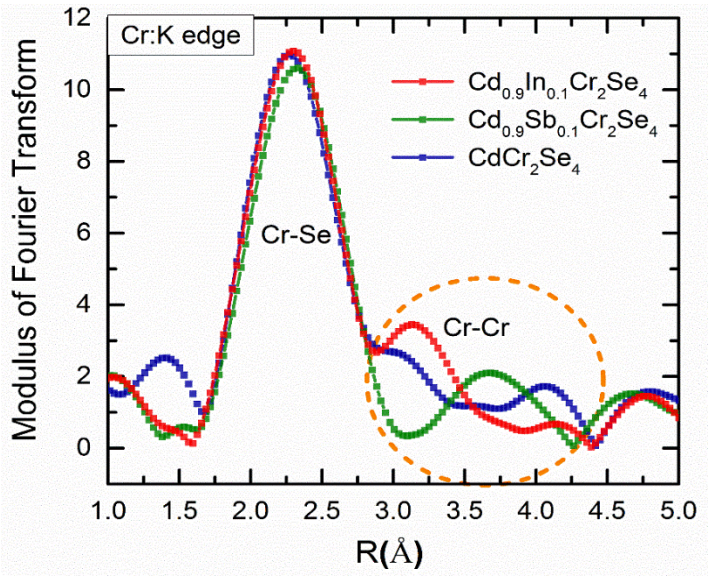

Figure 3.30: Room temperature Cr K-edge EXAFS measured for $Cd_{1-x}Sb_xCr_2Se_4$ $Cd_{1-x}In_xCr_2Se_4$ (x = 0, 0.1).

Above Fig. 3.30 shows the radial distribution functions around the Cr site measured at the Cr-Kedge, where, only x = 0.1 compositions are included here to

maintain the clarity of the figure. The first sharp peak centered ~ 2.3 Å corresponds to the octahedral Cr-Se shell. Irrespective of the changes observed in the unit cell dimensions of the substituted compositions, we find no change in this shell for the Sb/In substituted samples. However, changes are observed in the next shell (3 - 4 Å) that corresponds to Cr-Cr scattering. The contrast between the parent and the substituted compositions is quite glaring. Moreover, there is a difference between Sb and In-substituted samples. The relative intensities of the features in the parent and In-substituted samples look similar, but Sb-substituted composition shows clear separation of the feature related to Cr-Cr interaction from that of Cr-Se interaction. This indicates that our surmise of mixed valence state of Cr ions and further formation of high spin and low spin states is not only reflected through its magnetic moment, but also from local crystal structure.

3.4 Summary

In this chapter, we report the crystal structure and magnetic properties of $CdCr_2Se_4$ system with ≤ 10% substitution at the Cd-site by non-magnetic ions like Sb, In and Sn. The results for Sn-substitution at Cd-site are reported for the first time. As discussed from XRD and Raman results, in spite of the differences between the cationic radii, all the compositions maintain the same cubic symmetry. While the Sb and In substituted samples reflect systematic trends in its crystal and magnetic properties, the Sn-substituted compositions show interesting deviations that lead to unraveling of interesting low-temperature transition. Overall, the profiles of magnetic properties for all the studied compositions display the manifestation of competing ferro-and antiferromagnetic interactions. Further, substituting a fraction of Cd^{2+} ions with ions having valence other than 2+ introduces the possibility of mixed valence of Cr ions, which was confirmed by XANES results. Eventually, samples with higher composition of Sn converges towards the parent $CdCr_2Se_4$ system. So, it is argued that the changing crystal structural parameters and formation of mixed valence $Cr^{2+/3+}$ states have a great influence on the magnetic phase of Se-based spinel chalcogenides, which was successfully proved by EXAFS. It is established that both these factors are playing the vital role in governing its physical properties.

Chapter 4

Local Lattice Distortion and Spin Phonon Coupling in $CdCr_2Se_{4-x}S_x$ and $Cd_{1-x}Sn_xCr_2Se_4$

4.1 Overview

Interplay between structural disorder, magnetic interaction and the associated spin phonon coupling are investigated here for the much envisaged multiferroic candidate material, $CdCr_2Se_4$. Ferromagnetic order in $CdCr_2Se_4$ sets in below T_C ~130 K as a result of competition between the direct Cr-Cr spin coupling and the near neighbor Cr-Se-Cr exchange interactions. Hence, a small change in the crystal structure is expected to drastically affect its magnetic order. In this chapter, we discuss the local lattice distortions within the overall cubic symmetry that were brought about by replacing a small percentage of Se by isovalent S. Detailed crystal structure study using EXAFS and Raman Spectroscopy reflects the presence of local distortions within the overall cubic symmetry. Contrary to the expectation, magnetic properties of the S-substituted compositions do not show any drastic changes. Whereas the static chemical disorder created by the Sn^{4+} substitution at the Cd^{2+} site in $CdCr_2Se_4$ affects the local crystal structure around Cr-ions, and hence its magnetism. Although the spinel structure is maintained, the trends in lattice parameters and magnetic properties are not a linear function of increasing Sn concentration as discussed in previous chapter. Hence, a detailed investigation into the changing local crystal structure of $Cd_{1-x}Sn_xCr_2Se_4$ for ($0 \leq x \leq 0.1$) using EXAFS and XRD was carried out. Variation in the Cr-Se and Cr-Cr bonding is traced across the changing Sn-content. Our results highlight the significance of an intricate balance between spin and lattice degrees of freedom in controlling the magnetoelasticity and, hence, the spin-phonon coupling in $CdCr_2Se_4$.

4.2. Results and Discussion

4.2.1 Crystal Structure by XRD

The room temperature XRD patterns recorded for $CdCr_2Se_{4-x}S_x$ ($0 \leq x \leq 0.4$) are presented in Fig. 4.1 All the observed peaks could be indexed to a face centered cubic cell with *Fd3m* symmetry, confirming the phase purity of the prepared samples. A shift in the peak positions towards higher 2θ (see inset) of the substituted compositions indicate that S-doping leads to the decrease in the unit cell parameters. The lattice constant values determined from Rietveld refinement of XRD profiles using FULLPROF suite [79] are listed in Tab. 4.1.

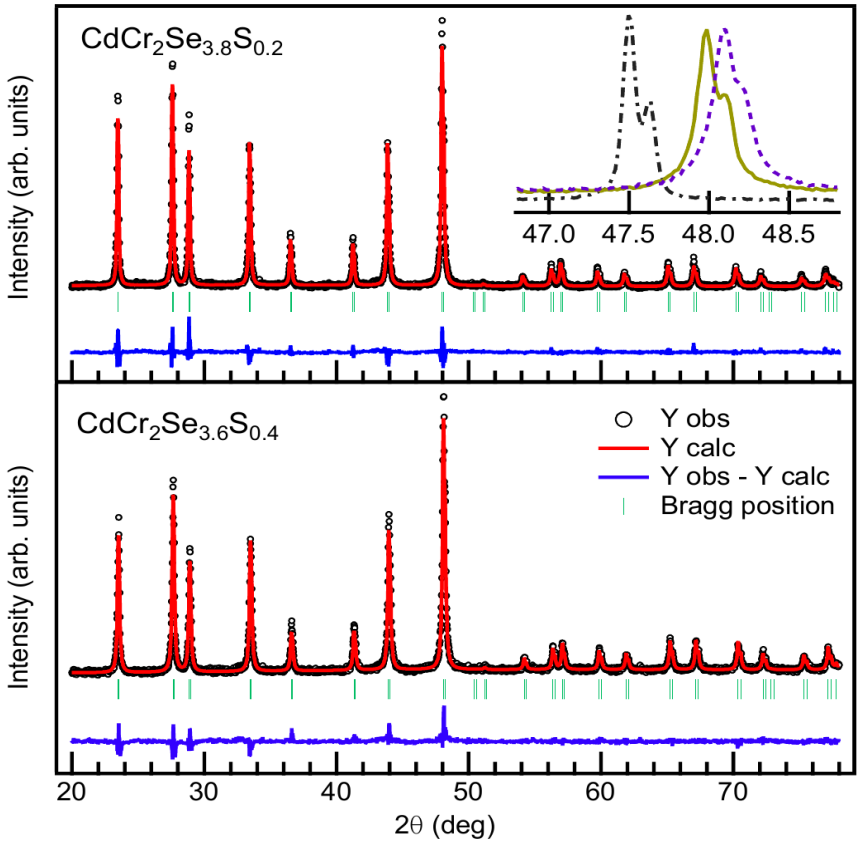

Figure 4.1: Rietveld refinement of the powder XRD patterns for $CdCr_2Se_{4-x}S_x$ recorded at room temperature. The inset shows the shift towards higher 2θ with increasing S-content, starting with dashed-dotted line representing $x = 0$ composition.

The x-ray diffraction patterns (XRD) measured at room temperature indicate that all the samples of $Cd_{1-x}Sn_xCr_2Se_4$ (x = 0, 0.03, 0.05, 0.07, 0.1) form

phase pure compositions with cubic *Fd3m* symmetry. The substitution of Cd^{2+} with a smaller sized Sn^{4+} ion initially seems to expand the lattice reaching 'a' maxima for $x = 0.05$. With a further increase in x, the lattice starts to shrink and match with the parent $CdCr_2Se_4$ for Sn^{4+} content x = 0.1 as shown in chapter 3. Room temperature values of lattice parameters are plotted in below Fig. 4.6 (a).

4.2.2 Magnetic Properties

Matching with the parent composition $CdCr_2Se_4$, the *M(T)* and *M(H)* curves for S-substituted compositions also show ferromagnetic ordering as depicted in Fig. 4.2. The splitting of the ZFC-FC curves in the low applied field *M(T)* data signifies the presence of competing interactions within the material. Such splitting is easily overcome by applying slightly higher value of magnetic field. We observe that $x = 0.2$ shows splitting of ZFC-FC curves over larger temperature in comparison to $x = 0.4$ composition. Further, the sharp change in *M(T)* that marks the transition between the ordered-disordered magnetic state in $x = 0.2$ changes to smoothly rising function with fall in temperature for $x = 0.4$. The enchanting point is that neither the T_C nor the magnetic moment seems to be much affected by S-substitution (refer Tab. 4.1). Also, the Curie temperature θp and effective paramagnetic moment μ_{eff}^{Cal} obtained from fitting the high temperature region of inverse dc susceptibility with the Curie-Weiss law ($\frac{1}{\chi} = \frac{T-\theta}{C}$) give values matching with the parent composition (see Fig. 4.3). We obtain the Curie-temperature θp as the intercept of the fitted line. The effective paramagnetic moment (μ_{eff}^{Cal}) is obtained from the relation, $C = \frac{N_A \mu_B^2 \left(\mu_{eff}^{cal}\right)^2}{3k_B \, Mole.\ wt.}$, where N_A is the Avogadro's number, k_B is the Boltzmann constant, and μ_B is the value of Bohr magneton.

The changing lattice parameters in $Cd_{1-x}Sn_xCr_2Se_4$ should affect the interatomic distances and, hence, influence its magnetic ground state that depends on Cr-Cr and Cr-Se-Cr exchange interactions. From our previous results in chapter 3, it was found that the magnetic ordering temperature (T_C) and the total magnetic moment mirror the variation seen in the lattice parameters with changing Sn-content. While the parent $CdCr_2Se_4$ shows the well-documented T_C of 130 K, with increasing Sn-content, this value drops to 116 K for $x = 0.05$ but

slowly regains the value of ~124 K for x = 0.1. Such a variation in T_C with the Sn-concentration is also plotted in Fig. 4.6 (a).

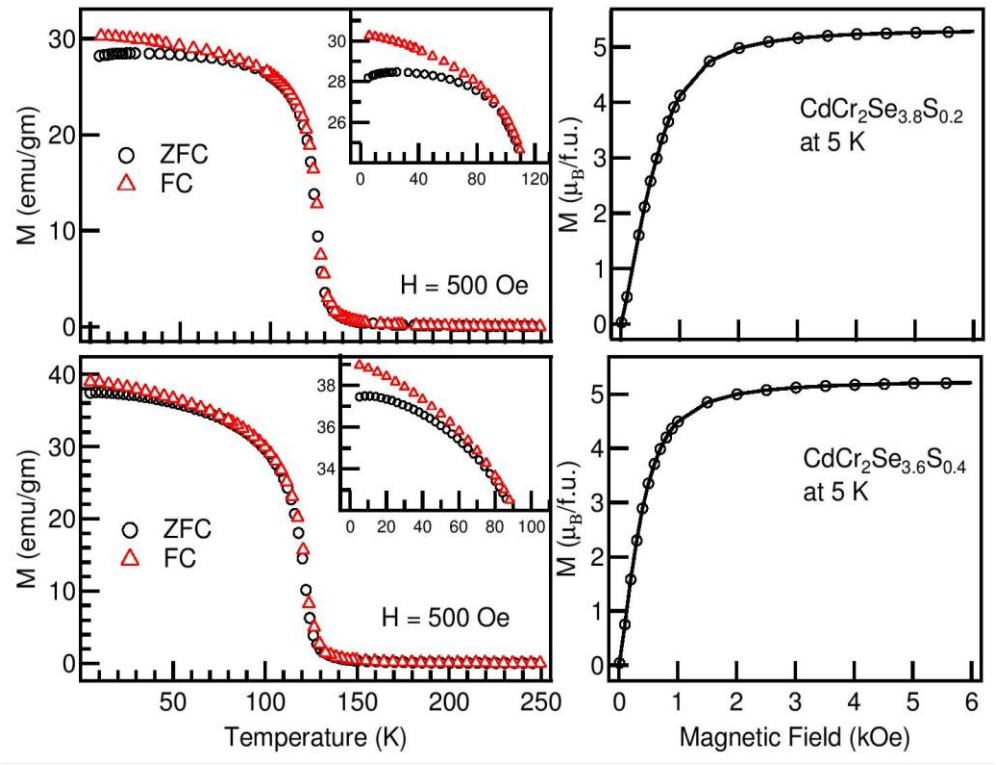

Figure 4.2: Left panel: Magnetization as a function of temperature recorded in an applied field of 500 Oe. Right panel: Magnetization as a function of applied field recorded at 5K. The inset shows the splitting of ZFC and FC curves.

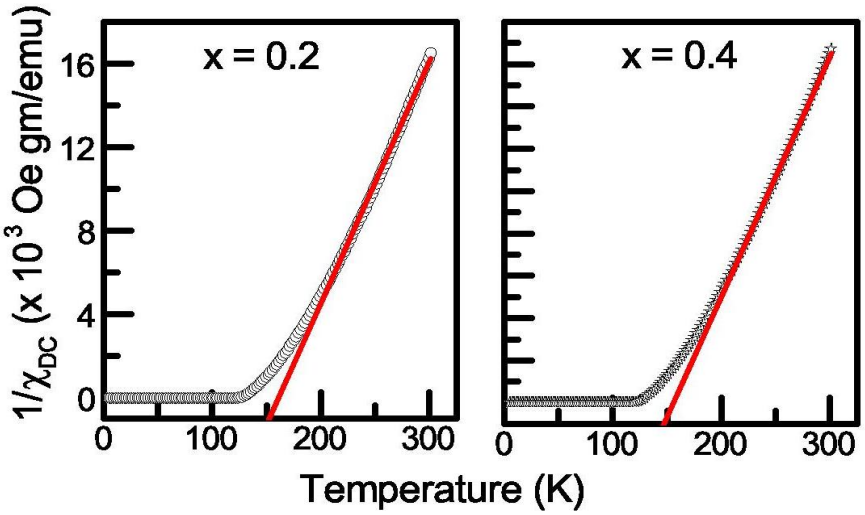

Figure 4.3: Curie-Weiss fit (solid line) to the paramagnetic region of inverse χ_{dc} obtained for $CdCr_2Se_{4-x}S_x$ compositions.

	$CdCr_2Se_4$	$CdCr_2Se_{3.8}S_{0.2}$	$CdCr_2Se_{3.6}S_{0.4}$
a (Å)	10.744 ± 0.0001	10.718 ± 0.0001	10.696 ± 0.0001
T_c (K)	130	126	122
θ_P (K)	157	160	157
M_S (μ_B/f.u.) (at 5 K)	5.38	5.39	5.32
μ_{eff}^{cal}	6.1	6.01	6.01
EXAFS Analysis			
R-factor	0.03	0.027	0.08
Cr-Se			
r (Å)	2.6108(86)	2.6693(83)	2.6537(90)
σ^2	0.00528	0.00537	0.00615
Cr-S			
r (Å)		2.4310(91)	2.3946(82)
σ^2		0.00404	0.00042

Table 4.1: Structural parameters and magnetic properties obtained for $CdCr_2Se_{4-x}S_x$.

4.2.3 Observation of local lattice distortions by EXAFS

The atomic arrangement in normal spinels is such that the primary contributor to Cr K-edge EXAFS in $CdCr_2Se_4$ is its first nearest neighbour, viz., the octahedral cage of Se ions. With the knowledge of unit cell parameters obtained from the XRD analysis, the EXAFS data for parent composition was analysed with Cr-Se as a direct scattering path having coordination number 6. The bond distance (r) and the corresponding thermal mean square factor (σ^2) for Cr-Se path were varied until a good fit was obtained in the range of 1–3 Å in the R-space and 2–10 $Å^{-1}$ in the k-space. The magnitude and real components of Fourier Transform (FT) of $k^2\chi(k)$ are shown in Fig. 4.4. Evidently, the fit for the parent composition is quite satisfactory, and the refined parameters for Cr-Se interaction are presented in above Tab. 4.1. Same fitting strategy was adopted for the two S-substituted compositions, albeit inclusion of S in the octahedral cage of anions. The fit adequately replicates the magnitude as well as the real part of the FT signal, as shown in Fig. 4.4 (b) and Fig. 4.4 (c). The resultant Cr-Se/S bond distances and

σ^2 are listed in Tab. 4.1. A slightly higher value of R-factor is obtained for $x = 0.4$ probably due to larger amount of disorder in the sample. We obtain unequal bond distances for Cr-Se and Cr-S, indicating structural distortion of the Cr octahedra at a local level within the overall cubic unit cell. This discrepancy in bond distances is not much surprising as S^{2-} has a smaller ionic radius (1.84 Å) in comparison to Se^{2-} (1.98 Å) [111]. Hence, S-doping should introduce significant lattice distortions at a local structure level. The interesting fact is that despite the sizable lattice distortions, neither the T_C nor the magnetic moment seems to be much affected by S-substitution.

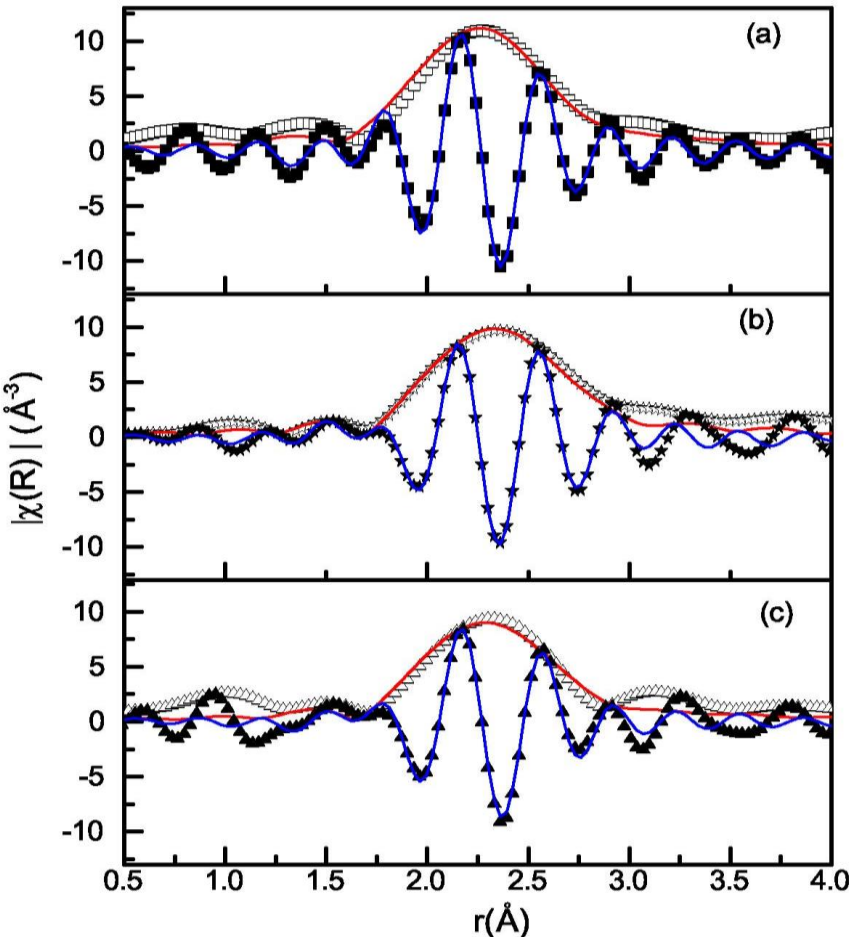

Figure 4.4: Fitting of the magnitude and real component of Fourier transform of Cr K-edge EXAFS spectra in (a) $CdCr_2Se_4$, (b) $CdCr_2Se_{3.8}S_{0.2}$, and (c) $CdCr_2Se_{3.6}S_{0.4}$.

The local crystal structure becomes quite relevant in understanding the magnetic behavior and the related functional properties of $CdCr_2Se_4$. It becomes pertinent to identify whether it is the Cr-Se-Cr FM or the Cr-Cr AFM, or both

interactions that get affected by the Sn substitution. The Cr-Se and Cr-Cr bond distances can be obtained from the refined crystal structure parameters using the simple relations $d_{Cr-Se} = a\sqrt{(3u^2 - 2u + 0.375)}$ and $d_{Cr-Cr} = a\frac{\sqrt{2}}{4}$, where a is the lattice constant, and u is the anionic parameter for Se ions [29]. As these relations are some fractional multiples of 'a', both these distances emulate the same trend as 'a'.

To further explore the changes in the local environment around the magnetic ion in case of Sn-substituted compositions, a room temperature EXAFS measurement at Cr K-edge was also carried out. The fittings for all Sn compositions were carried out up to 3 Å in R-space and k-range of (2–10) Å same as S-doped compounds is shown in Fig. 4.5. Parameters such as the Cr–Se bond length and the corresponding thermal mean square variation were refined until a good fit was obtained. The final parameters are listed in Tab. 4.2.

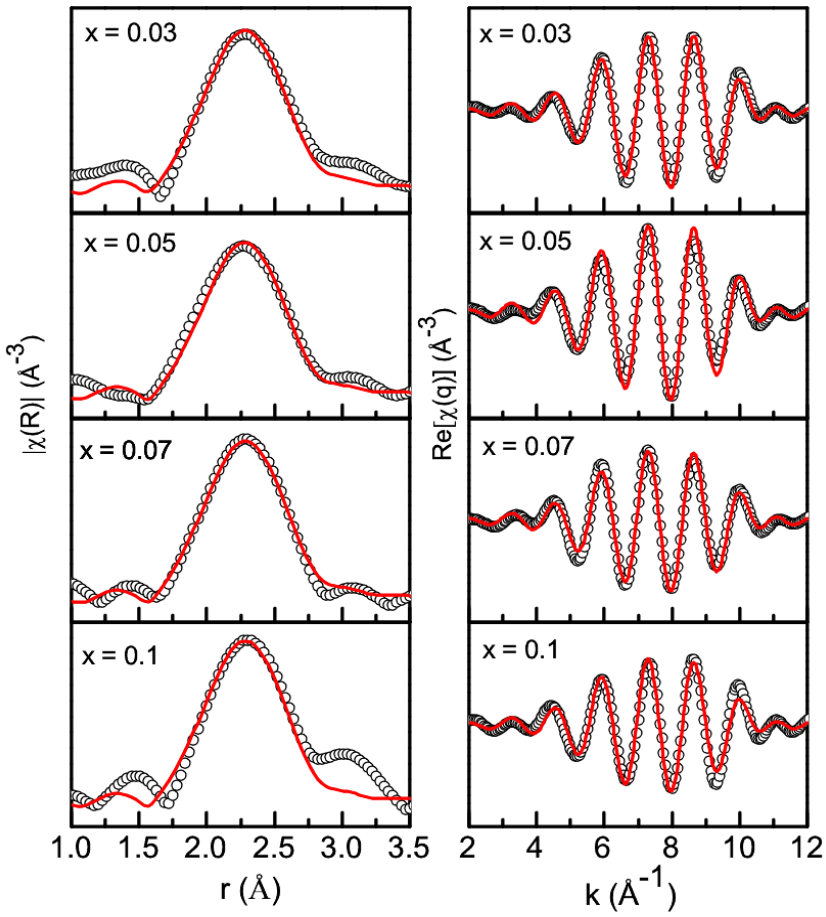

Figure 4.5: Fitting of the magnitude (left panel) and real component (right panel) of Fourier transform of Cr K-edge EXAFS spectra in $Cd_{1-x}Sn_xCr_2Se_4$ series.

x	u	χ^2	R_p	R_{wp}	$d_{Cr\text{-}Se}$ (Å)	$d_{Cr\text{-}Cr}$ (Å)	$d_{(Cr\text{-}Se)\ expt.}$ (Å)	σ^2
0	0.2643	1.92	5.01	10.9	2.542	3.798	2.6108(86)	0.0053(1)
0.03	0.2641	2.55	6.59	11.3	2.545	3.800	2.6224(77)	0.0077(9)
0.05	0.2638	2.89	7.49	12.8	2.548	3.801	2.6238(94)	0.0094(1)
0.07	0.2639	2.93	8.08	14.5	2.547	3.802	2.6242(84)	0.0084(2)
0.1	0.2644	5.75	9.3	15.2	2.541	3.799	2.6244(80)	0.0089(3)

Table 4.2: Structural parameters as obtained from room temperature XRD and EXAFS analysis for $Cd_{1-x}Sn_xCr_2Se_4$. From Rietveld refinement, the goodness of fit parameters are χ^2, R_p and R_{wp}. σ^2 refers to the thermal mean square parameter corresponding to bond-distance. Atomic positions of Cd (Sb): 8*a* (1/8,1/8,1/8), Cr: 16*d* (1/2,1/2,1/2) and Se: 32*e* (u, u, u).

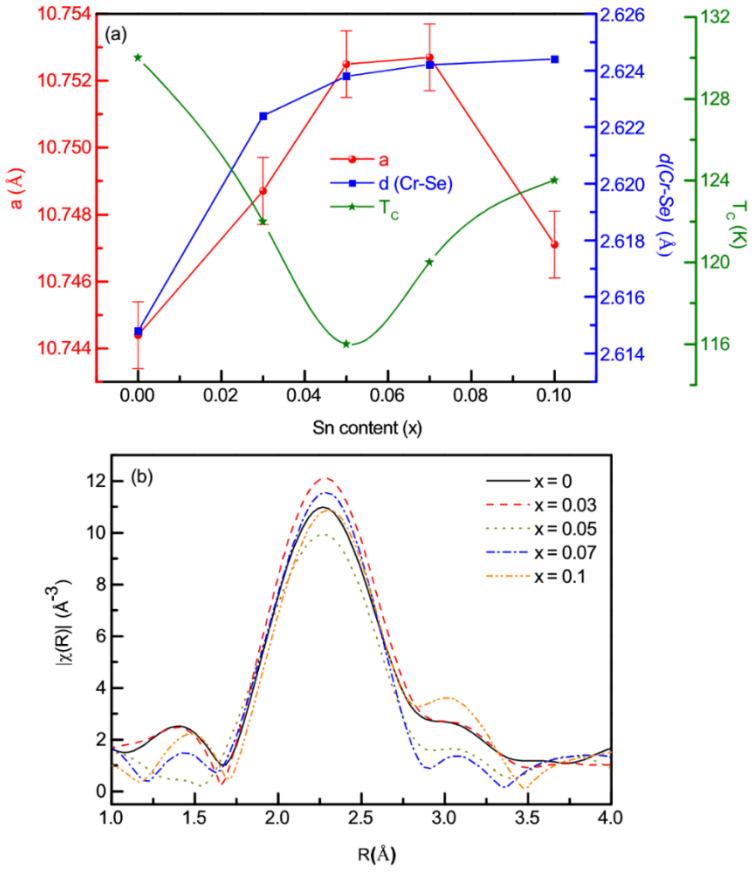

Figure 4.6: (a) The lattice constants obtained from XRD, Cr-Se bond distance obtained from EXAFS, and T_C values obtained from magnetic measurements, are plotted as a function of Sn concentration. (b) Radial distribution around Cr-ion for all the compositions.

First, the bond distance values obtained from EXAFS show considerable deviation from those calculated from the XRD profile. Second, as it can also be seen from Fig. 4.6(b), there is not much variation amongst the Cr–Se bond lengths for Sn-substituted compositions, although it differs from the parent $CdCr_2Se_4$. Hence, the variation in the magnetic properties observed as a function of Sn-concentration seems to be less influenced by the Cr-Se bond distances. The next interaction in question is that of Cr-Cr, which occurs as a second neighbor radial distribution around the central absorbing ion in the EXAFS data. From the profile shown in Fig. 4.6(b), considerable changes in this Cr-Cr local structure are evident. However, given the limited range of the data, the Cr-Cr distances that can be extracted from fitting the EXAFS data do not have better accuracy than those obtained from XRD analysis presented earlier. Hence, we will refer to the Cr-Cr distances extracted from XRD analysis. We have already seen that the lattice constant is directly related to the Cr-Cr distance. Hence, it can be concluded that the difference in the direct exchange coupling between Cr-Cr drives the magnetic interactions in $Cd_{1-x}Sn_xCr_2Se_4$. Correspondingly, a lowest T_C of ~116 K is recorded for x = 0.05, which shows maximum value a of lattice parameters, and hence the Cr-Cr distance. On the other hand, the lattice seems to contract for x = 0.1 with a decreased lattice constant that matches closely with the parent composition. Likewise, its T_C ~ 124 K also shows an increase and close to the T_C (~130 K) reported for $CdCr_2Se_4$.

4.2.4 Temperature dependence of Raman spectra

The room temperature Raman spectra for $CdCr_2Se_{4-x}S_x$ compositions are shown in Fig. 4.7 and for $Cd_{1-x}Sn_xCr_2Se_4$ was already shown in Fig. 3.8 from chapter 3. As evidenced from the XRD profiles, both these S and Sn substituted compounds are iso-structural suggesting similar lattice dynamics. However, shift in Raman mode positions is expected due to the difference in bond-length of the atoms (Se/S) responsible for specific vibrations. Phonon representation for spinels with *Fd3m* space group gives $\Gamma = A_{1g} + E_g + 3T_{2g} + T_{1g} + 2A_u + 2E_u + 5F_{1u} + 2F_{2u}$ modes [28, 112]. Amongst these five Raman active modes are A_{1g}, E_g, $3T_{2g}$, four out of five F_{1u} modes are Infra-Red (IR) active, and one is an acoustic mode. The T_{1g}, $2A_u$, $2E_u$, and $2F_{2u}$ modes are silent. Here, we discuss three most intense

Raman active modes such as *Eg*, one low frequency T_{2g} and one high frequency T_{2g} that involve interactions only between the nearest neighbours in the frequency range of 80–300 cm^{-1}. As per the literature, [107,113-114], the first peak is quite obscure and appears at ~82 cm^{-1}. It is associated with T_{2g} translational motion of the $CdSe_4$. The E_g mode at ~154 cm^{-1} is the strongest in intensity and associated with the symmetric bending motion of the selenium atoms (Se-Cd-Se) within the $CdSe_4$ tetrahedra. The feature at ~166 cm^{-1} is associated with T_{2g} internal mode and represents an antisymmetric breathing mode of the $CdSe_4$ tetrahedra. The third T_{2g} internal mode (~225 cm^{-1}) is generally very weak and scattered easily by thermal phonons. Hence, it is generally not observed at 300K and appears only at sufficiently low temperatures [106, 27]. With S-doping, we observe a distinct broadening and a decrease in the intensity of the peak-features which is quite reasonable expectation, given that the vibrations now involve atoms (Se/S) with different atomic masses.

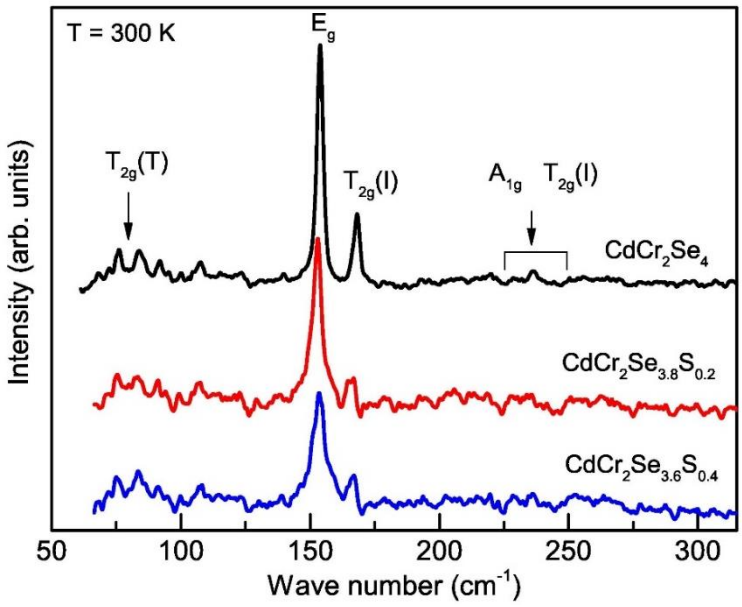

Figure 4.7: Room temperature Raman spectra measured with excitation wavelength of 488 nm.

Next, we inspect the Raman spectra for each composition at different temperatures so as to explore the vibrational modes across magnetic transition. All the spectra in the temperature range of 300 K to 80 K for $CdCr_2Se_{4-x}S_x$ and $Cd_{1-x}Sn_xCr_2Se_4$ compositions are as shown in Fig. 4.8 and Fig. 4.9. For the case of $CdCr_2Se_4$, we observe a broad hump-like feature at the lowest measured

temperature, in the frequency range of 200–280 cm^{-1}. This feature evolves with rising temperature up to 110 K and thereafter merges with the background. As discussed earlier, these features are the overall of weak T_{2g} internal modes at ~225 cm^{-1} and A_{1g} mode at ~240 cm^{-1}, attributable to Cd-Se stretching/bending and Cd-Se symmetric stretching, respectively. At the outset, no extra spectral signatures appear in both the S and Sn-doped samples with the changing temperature. This confirms no change in the crystal symmetry leading to structural phase transition in the temperature range investigated here.

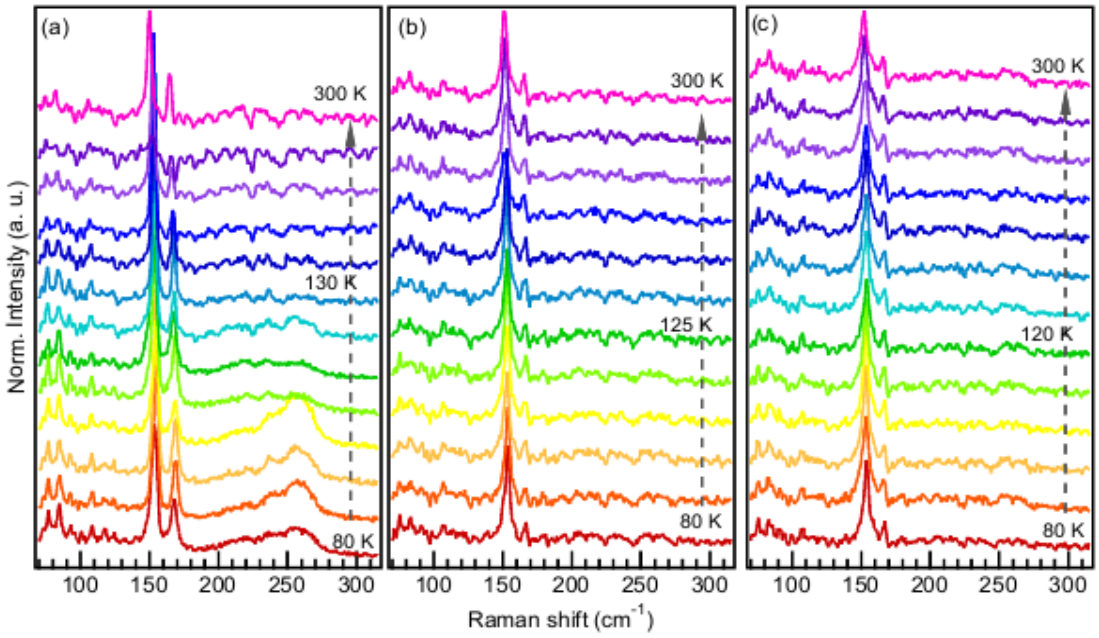

Figure 4.8: T-dependent Raman spectra recorded for (a) $CdCr_2Se_4$, (b) $CdCr_2Se_{3.8}S_{0.2}$, and (c) $CdCr_2Se_{3.6}S_{0.4}$.

However, the peak-features of Sn-substituted compounds also representing the three low frequency modes ($T_{2g}(T)$, E_g, $T_{2g}(I)$) show quite subtle temperature dependencies as displayed in Fig. 4.9. Raman spectrum of the variation of specific modes with composition at 80 K are shown in Fig. 4.10 (a) and Fig. 4.10 (b). As the lowest-frequency mode T_{2g} (T) ~ 82cm^{-1} corresponds to the translational motion of the $CdSe_4$ within the spinel lattice, any change in the cation distribution at the tetrahedral site should affect this mode. Indeed, this mode gets distorted and merges with the high background as Sn replaces the targeted Cd site as shown in Fig. 4.10 (a). Next, the highest intensity E_g mode at ~154 cm^{-1} is associated with the symmetric bending motion of the selenium (Se-

Cd-Se). The feature at ~166 cm^{-1} is associated with T_{2g} *(I)* internal (I) mode and represents antisymmetric breathing of the $CdSe_4$ tetrahedra. Fig. 4.10 (b) depicts the evolution of these two modes with Sn concentration; the x = 0.05 shows an exceptional shift towards the lower wave number compared to rest of the series. No extra mode or spectral signatures appear in the low temperature spectra of all the samples confirming that the spinel crystal symmetry is maintained even in the magnetically ordered phase.

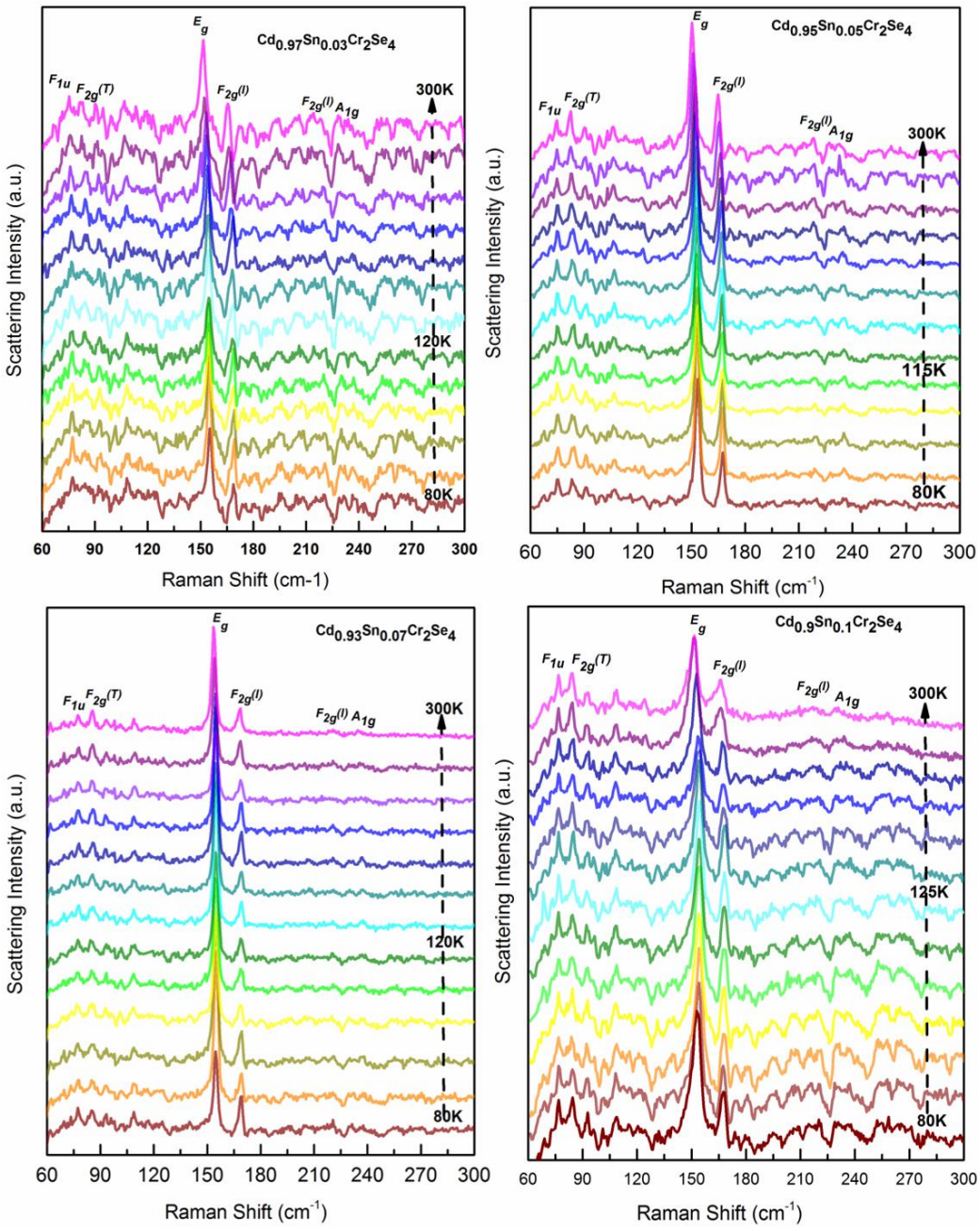

Figure 4.9: T-dependent Raman spectra recorded for $Cd_{1-x}Sn_xCr_2Se_4$ series.

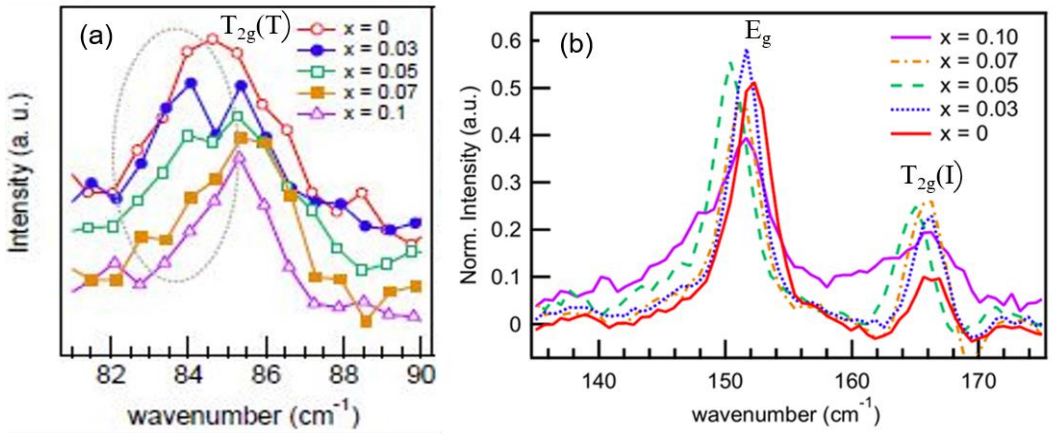

Figure 4.10: Raman spectra obtained (at 80 K) with an excitation wavelength of 488 nm for (a) and (b) Evolution of the three modes with Sn concentration. For better comparison, each spectrum has been normalized by the integrated intensity.

The spin-lattice anomalies in S-substituted compositions pose interesting dependencies of Raman modes across T_C that needs detailed investigations. From EXAFS results presented earlier, we discussed the presence of local structural distortions within the unit cell. These distortions could produce strain in magnetic interactions and could likely affect its magnetic ground state. As can be seen from Fig. 4.11, the mode at ~164 cm^{-1} in the parent systems seems to be split into two peaks for the S-doped samples. Also, this two-peak feature occurs at temperatures across the magnetic T_C of the samples, hence cannot be related to the magnetic order-disorder transition. As this mode represents the Cd-Se tetrahedral vibrations, it indicates the presence of local disorder in the system wherein the Cd-Se/Cd-S bonds vibrate at slightly different frequencies due to the difference in corresponding bond lengths. This two-peak feature is also found in the highest intensity peak, causing it to broaden and decrease in intensity with S-doping (see Fig. 4.7).

The Raman active peak-features representing the above explained three modes; E_g and $2T_{2g}$ show quite subtle temperature dependencies. In order to bring out the peculiarities more effectively, each mode was analysed separately by fitting a Lorentzian function, and the results are presented in Fig. 4.12. Here, the wave-number and the corresponding FWHM (full-width-half-maximum) of the

highest intensity E_g mode are plotted as function of temperature, for each composition.

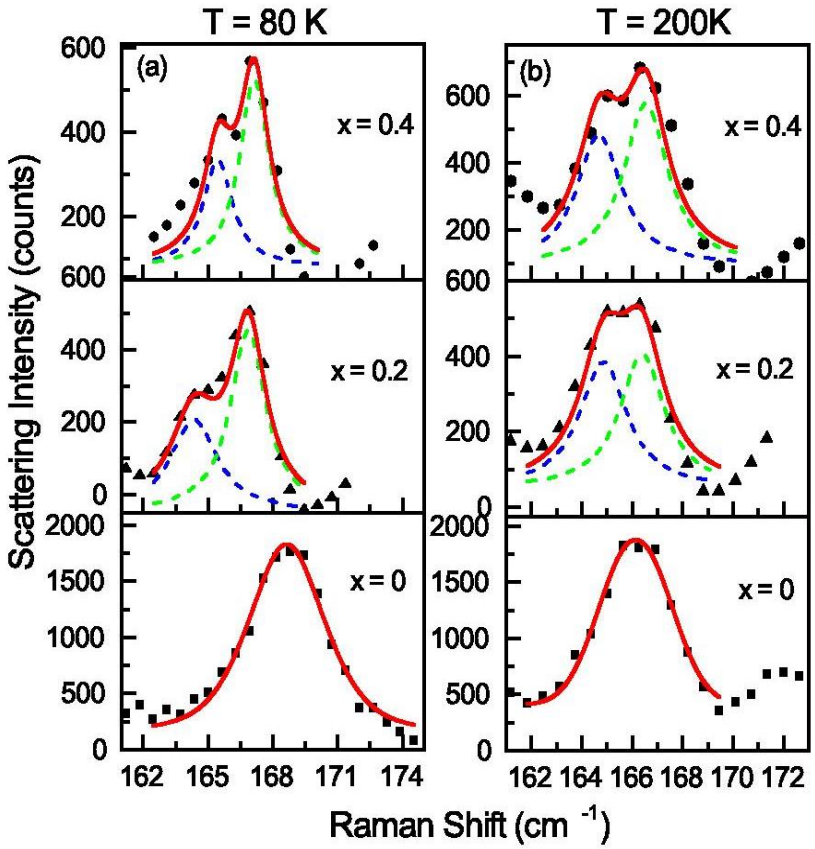

Figure 4.11: An internal vibrational mode (T_{2g}) for $CdCr_2Se_4$ splits into two modes with S doping. The solid symbols represent measured data and dashed lines are the two contributing modes that add up to give the total representative fit shown using solid line. Spectra at two representative temperatures above and below T_C emphasizes that the splitting occurs irrespective of the magnetic state of the compositions.

From Fig. 4.12, it is observed that the peak position of the mode consistently shifts to higher wave-number with falling temperature and a sudden dip occurs at magnetic ordering temperature (T_C). The corresponding plot of FWHM also mirrors this trend. Generally, shift of mode-frequencies to higher wave-number along with the sharpening of the mode with decreasing temperature are purely due to thermal effects, whereas the anomaly in the mode frequency across T_C has been attributed to spin-phonon coupling in a magnetic system [115, 116]. In other words, for systems where the spin and lattice degrees of freedom

are correlated, the phonon frequencies and life-time get modulated across the order-disorder transition. In the case of spin-phonon coupling alone, the frequencies show modulation; while, when the life-time is also getting modulated (indicating the involvement of lattice), the peak widths show anomalies across magnetic ordering transitions. To further clarify the observed anomaly as spin-phonon coupling, the change in phonon-frequency was fitted with an anharmonic dependence given by $\omega_{anh}(T) = \omega_0 - A\left[1 + \frac{2}{e^{\frac{\hbar\omega_0}{KT}} - 1}\right]$, where ω_0 and A are adjustable parameters. The fit is as shown in Fig. 4.13. The anomalous jump in the frequency value in itself is rather small and of the order ~2 cm^{-1}. It is important to mention here that earlier calculations of spin correlation function as well as experimental studies report a larger change in the temperature dependence of T_{2g} Raman modes [114, 117]. Temperature evolution of E_g mode is not a good choice to observe spin-phonon coupling. However, in the present samples, other modes being quite weak give higher percentage of error in the quantities obtained from the fittings. Hence, the strongest intensity E_g mode was plotted here. Besides, our intention here is to understand the role of static chemical disorder associated with the X-site ions.

It should be recalled here that magnetism in $CdCr_2Se_4$ is quite complex with manifestation of equally strong Cr-Cr direct interaction, Se-Cr-Se nearest neighbour interaction, and subtle contribution from Se-Cd-Se-Cr-Se-Cd-Se next-nearest neighbour interactions. In the present data, because we carried out the measurements on finely powdered samples, we are able to monitor only high intensity Cd-Se related phononic behavior for E_g mode with better accuracy.

Ideally, it is expected that the FWHM show an increase with increasing temperature due to thermal disorder. Instead, here we see a strong lifetime modulation in all the compounds around magnetic ordering temperature indicating coupling of lattice distortions with the spin order. The spin-phonon signature occurs prominently only for $CdCr_2Se_{3.8}S_{0.2}$, but not at its magnetic ordering temperature. The dip in peak position and corresponding jump in FWHM occurs near its paramagnetic Curie-Weiss temperature, θp ~160 K. $CdCr_2Se_{3.6}S_{0.4}$, on the other hand, does not show any dramatic change in the wave-number of the peak within the measurement accuracy of 1 cm^{-1}. Though, the corresponding FWHM shows the trend. The obvious reason for this could be

an increase in scattering of phonons brought about by the difference in atomic masses of Se and S ions, causing disruption of spin-phonon coupling.

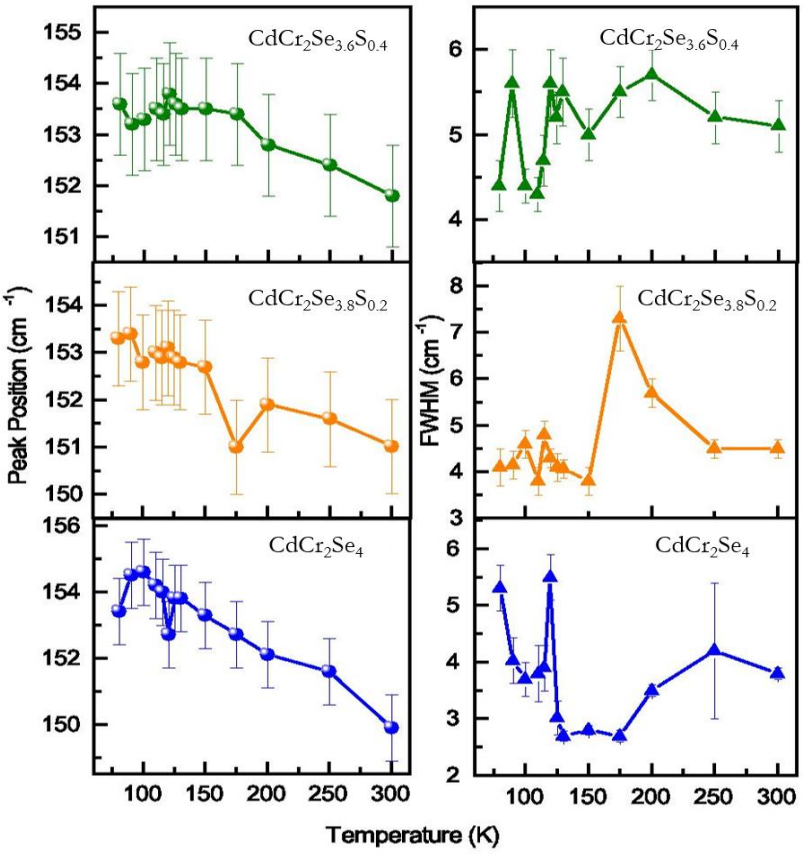

Figure 4.12: Temperature variation in the peak position of *Eg* mode (at ~154 cm^{-1}) and its FWHM in $CdCr_2Se_{4-x}S_x$. Solid line represents straight line connecting the data points.

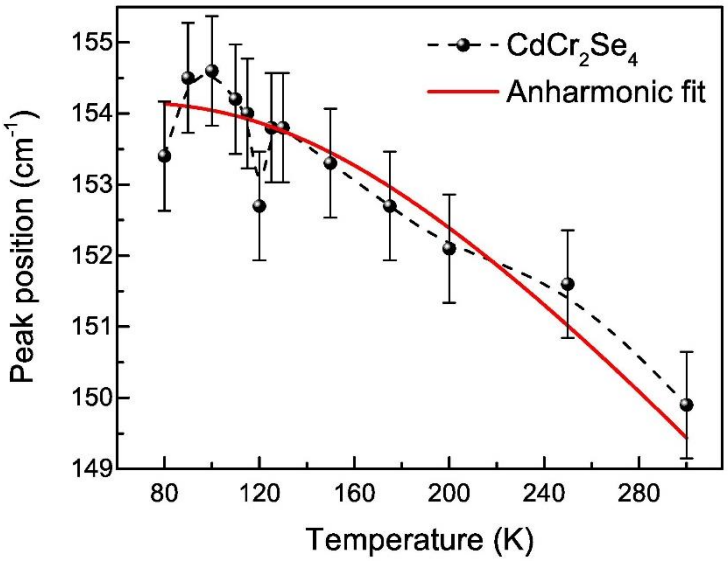

Figure 4.13: Anharmonic model function (solid line) fit to the temperature variation of peak position of the *Eg* mode.

The impact of changing lattice parameters and hence the Cr-Cr bond distance should also be seen on the spin-phonon coupling of the $Cd_{1-x}Sn_xCr_2Se_4$ series across its magnetic ordering temperature. Temperature dependencies of the E_g and F_{2g} *(I)* modes were analyzed for its peak position and corresponding FWHM, at each measurement temperature. Fig. 4.14 and 4.15 depicts the representation of such analysis, where the two compositions (x = 0.05 and 0.1) exhibiting a maximum change in lattice constants and T_C are displayed.

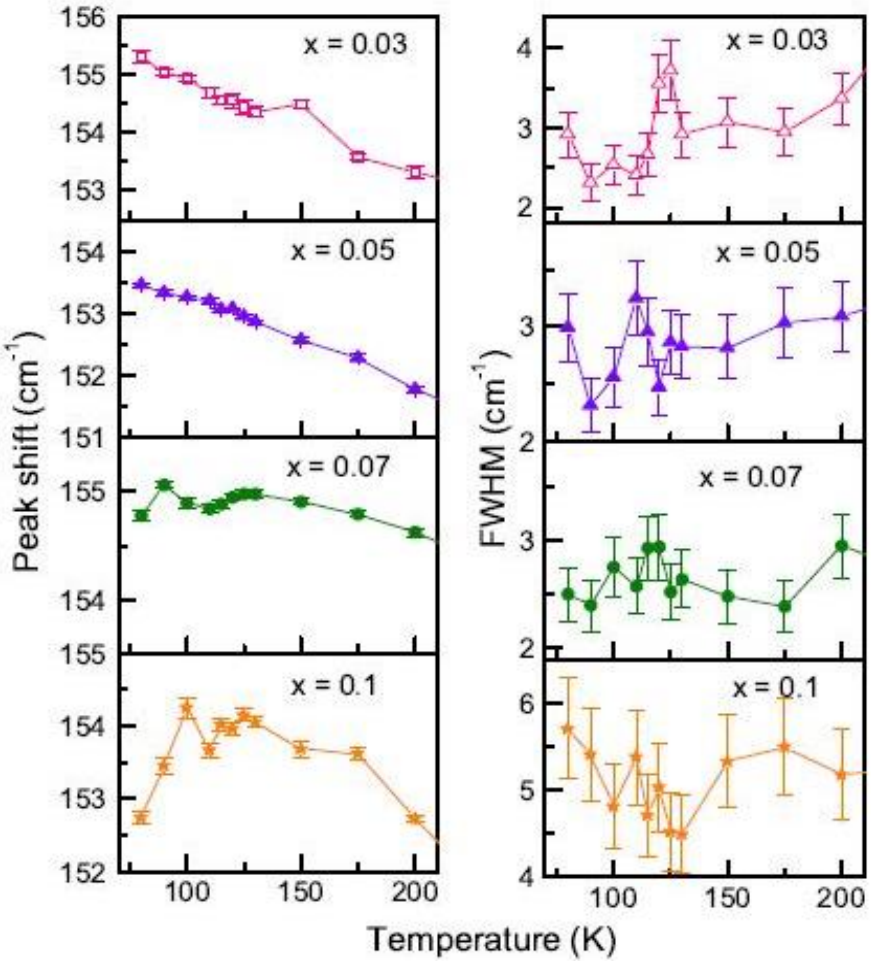

Figure 4.14: Temperature variation in the peak position and corresponding FWHM for *Eg* mode. Solid line represents straight line connecting the data points.

In the vicinity of T_C, the x = 0.1 composition shows considerable softening of mode, while a subtle change is seen for x = 0.05. The corresponding FWHM of these modes show considerable modulations for both the compositions. Such softening of mode with associated modulation in FWHM

hints towards the occurrence of spin-phonon coupling in x = 0.1. On the other hand, for x = 0.05, it appears that the lattice is involved in modulating the lifetime of phonon, but the coupling with spin is not sufficiently strong to modulate its frequency.

This is plausible since the crystal structure results indicate an increase in the bond lengths in comparison to that of the parent compound. Such expansion weakens the spin-lattice interaction. Whereas, it appears that the increase in Sn content to x = 0.1 further increases the Cr–Cr interactions as a result of lattice contraction, restoring the spin-phonon coupling. At the outset, the changes in the bond lengths discussed here are quite subtle. However, it may be noted that Cr-based spinel chalcogenides are known to show dramatic properties with very little changes in the lattice. For example, the relaxor ferroelectricity seen in $CdCr_2S_4$ corresponds to dynamic off-centering of Cr with an observed displacement of about ~0.012 Å [118].

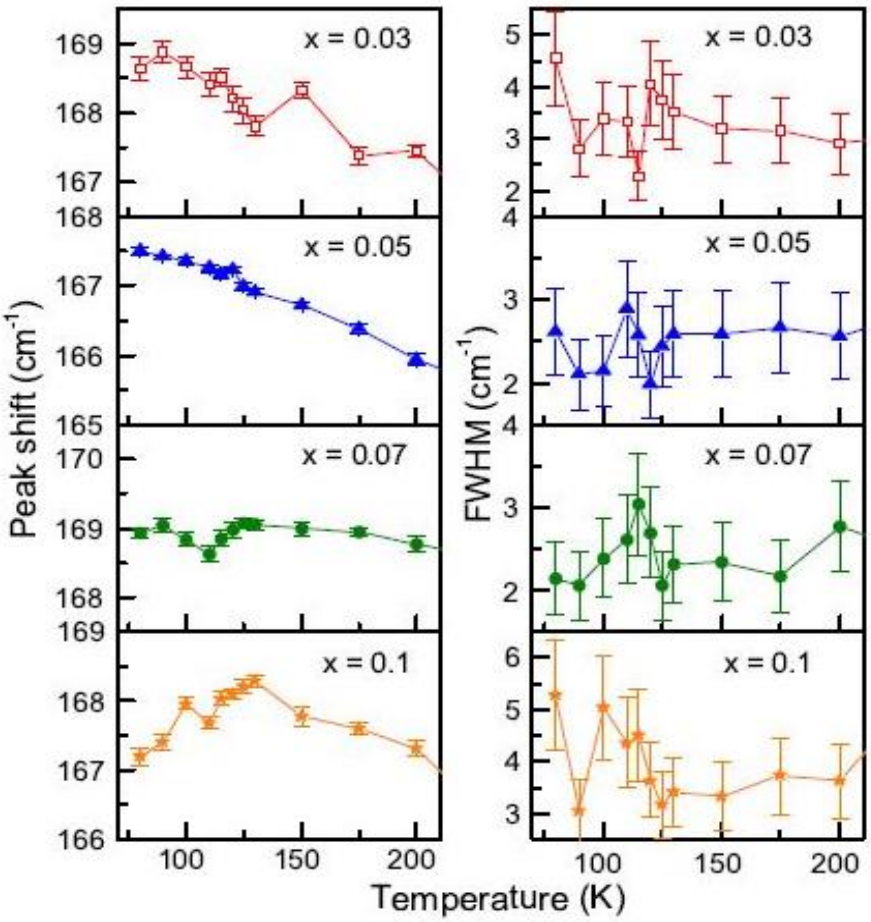

Figure 4.15: Temperature variation in the peak position and corresponding FWHM for $T_{2g}(I)$ mode.

4.3 Summary

The influence of local lattice distortions on the magnetic interactions and static chemical disorder on the spin-phonon coupling of $CdCr_2Se_4$ spinel chalcogenide were explored here. The distortions within the overall cubic symmetry of $CdCr_2Se_4$ was brought about by substituting small percentage of S for Se and Sn^{4+} at Cd^{2+} site. But, Sn^{4+} not only creates disorder, it also creates a charge imbalance at the Cr-site. Investigation into the crystal structure was carried out by performing room temperature XRD and Cr K-edge EXAFS and temperature dependent Raman spectroscopy experiments. The magnetic properties of all the above studied compositions were measured using SQUID magnetometry. Interestingly, the magnetic properties in the ordered state as well as in the non-ordered state do not show much deviation in the S-substituted compositions with respect to the parent system. But in case of Sn-substituted compositions, the changing Cr–Se and Cr–Cr bond lengths is significant in controlling its magnetism. While XRD profiles for both S and Sn-doped compounds show an overall cubic symmetry for all the studied compositions, but the analysis of the room temperature EXAFS data for yields two separate bond lengths for Cr-Se and Cr-S within the Cr-Se/S octahedra. Raman spectra also show splitting of the peak feature associated with modes originating from the Cd-Se/S vibrations. Moreover, this splitting exists across the magnetic ordering temperature in case of $CdCr_2Se_{4-x}S_x$ series. The temperature dependent Raman spectra for both $CdCr_2Se_{4-x}S_x$ and $[Cd_{1-x}Sn_x]Cr_2Se_4$ further suggest that there is no structural phase transition in the investigated temperature range. It also reveals anomalous variation in the peak position of vibrational modes across the magnetic transition temperature, suggesting spin-phonon coupling in both the S and Sn substituted system. Further the spin-phonon coupling that is crucial for the much envisaged multiferroicity in $CdCr_2Se_4$ spinel chalcogenide is seen to weaken for $[Cd_{1-x}Sn_x]Cr_2Se_4$ series. Thus, the significance of an intricate balance between the spin and lattice degrees of freedom in controlling the magnetoelasticity in $CdCr_2Se_4$ is demonstrated. Such study helps us in guiding the path towards tailoring the properties of Cr-chalcogenides using different substitutions.

Chapter 5

Magnetic and Transport Properties of Transition Metal Doped $CuCr_2Se_4$ Spinel System

5.1. Overview

The magneto-resistance (MR) effect of ferromagnets has attracted considerable attention because it can be used in spintronic applications, like magnetic reading heads, magnetic sensors, spin-valves and magnetic random-access memory devices [119]. Recent advances in the science of modern materials, chalcogenide spinels have identified these materials, which shows potentially useful for magnetoresistance (MR) application [7-8,48,51,120].

$CuCr_2Se_4$ is a p-type ferromagnetic metal with a Curie temperature T_C ~ 430 K. It exhibits magnetic moment of approximately 5 μ_B/f.u. This large magnetic moment and high T_C has promoted interest in $CuCr_2Se_4$ and its related chalcospinels as promising materials for spintronic applications [58]. The present chapter is focused on Cr based Chalcogenides system $Cu_{1-x}M_xCr_2Se_4$ (M = Mn, Co, Fe, Ni and x = 0.1), wherein B site is occupied by chromium and the A site is a mixture of 90 % copper and 10 % transition metal with partially filled *d* orbital. The study is aimed at finding a suitable composition displaying sizable magneto-resistance effect. One of the challenges in $Cu_{1-x}M_xCr_2Se_4$ is related to the charge and valence state of the Cu, Fe, Co, Ni and Cr ions. Goodenough predicted Cu^{2+} and Cr^{3+} ions to be present in $CuCr_2Se_4$ [40], while Lotgering assumed that Cu in monovalent state and Cr-ions to be in a mixed Cr^{3+} - Cr^{4+} state [39]. It is very important to obtain a clear understanding of the charge states of these ions in view of elucidating the origin of the magnetoresistance found in these materials. Another important challenge is to make suitable doping in $CuCr_2Se_4$ so that its Curie temperature (T_C) reduces from 430 K to 300 K for the viewpoint of room temperature magnetic switching application.

Colossal magnetoresistance has recently been observed in Cr-based spinel Chalcogenides like $Cu_{1-x}Fe_xCr_2S_4$ ($x \geq 0.5$) [121]. The authors of Ref. [122-124] showed $Cu_{1-x}M_xCr_2Se_4$ (Fe, Co and Ni) bulk compounds crystallize with a spinel structure for $0 \leq x \leq 0.3$ and with a monoclinic structure for $0.8 \leq x \leq 1$. For $0.3 < x < 0.8$, both the phases coexist.

Keeping all these above aspects in mind, in this chapter, we present an experimental finding of the structure, valence distribution, magnetic and magnetotransport properties of transition metal substitution at Cu-site in $CuCr_2Se_4$ spinel with an aim to reduce T_c near room temperature.

5.2. Results and Discussion

5.2.1 Crystal Structure

The powder XRD profiles for polycrystalline samples of $CuCr_2Se_4$ and $Cu_{0.9}M_{0.1}Cr_2Se_4$ (M = Mn, Fe, Co, Ni) series, obtained using the solid-state synthesis method described in the chapter 2, were analysed for its crystal structure. The Rietveld refined room temperature XRD patterns for parent $CuCr_2Se_4$ and $Cu_{0.9}M_{0.1}Cr_2Se_4$ (M = Mn, Fe, Co, Ni) series are shown in Fig. 5.1 and 5.2 respectively. The refined XRD pattern indicated that all reflection peaks corresponded to the normal cubic spinel structure with the space group no. *Fd3m* (no. 227). The structure model with the 90% Cu ions and 10% Mn, Fe, Co and Ni ions sharing the tetrahedral 8*a* positions, Cr ions occupying the octahedral 16*d* sites and Se anions at 32*e* sites converged satisfactorily. The lattice parameters, unit cell volume, R_f, R_{Bragg} and χ^2 are presented in Tab. 5.1. No secondary phases were detected in XRD patterns for $CuCr_2Se_4$ and $Cu_{0.9}M_{0.1}Cr_2Se_4$ (M = Mn, Fe, Co) samples. But we obtained small extra peaks at $2\theta \sim 15.4^\circ$, 30.3° and 32.1° in $Cu_{0.9}Ni_{0.1}Cr_2Se_4$ which is identified as that of Cr_2Se_3 phase from *JCPDS* data file [125].

The lattice parameters of the parent $CuCr_2Se_4$ composition was found to be a = 10.334Å, matching with the previously reported literature [58]. With 10% Mn substitution, a change to 10.344Å, reconciling to the fact that a bigger sized Mn ion (atomic radius ~ 0.64 Å) substitutes smaller Cu ions (atomic radius ~ 0.60 Å). we found systematic decrease in the lattice constants for Fe (0.63 Å), Co (0.58 Å) and

Ni (0.55 Å) substituted compositions. From Fig. 5.3, where a single main peak is shown for different compositions, we see a systematic shift in the peak positions with respect to the parent $CuCr_2Se_4$ composition.

Composition	*a (Å)*	R_{Bragg}	R_f	χ^2
$CuCr_2Se_4$	10.3338 ± 0.0001	9.12	6.85	1.35
$Cu_{0.9}Mn_{0.1}Cr_2Se_4$	10.3461 ± 0.0001	5.70	4.99	1.24
$Cu_{0.9}Fe_{0.1}Cr_2Se_4$	10.3328 ± 0.0001	5.87	5.45	1.39
$Cu_{0.9}Co_{0.1}Cr_2Se_4$	10.3268 ± 0.0001	8.44	6.12	1.76
$Cu_{0.9}Ni_{0.1}Cr_2Se_4$	10.3227 ± 0.0002	21.8	10.8	3.19

Table 5.1: Rietveld refined structure parameters for $CuCr_2Se_4$ and $Cu_{0.9}M_{0.1}Cr_2Se_4$ (M = Mn, Fe, Co, Ni).

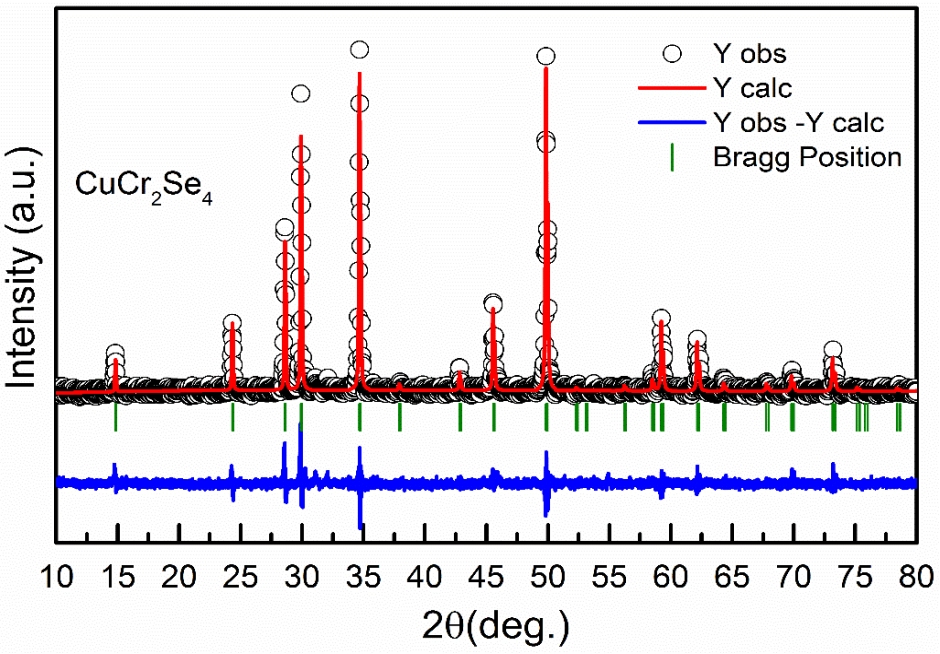

Figure 5.1: Rietveld Refined XRD patterns for the parent compound, $CuCr_2Se_4$ at room temperature

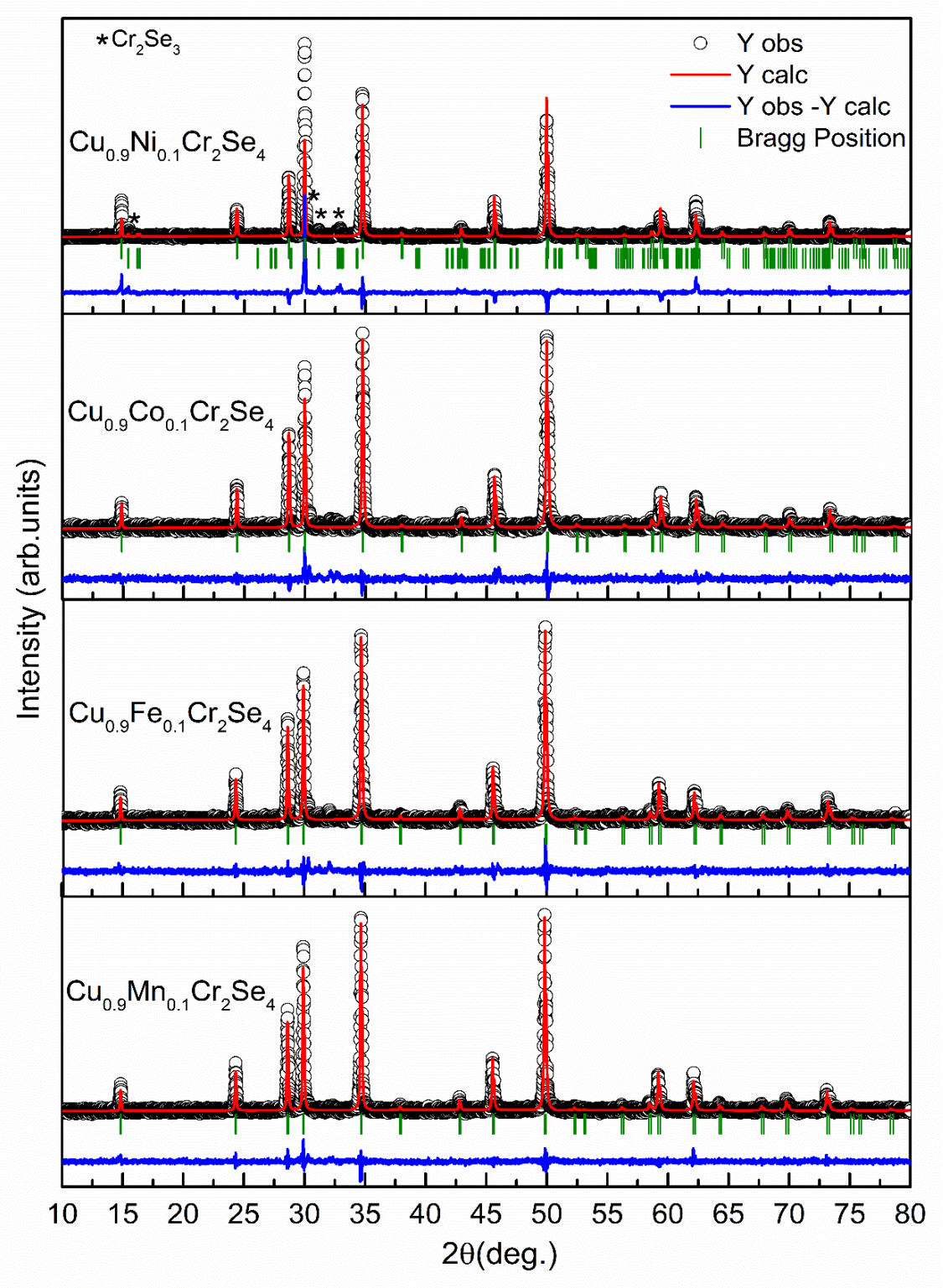

Figure 5.2: Refined XRD patterns of $Cu_{0.9}M_{0.1}Cr_2Se_4$ (M = Mn, Fe, Co and Ni) at room temperature.

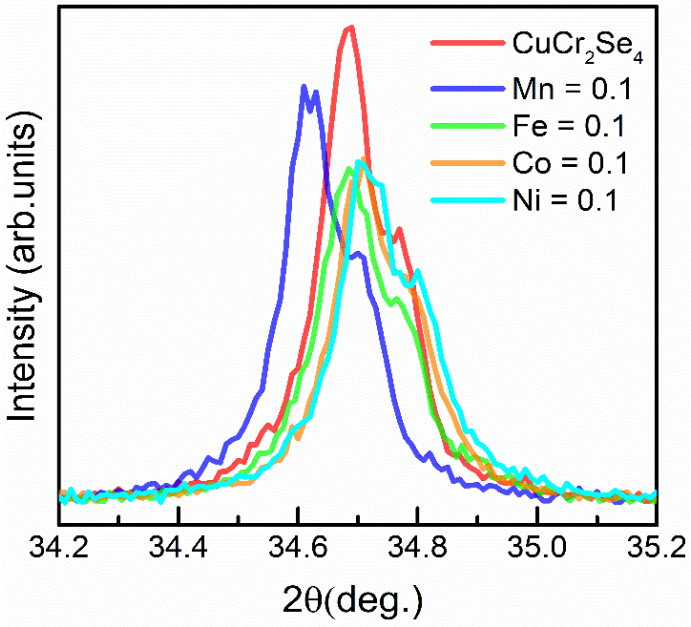

Figure 5.3: Single main peaks of all the substituted compounds display the shift in *2θ* value with respect to parent compound.

5.2.2 XANES Analysis

Analysis of the XANES region gives information on the valence state of the absorbing atom and on its local atomic environment. Fig. 5.4 shows XANES spectra of Cu metal foil, CuO, $CuCr_2Se_4$, $Cu_{0.9}Mn_{0.1}Cr_2Se_4$, $Cu_{0.9}Fe_{0.1}Cr_2Se_4$, $Cu_{0.9}Co_{0.1}Cr_2Se_4$ and $Cu_{0.9}Ni_{0.1}Cr_2Se_4$ in the vicinity of the Cu K-edge. As shown by the arrow from the Fig.5.4, the spectra for the samples of $Cu_{0.9}M_{0.1}Cr_2Se_4$ (M = Mn, Fe, Co, Ni) are similar to the spectra obtained for the $CuCr_2Se_4$ standard and similar to that of Cu metal but distinctly different and shifted to lower energy side with respect to CuO, which suggests that Cu ions exist in a monovalent state. Fig. 5.5 displays the Cr K-edge XANES spectra of $Cu_{0.9}M_{0.1}Cr_2Se_4$ (M = Mn, Fe, Co, Ni) as compared with Cr metal, Cr_2O_3 and $CuCr_2Se_4$, indicating the presence of mix valence state of Cr^{3+}-Cr^{4+} ions as the threshold energy (E_0) of $Cu_{0.9}Mn_{0.1}Cr_2Se_4$, $Cu_{0.9}Fe_{0.1}Cr_2Se_4$, $Cu_{0.9}Co_{0.1}Cr_2Se_4$ and $Cu_{0.9}Ni_{0.1}Cr_2Se_4$ samples are higher than that of Cr metal, but close to the energy of $CuCr_2Se_4$. XANES spectra of Mn K-edge of $Cu_{0.9}Mn_{0.1}Cr_2Se_4$, Fe K-edge of $Cu_{0.9}Fe_{0.1}Cr_2Se_4$ and Co K-edge of $Cu_{0.9}Co_{0.1}Cr_2Se_4$ and Ni K-edge of $Cu_{0.9}Ni_{0.1}Cr_2Se_4$, the threshold energy shifted to higher energy side as compared with Mn metal, Fe metal, Fe_2O_3, CoO

and Ni metal standards, suggesting the existence of divalent state of Mn, Fe, Co and Ni ions respectively (see Fig.5.6).

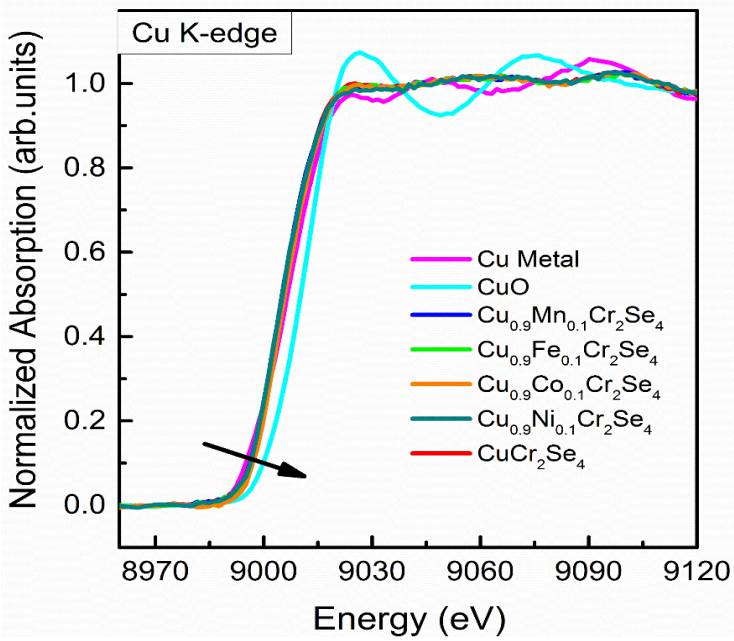

Figure 5.4: Room temperature XANES spectra of $CuCr_2Se_4$ and $Cu_{0.9}M_{0.1}Cr_2Se_4$ (M = Mn, Fe, Co and Ni) samples and the standards obtained at Cu K-edge

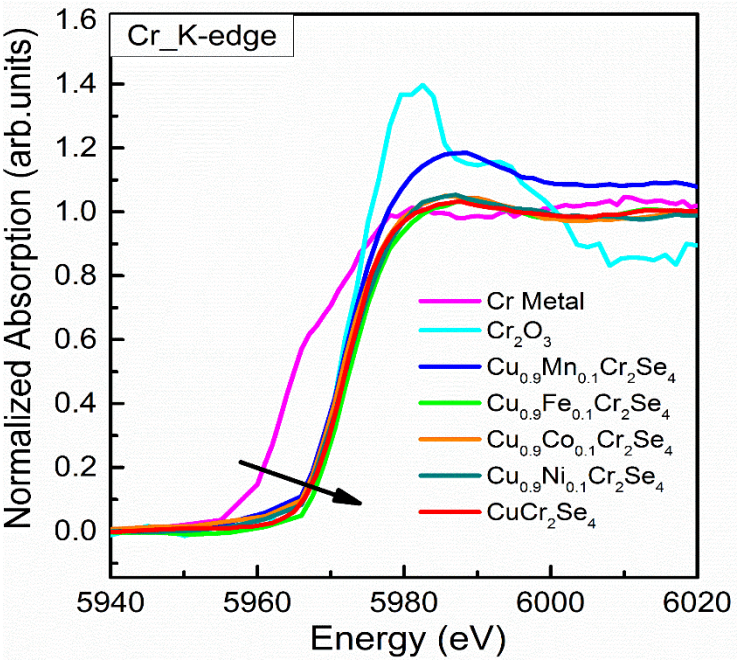

Figure 5.5: Room temperature XANES spectra of $CuCr_2Se_4$ and $Cu_{0.9}M_{0.1}Cr_2Se_4$ (M = Mn, Fe, Co and Ni) samples and the standards obtained at Cr K-edge.

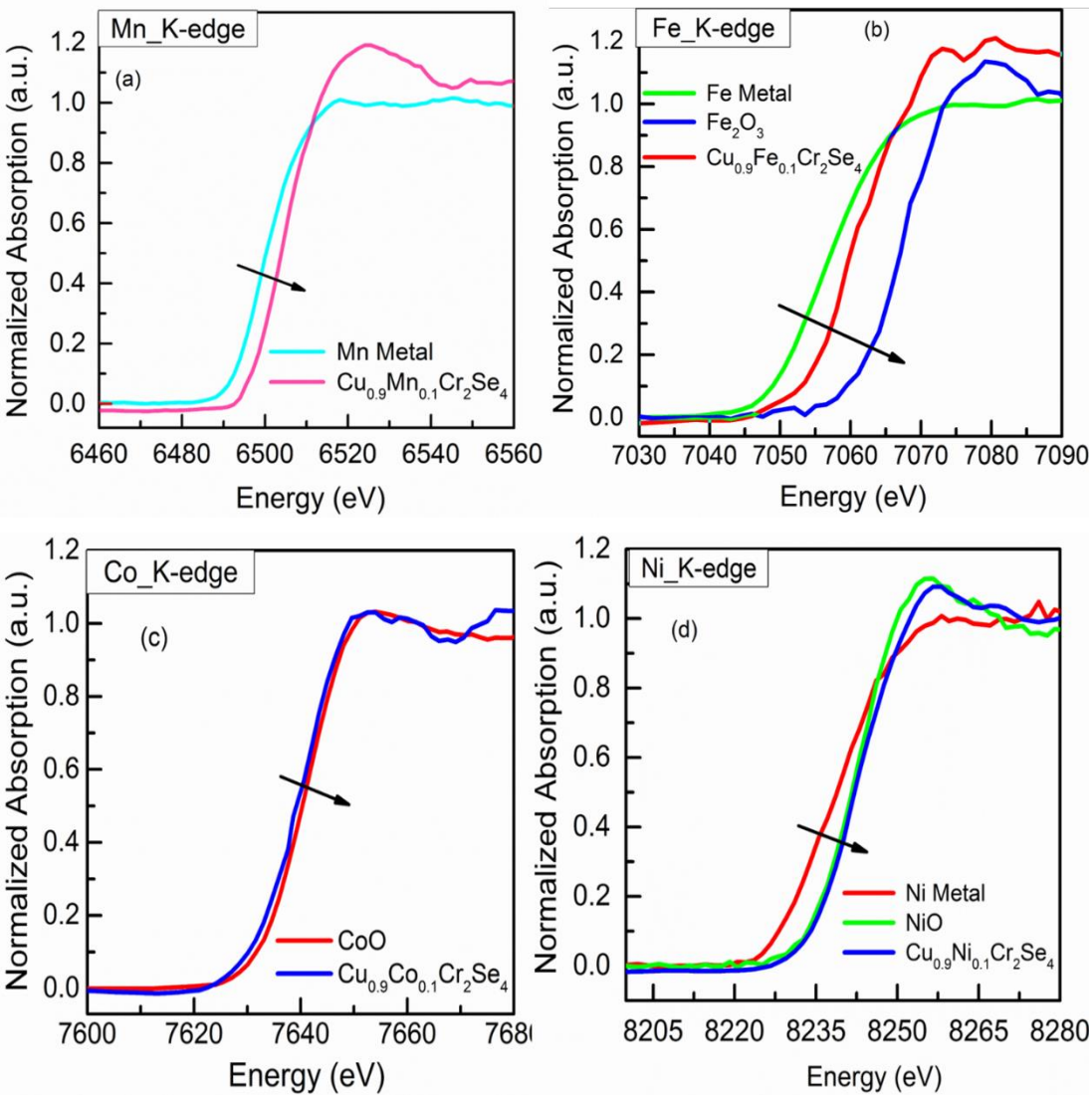

Figure 5.6: Room temperature XANES spectra of $Cu_{0.9}M_{0.1}Cr_2Se_4$ (M = Mn, Fe, Co and Ni) samples and their standards obtained at (a) Mn K-edge, (b) Fe K-edge and (c) Co K-edge (d)Ni K-edge respectively.

5.2.3 Magnetic properties

The temperature dependence of magnetization in an external magnetic field (*H*) of 500 Oe for $CuCr_2Se_4$ and $Cu_{0.9}M_{0.1}Cr_2Se_4$ (M = Mn, Fe, Co, Ni) are plotted in Fig.5.7 to 5.11 respectively. $CuCr_2Se_4$ is known to order from paramagnetic (PM) to ferromagnetic (FM) state with a T_C ~ 430 K [126]. Accordingly, with increase in temperature the *M(T)* curves obtained here indicates a downturn in magnetization as we approach the T_C. However, within the measurement limit of

400 K available to us, we were not able to record the complete transition, that is observed here may be due to reversal in temperature variation before the magnetic transition was fully complete. Besides, a significant bifurcation in ZFC-FC curves obtained even at sizeable applied field of 500 Oe (see Fig.5.7). However, it is important to note that such splitting was also observed in Ref. [127] for *M (T)* data obtained using 50 Oe field. This shows applicability of *3D*-Heisenberg model and support the view that ferrimagnetic order exists in $CuCr_2Se_4$ may be resulting from interaction of monovalent Cu and a delocalized hole in the Se 4*p* band with localized electrons of the Cr^{3+} ions.

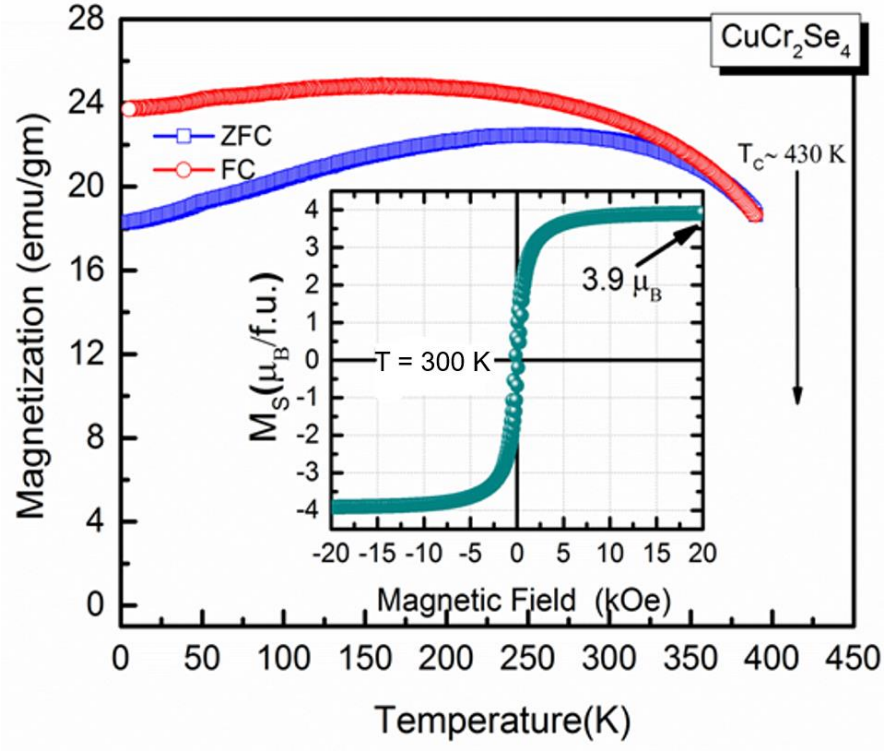

Figure 5.7: Temperature dependence of magnetization of $CuCr_2Se_4$ from 5 to 390 K under a magnetic field of 500 Oe. The inset shows the magnetic field dependence of magnetization at 5 K. Arrows indicate the Curie Temperature (T_C) and magnetic moment.

The partial (10%) of Mn^{2+}, Fe^{2+}, Co^{2+} and Ni^{2+} substitution for Cu^{+} in $CuCr_2Se_4$ causes a gradual change of valence of chromium ions from 3+ into 4+ according to the formula;

$$Cu^{+}_{1-x}M^{2+}_{x}[Cr^{3+}_{2-x}Cr^{4+}_{x}]Se^{2-}_{4} \ (M = Mn, Fe, Co, Ni)$$

This valence distribution satisfies Lotgering model [39] and confirmed by the XANES measurements presented in the previous section. With the incorporation of Mn, a rapid decrease in T_C from 430 K to 350 K was observed, whereas Fe, Co and Ni ions substitution at $CuCr_2Se_4$ causes only slight reduction of T_C from ~ 430 K to ~ 390 K. From Fig. 5.8, $Cu_{0.9}Mn_{0.1}Cr_2Se_4$ also shows large ZFC-FC splitting like parent, $CuCr_2Se_4$ with another magnetic transition temperature (T_m) near 100 K. Contrary to the effect caused by Fe^{2+}, Co^{2+} and Ni^{2+}, Mn^{2+} substitution gives rise to slight lattice expansion which generally results in the decrease of carrier density and might be the reason for shifting of the magnetic transition T_C towards lower temperature. Also, the transition takes place over a broad region of temperature, indicating weakening of the Cr^{3+} related interactions.

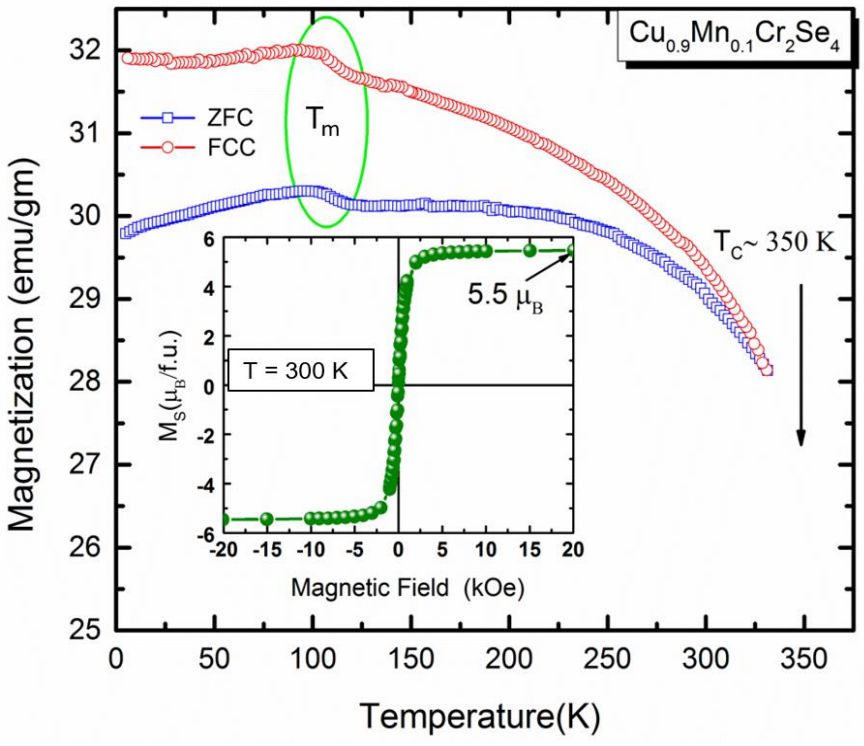

Figure 5.8: Temperature dependence of magnetization of $Cu_{0.9}Mn_{0.1}Cr_2Se_4$ from 5 to 390 K under a magnetic field of 500 Oe. The inset shows the magnetic field dependence of magnetization at 300 K. Arrows indicate the Curie Temperature (T_C) and magnetic moment. Green circle indicates T_m.

In present study, the experimental XANES results confirm the monovalent state of Cu and divalent state of Fe, Co and Ni. The existence of long range ferromagnetic ordering in these studied compounds are due to the magnetic coupling between high spin Fe^{2+} /Co^{2+}/Ni^{2+} at tetrahedral t_{2g} orbital with the octahedral t_{2g} orbital of high spin Cr^{3+} via 4*p* orbital of Se^{2-}. Here also we observed splitting in ZFC-FC-ZFH curves towards low temperature region (below 150 K) in the *M vs. T* data in Fig. 5.9 to 5.11 that might be an indication of the presence of some competing magnetic interactions. In comparison with Fe and Co substituted compounds, Ni incorporated samples shows lower total magnetic moments, which might be due to the presence of Cr_2Se_3 phase. Cr_2Se_3 phase is known to order antiferromagnetically at Neel temperature of T_N ~ 43 K [128] and the feature seen in the *M(T)* data at ~ 48 K might be attributed to Cr_2Se_3 phase.

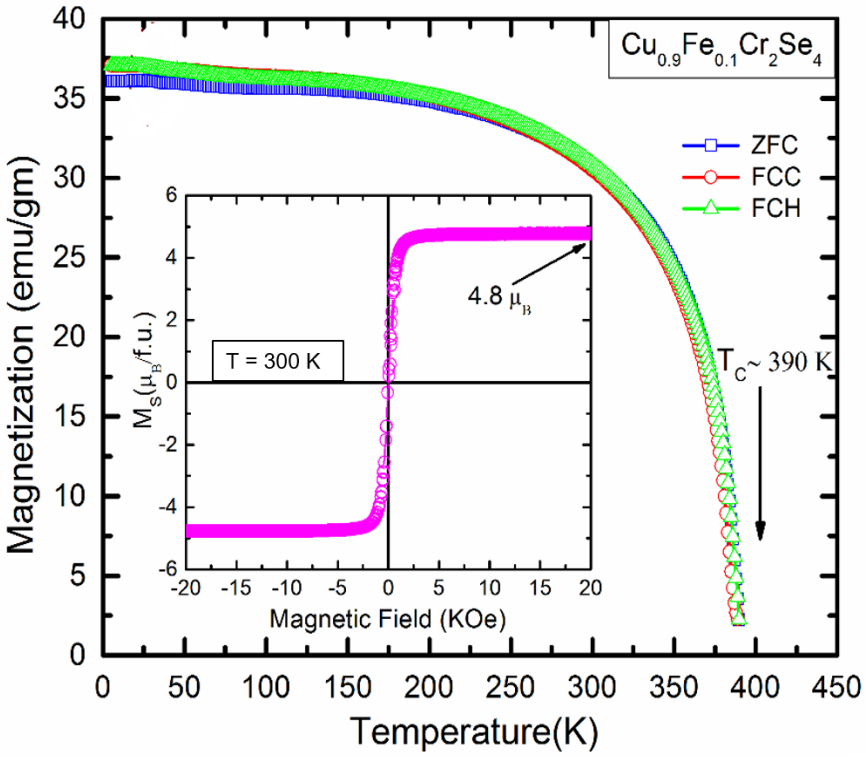

Figure 5.9: Temperature dependence of magnetization of $Cu_{0.9}Fe_{0.1}Cr_2Se_4$ from 5 to 390 K under a magnetic field of 500 Oe. The inset shows the magnetic field dependence of magnetization at 5 K. Arrows indicate the Curie Temperature (T_C) and magnetic moment.

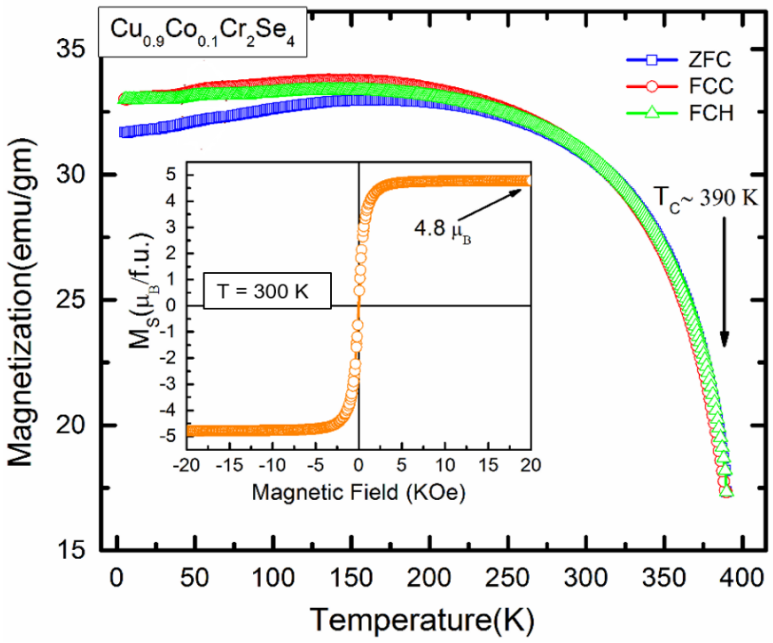

Figure 5.10: Temperature dependence of magnetization of $Cu_{0.9}Co_{0.1}Cr_2Se_4$ from 5 to 390 K under a magnetic field of 500 Oe. The inset shows the magnetic field dependence of magnetization for all the above samples at 300 K. Arrows indicate the Curie Temperature (T_C) and magnetic moment.

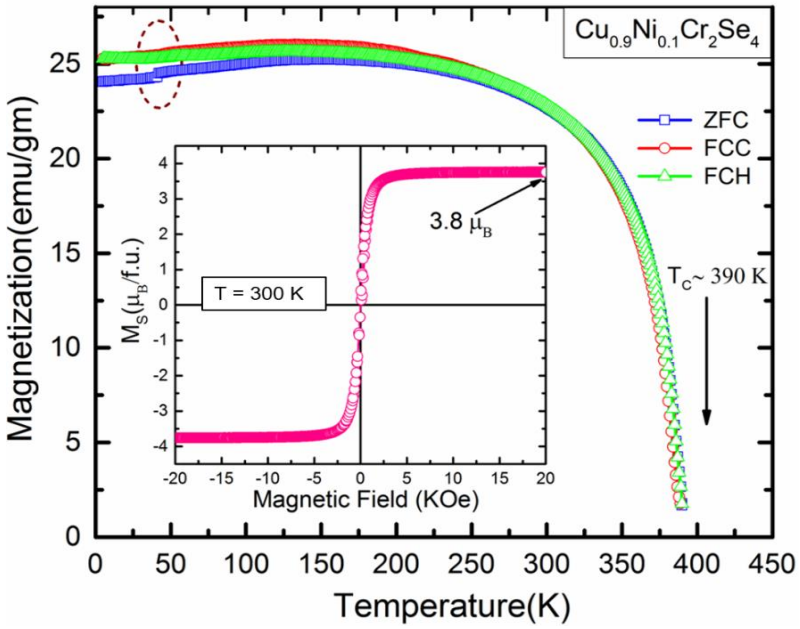

Figure 5.11: Temperature dependence of magnetization of $Cu_{0.9}Ni_{0.1}Cr_2Se_4$ from 5 to 390 K under a magnetic field of 500 Oe. The inset shows the magnetic field dependence of magnetization for all the above samples at 300 K. Arrows indicate the Curie Temperature (T_C) and magnetic moment.

Insets of all the *M vs. T* figures presents the *M (H)* plots measured at 300 K for the corresponding samples. The characteristic of soft ferromagnetic phase with small coercivity and strong saturation magnetization is seen for all the samples. The value of total saturation moment of $CuCr_2Se_4$ is 3.92μ_B/f.u., matching with that reported in [127] for measurement carried out at T = 300 K. The saturation magnetization value for $Cu_{0.9}Mn_{0.1}Cr_2Se_4$ is found to be 5.5μ_B/f.u. As it is known that 3*d* levels of Cu^+ is full filled does not contain any magnetic moment. But the partially occupied 3*d* levels of Mn^{2+} and Cr^{3+}/Cr^{4+} are degenerated by the crystal field (CF) split. The $3d^5$ level of Mn^{2+} is split into higher t_{2g} and lower e_g levels due to tetrahedral CF splitting, resulting into magnetic moment of (S= 5/2). Meanwhile, the $3d^{3+}$ and $3d^{2+}$ level of Cr^{3+} and Cr^{4+} are split into higher e_g and lower t_{2g} orbits due to the octahedral CF splitting leading to *S*= 3/2 and *S* =1 respectively. Thus, the magnetic moment of $\mu_S(Mn^{2+}) = 2\sqrt{S(S+1)}\mu_B \sim 5.9\mu_B$, while $\mu_S(Cr^{3+}) \sim 3\mu_B$ and μ_S $(Cr^{2+}) \sim 2\mu_B$. Since Mn lies in the middle of the transition metal series and can have competing ferromagnetic (FM) and antiferromagnetic (AFM) interatomic exchange interactions lying between those of the early transitions metals, which are largely AFM, and those of the late transition metals, which are largely FM. So, we believe that the overall long-range magnetic ordering is mainly due to the ferrimagnetic alignment of the Mn and Cr sub-lattices.

Similarly, from rest of the *M(H)* curves, we also observed that a full saturation state is achieved under a field of ~ 5 kOe with a moment of 4.8 μ_B/f.u. for Fe and Co substituted samples and 3.8 μ_B/f.u. for Ni substituted sample respectively. Presence of an impurity phase Cr_2Se_3, leads to decrease in the total magnetic moment in case of $Cu_{0.9}Ni_{0.1}Cr_2Se_4$ compound.

5.2.4. Transport properties

The temperature variation of the electrical resistance was measured for the respective compositions $Cu_{1-x}Mn_xCr_2Se_4$ (x = 0 and 0.1) in fields of 0 (heating and cooling), 10 kOe and 50 kOe and are shown in Fig. 5.12 and 5.13. There is a clear change of slope near the transition temperatures (T_m and T_C). According to Fig. 5.12, the zero-field heating and cooling resistance of both the studied samples decreases monotonically indicating the metallic behavior. With Mn^{2+} substitution

the resistance value increases but interestingly shows a kink appears exactly at T_m in the cooling data and absent in the warming curve. Also, the zero-field heating and cooling curve shows a hysteresis-like feature between 170 to 380 K, the reason for which is not clear as yet. Similarly, Fig.5.13 shows resistance as a function of temperature for $CuCr_2Se_4$ and $Cu_{0.9}Mn_{0.1}Cr_2Se_4$ in a field of 0, 10 kOe and 50 kOe. It is clear that the Mn substitution changed the temperature dependence of the resistance behavior. The coexistence of FM and AFM competing like order below T_m might modify the magneto-transport nature in $Cu_{0.9}Mn_{0.1}Cr_2Se_4$. With increase of applied field from 0 to 10 kOe and 50 kOe, the resistance values decrease for both the samples and display different field and temperature dependent behavior.

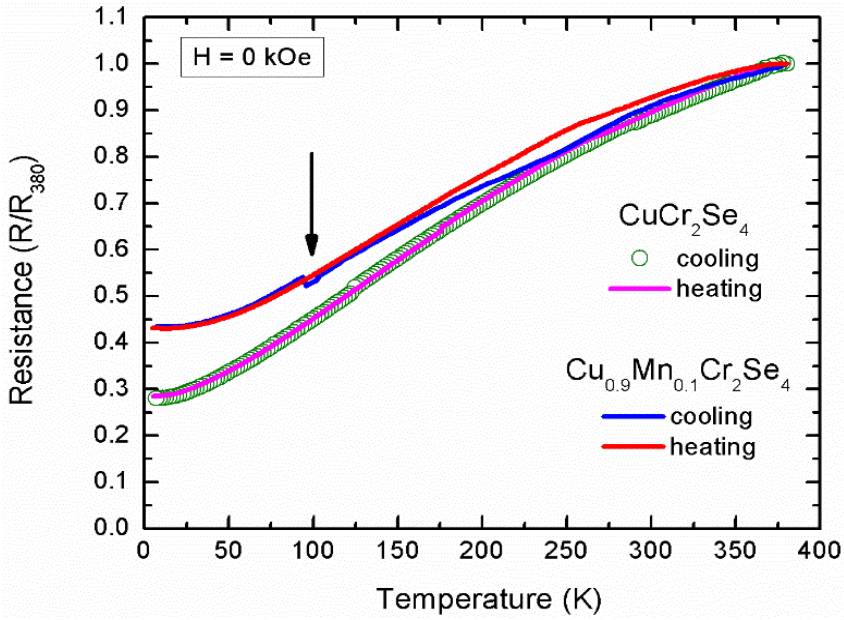

Figure 5.12: Electrical resistance 'R' normalized to its value at 380 K, R/R_{380K}, as a function of temperature in a zero-field heating and cooling for $CuCr_2Se_4$ and $Cu_{0.9}Mn_{0.1}Cr_2Se_4$ samples. Since, all the samples are very soft, we are unable to calculate the exact length and area of the samples, hence resistivity of the material. In order to know the conduction behavior and magnetoresistance, we have used resistance data for this study.

Similarly, the temperature variation of the electrical resistance was measured for the other compositions $Cu_{0.9}M_{0.1}Cr_2Se_4$ (M = Fe, Co, Ni) in heating and cooling cycles as shown in Fig. 5.14 to 5.16. We noticed that resistance while

cooling from 380 K to 2 K and upon subsequent warming is similar in nature but not overlap with each other for $Cu_{0.9}Fe_{0.1}Cr_2Se_4$. while in the case of $Cu_{0.9}Co_{0.1}Cr_2Se_4$ and $Cu_{0.9}Ni_{0.1}Cr_2Se_4$ the curves are overlap with the exception of tiny hysteresis across the *Tc*.

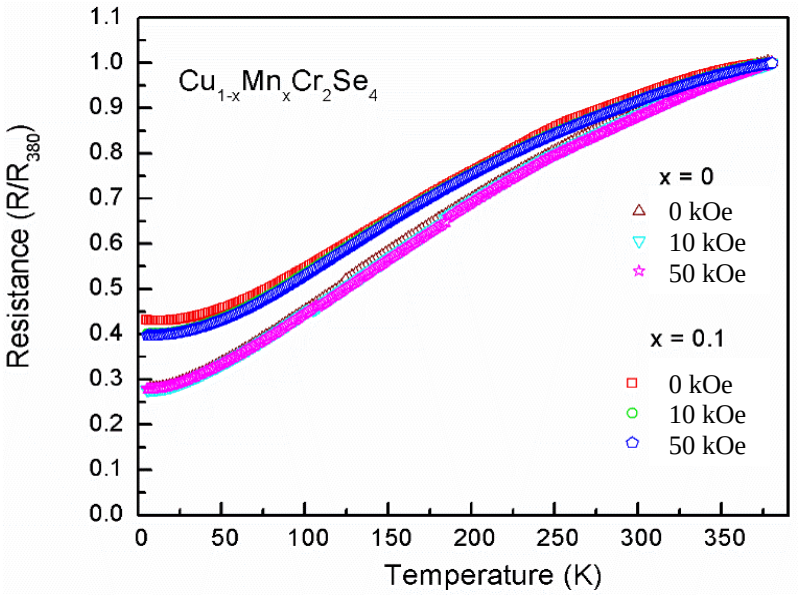

Figure 5.13: Electrical resistance 'R' normalized to its value at 380 K, R/R_{380K}, as a function of temperature in a field of 0, 10 kOe and 50 kOe for $Cu_{1-x}Mn_xCr_2Se_4$ compounds.

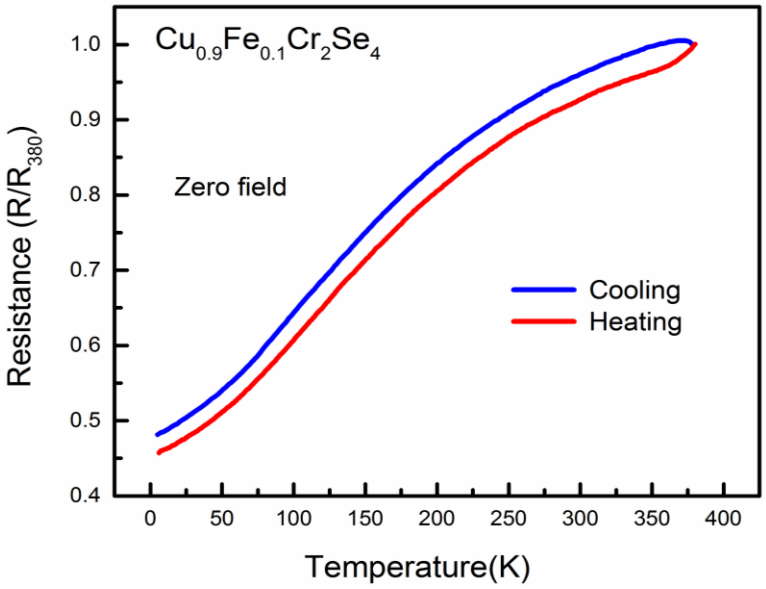

Figure 5.14: Electrical resistance 'R' normalized to its value at 380 K, R/R_{380K}, as a function of temperature in a zero-field heating and cooling for $Cu_{0.9}Fe_{0.1}Cr_2Se_4$ samples.

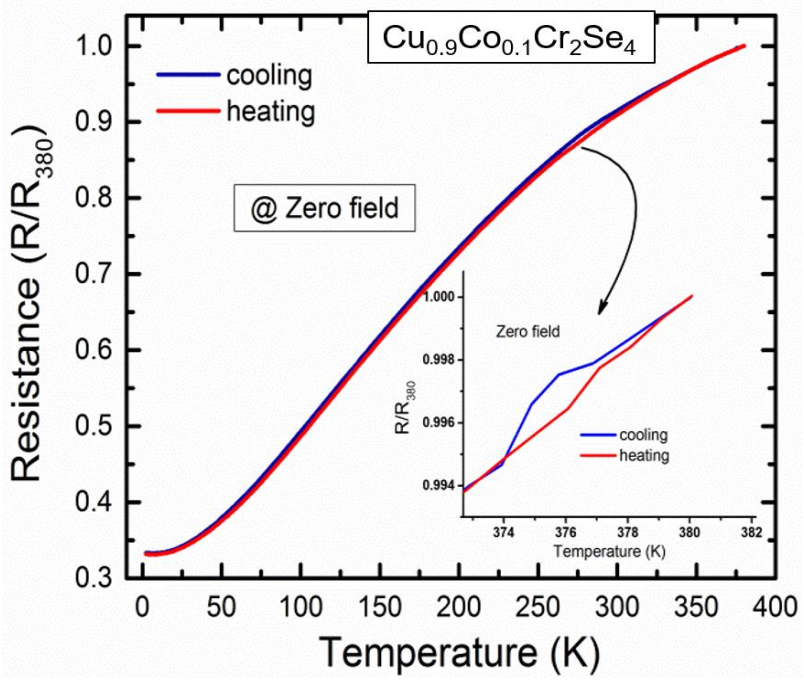

Figure 5.15: Electrical resistance 'R' normalized to its value at 380 K, R/R_{380K}, as a function of temperature in a zero-field heating and cooling for $Cu_{0.9}Co_{0.1}Cr_2Se_4$ samples.

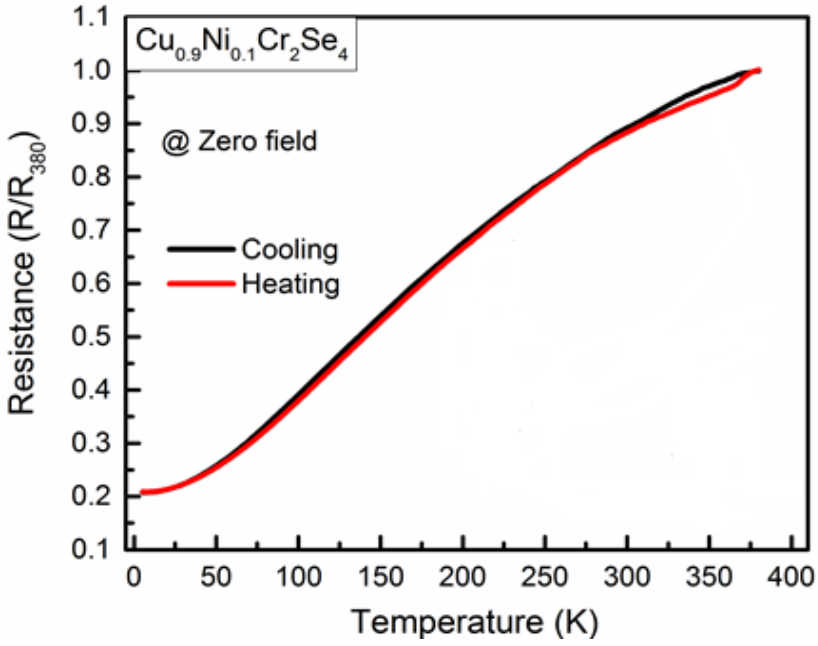

Figure 5.16: Electrical resistance 'R' normalized to its value at 380 K, R/R_{380K}, as a function of temperature in a zero-field heating and cooling for $Cu_{0.9}Ni_{0.1}Cr_2Se_4$ samples.

By analyzing the temperature dependence of resistance, one can get some insight into the influence of magnetic order on transport behavior of these type of Cr-based selenospinels. Generally, the total resistance of a ferromagnetic material is the sum of the residual resistance, the phonon contribution (ρ_{ph}) and the magnon contribution (ρ_{mag}). The data for $CuCr_2Se_4$ and substituted compositions was fitted in the high temperature region (T > 50 K for x = 0) and (T > 100 K for x = 0.1) using the relation $\rho = \rho_0 + aT + bT^2 + cT^3$; where ρ_0 is the residual resistivity due to defect scattering and a, b, c are constants that depends on the velocity of electrons at the Fermi surface, the Debye radius and the number density of electrons in the metal. Again, the power of temperature is an integer and depends upon the nature of interaction; such as T, T^2 and T^3 dependence implies that the resistance is due to the electron-phonon interaction, electron-electron interaction and *s-d* electron scattering respectively. In the low temperature region, the resistance curve was fitted using the relation; $\rho = \rho_0 + bT^n$, both sample exhibit T^2 dependence implies a strong magnon scattering from the spin periodicity as shown in Fig.5.17 and 5.18. At the lowest temperature limit, we see an upturn of the resistance which is absent in parent one, presumably indicates the localization of carriers as shown in Fig. 5.19. Together with the fact that the value of the residual resistance increases with Mn substitution, the system seems to be substantially influenced by the spin fluctuation due to the magnetic substitution at A-site ions. Nevertheless, we see T^2 dependence of resistance which indicates the robustness of the one-magnon scattering processes like half-metals. Here we would like draw an analogy with the T^2 behavior seen in the low temperature resistivity dependence reported for colossal magnetoresistance (CMR) manganites and CrO_2 films [129,130], which are another candidate for a half-metal. Based on the above discussion, we speculate that $Cu_{0.9}Mn_{0.1}Cr_2Se_4$ might be a candidate material displaying half-metallicity at low temperature. We base our assumption on the electronic structure calculation carried out by Ref. [68], wherein the authors predict half-metallic ground state in suitably doped $CuCr_2Se_4$.

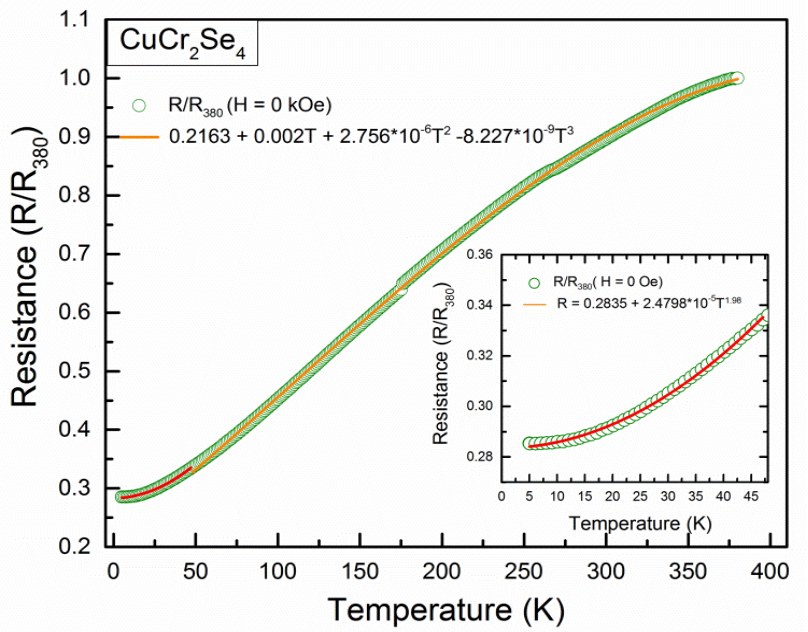

Figure 5.17: The fitted curve of the zero-field electrical resistance (R/R_{380K}) of $CuCr_2Se_4$ sample in different temperature regimes respectively. Inset shows the fitting of the low temperature regime (< 50 K for $CuCr_2Se_4$).

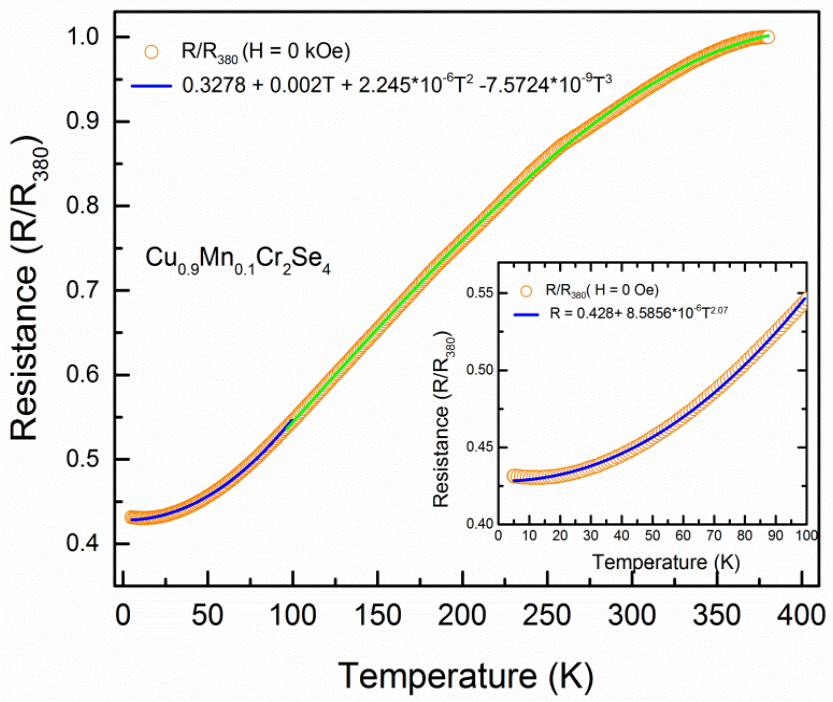

Figure 5.18: The fitted curve of the zero-field electrical resistance (R/R_{380K}) of $Cu_{0.9}Mn_{0.1}Cr_2Se_4$ samples in different temperature regimes respectively. Inset shows the fitting of the low temperature regime (< 100 K).

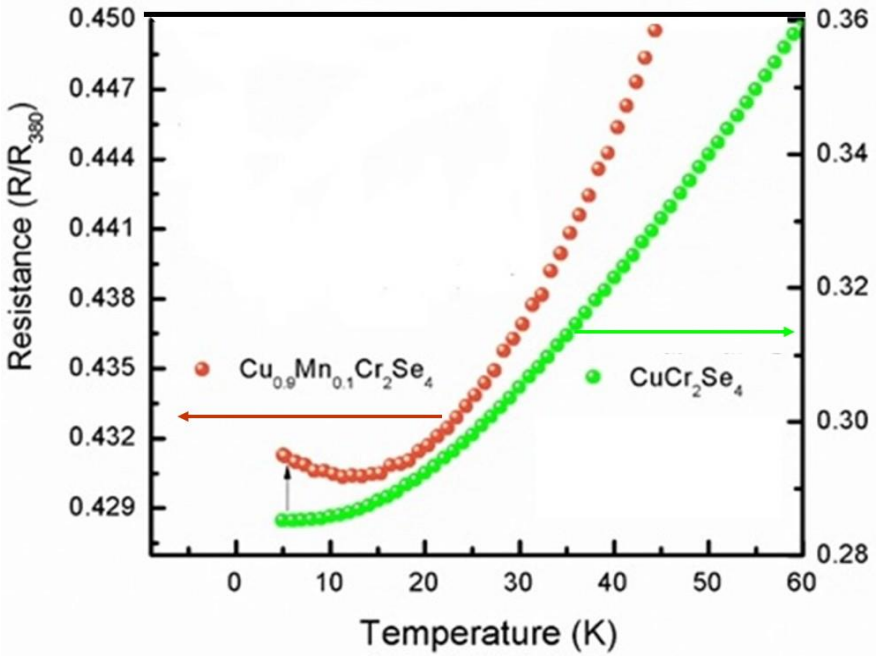

Figure 5.19: Zero field electrical resistance (R/R_{380K}), as a function of temperature (T< 60 K) for $Cu_{1-x}Mn_xCr_2Se_4$ (x = 0, 0.1) compounds.

We now move to the temperature dependence of the resistance of $Cu_{0.9}Fe_{0.1}Cr_2Se_4$ sample. By fitting the temperature variation resistance in different temperature regimes (Fig.5.20), once again electron-magnon scattering is found to be a dominant scattering process. In the temperature range below 90 K, a good fit was obtained for the relation $\rho = \rho_0 + AT^n$ with $n \sim 1.5$. The fact that 'n' is not equal to 2 may be due to the pinning effect of the magnetic clusters in their ferromagnetic phase. As it is known from literature, the magnetic impurity substitution causes mixing of spin up and spin down electrons and violates Matthiessen's rule in ferromagnetic alloys [131-133]. In such cases electron – magnon scattering results from incoherent scattering and resistance follows a $T^{3/2}$-law as the relaxation or scattering rate is proportional to the number of magnons. For temperature range from 90 K to 340 K, the resistance has been fitted successfully to the expression by $\rho = \rho_0 + AT + BT^2 + CT^3$. This resistance behavior is not similar to that of regular metals as its resistivity has negative slopes in terms of T^2 and T^3 dependent. These negative slopes may be the indication of large spin disorder scattering as more than one magnetic ion is present. Above 340 K, nearer

to the Curie temperature, the scattering originates from the disorder caused by localized spin fluctuations and can not be fitted in a wider temperature interval.

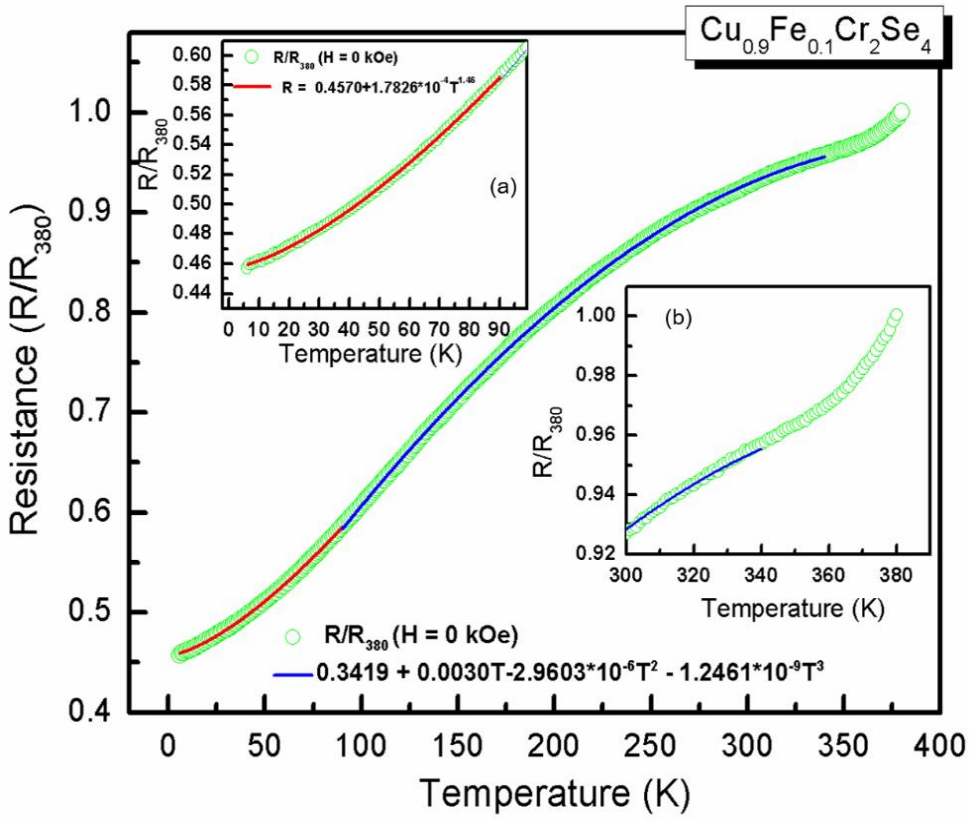

Figure 5.20: Fitted curves of the zero-field electrical resistance (R/R_{380K}) of $Cu_{0.9}Fe_{0.1}Cr_2Se_4$ samples in different temperature regimes. Insets (a) displays the fitting of the low temperature regime (< 90 K) and (b) displays the behavior of zero field resistance above 340 K.

The above discussed strategy was used to fit the Co and Ni substituted samples as well. The representative plots are shown in Fig.5.21 and Fig.5.22.

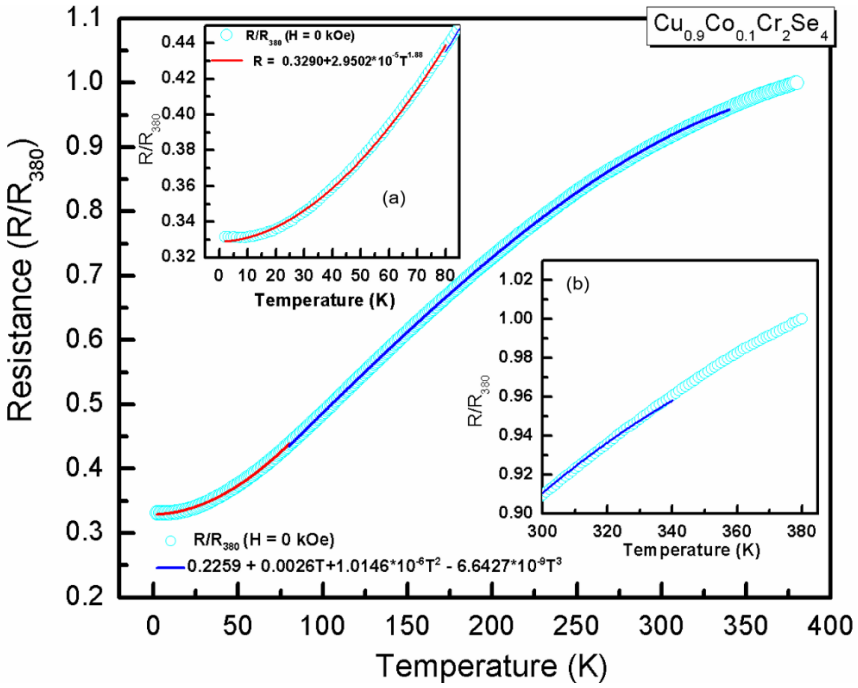

Figure 5.21: Fitted curves of the zero-field electrical resistance (R/R_{380K}) of $Cu_{0.9}Co_{0.1}Cr_2Se_4$ samples in different temperature regimes. Insets (a) displays the fitting of the low temperature regime (< 80 K) and (b) displays the behavior of zero field resistance above 340 K.

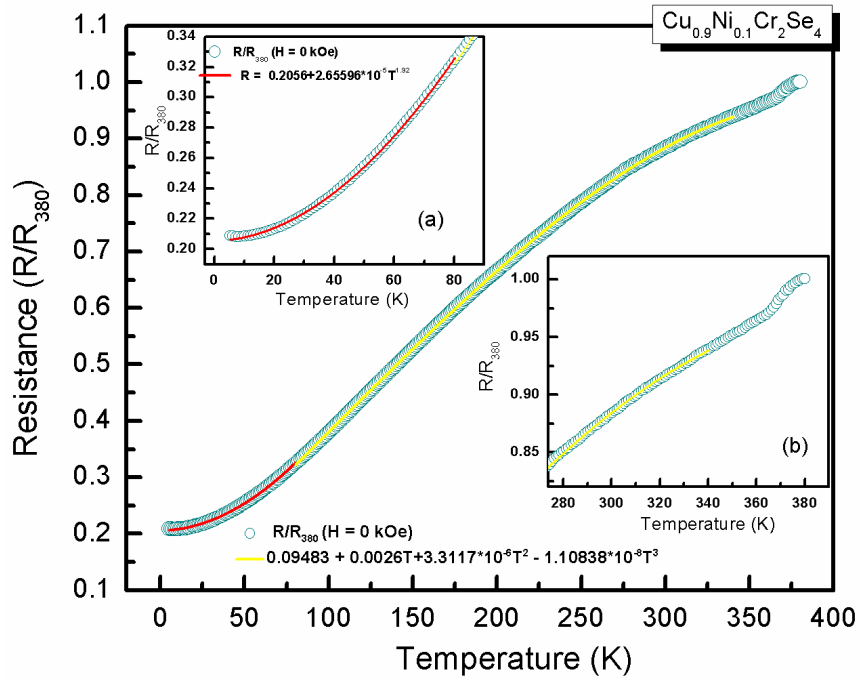

Figure 5.22: Fitted curves of the zero-field electrical resistance (R/R_{380K}) of $Cu_{0.9}Ni_{0.1}Cr_2Se_4$ samples in different temperature regimes. Insets (a) displays the fitting of the low temperature regime (< 80 K) and (b) displays the behavior of zero field resistance above 340 K.

5.2.4.1 Magnetoresistance (MR) studies

Fig.5.23 represents the MR as a function of temperature at 10 kOe and 50 kOe for parent and Mn-substituted samples, where the percentage of MR is calculated by using the given formula:

$$\text{MR } \% = \frac{[R(H)-R(0)]}{R(0)} \times 100 \quad (1)$$

As we have already seen from Fig. 5.12, Fig. 5.13 and Fig. 5.19, the temperature dependences of resistance show the significant change at T_m in $Cu_{0.9}Mn_{0.1}Cr_2Se_4$. In the application of magnetic field (10 kOe and 50 kOe), an unexpected transition near T_m was observed in $CuCr_2Se_4$, exhibits total maximum negative MR of 3.6 % at 5 K below T_m, while it shows decrease in negative nature of MR above T_m and the minimum negative MR was obtained upto 0.4 %. In contrast, $Cu_{0.9}Mn_{0.1}Cr_2Se_4$ shows sudden increase of negative MR at T_m and the sample exhibits large negative MR of 8%. This large negative MR at low temperature reaffirms the presence of spin polarized transport in 10 % Mn substituted $CuCr_2Se_4$. So, the simultaneous existence of low temperature (T< 50 K) large negative MR and T^2 dependence of resistance qualify $Cu_{0.9}Mn_{0.1}Cr_2Se_4$ as a candidate for half-metallicity. Positive MR < 1 % observed just above T_m (134 K- 224 K) then at T_C in field of 10 kOe and goes away with the application of higher field of 50 kOe. This type of crossover from negative to positive MR at certain temperatures, suggest the presence of competing AFM and FM phases. The temperature dependent anomalous resistance behavior with respect to field below transition temperatures of T_m and above T_m (~ 250 K and ~ T_C) was already noticed from Fig. 13. MR behavior (Fig.23) also reflected the magnetic anomaly at same temperatures of ~ 250 K and ~ 350 K for both the samples.

The field dependence of MR for both the compounds measured at 5 K, 50 k, 100 K, 200 K and 300 K are shown in Fig.5.24. As evident form the figure, MR plots for both samples show strong field induced irreversibility at 300 K. That means the zerofield value at the beginning of the first field increasing path is quite different from the subsequent decreasing path, indicating the field-induced irreversibility. Presence of field induced irreversibility in both the studied sample at 300 K further support our conjuncture of existence of two magnetic phases. The

parent compound shows the maximum negative MR of about 0.8 % at 100 K at the field of 50 kOe, and for $x = 0.1$, it is about 3% at same temperature. Generally, the magnetic scattering of the conduction carrier by magnetic ions gets suppressed because of the alignment of the magnetic spins in higher field.

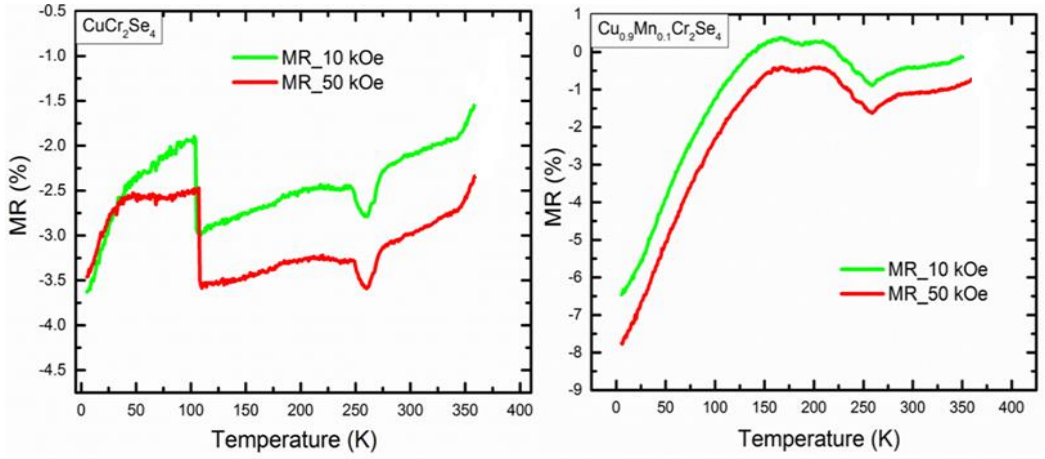

Figure 5.23: Left and Right panel shows temperature dependent MR in a field of 10 kOe and 50 kOe for $CuCr_2Se_4$ and $Cu_{0.9}Mn_{0.1}Cr_2Se_4$ samples respectively.

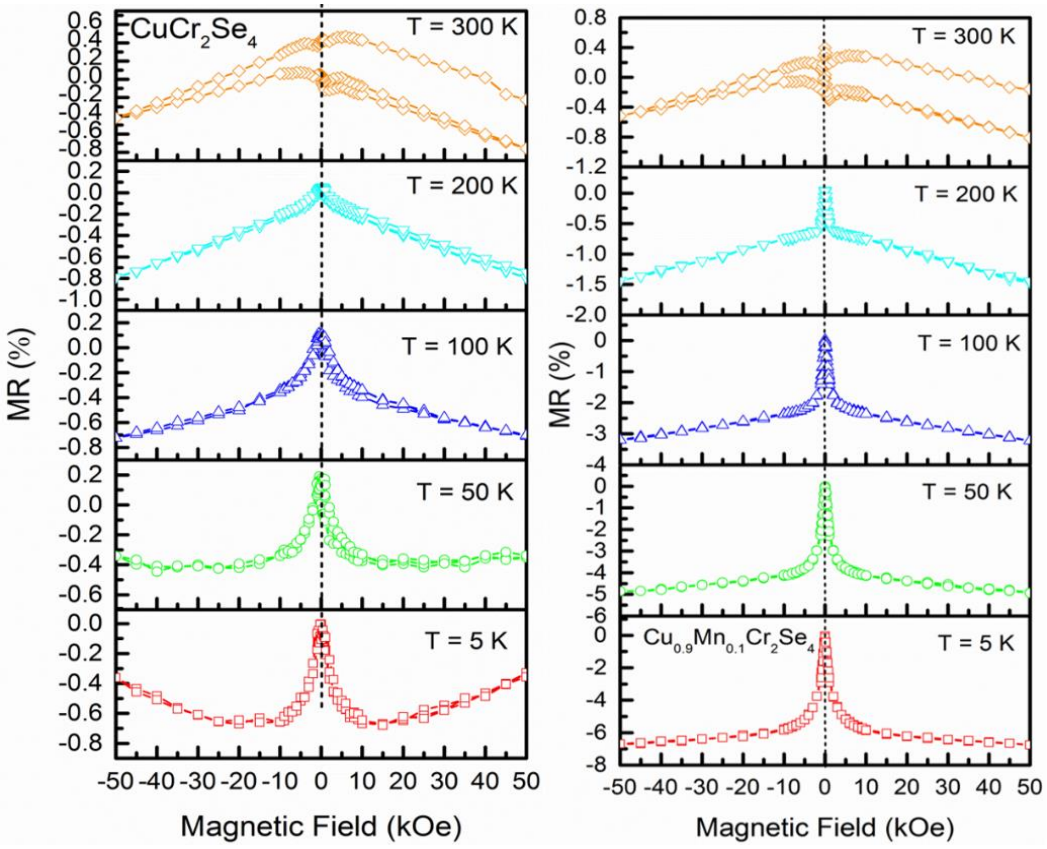

Figure 5.24: Left and Right panel shows field dependent MR at different temperatures of 5 K, 50 K, 100 K, 200 K and 300 K for $CuCr_2Se_4$ and $Cu_{0.9}Mn_{0.1}Cr_2Se_4$ samples respectively.

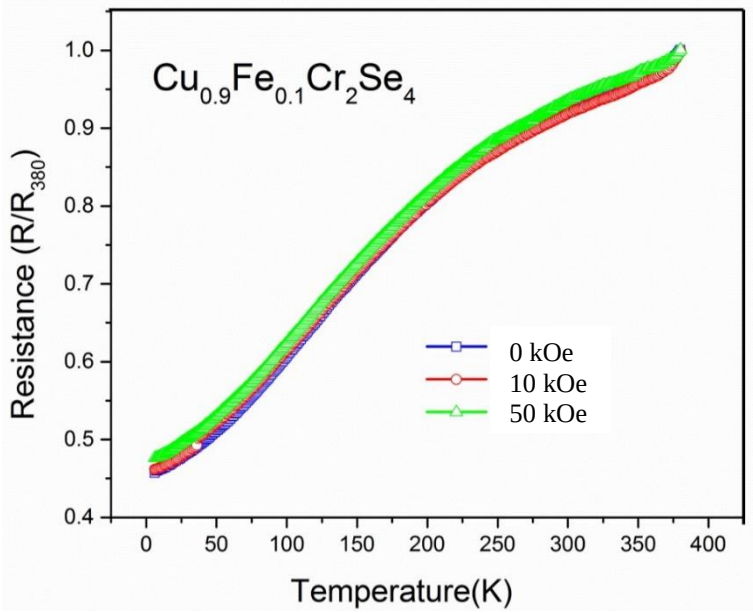

Figure 5.25: Electrical resistance R/R_{380K} vs. temperature at zero field and field of 10 kOe and 50 kOe of $Cu_{0.9}Fe_{0.1}Cr_2Se_4$.

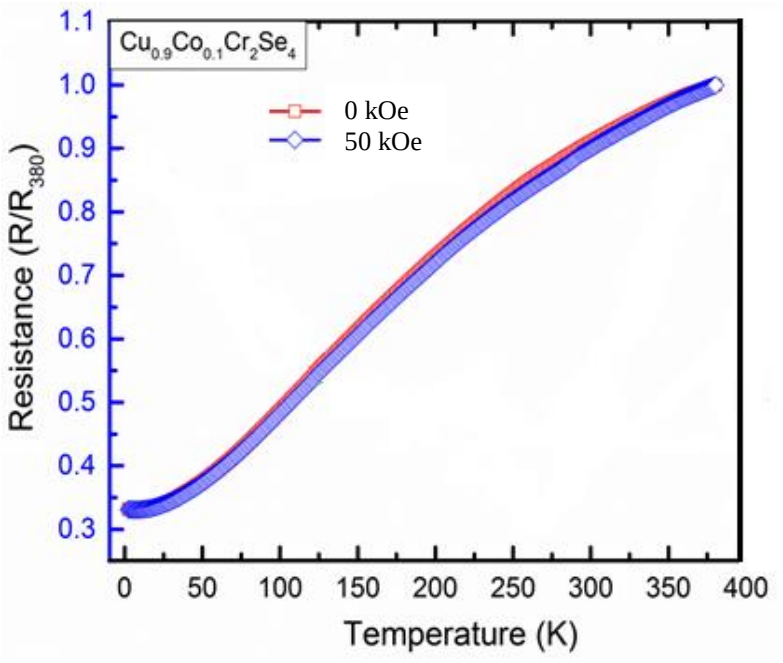

Figure 5.26: Electrical resistance R/R_{380K} vs. temperature at zero field and field of 10 kOe and 50 kOe of $Cu_{0.9}Co_{0.1}Cr_2Se_4$.

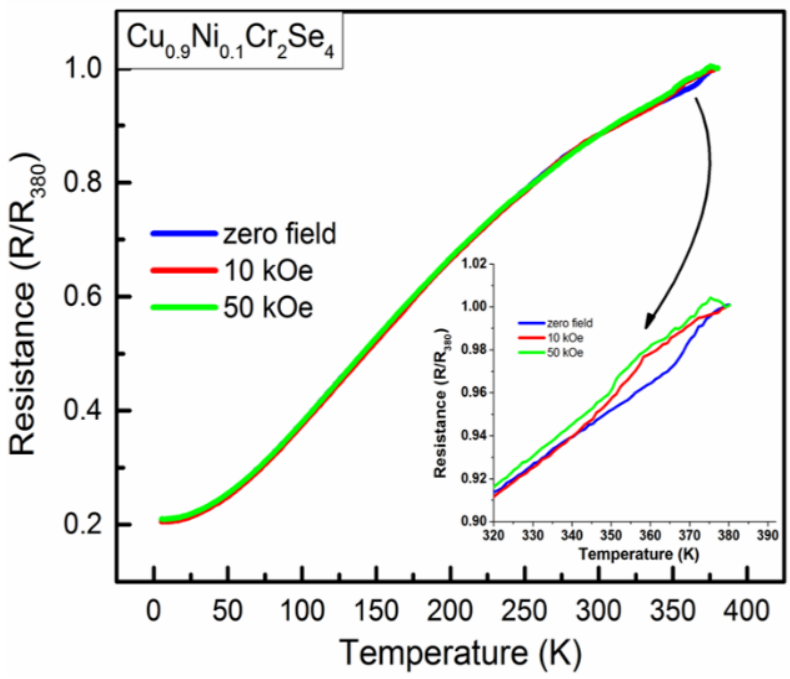

Figure 5.27: Electrical resistance R/R_{380K} vs. temperature at zero field and field of 10 kOe and 50 kOe of $Cu_{0.9}Ni_{0.1}Cr_2Se_4$.

Fig.5.25 represents the temperature variation of the electrical resistance for $Cu_{0.9}Fe_{0.1}Cr_2Se_4$ without field and with a field of 10 kOe and 50 kOe. Similarly, Fig.5.26 and 5.27 display the electrical resistance for $Cu_{0.9}Co_{0.1}Cr_2Se_4$ and $Cu_{0.9}Ni_{0.1}Cr_2Se_4$ with a field of 0 kOe and 50 kOe. The resistance shows temperature dependence characteristic of metallic behavior. As evident from plots of temperature dependent resistance, which does not show any change with and without field. Hence, we did not observe any sizable MR for these compositions and that is why not presented here.

5.3 Summary

$Cu_{1-x}M_xCr_2Se_4$ (M= Mn, Fe, Co, Ni and x = 0.1) selenospinels were investigated for their structure, magnetic and transport properties with an aim to reduce the Curie temperature (T_c) upto 300 K in view of the expected colossal magnetoresistance (CMR) for room temperature application. With the 10% of magnetic ion (Fe, Co, Ni) substitutions at Cu site in $CuCr_2Se_4$, reduce the T_C from

430 K to 390 K, in case of Fe and Co-substituted compositions. The saturation magnetic moment reduces from 4.8μ_B/f.u. to 3.8 μ_B/f.u. in Ni-incorporated compound. But fascinatingly, 10% of Mn substitutions causes a drastic reduction of T_C from 430 K to 350 K and significant increase of the saturation magnetic moment of 5.5 μ_B/f.u. X-ray absorption near edge spectroscopy (XANES) confirms the monovalent state of Cu and divalent state of Mn, Fe, Co and Ni. Electrical measurement of all these samples show the metallic-type conductivity. $Cu_{0.9}Fe_{0.1}Cr_2Se_4$, $Cu_{0.9}Co_{0.1}Cr_2Se_4$ and $Cu_{0.9}Ni_{0.1}Cr_2Se_4$ sample did not show sizable MR, whereas $Cu_{0.9}Mn_{0.1}Cr_2Se_4$ shows large negative magnetoresistance (MR) (~ 8%) and (~ 3.5 %) for parent compounds in an applied field of 50 kOe.

Chapter 6

Influence of Ti Substitution on Magnetic and Transport Properties of $CuCr_2Se_4$

6.1. Overview

Recent demonstration of $CuCr_2Se_4$ compounds paid considerable attention because of the theoretical prediction of a highly spin-polarized DOS with half-metallic properties by suitable dopings and exhibition of significant magneto-optic Kerr rotation, which makes it a promising candidate material for new magneto-optical devices [126,134-135].

From the previous chapters, it is clear that the valence state of Cu, Cr and Ti ions play a vital role in determining the fascinating magnetic and electrical properties of $CuCr_2Se_4$. It will be quite interesting that what happens when we systematically substitute Cr by Ti ions in $CuCr_2Se_4$ selenospinel electron shell. Therefore, our main purpose of this work is an attempt to study an influence of valence state, magnetic double-exchange and superexchange interactions and the electronic transport induced by the temperature of the $CuCr_{2-x}Ti_xSe_4$ spinel.

6.2. Results and Discussion

6.2.1 Compositional Analysis

All the polycrystalline samples of $Cu[Cr_{2-x}Ti_x]Se_4$ (x = 0, 0.3, 0.4, 0.5, 0.75, 1.0) series, prepared by conventional solid-state synthesis method as described in chapter 2. The ratio of elemental compositions of Cu, Cr, Ti and Se in all the prepared $Cu[Cr_{2-x}Ti_x]Se_4$ samples are presented in Tab. 6.1. These numbers match well with the ratio of starting compositions, indicating that the stoichiometry of starting composition is maintained in the final product.

	Atomic percentage (error ~ ± 3%)			
Composition	**Cu**	**Cr**	**Ti**	**Se**
$CuCr_2Se_4$	17.65	35.29	-	70.55
$CuCr_{1.7}Ti_{0.3}Se_4$	15.44	26.30	7.96	61.68
$CuCr_{1.6}Ti_{0.4}Se_4$	15.26	24.41	9.85	60.98
$CuCr_{1.5}Ti_{0.5}Se_4$	14.94	22.46	11.30	59.90
$CuCr_{1.25}Ti_{0.75}Se_4$	14.11	17.68	13.28	56.86
$CuCrTiSe_4$	15.05	15.56	15.81	60.17

Table 6.1: Elemental ratio obtained by EDX for $Cu[Cr_{2-x}Ti_x]Se_4$ $(0 \leq x \leq 1)$

6.2.2 XRD

The refined XRD patterns of Cu $[Cr_{2-x}Ti_x]$ Se_4 samples were fully indexed in the space group no. *Fd-3m* (no. 227) as shown in Fig. 6.1, providing evidence that all the prepared compounds have single phase cubic spinel-type structures. The lattice parameters, unit cell volume, R_f, R_{Bragg} and χ^2 are presented in Tab.6.2. In $Cu[Cr_{2-x}Ti_x]Se_4$ selenospinel series, the volume of the unit cell grows with concentration of Ti^{4+} ions. The lattice parameter '*a*' increased gradually from 10.33 Å to 10.43 Å as Ti^{4+} was replaced by Cr^{3+} from 15% to 50%, and obeys Vegard's law (Tab. 6.2). In the below Fig. 6.2, where a single main peak is shown for different compositions, where a systematic shift in the peak positions with respect to the parent $CuCr_2Se_4$, reflects change in the unit cell parameters.

Composition	***a (Å)***	***Vol.(Å^3)***	R_{Bragg}	R_f	χ^2
$CuCr_2Se_4$	10.3338 ± 0.0001	1103.53	9.12	6.85	1.35
$CuCr_{1.7}Ti_{0.3}Se_4$	10.3684 ± 0.0001	1114.64	7.44	5.91	1.50
$CuCr_{1.6}Ti_{0.4}Se_4$	10.3789 ± 0.0001	1118.03	11.6	7.85	2.17
$CuCr_{1.5}Ti_{0.5}Se_4$	10.3809 ± 0.0003	1128.67	8.23	6.55	1.29
$CuCr_{1.25}Ti_{0.75}Se_4$	10.4188 ± 0.0003	1130.98	9.72	7.27	2.18
$CuCrTiSe_4$	10.4315 ± 0.0001	1135.11	7.21	6.91	1.34

Table 6.2: Rietveld refined structure parameters for $Cu[Cr_{2-x}Ti_x]Se_4$ $(0 \leq x \leq 1)$

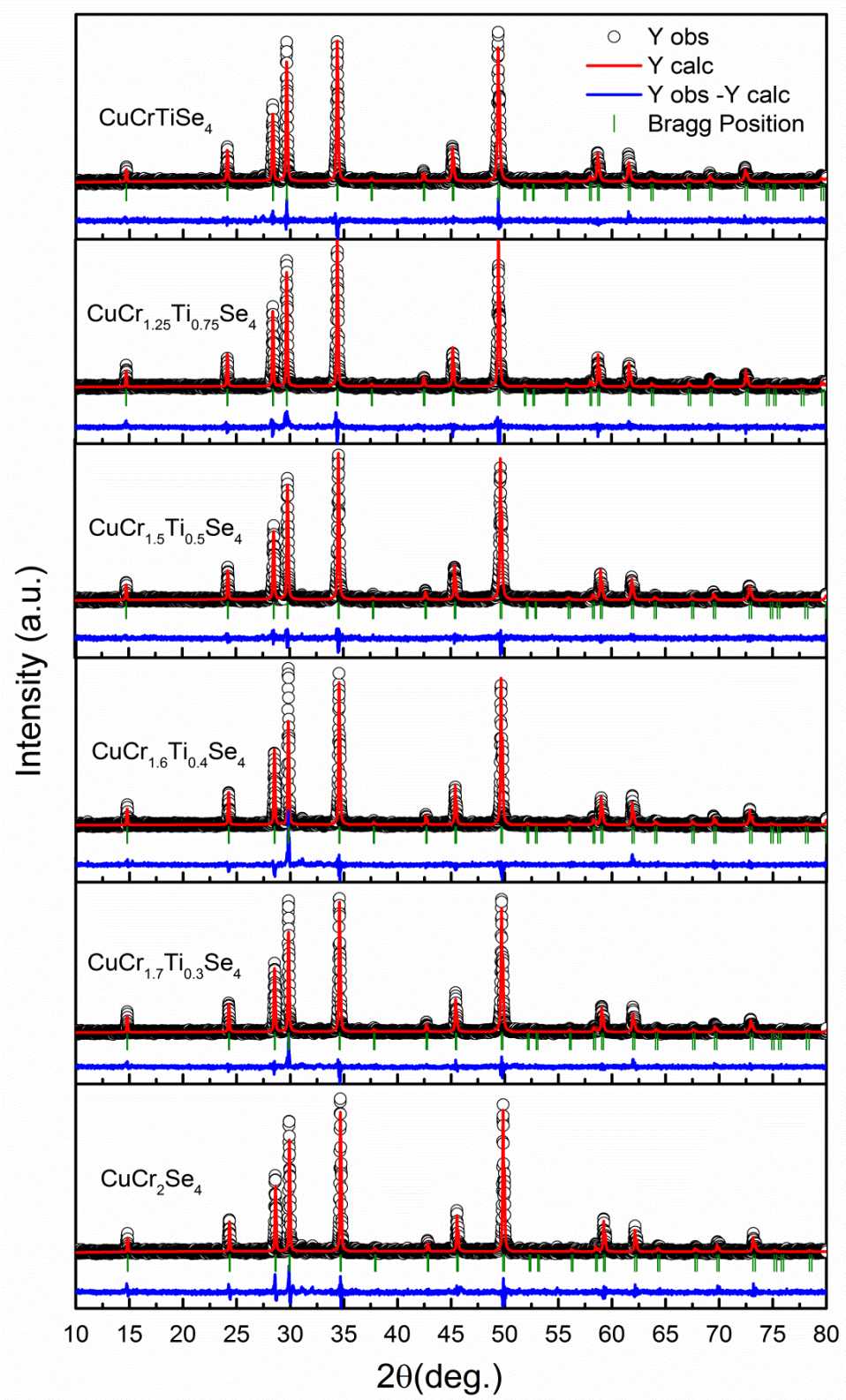

Figure 6.1: Refined XRD patterns of $Cu[Cr_{2-x}Ti_x]Se_4$ ($0 \leq x \leq 1$) at room temperature.

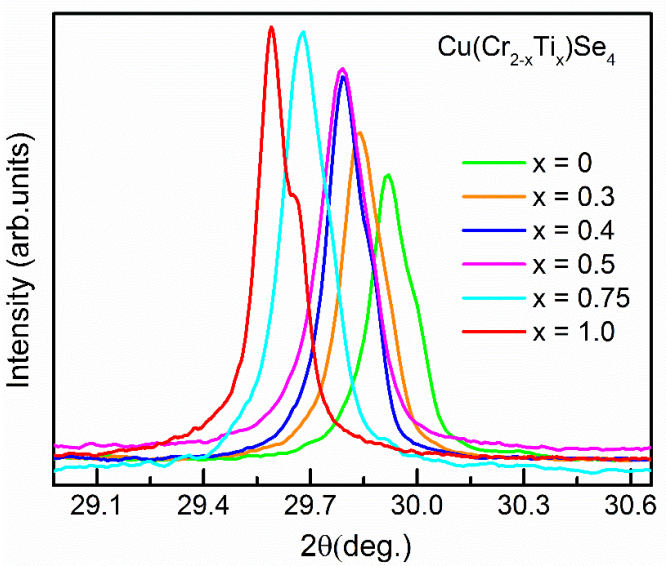

Figure 6.2: Single main peaks of all the Ti substituted $CuCr_2Se_4$ compounds display the shift in *2θ* value with respect to changing Ti content.

6.2.3 XANES Results

XANES analysis gives information related to the valence state of the absorbing atom and on its local atomic environment.

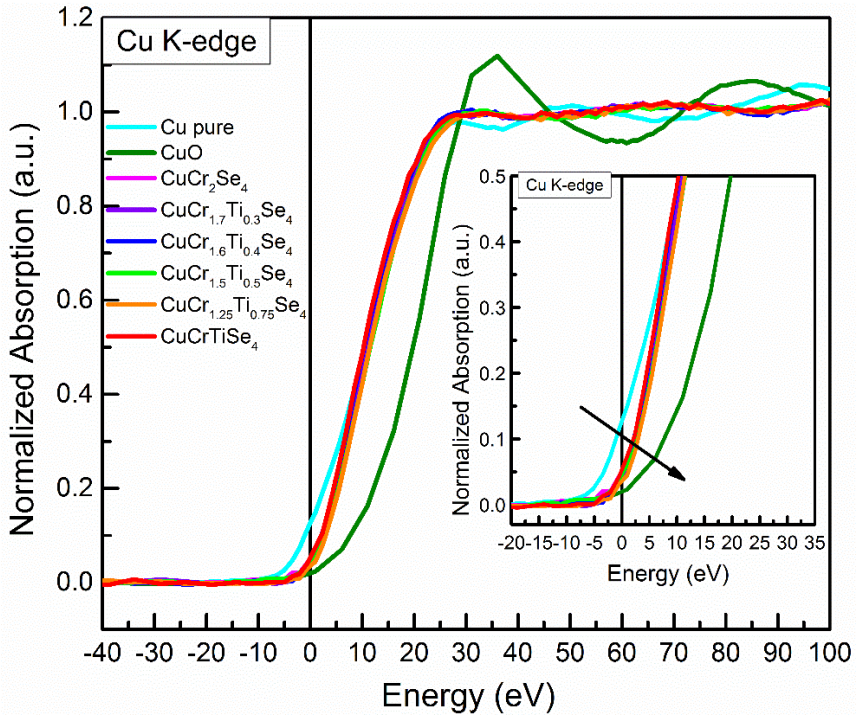

Figure 6.3: Room temperature XANES spectra of $Cu[Cr_{2-x}Ti_x]Se_4$ ($0 \leq x \leq 1$) samples and the standards obtained at Cu K-edge

Fig. 6.3 shows XANES spectra of Cu metal foil, CuO, parent $CuCr_2Se_4$ and $Cu[Cr_{2-x}Ti_x]Se_4$ (x = 0,0.3,0.4,0.5,0.75 and 0.1) samples in the vicinity of the Cu K-edge. As shown by the inset of Fig.6.3, the spectra for all the Ti-substituted samples are shifted to higher energy side as compared to the spectra of Cu metal, which suggests that Cu ions exist in a monovalent state. Fig. 6.4 displays the Cr K-edge XANES spectra of $Cu[Cr_{2-x}Ti_x]Se_4$ samples as compared with Cr metal, Cr_2O_3 and $CuCr_2Se_4$. As the threshold energy of all the Ti-incorporated compounds are higher than that of Cr metal, but close to the energy of $CuCr_2Se_4$ and standard Cr_2O_3 compounds, it is safe to assume that Cr ions exist in mixed valence state.

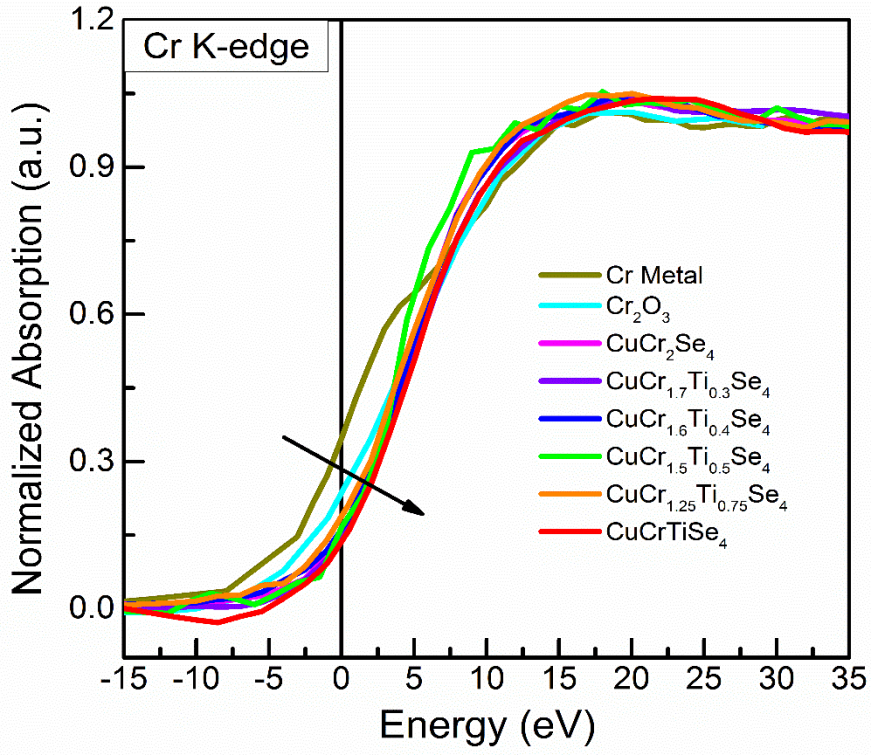

Figure 6.4: Room temperature XANES spectra of $Cu[Cr_{2-x}Ti_x]Se_4$ ($0 \leq x \leq 1$) samples and the standards obtained at Cr K-edge.

6.2.4 XAS Studies

The Cr $L_{2,3}$ XAS spectra of $CuCr_{2-x}Ti_xSe_4$ are displayed in Fig 6.5. All the spectra are split into L_3 and L_2 regions due to the spin-orbit splitting energy of the 2p core hole. Due to crystal field splitting L_3 and L_2 edges are further split into t_{2g} and e_g levels (marked for L_3 edge). From L-edge XAS spectra, we can identify two

dominant peaks in each of the L_3 and L_2 regions, denoted as A, B, and C, D showing very small changes in their position and intensity with increase of Ti substitution respectively.

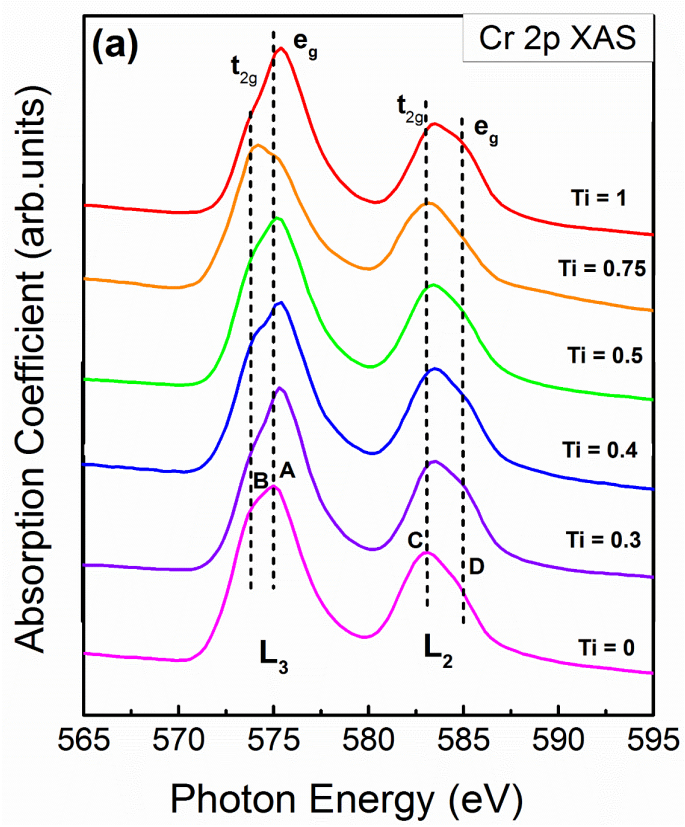

Figure 6.5: (a) Cr $L_{2,3}$-edge XAS spectra of $Cu[Cr_{2-x}Ti_x]Se_4$ ($0 \leq x \leq 1$)

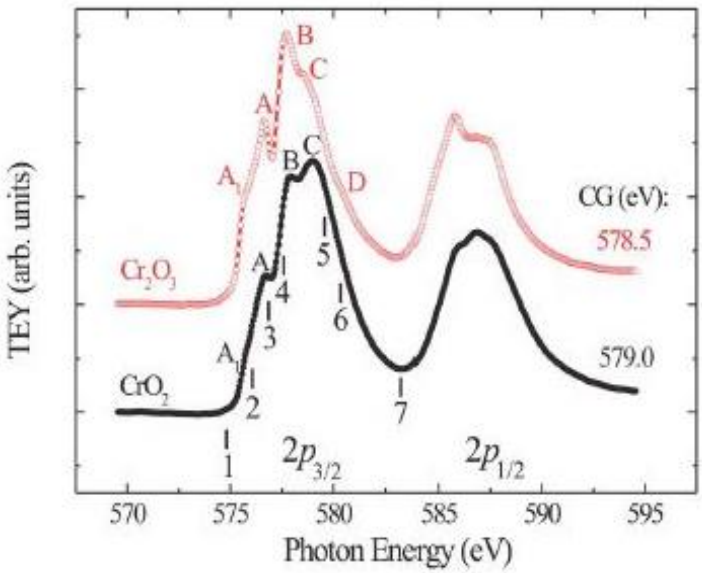

Figure 6.6: Experimental XAS $2p_{3/2,1/2}$ spectra of CrO_2 (solid circles) and Cr_2O_3 (open circles) (Figure taken from Ref. [136]).

As compared to reference of Cr^{4+} and Cr^{3+} standard XAS spectra, one can notice the suppression of t_{2g} feature of L_3 edge. A weaker t_{2g} feature in the L_3 edge of Cr is indicative of less un-occupancy in the t_{2g} state, which is the case for Cr^{4+}. In order to assess the presence of Cr^{3+} and Cr^{4+} cations, we have also referred with the Cr XAS spectra for Cr_2O_3 (Cr^{3+}), CrO_2(Cr^{4+}) from [136] as shown in Fig.6.6 and for comparison. By comparing all the samples with their energy position and relative intensity to the ones of Cr_2O_3 and CrO_2, it is clear that a Cr^{3+} electronic configuration is more suitable representation of our compounds. we compare our data to that of spinel structure $CuCr_2O_4$ known to have a Cr^{3+} electronic configuration [137]. Except for the effects of different spin-orbit splitting due to the Cr ions being in an O octahedra as opposed to Se octahedra, our chalcogenide spinels spectra match very well to that of the oxide spinel. All main peaks at the L_3 edge and the double peak at the L_2 edge reveal that the dominant Cr ions are trivalent and the tetravalent Cr ions are very few. In Lotgering and van Stapele's original model, they proposed mixed valent of Cr ions, i.e. Cr (3+) and Cr (4+), and attributed the strong ferromagnetic metallic property to the double exchange mechanism. However, the original model was modified after many experimental observations supporting the pure trivalent Cr ion [64,138]. In their modified model, Cr ion is all trivalent, Cu ion is still monovalent, and one hole resides on the top part of the chalcogen p orbital valence band.

Fig. 6.7 shows the XAS spectrum measured at the Ti L-edge. The Ti L-edge shows two groups of peaks within the spin orbit split into $2p_{1/2}$ (L_2-edge) and $2p_{3/2}$ levels (L_3-edge). These levels are split by the strong ligand field arising from the surrounding selenium atoms. For $TiSe_6$ octahedra, the Ti 3*d* band is split into two sublevels with t_{2g} and e_g symmetry [139]. From our results, the e_g-like band at about 457 eV and t_{2g} band at 455.2 eV were observed at L_3 edge. Similarly, the e_g-like band at about 460.6 eV and t_{2g} band at 462.5eV were obtained at L_2 edge. Though chalcogenides, unlike oxides, do not show sharp multiplet structure due to their strong covalency, two combined features can be used to determine the valency of Ti ion. One is to see the pre-edge peaks in Ti (IV) spectra, denoted as P at 453 eV in Fig. 6.7. Meanwhile $x = 0.75$ sample displayed the sharp and highly intense L_3–

t_{2g} feature along with L_3–e_g peak broadening. According to the above discussion, we can ascertain that Ti ions are in tetravalent state.

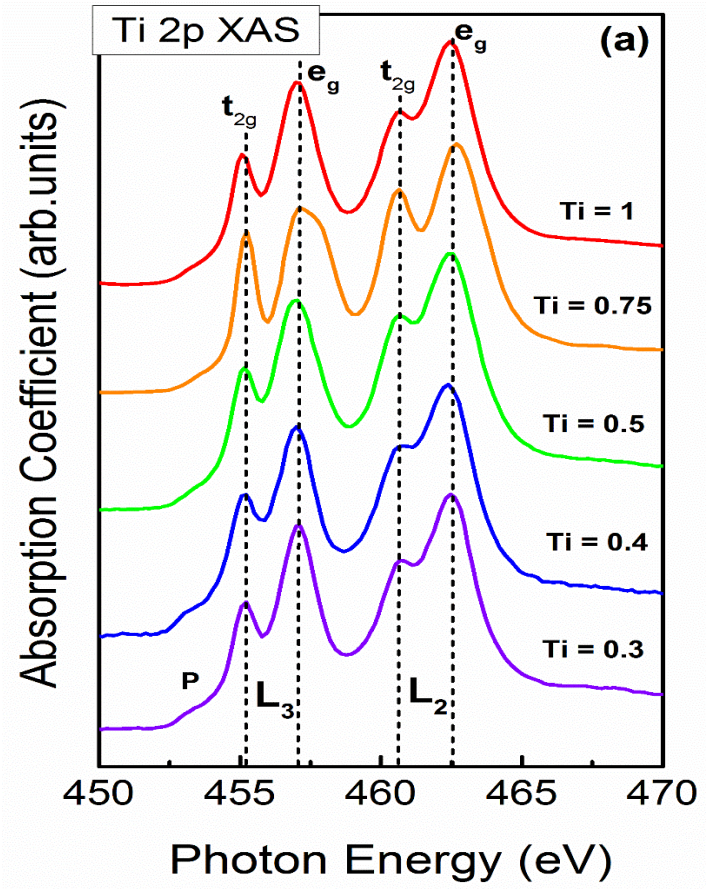

Figure 6.7: Ti $L_{2,3}$-edge XAS spectra of $Cu[Cr_{2-x}Ti_x]Se_4$ ($0 \leq x \leq 1$)

After inspection of Cr and Ti valence state, it is necessary to know about the Cu valency state in the studied compositions. The measured Cu $L_{2,3}$ absorption spectra of the $CuCr_{2-x}Ti_xSe_4$ compounds are presented in Fig. 6.8 (a) and (b) is corresponding to experimental data of typical Cu metal. The parent $CuCr_2Se_4$ displays the spectral shape typical of previous studies [140,141] with a strong peak at 932.6 eV and a broader region of intensity in the range of 935–942 eV with specific features at ~935.6 and ~939.2 eV. We will label these peaks as A(t_{2g}), B and C (e_g), respectively for L_3 edge (see Fig. 6.8). The Cu L_3 spectra for all the Ti-incorporated samples show striking variations in terms of intensity and peak positions. First, there are differences in the intensity of peak A, which changes from a distinct feature to a small shoulder on the peak at higher energy of ~934 eV and

splitting of peak A is noticed in the x = 0.4, 0.75 and 1.0 samples. There is also spotted a clear correlation between the loss of intensity in peak A and a relative increase in peak B. The L_2 structure is broadened and of not much consequence. Splitting of e_g band (B, C peak) at L_3 edge is merged with higher substitution of Ti (x = 0.5,0.75 and 1.0) to produce single peak. The XAS shows that all the samples in this study are apparently Cu (1+). In some of the spectra in Fig. 6.7 (a), a very small peak at 929 eV, characteristic of Cu (2+) compound, is visible and it vanishes with increase of Ti -content. This might be the result of oxidation of the sample at the surface. Comparison of the variation in peak intensities with Ti composition reveals a strong correlation with the number of cation and anion valence electrons available for bonding in these selenospinels. However, growing peak A with the decrease of the Ti concentration raises the question of whether the copper ion in $CuCr_2Se_4$ (x = 0,0.3 and 0.4) should be interpreted as purely monovalent. Further, more studies are required to gain full insight into this issue.

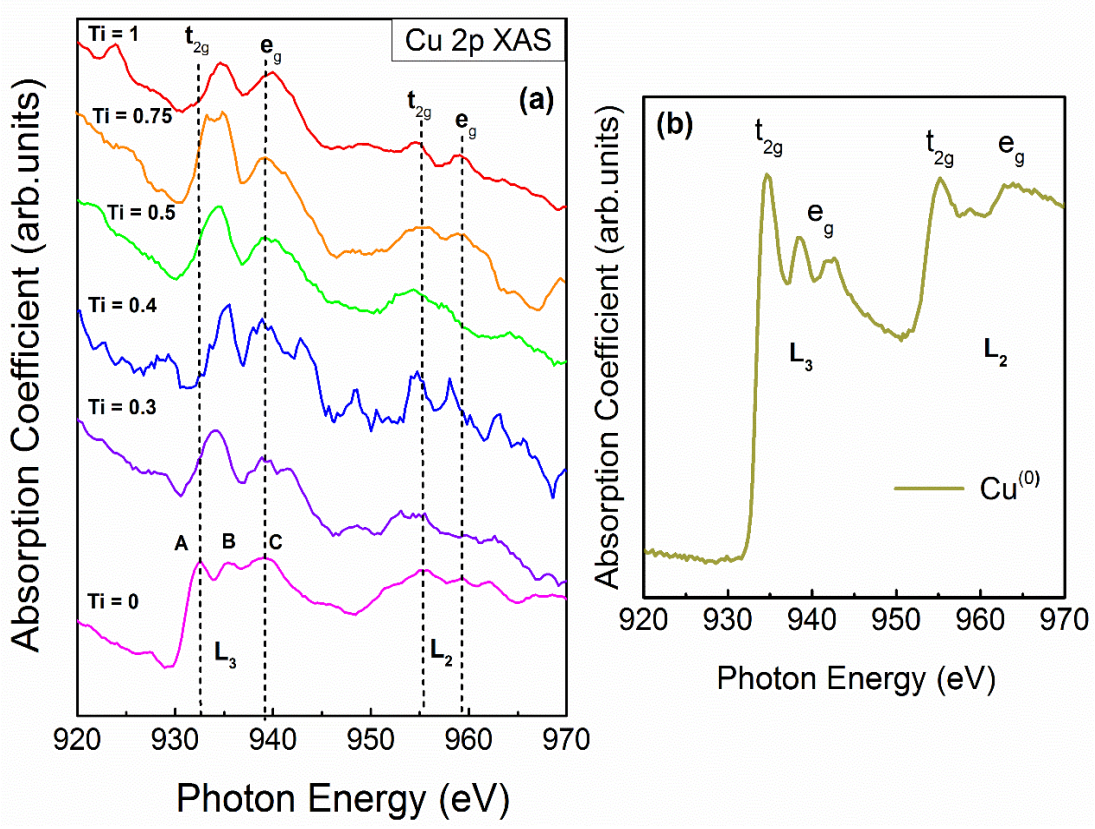

Figure 6.8: (a) Cu $L_{2,3}$-edge XAS spectra of $Cu[Cr_{2-x}Ti_x]Se_4$ ($0 \leq x \leq 1$), (b) Experimental standard Cu $L_{2,3}$-edge XAS spectra of Cu holder.

6.2.5 Magnetic Properties

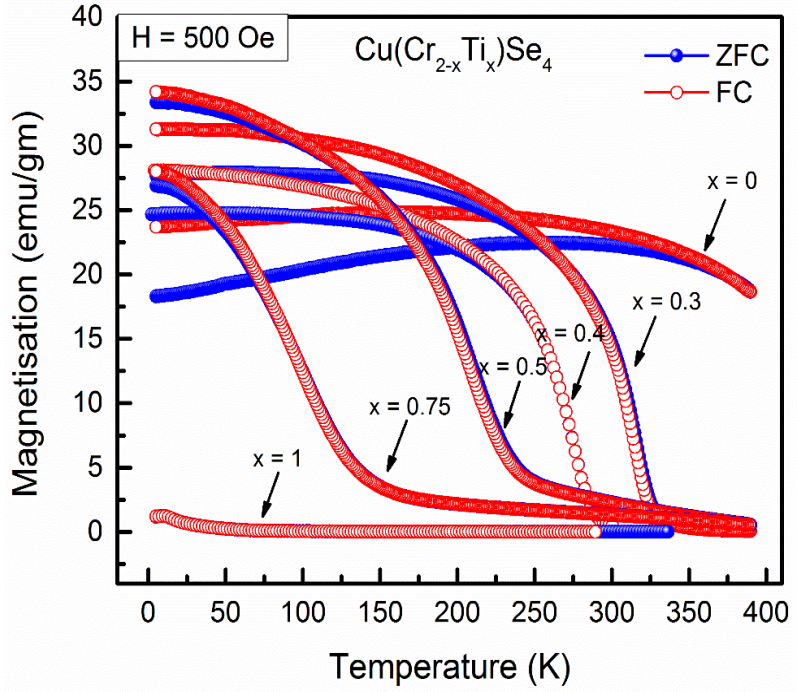

Figure 6.9: ZFC/FC magnetization cycles measured at applied field of 500 Oe for given selenospinels $CuCr_{2-x}Ti_xSe_4$ in the ferromagnetic regime.

The zero-field-cooled (ZFC) and field-cooled (FC) magnetization cycles for $CuCr_{2-x}Ti_xSe_4$ samples (x = 0, 0.3, 0.5, 0.75 and 1.0), performed under magnetic field of 500 Oe, are shown in Fig.6.9. Within the measurement limit of 400 K available to us, we were not able to record the complete transition for some samples. An evident ferromagnetic behavior is observed for all compounds except (x = 1.0), characterized by a high transition temperature T_C and large ZFC and FC ferromagnetic components. A significant bifurcation in ZFC-FC curves even at sizeable applied field of 500 Oe is observed for x = 0.3 and x = 0.4 samples. Given that $CuCr_2Se_4$ has been accepted as a ferrimagnet, so the observed splitting in broad temperature region (below T_C) of ZFC-FC curves only reaffirm the presence of competing magnetic interactions. In the magnetization behavior in x = 0.5, 0.75 and 1.0, both the ZFC and FC cycles were almost superimposed. Curie temperature (T_C) of the compounds calculated by taking the derivative of magnetization vs temperature curves and decreases abruptly with increasing x, going from ~ 430 to

14 K. It can be noticed from Fig. 6.9 that in $CuCr_{1.7}Ti_{0.3}Se_4$ and $CuCr_{1.6}Ti_{0.4}Se_4$ samples, T_C is near room temperature, making these materials very interesting for eventual applications.

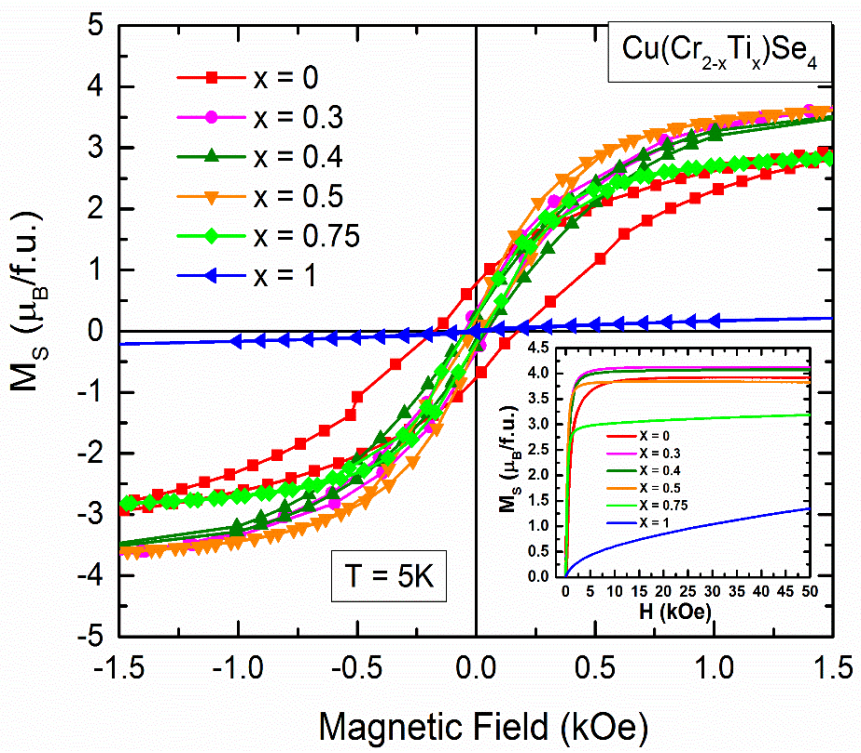

Figure 6.10: Magnetization versus magnetic field registered at 5K for the $CuCr_{2-x}Ti_xSe_4$ ($0 \leq x \leq 1$) Series showing the low field region of the ferromagnetic hysteresis loops and the inset shows, M vs H plot upto 50 kOe.

Fig.6.10 presents the M (H) plots measured at 5 K for all the studied samples. One can see that, hysteresis was observed like the characteristic of soft ferromagnetic type with small coercivity of ± 0.2 kOe for parent $CuCr_2Se_4$ and the coercivity decreases upon Ti^{4+} substitution. As the ionic radii of Ti^{4+} is smaller compared to Cr^{3+}, the substitution of chromium ions by the titanium ions causes both, break in paths of magnetic interactions and the decrease of the distances between the ions. It means that there appears an increase of the ferromagnetic component of the magnetic interactions and the samples reach the magnetic saturation very easily as seen in inset of Fig.6.10. Saturation magnetization changes from M_S = 4.38 to 3.84 μ_B/f.u. with x changing from 0.5 to 0.75, implies a change

in the magnetic regime i.e. $CuCr_{1.25}Ti_{0.75}Se_4$ is at compositional limit of ferromagnetism. $CuCr_1Ti_1Se_4$ allows to identify two main mechanisms of interaction: one due to a ferromagnetic contribution which tends to saturate (M_S = 1.35 μ_B/f.u.) fast with the applied field, and an antiferromagnetic contribution. This type of mixed ferromagnetic and antiferromagnetic behavior in x = 1.0 might be a result of formation of ferromagnetic clusters which interact antiferromagnetically with each other, inducing weak magnetic hysteresis and negligible coercive fields. The interaction between Cr–Se–Cr is ferromagnetic because of 90° super exchange interaction and the interactions between Cr-Cr is antiferromagnetic. These ferro- and antiferromagnetic- competing interactions lead to the spin frustration. Since the antiferromagnetic interactions are not sufficiently strong to compete with the ferromagnetic ones, it is expected that the substitution of Ti weaken gradually the strength of the ferromagnetic interaction with increasing value of x.

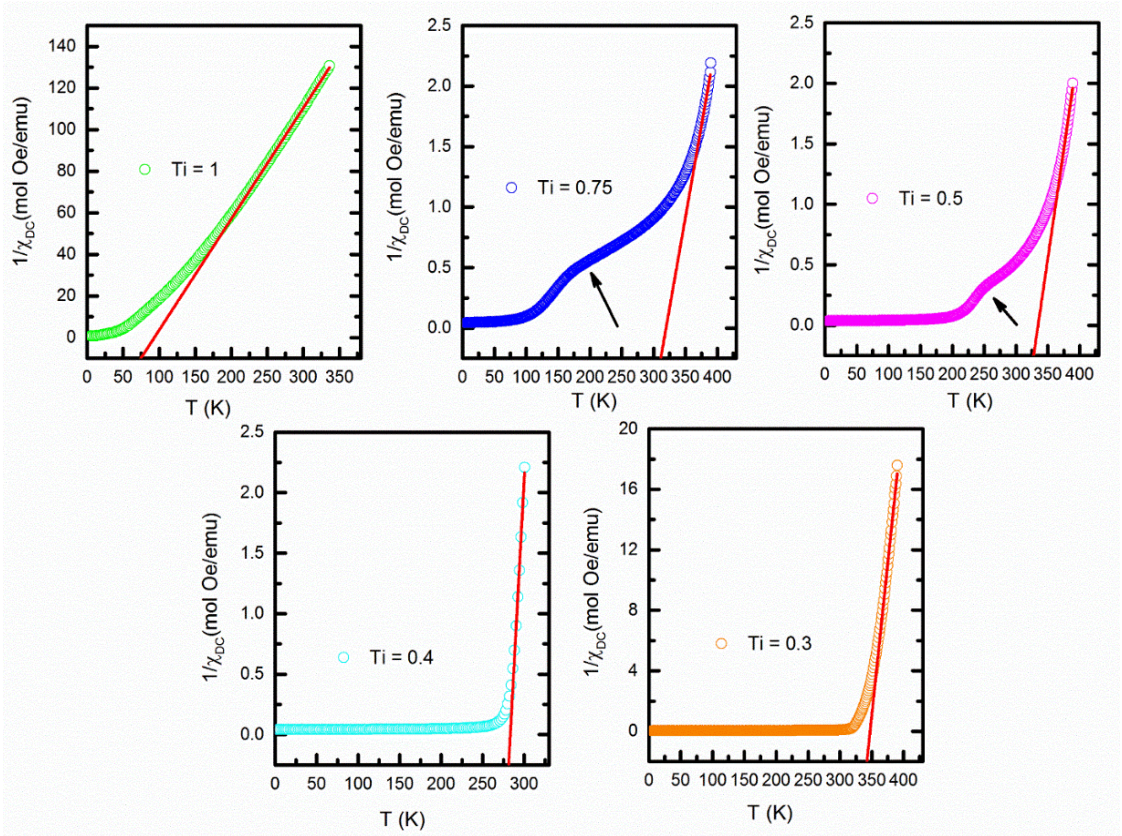

Figure 6.11: The temperature dependence of the inverse dc magnetic susceptibility for $CuCr_{2-x}Ti_xSe_4$ ($0 \leq x \leq 1$) and the solid (red) line is the fit to Curie Weiss law.

Figure 6.11 includes the inverse *dc* susceptibility plotted as function of temperature. one can be noticed that magnetic susceptibility behavior just above T_C shows unusual behavior for the samples of x = 0.5 and 0.75 as compared to other samples. Moreover, the range of temperature over which the Curie-Weiss law can be fitted, keeps decreasing. These observations are indication of short range magnetic interactions being present much over T_C. $CuCrTiSe_4$ compound, shows absence of double exchange interaction with antiferromagnetic coupling between Cr ions being the dominant interaction. Thus, non-magnetic Ti substitution reduces long range ferromagnetic ordering and increases some short range magnetic ordering, the downturn in inverse susceptibility as a function of temperature above T_C can be considered with in the realms of Griffiths singularity [142]. Griffiths phase, which neither exhibits pure paramagnetic (PM) behaviour nor long-range ferromagnetic ordering.

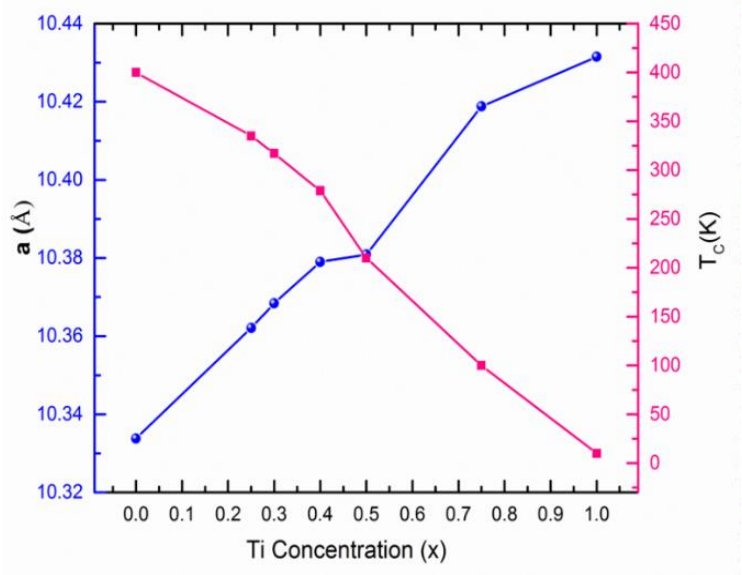

Figure 6.12: Curie temperature and lattice parameter vs. Ti concentration.

The above-mentioned results suggest that nonmagnetic titanium ions significantly influence on the lattice constants and magnetic ordering temperatures as shown in Fig.6.12. All the obtained magnetic parameters are given in Tab.6.3.

Composition	T_C *(K)*	M_S *(μ_B/f.u.)*	θ_P *(K)*	μ_{eff}^{Cal} *(μ_B)*
$CuCr_2Se_4$ [ref]	416	4.76	436	4.76
$CuCr_{1.7}Ti_{0.3}Se_4$	317	4.13	342	4.47
$CuCr_{1.6}Ti_{0.4}Se_4$	278	4.08	281	7.96
$CuCr_{1.5}Ti_{0.5}Se_4$	208	3.84	-	-
$CuCr_{1.25}Ti_{0.75}Se_4$	101	3.19	-	-
$CuCrTiSe_4$	14	1.35	74	3.87

Table 6.3: Magnetic parameters for $CuCr_{2-x}Ti_xSe_4$ ($0 \leq x \leq 1$).

6.2.6 Transport Properties

Fig. 6.13 shows the temperature dependence of the electrical resistance (R/R_{300K}) of the series $CuCr_{2-x}Ti_xSe_4$ (x = 0, 0.3, 0.4, 0.5, 0.75 and 1.0) in the temperature range from 5 K to 400 K. The resistance curve displays metallic behavior for all the Ti substituted compositions except x = 0.4, where the resistance value increases dramatically and the (R/R_{300K}) vs T curve changes from metallic to semiconducting-type. A distinct change in slope is seen at temperatures coinciding with the magnetic ordering temperatures (T_C), as indicated with an arrow in Fig. 6.13. In case of $CuCr_{2-x}Ti_xSe_4$ series, the metallic conduction takes place due to the strong hybridization between the ligand non-bonding *p* orbital of the selenium atoms and holes induced by Cu^+ ions. We observe enhancement in resistance values with Ti substitution because the concentration of these holes is suppressed due to the Ti^{4+} substituting Cr^{3+} ions. This argument is substantiated by the increasing residual resistance as x changes from 0 to 0.3. The x = 0.4 concentration shows maximum depletion of charge carriers and the resistance behavior shows negative temperature coefficient of resistance. Surprisingly, with further increase in Ti concentration to x = 0.5, the resistance behavior changes back to metallic and continues to remain so with x changing to 0.75 and then to x = 1. In fact, x = 0.5 composition displays minimum residual resistance ratio in comparison to all other compositions in the series. To understand such change in temperature dependence of resistance with Ti concentration, a detailed study of the electronic structure of

these materials becomes important. However, such study was beyond the scope of the present work and hence not undertaken.

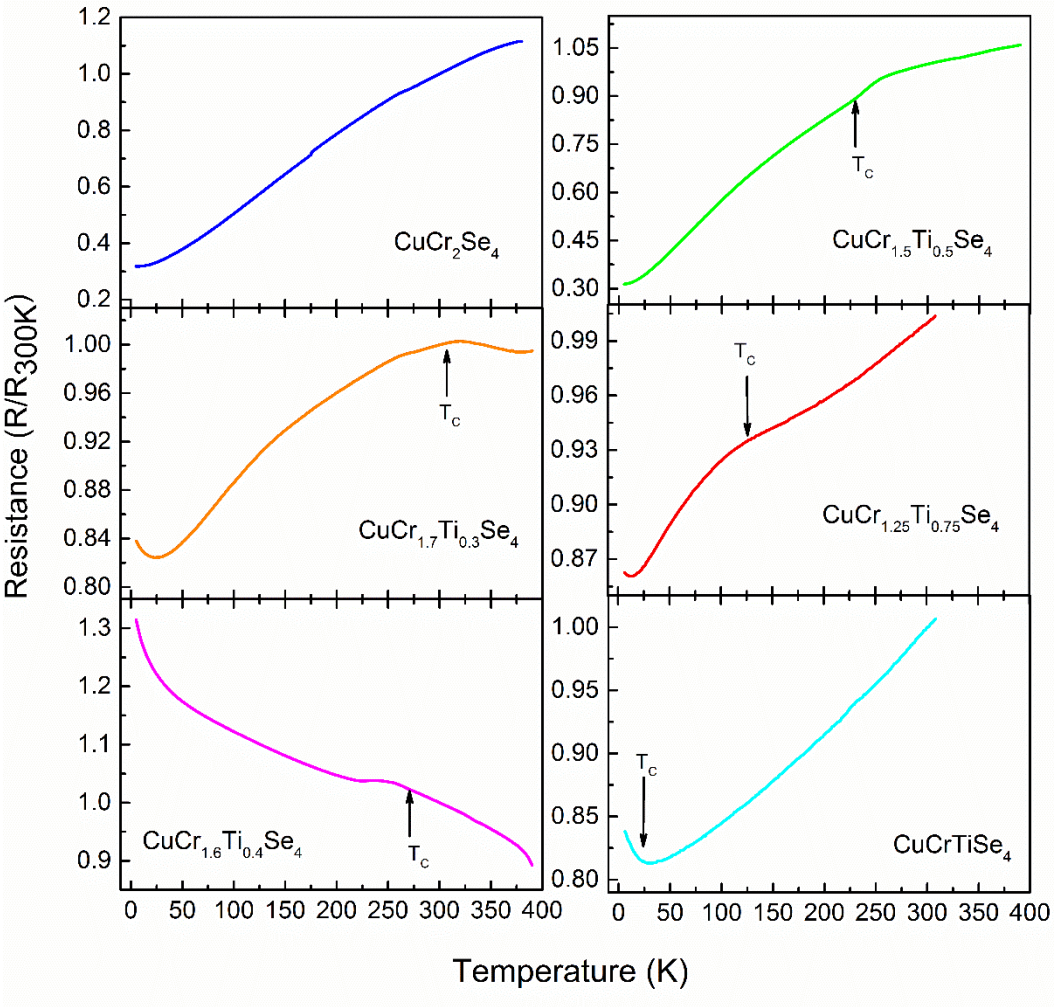

Figure 6.13: Zero-field electrical resistance (R/R_{300K}) of $CuCr_{2-x}Ti_xSe_4$ ($0 \leq x \leq 1$) series in different temperature regimes and the arrows present the corresponding T_c.

We now discuss the upturns in the resistance curve of x = 0.3,0.75 and 1.0 compounds at temperatures below ~20 K. Such behavior is widely observed in disordered electronic systems close to the metal insulator transition (MIT) (the manganites are a perfect example [143]) and it is due to weak localization or electron–electron interaction effects. Further, the temperature region between 60 K to T_C of all the Ti-substituted compositions (except x = 0.4) can be described

well with the electron-phonon as the dominant scattering mechanism. The electron-electron interactions gradually start to weaken in this region but magnon interactions are quite sizeable, giving rise to spin-polarized metallic conduction with respect to increase in temperature.

For the x = 0.4 composition, the regime below T_C, can be described by Mott's expression for variable-range hopping conduction. It may be noted that in the same temperature regime this composition shows a ferromagnetic response. Generally, ferromagnetism correlates well with the metallic conductivity in these spinels. It can be argued that the Ti ions (spin defects) located in the octahedral sites of the spinel structure cause the lowering of the Fermi level in the lowest Cr^{3+} Mott-Hubbard sub-band of $3d^3\ t_{2g}$ partly filled band allowing a collective electron behavior and causing a semiconductivity type behavior with conduction through hopping process that involves transfer of electrons from Cr^{3+} to Cr^{4+}.

6.3 Summary

With an aim to understand the effect of doping at Cr-site by a non-magnetic ion, we carried out investigation of magnetic, electrical and crystal structure properties of polycrystalline $Cu[Cr_{2-x}Ti_x]Se_4$ spinel with x = 0, 0.3, 0.4, 0.5, 0.75 and 1.0 respectively. The gradual increase of Ti substitution at Cr-site in $CuCr_2Se_4$ causes progressive increase in lattice parameters. The predominant ferromagnetic state appears in the range of $0 < x < 0.75$. A strong spin glass type of state is observed in $CuCrTiSe_4$ at 14 K as a result of competing ferromagnetic and antiferromagnetic inteactions. A systematic decrease in the saturation magnetization value measured at 5 K is also seen with increasing Ti content. XANES recorded at Cu and Cr K-edges suggests monovalent Cu^+ and Cr^{3+} states. All the Ti-substituted compositions fall on metallic regime, whereas x = 0.4 composition shows semiconducting type behaviour described by Mott's expression for variable-range hopping conduction. Meanwhile, ferromagnetic spinels (x = 0.3, 0.75 and 1.0) exhibit an anomalous high temperature dependence and an upturn below 20 K, suggests these spinels rather than being conventional metal are in fact tending towards itinerant behaviour at high temperatures to a half-metallic-like behaviour at low temperatures.

Chapter 7

Unusual Magnetic and Transport Behavior in Cd and Zn-Substituted $CuCr_2Se_4$

7.1. Overview

Suitable doping at tetrahedral sites in $CdCr_2S_4$, $HgCr_2S_4$, $CuCr_2Se_4$ and $ZnCr_2Se_4$ display unusual time dependent ferroelectric, colossal magnetocapacitance, dissipation less anomalous Hall current and colossal magnetoresistance properties [7,144-146]. Recent results on $Cd_xCu_{1-x}Cr_2S_4$ and $Cd_xCu_{1-x}Cr_2Se_4$ predict that their properties can be tuned from ferromagnetic metal/ semiconductor to half-metal by changing the concentration of cadmium [68]. All these observations have provoked strong interest in these materials for possible spintronic applications.

$CdCr_2Se_4$ orders magnetically below 130 K [6] and $CuCr_2Se_4$ displays a very high T_C ~ 430 K [58]. It is expected that replacing some Cd ions with Cu, will help increase the T_C towards room temperature values with unusual magneto-transport properties. $ZnCr_2Se_4$ is an electrical semiconductor with magnetic a magnetic spiral structure and its paramagnetic Curie–Weiss temperature θ_P is 115 K [69]. It shows a spontaneous helical spin ordering below T_N = 20 K [69]. Due to the positive value of θ_P, the nearest neighbor exchange interaction can be considered to be a ferromagnetic one. Magnetic properties of this compound may be appreciably altered by a cationic substitution of Cu at Zn site.

Hence, we have prepared samples of compositions: $Cd_{0.9}Cu_{0.1}Cr_2Se_4$, $Zn_{0.9}Cu_{0.1}Cr_2Se_4$ and $Zn_{0.1}Cu_{0.9}Cr_2Se_4$ with respect to their parent compounds. Further, these chalcospinels have been investigated by means of x-ray diffraction, XANES studies, various magnetic measurement techniques and transport properties. The correlation between structural, magnetic and transport properties are very prominent through EXAFS analysis. Introducing small amount of Cu^+ at Cd/Zn site not only causes the formation of multiple valences of Cr ions (Cr^{3+}/ Cr^{4+}) at octahedral sites, also reduces Cr-Se distance considerably. The magnetic ground state thus becomes quite rich and competing magnetic interactions results

as evidenced from inverse dc susceptibility curve above T_c. The electronic transport behavior follows Mott variable range hopping process.

7.2. Results and Discussion

7.2.1 Compositional Analysis

All the polycrystalline samples of $Cd_{0.9}Cu_{0.1}Cr_2Se_4$, $Zn_{0.9}Cu_{0.1}Cr_2Se_4$ and $Zn_{0.1}Cu_{0.9}Cr_2Se_4$ were prepared by solid-state synthesis method as described in chapter 2. The ratio of elemental compositions of cadmium (Cd), copper (Cu), chromium (Cr), zinc (Zn) and selenium (Se) as obtained from EDX, are presented in Tab. 7.1. These numbers match well with the ratio of starting compositions; hence it is justified to assume that the stoichiometry of starting composition is maintained in the final compounds.

Chemical	**Atomic percentage (error ~ ± 3%)**				
Composition	**Cd**	**Zn**	**Cu**	**Cr**	**Se**
$Cd_{0.9}Cu_{0.1}Cr_2Se_4$	14.40	-	1.56	27.68	56.68
$Zn_{0.9}Cu_{0.1}Cr_2Se_4$	-	15.05	1.48	28.24	55.93
$Zn_{0.1}Cu_{0.9}Cr_2Se_4$	-	1.51	14.69	28.15	56.52

Table 7.1: Elemental ratio obtained by EDX for $Cd_{0.9}Cu_{0.1}Cr_2Se_4$, $Zn_{0.9}Cu_{0.1}Cr_2Se_4$ and $Zn_{0.1}Cu_{0.9}Cr_2Se_4$.

7.2.2 Crystal Structure by XRD

The Reitveld refined room temperature XRD patterns for parent $CdCr_2Se_4$ and $CuCr_2Se_4$ have already been discussed in chapter 3 and 5. Here we present the XRD profiles for $Cd_{0.9}Cu_{0.1}Cr_2Se_4$, $Zn_{0.9}Cu_{0.1}Cr_2Se_4$ and $Zn_{0.1}Cu_{0.9}Cr_2Se_4$ compounds in Fig. 7.1 and Fig. 7.2 respectively. All the observed peaks could be indexed to a face centered cubic cell, space group *Fd3m*. Rietveld refinement was carried out for such a normal spinel with substituted Cu atoms at the Cd/Zn-site and refining the thermal displacement parameters and site occupancy factors for both Cd-site and Cr-site. In case of $Cd_{1-x}Cu_xCr_2Se_4$ (x = 0, 0.1, 1.0) and $Zn_{1-x}Cu_xCr_2Se_4$ (x = 0.1, 0.9) compounds, Cd and Zn ions are in stable 2+ state, but the valence state of Cu ion

is controversial. Since the ionic radius of Cd^{2+} ions (0.78 Å) are much bigger as compared to both Cu^{2+} and Cu^{+} ions (0.6 Å and 0.57 Å), the lattice constant (a) should decrease in case of $Cd_{0.9}Cu_{0.1}Cr_2Se_4$. But in case of $Zn_{1-x}Cu_xCr_2Se_4$ composition, the ionic radius of Zn^{2+} ions (0.60 Å) is same as Cu^{+}(0.60 Å) ions and little higher as compared to Cu^{2+} ions (0.57 Å). So, in that case 'a' should not get much affected when Cu^{+} ions are substituted by Zn^{2+}, whereas 'a' should decrease in case of Cu^{2+} substitution. Referring to the experimentally observed parameters listed in Tab. 7.2, the lattice constants decreases in both the case of $Cd_{1-x}Cu_xCr_2Se_4$ and $Zn_{1-x}Cu_xCr_2Se_4$ compounds as compared to the previously reported parent compound $CdCr_2Se_4$ and $ZnCr_2Se_4$ [147] respectively.

Composition	*a (Å)*	R_{Bragg}	R_f	χ^2
$CdCr_2Se_4$	10.7444 ± 0.0001	7.01	5.09	1.80
$Cd_{0.9}Cu_{0.1}Cr_2Se_4$	10.7375 ± 0.0002	9.02	6.50	1.52
$ZnCr_2Se_4$ [9]	10.4940	-	-	-
$Zn_{0.9}Cu_{0.1}Cr_2Se_4$	10.4814 ± 0.0003	8.23	6.55	1.29
$Zn_{0.1}Cu_{0.9}Cr_2Se_4$	10.3414 ± 0.0003	9.72	7.27	2.18
$CuCr_2Se_4$	10.3338 ± 0.0001	9.12	6.85	1.35

Table 7.2: Rietveld refined structure parameters for $CdCr_2Se_4$, $Cd_{0.9}Cu_{0.1}Cr_2Se_4$, $Zn_{0.9}Cu_{0.1}Cr_2Se_4$, $Zn_{0.1}Cu_{0.9}Cr_2Se_4$ and $CuCr_2Se_4$ respectively.

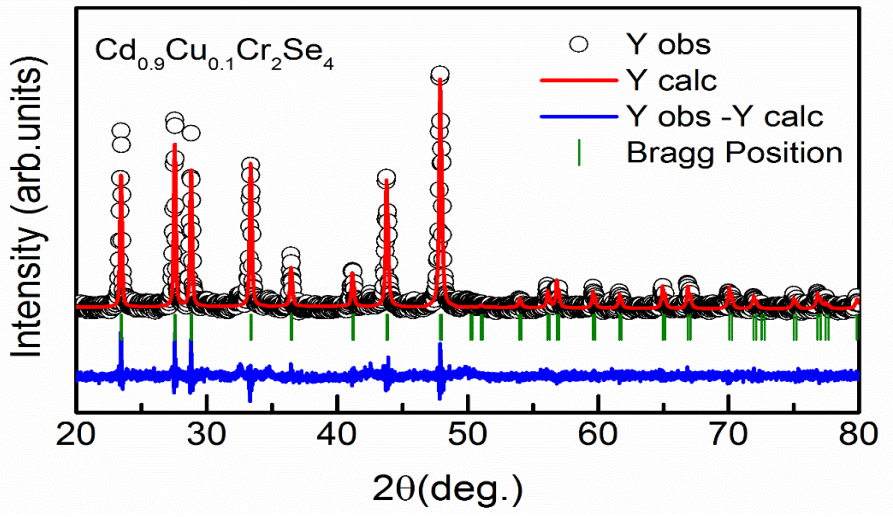

Figure 7.1: Rietveld refinement fit of the powder XRD pattern recorded at room temperature for $Cd_{0.9}Cu_{0.1}Cr_2Se_4$.

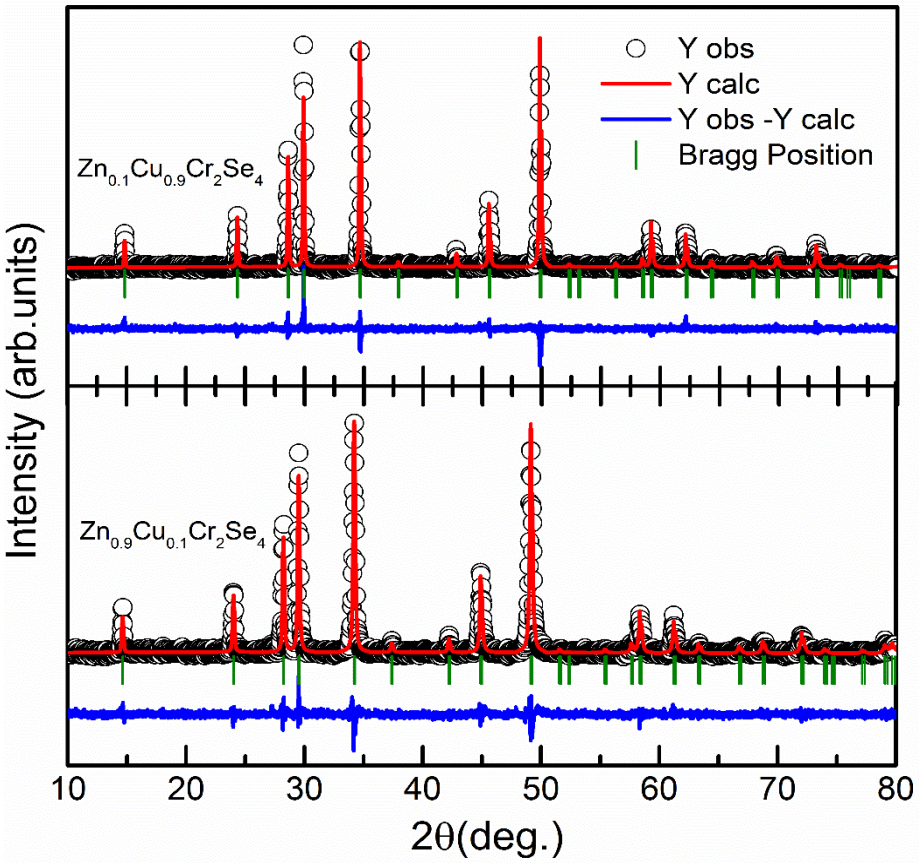

Figure 7.2: Rietveld refinement fit of the powder XRD pattern recorded at room temperature for $Zn_{1-x}Cu_xCr_2Se_4$ (x = 0.1 and 0.9).

7.2.3 XANES Results

It is important to explore the exact valence state of Cu and Cr ions to bring out the clarification about the obtained structural and magnetic properties. Fig. 7.3 shows XANES spectra of Cu metal foil, CuO, parent $CuCr_2Se_4$, $Cd_{0.9}Cu_{0.1}Cr_2Se_4$ (x = 0, 0.1 ,1.0) and $Zn_{1-x}Cu_xCr_2Se_4$ (x = 0.1, 0.9) samples in the vicinity of the Cu K-edge. As shown by the arrow from the given Fig.7.3, the spectra for all the substituted samples are nearly similar to the spectra obtained for the $CuCr_2Se_4$ standard, also shifted to higher energy side as compared to the spectra of Cu metal, which suggests that Cu ions exist in a monovalent state. Fig. 7.4 displays the Cr K-edge XANES spectra of $Cd_{1-x}Cu_xCr_2Se_4$ (x = 0, 0.1 ,1.0) and $Zn_{1-x}Cu_xCr_2Se_4$ (x = 0.1, 0.9) compounds as compared with Cr metal and Cr_2O_3, indicating the presence of mix valence state of Cr^{3+}/Cr^{4+} ions as the threshold energy of all the Cu

incorporated compounds are higher than that of Cr metal, but close to the energy of $CuCr_2Se_4$ and standard Cr_2O_3 compounds.

In Cr – based spinel compounds like $CdCr_2Se_4$ or $ZnCr_2Se_4$, the stability of Cd^{2+}/Zn^{2+} valence state allows Cr ion to be present in $3d^3$ configuration. The octahedral site occupancy of Cr leads to lifting of degeneracy of the *d* orbitals such that the electrons redistribute in the low energy t_{2g} orbitals with quenched orbital degeneracy and negligible spin-orbit interaction [110]. Superexchange, double exchange and complex ferromagnetic (FM) and antiferromagnetic(AFM) interactions mainly present in $CdCr_2Se_4$, $CuCr_2Se_4$ and $ZnCr_2Se_4$ compounds respectively, can be easily understood by considering a mixed valence configuration of Cr ions that develops upon Cu substitution at Cd/Zn site. In order to maintain the overall charge balance in the compositions. It was conjectured that, since partial replacement of Cd^{2+}/ Zn^{2+} takes place by Cu ions in its 1+ state, it causes an equivalent quantity of Cr^{4+} to appear at Cr^{3+}site.

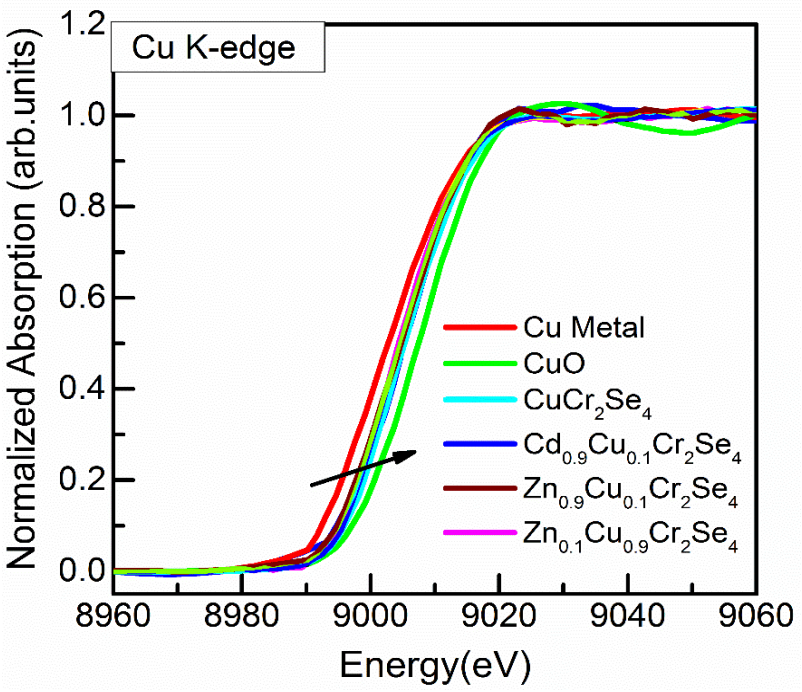

Figure 7.3: Cu K-edge XANES spectra for $Cd_{1-x}Cu_xCr_2Se_4$ (x = 0.1 and 1.0), $Zn_{1-x}Cu_xCr_2Se_4$ (x = 0.1, 0.9) series and the standards. The spectra have been displayed with some y-offset for better clarity.

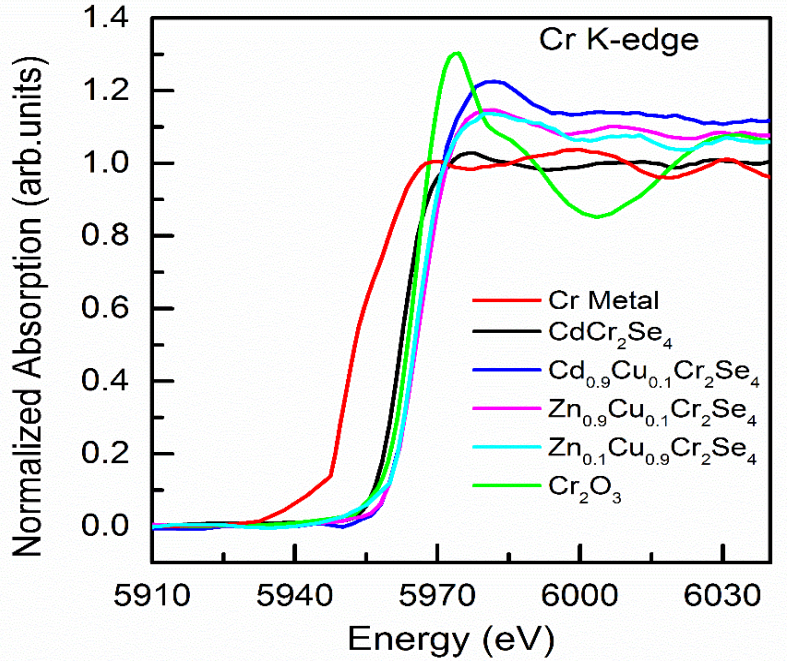

Figure 7.4: Cr K-edge XANES spectra for $Cd_{1-x}Cu_xCr_2Se_4$ (x = 0 and 0.1), $Zn_{1-x}Cu_xCr_2Se_4$ (x = 0.1, 0.9) series and the standards. The spectra have been displayed with some y-offset for better clarity.

7.2.4 Magnetic Properties

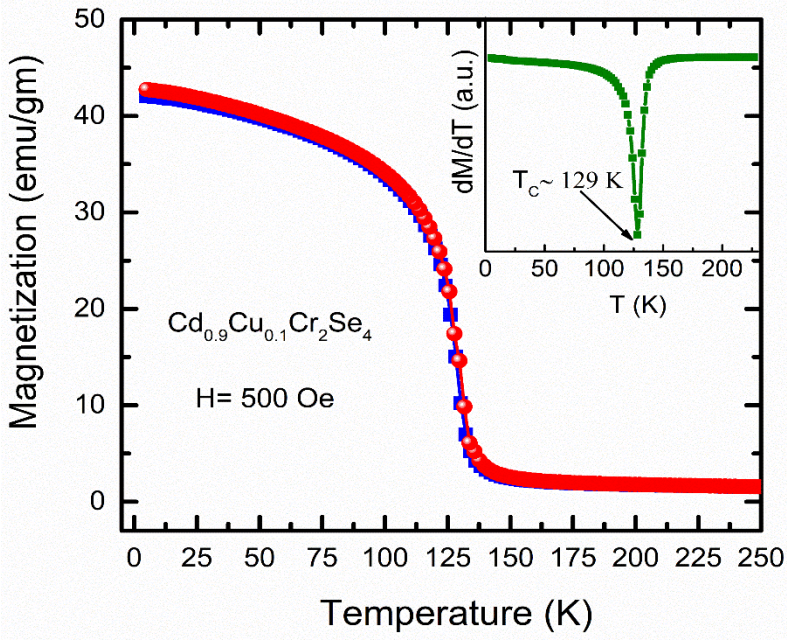

Figure 7.5: *M(T)* plots measured in the ZFC–FC mode under an applied field of 500 Oe for $Cd_{0.9}Cu_{0.1}Cr_2Se_4$. Inset shows the derivative plot of the *M(T)* Curve and the arrow indicates the exact value of T_C.

The temperature-dependent and field-dependent magnetization for the $Cd_{0.9}Cu_{0.1}Cr_2Se_4$ is presented in Fig. 7.5 and 7.6. The sharp rise in *M(T)* below the critical temperature of T_C ~130 K is seen. The magnetic moment ($M_S(\mu_B/f.u.)$) obtained from the saturation magnetization value of *M(H)* recorded at 5 K (see Fig. 7.6) is 5.93 μ_B/f.u. As shown in the Fig.7.6, coercivity increases with Cu substitution.

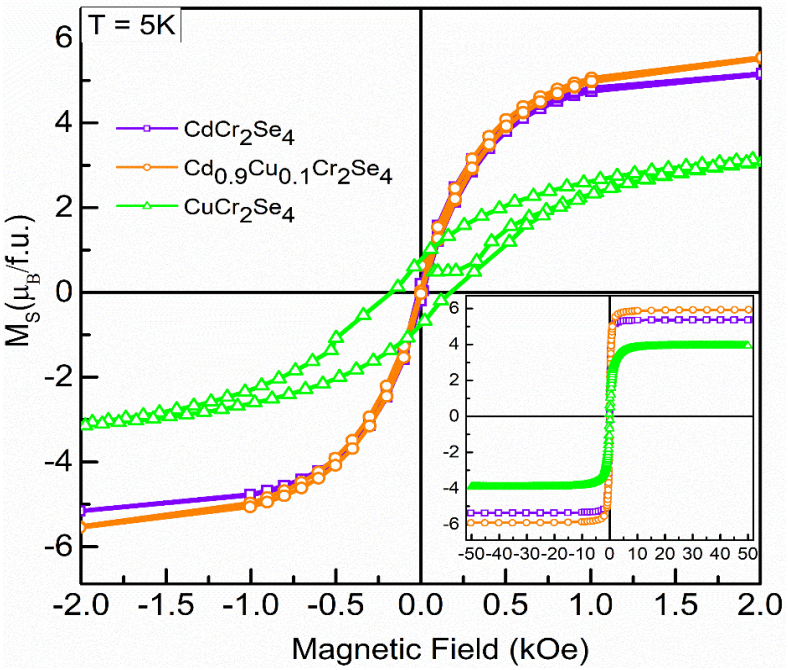

Figure 7.6: Main panel is shown on the expanded scale of magnetization as a function of field with maximum applied field upto ± 2 kOe and temperature of 5 K for clarity in coercivity. Inset shows the entire plots of *M(H)*.

Chemical Composition	***T_C (K)***	**$M_S(\mu_B/f.u.)$**	***θ (K)***	***$\mu_{eff}^{cal}(\mu_B)$***
$CdCr_2Se_4$	130	5.38	158	6.47
$Cd_{0.9}Cu_{0.1}Cr_2Se_4$	129	5.92	-	-
$ZnCr_2Se_4$ [7]	22 (T_N)	5.74	115	5.47
$Zn_{0.9}Cu_{0.1}Cr_2Se_4$	20 (T_N), ~180	4.92	-	-
$Zn_{0.1}Cu_{0.9}Cr_2Se_4$	390	4.90	-	-
$CuCr_2Se_4$	~430	3.92	-	-

Table 7.3: Magnetic ordering temperature (T_C), saturation magnetic moment, Curie temperature θ, and paramagnetic moment calculated from Curie constant *C*, for $Cd_{1-x}Cu_xCr_2Se_4$ (x = 0.1 and 1.0) and $Zn_{1-x}Cu_xCr_2Se_4$ (x = 0.1, 0.9).

Similarly, the *M(T)* curves for $Zn_{0.9}Cu_{0.1}Cr_2Se_4$ and $Zn_{0.1}Cu_{0.9}Cr_2Se_4$ compositions show interesting complex FM and AFM as depicted in Fig. 7.7 and Fig. 7.8 respectively. Insets of both figures show the magnetic field dependent saturation magnetic moment, the corresponding T_C and $M_S(\mu_B/f.u)$ values are listed in Tab. 7.3. Fig. 7.9 displays the inverse dc susceptibility plotted as a function of temperature for $Cd_{0.9}Cu_{0.1}Cr_2Se_4$. The inverse dc susceptibility response is not Curie-Weiss-like, but is dominated by $\chi^{-1}(T) \propto (T - T_C)^P$, Where '*P*' is the exponent characterizing strength of phase and found to be 0.21 ± 0.03. For $Zn_{0.9}Cu_{0.1}Cr_2Se_4$ and $Zn_{0.1}Cu_{0.9}Cr_2Se_4$ compositions, we are unable to fit high temperature paramagnetic region due to measurement temperature limit. The magnetic moments calculated from the saturation magnetization obtained from *M(H)* plots for all the samples under study are measured at 5 K and depicted in Fig. 7.6 to Fig.7.8.

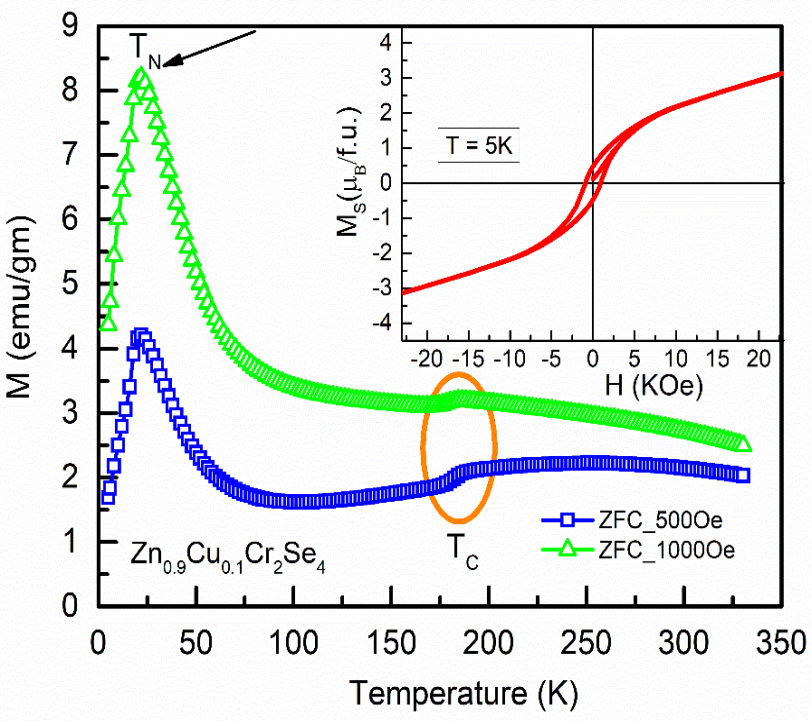

Figure 7.7: *M(T)* plots measured in the ZFC mode under an applied field of 500 Oe and 1000 Oe for $Zn_{0.9}Cu_{0.1}Cr_2Se_4$. Inset shows the plot of the *M(H)* at 5 K. T_N and T_C have been labeled in the figure.

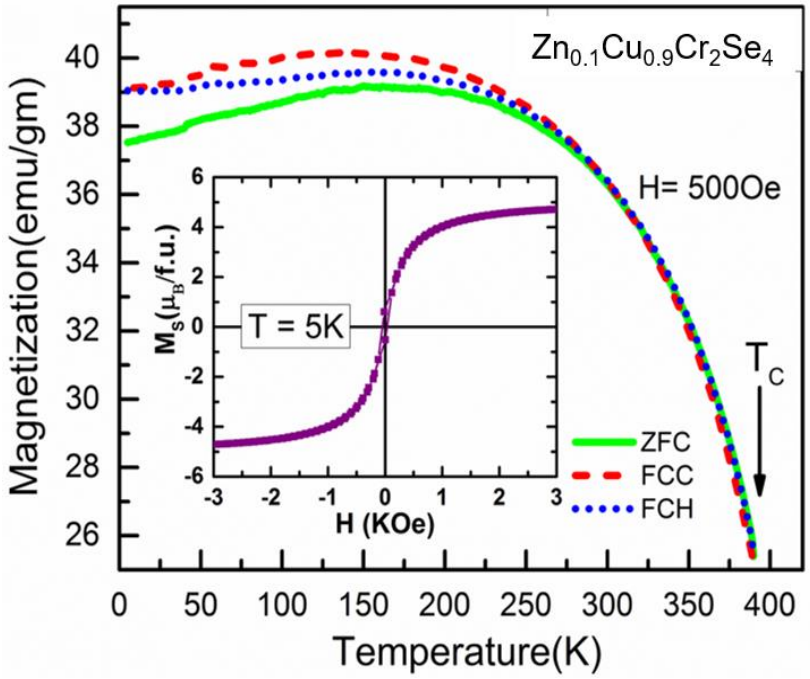

Figure 7.8: *M(T)* plots measured in the ZFC–FC mode under an applied field of 500 Oe for $Zn_{0.1}Cu_{0.9}Cr_2Se_4$. Inset shows the plot of the *M(H)* Curve at 5 K and the arrow indicates the T_C.

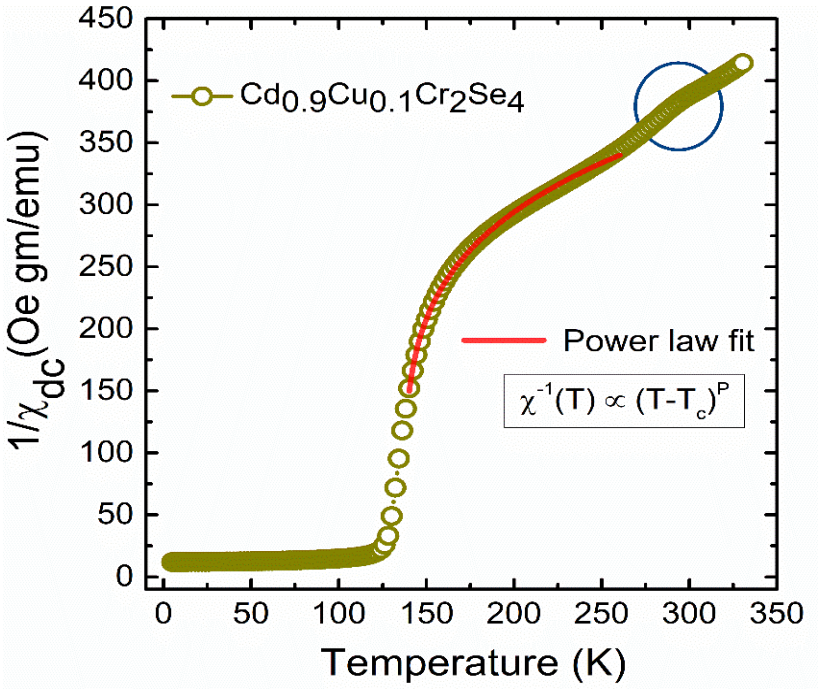

Figure 7.9: Inverse dc magnetization for $Cd_{0.9}Cu_{0.1}Cr_2Se_4$. The solid lines are the fit to power law.

Although substitution is carried out at the non-magnetic Cd and Zn site, altering the composition of parent compound is seen to impact its magnetic properties. Generally, the underlying complexities in magnetic ordering of a system get reflected through the ZFC and FC protocols followed during *M(T)* measurements. In the present case, the $Cd_{0.9}Cu_{0.1}Cr_2Se_4$ sample shows small splitting of the ZFC–FC plots similar to $CdCr_2Se_4$, and can be attributed to the variation in the particles grain-sizes. On the other hand, $Zn_{0.1}Cu_{0.9}Cr_2Se_4$ sample is showing less splitting of the ZFC–FC curves above ~250 K. Moreover, the magnetic hysteresis plot for all the Cu-substituted compounds display characteristics of a soft ferromagnetic phase with very small coercivity and strong saturation magnetization at moderate field value. In order to obtained more clarity on magnetic ground state of $Cd_{0.9}Cu_{0.1}Cr_2Se_4$ and $Zn_{0.9}Cu_{0.1}Cr_2Se_4$, ac magnetic susceptibility at three different frequencies was measured and the plots are presented in the Fig. 7.10 and 7.11. No drift with respect to frequency is observed below magnetic ordering temperature confirming strong FM and AFM order below their respective transition temperatures.

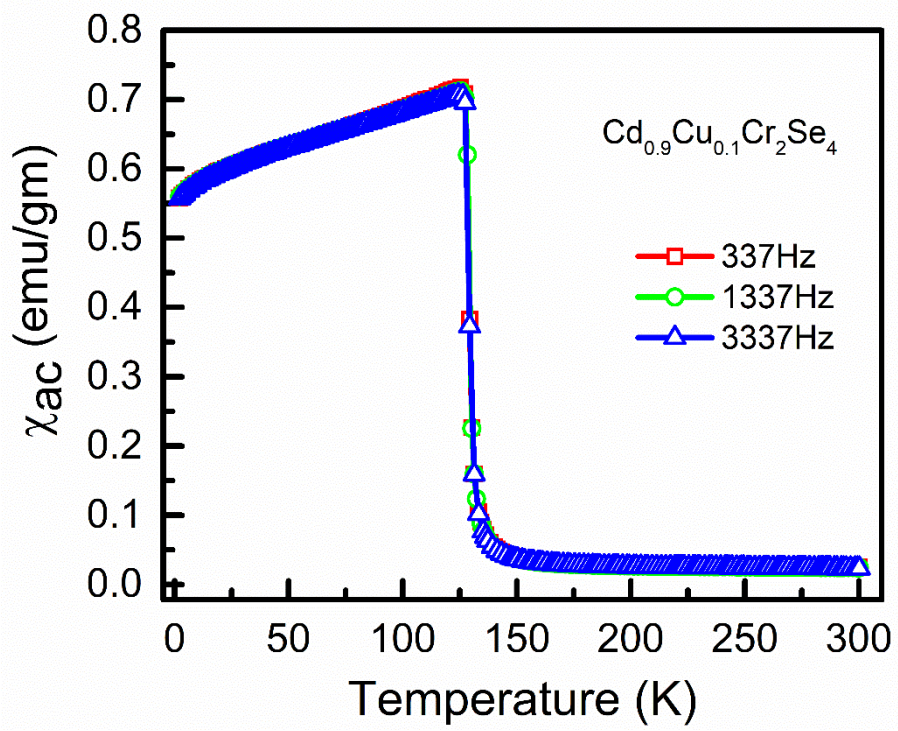

Figure 7.10: ac *χ(T)* measured at four different frequencies for $Cd_{0.9}Cu_{0.1}Cr_2Se_4$.

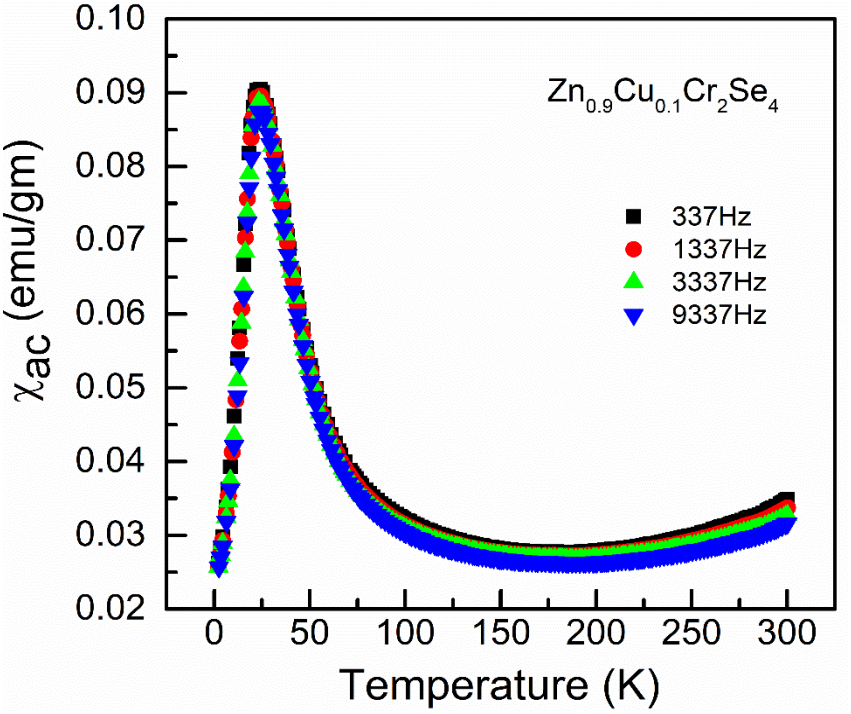

Figure 7.11: ac $\chi(T)$ measured at four different frequencies for $Zn_{0.9}Cu_{0.1}Cr_2Se_4$.

For $CuCr_2Se_4$ compound, since Cu is in monovalent state, the strong ferromagnetism observed due to the double – exchange (DE) mechanism between Cr^{3+} and Cr^{4+} ion spins through 90° Cr–Se–Cr interactions. Whereas, $ZnCr_2Se_4$ is a helical antiferromagnet with nearest neighbour FM Cr-Se-Cr interaction and overall magnetic order represent a compromise with next nearest neighbour AFM Cr-Se-Zn-Se-Cr coupling but surprisingly it exhibits saturation magnetic moment of 5.47μ_B/f.u at 4 K and 5.74μ_B/f.u at 300 K . Unusual inverse dc susceptibility can be a manifestation of strong competition between FM and AFM interactions. Again, the substitution of Cu^+ creates additional DE interactions as well as chemical disorder, so all these cannot explain by the obtained *ac* χ results. For this we need to focus on the transport properties and crystal structure parameters of these interesting $Cd_{0.9}Cu_{0.1}Cr_2Se_4$ and $Zn_{0.9}Cu_{0.1}Cr_2Se_4$ samples. We begin with the trends seen in magnetic properties of all compositions. For $Cd_{0.9}Cu_{0.1}Cr_2Se_4$ composition, T_C is almost same as that of $CdCr_2Se_4$, while the $Zn_{0.9}Cu_{0.1}Cr_2Se_4$ sample show a slight rise in T_N with another transition temperature (T_C) as compared to parent, $ZnCr_2Se_4$. On the other hand, with higher Cu^+ substituted

composition, $Zn_{0.1}Cu_{0.9}Cr_2Se_4$ shows drastic change in magnetic behavior from AFM to strong FM order with high T_c of 390 K with respect to $ZnCr_2Se_4$.

For the $Cd_{0.9}Cu_{0.1}Cr_2Se_4$ composition, even though the lattice constant change considerably with respect to the parent $CdCr_2Se_4$ composition, the tetrahedral occupation of Cd^{2+} site with Cu^{+} has less impact on the magnetic sub-lattice. This reflects through the observation of nearly same ordering temperatures and only slight splitting of ZFC-FC plots. However, change in the valence at tetrahedral-site from 2+ to 1+ implies an appearance of Cr^{4+} state at Cr-sites in order to form a charge balanced composition. Then the appearance of the DE interaction with a jump of an electron between Cr^{3+} ($3\mu_B$) and Cr^{4+} ($2\mu_B$) gives rise to strongly ferromagnetic coupling and increase of saturation magnetization from 5.38 μ_B/f.u. to 5.92 μ_B/f.u. Further strongly coupled Cr^{3+} and Cr^{4+} ions manifest itself in terms of deviation in $1/\chi_{dc}$ vs temperature curve from linear behavior above T_C (see fig.7.9).

In case of $Zn_{1-x}Cu_xCr_2Se_4$ (x = 0.1, 0.9) samples, the magnetic ordering temperatures change dramatically but saturation magnetic moment value obtained upon 10 % of Cu incorporation at Zn-site remains unchanged even as Cu concentration is raised to 90 %. Slight suppression of T_N is observed for $Zn_{0.9}Cu_{0.1}Cr_2Se_4$ as compared to $ZnCr_2Se_4$ (T_N ~20 K), and it is largely determined by the nearest neighbour Cr-Se-Cr interaction. Both FM and AFM superexchange interaction strongly depend on its lattice constant. Incorporation of Cu^{+} (0.60 Å) at Zn^{2+} (0.60 Å), inspite of being similar in ionic radii, lattice constants decrease, followed by sizable decrease in total saturation magnetic moment from 5.47 μ_B/f.u. to 4.92 μ_B/f.u. At higher Cu substitution, DE mechanism between Cr^{3+}/Cr^{4+} ions dominates and exhibits overall FM ordering in $Zn_{0.1}Cu_{0.9}Cr_2Se_4$.

7.2.5 Transport Properties

Fig. 7.12 shows the temperature dependence of the electrical resistance (R/R_{300K}) of the parent, $CdCr_2Se_4$ in the temperature range from 180 K to 400 K, whereas Fig. 7.13 displays the resistance, as a function of temperature in a field of 0, 5 kOe, 10 kOe and 50 kOe for $Cd_{0.9}Cu_{0.1}Cr_2Se_4$. The resistance curve for $CdCr_2Se_4$ displays semiconducting behavior, meanwhile 10% Cu substitution at Cd site also

exhibiting semiconducting nature but the resistance values systematically decreases with increase of magnetic field and prominent in the vicinity of magnetic ordering temperature.

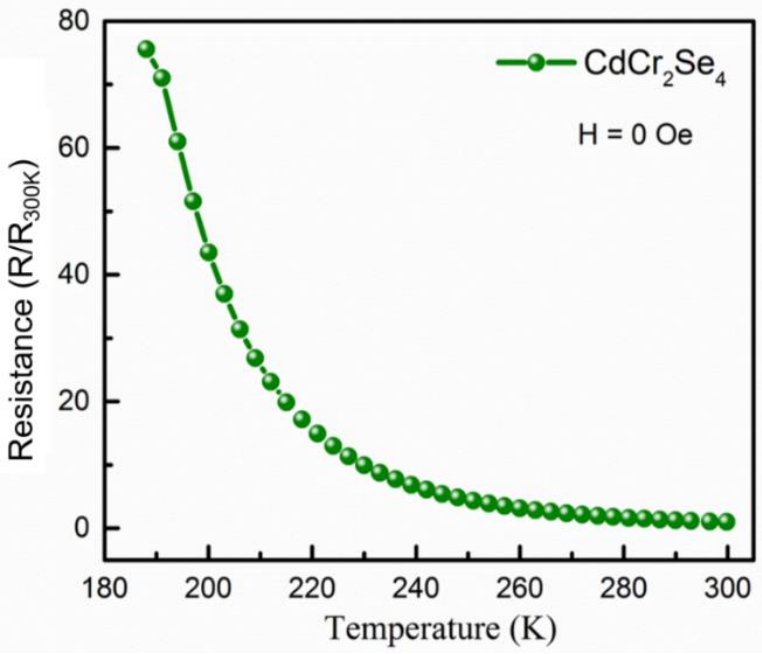

Figure 7.12: Electrical resistance 'R' normalized to its value at 300 K, R/R_{300K}, as a function of temperature at zero-field for $CdCr_2Se_4$

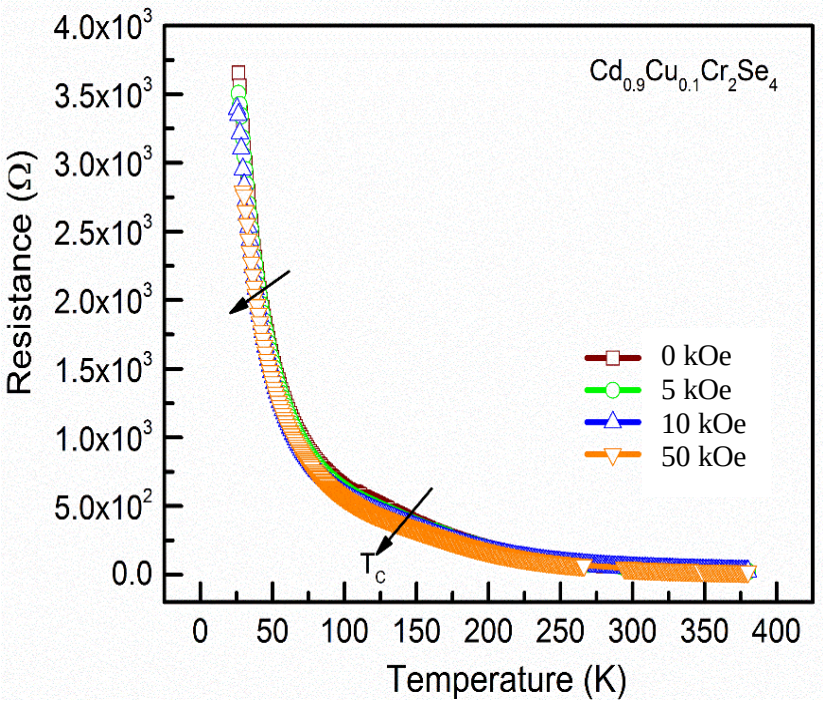

Figure 7.13: Electrical resistance as a function of temperature in a field of 0, 5 kOe, 10 kOe and 50 kOe for $Cd_{0.9}Cu_{0.1}Cr_2Se_4$ compounds.

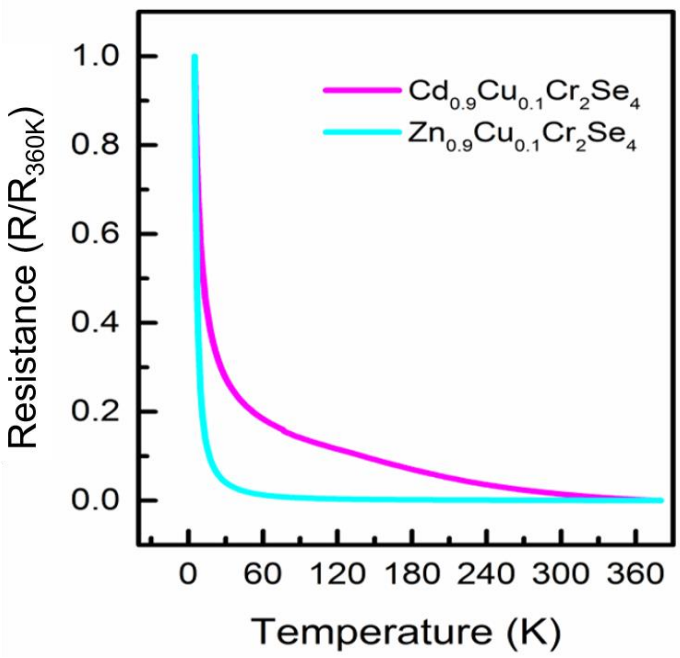

Figure 7.14: Electrical resistance 'R' normalized to its value at 360 K, R/R_{360K}, as a function of temperature at zero field for $Cd_{0.9}Cu_{0.1}Cr_2Se_4$ and $Zn_{0.9}Cu_{0.1}Cr_2Se_4$ compounds.

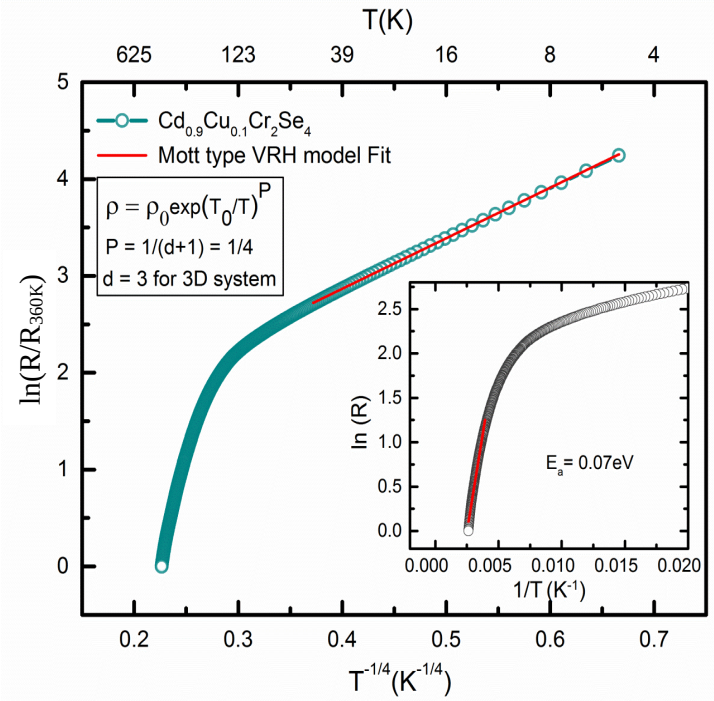

Figure 7.15: Mott 3D VRH model fitting Plot (ln (R/R_{360K}) vs $T^{-1/4}$) for $Cu_{0.9}Cu_{0.1}Cr_2Se_4$ sample and the inset shows the plot for calculation of activation energy.

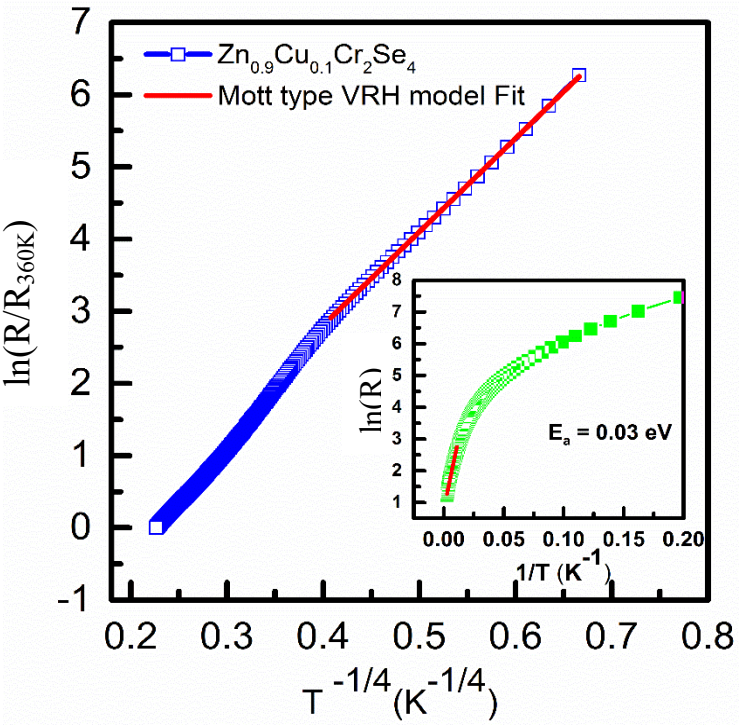

Figure 7.16: Mott 3D VRH model fitting Plot (ln (R/R_{360K}) vs $T^{-1/4}$) for $Zn_{0.9}Cu_{0.1}Cr_2Se_4$ sample and the inset shows the plot for calculation of activation energy.

Similarly, $Zn_{0.9}Cu_{0.1}Cr_2Se_4$ composition shows typical semiconductor (see Fig.7.14) behavior as reported for the parent, $ZnCr_2Se_4$ in literature [36]. The rapid decrease of resistance value on increase of temperature is indicative of thermally activated conduction. In the low temperature regime, the temperature dependence of the resistance, for both the $Zn_{0.9}Cu_{0.1}Cr_2Se_4$ and $Cd_{0.9}Cu_{0.1}Cr_2Se_4$ samples *R(T)*, is much better described by Mott's expression for variable-range hopping conduction than it is by the expression for excitation of carriers across a fixed band gap [148] conduction as shown in Fig. 7.15 And 7.16. It can be argued that the Cu^+ ions located in the tetrahedral sites of the spinel structure cause the lowering of the Fermi level with conduction through hopping process that involves transfer of electrons from Cr^{3+} to Cr^{4+}.

Fig. 7.17 and 7.18 display the resistance (R/R_{380K}), as a function of temperature in a field of 0, 10 kOe and 50 kOe for $CuCr_2Se_4$ and $Zn_{0.1}Cu_{0.9}Cr_2Se_4$ respectively. The resistance value increases dramatically with increase in

temperature and the normalized resistance vs temperature curve changes from semiconducting to metallic type. Change in slope with field dependent resistance value near T_C is observed for $Zn_{0.1}Cu_{0.9}Cr_2Se_4$. This type of crossover from semiconducting to metallic behavior is due to the localization of electron involved in exchange between Cr^{3+} and Cr^{4+} ions.

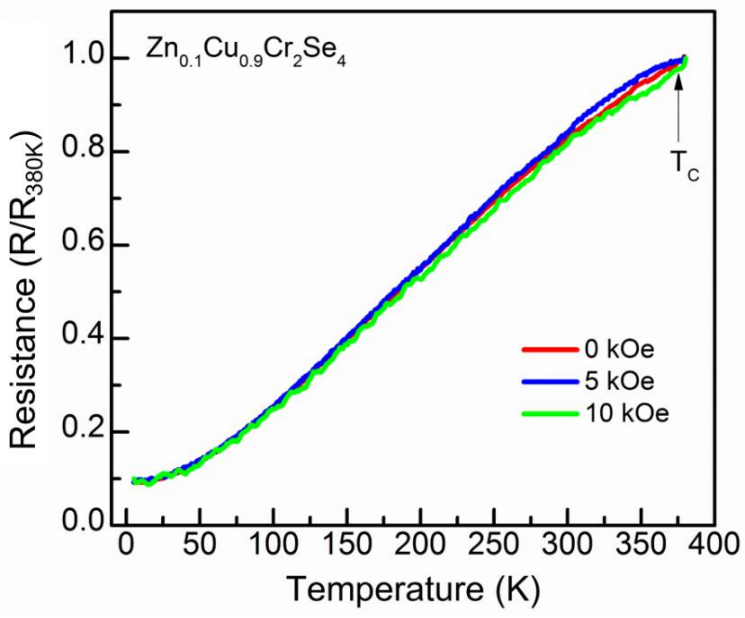

Figure 7.17: Electrical resistance 'R' normalized to its value at 380 K, R/R_{380K}, as a function of temperature in a field of 0, 5 kOe and 10 kOe for $Zn_{0.9}Cu_{0.1}Cr_2Se_4$.

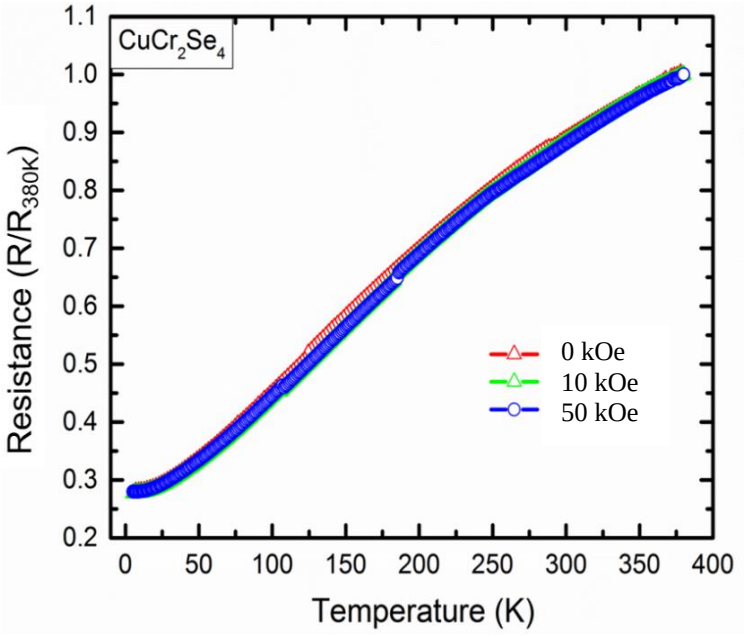

Figure 7.18: Electrical resistance 'R' normalized to its value at 380 K, R/R_{380K}, as a function of temperature in a field of 0, 10 kOe and 50 kOe for $CuCr_2Se_4$.

7.2.6 EXAFS Analysis

It becomes pertinent to identify whether it is the Cr-Se-Cr FM or the Cr-Cr AFM, or both interactions that get affected by the Cu substitution. The Cr-Se and Cr-Cr bond distances can be obtained from the refined crystal structure parameters using the simple relations $d_{Cr-Se} = a\sqrt{(3u^2 - 2u + 0.375)}$ and $d_{Cr-Cr} = a\frac{\sqrt{2}}{4}$, where *a* is the lattice constant, and *u* is the anionic parameter for Se ions [29]. As these relations are some fractional multiples of '*a*', both these distances emulate the same trend as '*a*'.

To further explore the changes in the local environment around the magnetic ion in case of Cu-substituted compositions, a room temperature EXAFS measurement at Cr K-edge was also carried out. The EXAFS data for $CdCr_2Se_4$, $Cd_{0.9}Cu_{0.1}Cr_2Se_4$ and $Zn_{0.9}Cu_{0.1}Cr_2Se_4$ were analysed with Cr-Se as a direct scattering path having coordination number 6. The bond distance (*r*) and the corresponding thermal mean square factor (σ^2) for Cr-Se path were varied until a good fit was obtained in the range of 1–3 Å in the R-space and 2–10 $Å^{-1}$ in the k-space. The fittings for the magnitude and real components of Fourier Transform (FT) of $k^2\chi(k)$ are shown in Fig. 7.19 and 7.20 for 10% Cu-substituted compounds and the refined parameters for Cr-Se interaction are presented in below Tab. 7.4.

Composition	***u***	d_{Cr-Se} ***(Å)***	d_{Cr-Cr} ***(Å)***	***(Cr-Se)*** $_{expt.}$ ***(Å)***	σ^2
$CdCr_2Se_4$	0.2643	2.542	3.799	2.6108(86)	0.0053(1)
$Cd_{0.9}Cu_{0.1}Cr_2Se_4$	0.2637	2.512	3.796	2.5542(88)	0.0085(7)
$Zn_{0.9}Cu_{0.1}Cr_2Se_4$	0.2594	2.526	3.706	2.5482(84)	0.0078(2)

Table 7.4: Structural parameters as obtained from room temperature XRD and EXAFS analysis for $CdCr_2Se_4$, $Cd_{0.9}Cu_{0.1}Cr_2Se_4$ and $Zn_{0.9}Cu_{0.1}Cr_2Se_4$ respectively

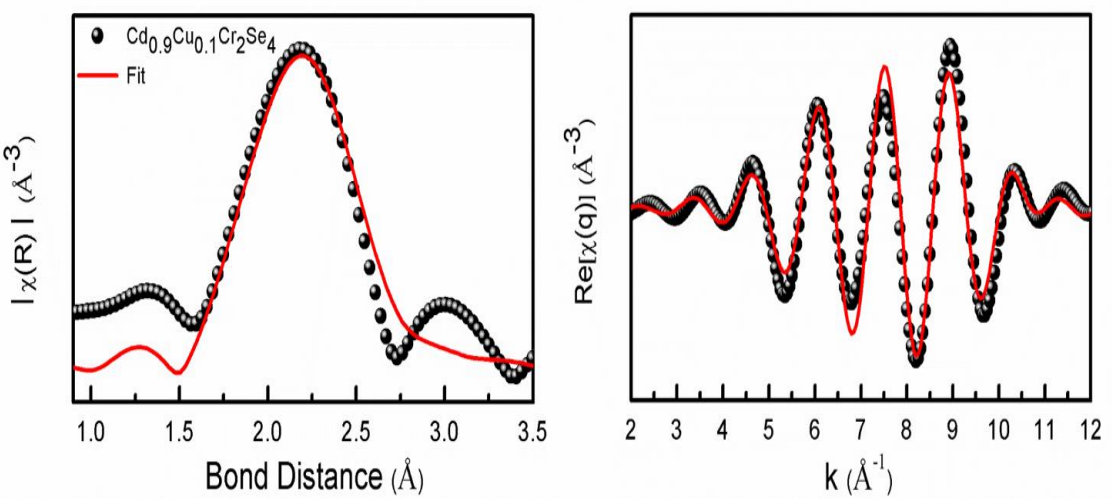

Figure 7.19: Fitting of the magnitude (left panel) and real component (right panel) of Fourier transform of Cr K-edge EXAFS spectra in $Cd_{0.9}Cu_{0.1}Cr_2Se_4$ compound.

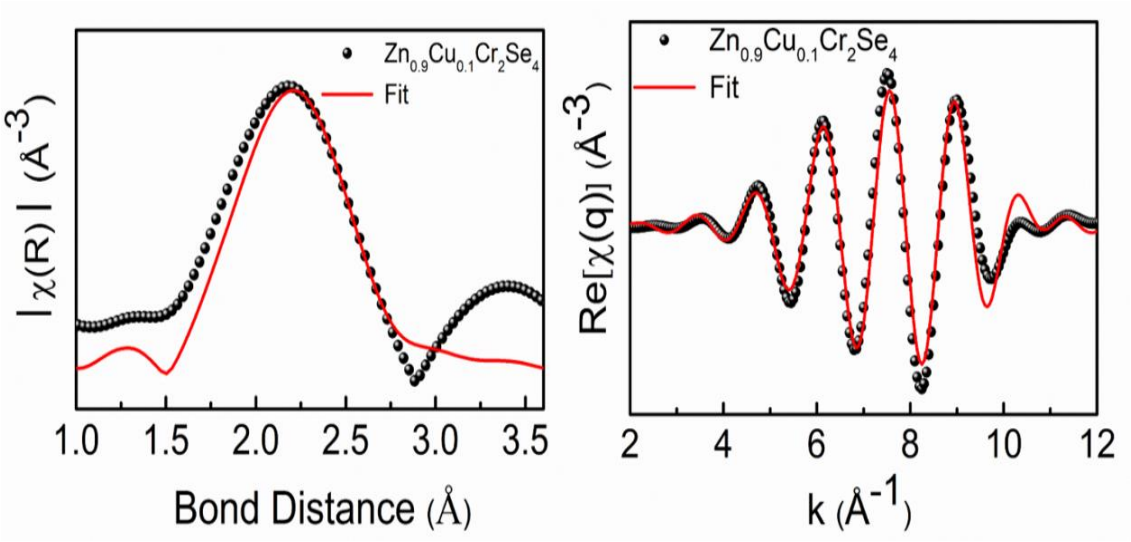

Figure 7.20: Fitting of the magnitude (left panel) and real component (right panel) of Fourier transform of Cr K-edge EXAFS spectra in $Zn_{0.9}Cu_{0.1}Cr_2Se_4$.

All the substituted compositions show systematic decrease in Cr-Cr and Cr-Se bond lengths as compared to their parent one. Second, as it can also be seen from Fig. 7.21, there is not much variation in the Cr–Se bond lengths for $Cd_{0.9}Cu_{0.1}Cr_2Se_4$ and $Zn_{0.9}Cu_{0.1}Cr_2Se_4$ compositions, although it differs from the parent $CdCr_2Se_4$. The next interaction in question is that of Cr-Cr, which occurs as

a second neighbor radial distribution around the central absorbing ion in the EXAFS data. From the profile shown in Fig. 7.21, considerable changes in this Cr-Cr local structure are evident. However, given the limited range of the data, the Cr-Cr distances that can be extracted from fitting the EXAFS data do not have better accuracy than those obtained from XRD analysis presented earlier. Hence, we will refer to the Cr-Cr distances extracted from XRD analysis. We have already seen that the lattice constant is directly related to the Cr-Cr distance. Hence, it can be concluded that the difference in the direct exchange coupling between mixed valence Cr-Cr drives the magnetic interactions in both $Cd_{0.9}Cu_{0.1}Cr_2Se_4$ and $Zn_{0.9}Cu_{0.1}Cr_2Se_4$ compounds. Correspondingly, a higher magnetic moment $M_S(\mu_B/f.u.)$ of ~ 5.92μ_B/f.u. and deviation in inverse *dc* susceptibility curve was obtained for $Cd_{0.9}Cu_{0.1}Cr_2Se_4$.

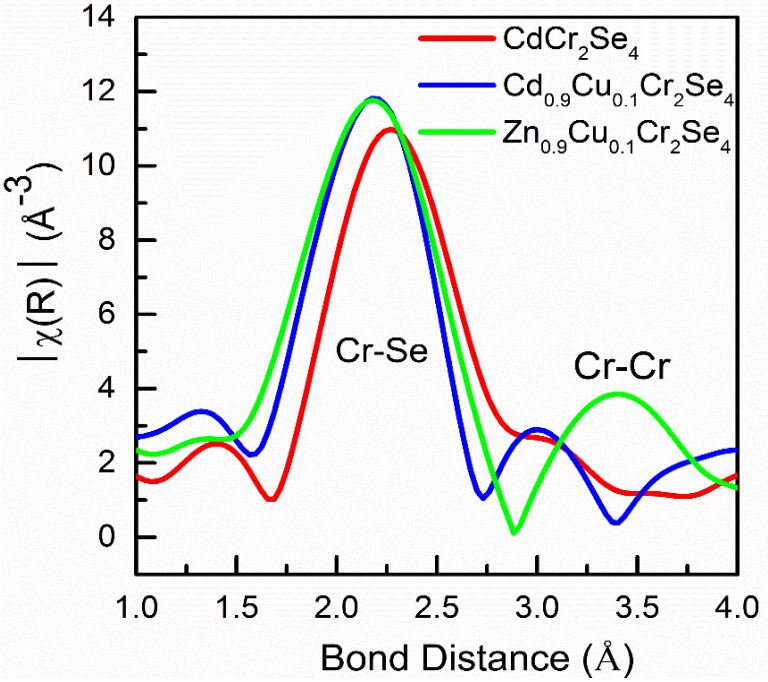

Figure 7.21: Radial distribution of room temperature Cr K-edge EXAFS measured for $CdCr_2Se_4$, $Cd_{0.9}Cu_{0.1}Cr_2Se_4$ and $Zn_{0.9}Cu_{0.1}Cr_2Se_4$.

7.3 Summary

In order to understand the unusual magnetic and transport properties of Cu substitution at Cd/Zn site in parent $CdCr_2Se_4$ and $ZnCr_2Se_4$, the systematic structural, magnetic and transport properties were carried out. Rietveld refinement of room temperature XRD patterns indicate decrease in lattice constant 'a' for $CuCr_2Se_4$, $Cd_{0.9}Cu_{0.1}Cr_2Se_4$ compositions with respect to $CdCr_2Se_4$ as Cu^+ has a lower ionic radius (0.6 Å) compared to Cd^{2+} (0.78 Å). Interestingly, for $Zn_{0.9}Cu_{0.1}Cr_2Se_4$ and $Zn_{0.1}Cu_{0.9}Cr_2Se_4$ compounds, lattice parameters are decreasing inspite of being same ionic radii of Cu^+ and Zn^{2+} (0.6 Å). Refinement also confirms the tetrahedral distribution of Cu at Cd/Zn site. XANES spectrum revealed that Cu^+ enters the spinel lattice and occupies the tetrahedral A site. Introducing small amount of Cu at Cd /Zn site causes the formation of multiple valences of Cr ions (Cr^{3+}/ Cr^{4+}) at octahedral sites as confirmed from Cr K-edge XANES data. The magnetic ground state thus becomes quite rich and competing magnetic interactions results. Even though the electronic transport behaviour of both $A_{0.9}Cu_{0.1}Cr_2Se_4$ (A = Cd/Zn) compounds follows Mott variable range hopping process (semiconducting nature) but $Cd_{0.9}Cu_{0.1}Cr_2Se_4$ shows ferromagnetic nature whereas $Zn_{0.9}Cu_{0.1}Cr_2Se_4$ compound displays complex AFM and FM behaviour. In case of higher Cu^+ substitution at Zn site, strong FM behaviour and metallic conduction was observed. Cr K-edge EXAFS of $Cd_{0.1}Cu_{0.9}Cr_2Se_4$ and $Zn_{0.1}Cu_{0.9}Cr_2Se_4$ shows considerable changes at its first nearest neighbor shell ($CrSe_6$octahedra) in terms of (Cr-Se) and second nearest neighbor (Cr-Cr) bond length, reiterating the presence of C^{4+} (0.55 Å) and Cr^{3+} (0.615 Å) at octahedral site.

Chapter 8

Conclusions and Future Scope

In this chapter, we summarize the main conclusions and achievements accomplished in this thesis. First, we will focus on the novel results achieved, in this study and follow it up with an outlook on further study.

8.1. Major Findings

The major findings/conclusions of the research work reported in this thesis are sequentially summarized as follows:

- The significance of an intricate balance between spin and lattice degrees of freedom in controlling the magneto elasticity in $Cd_{1-x}Sn_xCr_2Se_4$ was demonstrated for the first time. Such study helps us to guide the path towards tailoring the properties of Cr-chalcogenides using different substitutions.
- Changing crystal structural parameters and formation of mixed valence $Cr^{2+/3+}$ states have a great influence on the magnetic phase of Se-based spinel chalcogenides as demonstrated from the study of $Cd_{1-x}M_xCr_2Se_4$ (M= Sb, In, Sn and $x \leq 10\%$).
- In contrast, local lattice distortions created in the $CrSe_6$ octahedra by small percentage substitution of S at Se site in $CdCr_2Se_4$, does not seem to affect its magnetic properties, as demonstrated by Raman and EXAFS studies. This is in spite of the fact that Se-Cr-Se near neighbour and next near neighbour interactions play a crucial role in governing the magnetic properties of $CdCr_2Se_4$. The study of basic physical properties of such nature are reported for the first time for this particular system, which may prove crucial in understanding the prospects for spintronics applications of spinel chalcogenides.

- Near room temperature ferrimagnetic $Cu_{0.9}Mn_{0.1}Cr_2Se_4$, displays sizable low temperature large negative magnetoresistance and strong spin disorderness. The low temperature transport and magnetic properties can be ascribed to a half-metallic like behavior matching with the other materials like CrO_2.
- Metallic ferrimagnet, $CuCr_2Se_4$, when substituted with Ti (x = 0.3, 0.4, 0.5, 0.75, 1.0) at Cr site, only x = 0.4 composition shows semiconducting type behavior described by Mott's expression for variable-range hopping conduction, whereas other compositions (x = 0.3, 0.5, 0.75 and 1.0) display metallic conduction.
- Introducing small amount of Cu^+ at tetrahedral Cd^{2+} in $CdCr_2Se_4$ and site causes the formation of multiple valences of Cr ions (Cr^{3+}/ Cr^{4+}) at octahedral sites. The magnetic ground state thus becomes quite rich and competing magnetic interactions results as evidenced from inverse dc susceptibility curve above magnetic ordering temperature (T_c). Dramatic change in magnetism (antiferromagnetic to ferromagnetic) and electrical conductivity (semiconductive to metallic) in going from substitution of 10% to 90% Cu^+ at Zn^{2+} site in $ZnCr_2Se_4$ system.
- Besides, local structure analysis of both $Cd_{0.1}Cu_{0.9}Cr_2Se_4$ and $Zn_{0.1}Cu_{0.9}Cr_2Se_4$ show the considerable changes at its first nearest neighbor shell ($CrSe_6$ octahedra) in terms of (Cr-Se) and second nearest neighbor (Cr-Cr) bond length.

In conclusion, the overall magnetic properties of all the magnetic and non-magnetic substitutions at different crystallographic sites in single phase polycrystalline $CdCr_2Se_4$ $CuCr_2Se_4$ and $ZnCr_2Se_4$ systems are completely governed by strong competition between the direct Cr-Cr spin couplings and the Cr-Se-Cr exchange interactions and it is not necessary to invoke the next near neighbor interactions. Most importantly, occurance of mixed valence state, local lattice distortion and magnetic frustration are the key features for possible origin of multiferroic state. Hence this aspect has to be specially beared in mind when studying technologically important properties observed in single crystals of these

materials. Such single crysals are grown using chemical vapour deposition techniques and have been shown in umpteen studies to have surface contamination.

8.2. Scope

- Firstly, in the substituted spinel $CdCr_2Se_4$, $CuCr_2Se_4$ and $ZnCr_2Se_4$ system, in order to have an overall picture of the mechanism that is playing the role, some studies can be envisaged, namely, measurements of diffraction patterns at different temperatures spanning the magnetically ordered and disordered state. Additionally, temperature dependent EXAFS at Cr K-edge will also be helpful in decoding the complex magnetic interactions that are at play in these systems.
- Attempt towards achieving half-metallicity in Cr-based chalcospinels met with some success. More sophisticated experiments like PES could be conducted on clean, disorder free, thin films to obtain the exact gap value and nature of DOS at Fermi-level.
- Study of magnetically frustrated material, $ZnCr_2Se_4$ brings to fore intrinsic incompatibility between various exchange interactions. Such system needs to be explored more for the fascinating effects that might come to fore, formation of exotic states like spin ice, spin liquids and spin glasses. Moreover, frustrated magnets are sought materials allow easy control of electric properties by magnetic fields.
- Apart from structural and magnetic properties of the polycrystalline samples, there will be lots of scope for detailed study of the interesting transport and thermal properties of all the above studied compounds in the single crystal and thin film forms.
- In future, fabrication of thin films can be taken up from the bulk compounds to get better enhancement in physical properties, getting rid of the issues like disorder or grain boundaries encountered in polycrystalline samples to find application in the field of spintronic devices.

BIBLIOGRAPHY

[1] Peplow M., (2015), March of the machines, Nature 525 (7567) 18–21 (DOI:10.1038/525018a).

[2] Grimes N. W., (1972), 'Off-centre 'ions in compounds with the spinel structure, Phil. Mag. 26, 1217-1226 (10.1080/14786437208227375)

[3] Hemberger J., Rudolf T., H. Krug von Nidda A., *et al*., (2006), Spin-Driven Phonon Splitting in Bond-Frustrated $ZnCr_2S_4$, Phys. Rev. Lett. 97 (8) 087204. (DOI:10.1103/PhysRevLett.97.087204).

[4] Lee S. H., Broholm C. L., Ratcliff W., *et al*., (2002), Emergent Excitations in a Geometrically Frustrated Magnet, Nature 418 (6900) 856–858. (DOI:10.1038/Nature00964).

[5] Hemberger J., Krug von Nidda H. A., Tsurkan V., *et al*., (2007), Large Magnetostriction and Negative Thermal Expansion in the Frustrated Antiferromagnet $ZnCr_2Se_4$, Phys. Rev. Lett. 98 (14) 147203–4 (DOI:10.1103/PhysRevLett.98.147203).

[6] Tsurkan V., Hemberger J., Krimmel A., *et al*., (2006), Experimental evidence for competition between antiferromagnetic and ferromagnetic correlations in $HgCr_2S_4$ **73** (22) 224442 (DOI:10.1103/PhysRevB.73.224442).

[7] Hemberger J., Lunkenheimer P., Fichtl R., *et al*., (2005), Relaxor ferroelectricity and colossal magnetocapacitive coupling in ferromagnetic $CdCr_2S_4$, Nature (London) 434, 364-367 (DOI: 10.1038/nature03348).

[8] Weber S., Lunkenheimer P., Fichtl R. *et al*., (2006), Colossal magnetocapacitance and colossal Magnetoresistance in $HgCr_2S_4$, Phys. Rev. Lett. 96 (15), 157202. (DOI:10.1103/PhysRevLett.96.157202).

[9] Yamashita Y., Ueda K., (2000), Spin-Driven Jahn-Teller Distortion in a Pyrochlore System, Physical Review Letters 85 (2) 4960–4963 (DOI:10.1103/PhysRevLett.85.4960).

[10] Abramovich A.I., Koreleva L.I., Lukina L.N., (1999), Spin-glass and reentrant spin-glass states in iron sulfospinels having dilute A and B sublattices, Phys. Solid State 41, 73-79 (DOI: 10.1134/1.1131079)

[11] Hemberger J., Lunkenheimer P., Fichtl R., *et al*., (2006), Multiferroicity and colossal magneto-capacitance in Cr-thiospinels, Phase Transition, 96, 1065-1082, (DOI:10.1080/01411590601067193)

[12] Fedorov V. A., Kesler Ya. A., Zhukov E. G., (2003), Magnetic Semiconducting Chalcogenide Spinels: Preparation and Physical Chemistry, Inorg. Mater., 39, S68–S88

[13] Wagner V., Mitlehner H., Geick R., (1971), Infrared active phonons in $CdCr_2Se_4$, Opt. Commun. 2, 429-430.

[14] Lubecka M. and Maksymowicz L. J., (1991), Reentrant transition and spin-glass state in $CdCr_{2x}In_{2-2x}Se_4$ thin films, Phys. Rev. B, 44, 10106-10111 (DOI: 10.1103/PhysRevB.44.10106).

[15] Ohgushi K., Ogasawara T., Okimoto Y., et al., (2005), Gigantic Kerr-rotation induced by a d−d transition resonance in MCr_2S_4 (M = Mn, Fe), Phys. Rev. B, 72, 155114 (DOI: 10.1103/PhysRevB.72.155114).

[16] Goodenough J. B., Gräper W., Holtzberg F., *et al.*, (1970) Magnetic and Other Properties of Oxides and Related Compounds, Volume 4, Part 1 of Landolt-Börnstein: Numerical Data and Functional Relationships in Science and Technology - New Series Condensed Matter, Springer, (DOI:10.1007/b19968).

[17] Azzoni C. B., Mozzati M. C., Ghigna P., *et al*., (2001), Magnetic Investigation of Mn Ions in $(Cd_{1-x}Mn_x)$ Mn_2O_4 Spinels, Solid State Communications 117 (9) 511–515 (DOI:10.1016/S0038-1098(00)00514-7).

[18] Baltzer P. K., Wojtowicz P. J., Robbins M., *et al.*, (1966), Exchange interactions in ferromagnetic chromium chalcogenide spinels, Phys. Rev. 151 (2), 367–377 (DOI:10.1103/PhysRev.151.367).

[19] Samokhvalov V., Unterricker S., Burlakov I., (2003), Investigation of ferromagnetic spinel semiconductors by hyperfine interactions of implanted nuclear probes, Journal of Physics and Chemistry of Solids 64, 2069–2073. (DOI:10.1016/S0022-3697(03)00152-5).

[20] Baltzer P. K., Lehmann H. W., Robbins M., (1965), Insulating ferromagnetic spinels, Phys. Rev. Lett. 15 (1), 493–495 (DOI:10.1103/PhysRevLett15493).

[21] Rudolf T., Kant C., Mayr F., Hemberger J., *et al.*, (2007), Polar phonons and spin phonon coupling in $HgCr_2S_4$ and $CdCr_2S_4$ studied with far-infrared spectroscopy 76 (17), 174307 (DOI:10.1103/PhysRevB.76.174307).

[22] Ueda H., Ueda Y., (2008) Pressure-enhanced direct exchange coupling observed in chromium spinels 77 (2) 224411. (DOI:10.1103/PhysRevB.77.224411).

[23] Getzlaff M., (2008), Fundamentals of magnetism, Springer Berlin Heidelberg New York.

[24] Blundell S. J., (2001), Magnetism in Condensed Matter (Oxford University Press, New York).

[25] Cox P. A., (1992), Electronic Structure of Solids in, Solid State Chemistry: Compounds, edited by A.K. Cheetham and P. Day, (Oxford University Press, New York).

[26] Ramirez M., Kumar A., Denev S., *et al.*, (2009), Spin-charge-lattice coupling through resonant multimagnon excitations in multiferroic $BiFeO_3$, Appl. Phys. Lett. 94, 161905(DOI: 10.1063/1.3118576).

[27] Gnezdilov V., Lemmens P., Pashkevich Y. G., *et al.*, (2011), Phonon Anomalies and Possible Local Lattice Distortions in Giant Magnetocapacitive $CdCr_2S_4$ 84 (4), 045106 (DOI:10.1103/Physrevb.84.045106).

[28] White W. B. and DeAngelis B. A. (1967), Interpretation of the vibrational spectra of spinels, Spectrochim. Acta, Part A 23, 985-995 (DOI: 10.1016/0584-8539(67)80023-0).

[29] Hill R. J., Craig J. R., and Gibbs G. V. (1979), Systematics of the spinel structure type, Phys. Chem. Miner. 4, 317-339 (DOI: 10.1007/BF00307535).

[30] Lehmann H.W., (1967), Semiconducting Properties of Ferromagnetic $CdCr_2Se_4$, Phys. Rev. 163, 488 (DOI: 10.1103/PhysRev.163.488).

[31] Amith A., Gunsalus G. L. (1969), Unique Behavior of Seebeck Coefficient in N-Type $CdCr_2Se_4$, J. Appl. Phys 40, 1020 (DOI: 10.1063/1.1657511)

[32] Chaves M.R., Ribeiro J. L., Selmi A., Gibart P., (1985), Electrical resistivity and Seebeck effect in $HgCr_2Se_4$, Phys. Stat. Sol. 92, 263-271 (DOI:10.1002/pssa.2210920126)

[33] Minematsu K., Miyatani K., Takahashi T., (1971), Magnetic and Electrical Properties of Impurity Doped $HgCr_2Se_4$, J. Phys. Soc. Jpn. 31, 123-128 (DOI: 10.1143/JPSJ.31.123)

[34] Duda H., Gron T., Warczewski J., (1990), Electrical properties of the ferromagnetic spinels $Cd_{1-x}Cu_xCr_2Se_4$, J. Magn. Magn. Mater. 88, 55-57(DOI: 10.1016/S0304-8853(97)90011-1)

[35] Snyder G. J., Caillat T., Fleurial J. P., (2000), Thermoelectric, transport, and magnetic properties of the polaron semiconductor $Fe_xCr_{3-x}Se_4$, Phys. Rev. B 62, 10185-10193 (DOI:10.1103/PhysRevB.62.10185).

[36] Snyder G. J., Caillat T., Fleurial J. P., (2001), Thermoelectric Properties of Chalcogenides with the Spinel Structure Mat. Res. Innovat. 5, 67–73 (DOI: 10.1007/s100190100133).

[37] Hahn V. H., Lorent C. de, Harder B. Z., (1956) Anorg. Allg. Chem., 283, 138.

[38] Lotgering F. K., (1964a), Solid State Commun., 2, 55-6. Lotgering F. K., (1964b) Proc. Int. Conf. on Magnetism, Nottingham, 533.

[39] Lotgering F. K., R. P. van Stapele, (1967), Magnetic and electrical properties of copper containing sulphides and selenides with spinel structure Solid State Commun., 5, 143-146 (DOI: 10.1016/0038-1098(67)90013-0)

[40] Goodenough J. B., (1967), Tetrahedral-site copper in chalcogenide spinels Solid State Commun., 5, 577-580 (DOI:10.1016/0038-1098(67)90069-5); Goodenough J. B., (1969), Descriptions of outer d electrons in thiospinels, J. Phys. Chem. Solids , 30**,** 261-80 (DOI: 10.1016/0022-3697(69)90308-4)

[41] Matthiessen A., (1862), Rep. Brit. Ass. 32, 144.

[42] Seymour J. (1972) Physical Electronics, chapter 2, Pitman

[43] Viret M., Ranno L., Coey J. M. D., (1997), Colossal magnetoresistance of the variable range hopping regime in the manganites, J. Appl. Phys., 81, 4964 – 4966 (DOI: 10.1063/1.365013)

[44] Martin G. W., (2003), Exchangestriction in $CdCr_2S_4$ and $CdCr_2Se_4$, J. Appl. Phys., 40 (3) 1–2 (DOI:10.1063/1.1657509).

[45] Göbel H., (1976), Local lattice distortions in chromium chalcogenide spinels at low temperatures, Journal of Magnetism and Magnetic Materials 3, 143–146 (DOI:10.1016/0304-8853(76)90025-1).

[46] Harbeke G., Pinch H., (1966), Magnetoabsorption in Single-Crystal Semiconducting Ferromagnetic Spinels, Phys. Rev. Lett. 17 (21) 1090–1092. (DOI:10.1103/PhysRevLett.17.1090).

[47] Wakamura K., Arai T., (1988), Effect of magnetic ordering on phonon parameters for infrared active modes in ferromagnetic spinel $CdCr_2S_4$, J. Appl. Phys., 63 (12) (5824–7. DOI:10.1063/1.340321).

[48] Sun C. P., Huang C. L., Lin C. C., et al (2010), Colossal electroresistance and colossal magnetoresistance in spinel multiferroic $CdCr_2S_4$, Appl. Phys. Lett. 96 (1), 122109 (DOI:10.1063/1.3368123).

[49] Eerenstein W., Mathur N. D., Scott J. F., (2006), Multiferroic and magnetoelectric materials, Nature, 442 (7104) 759–765. (DOI:10.1038/nature05023).

[50] Catalan G., Scott J. F., (2007), Magnetoelectrics: Is $CdCr_2S_4$ a multiferroic relaxor? Nature, 448 (7156) E4–E5 (DOI:10.1038/nature06156).

[51] Hemberger J., Lunkenheimer P., Fichtl R., *et al.*, (2006), Multiferroic behavior in $CdCr_2X_4$ (X=S, Se), Physica B: Condens. Matter, 378-380, 363–366 (DOI: 10.1016/j.physb.2006.01.407).

[52] Sun C. P, Lin C. C., Her J. L., et al., (2009), Field-dependent dielectric and magnetic properties in multiferroic $CdCr_2S_4$, Phys. Rev. B 79 (2) 214116. (DOI:10.1103/PhysRevB.79.214116).

[53] Ramirez A. P., (2003), Geometric frustration: Magic moments, Nature, 421 (6) 483–483. (DOI:10.1038/421483a).

[54] Bebenin N. G., Zainullina R. I., Sukhorukov Yu P., *et al* (2015) Magnetocaloric effect and inhomogeneity of $CdCr_2Se_4$ and $HgCr_2Se_4$ single crystals, J. Magn. Magn. Mater. 387, 127-130 (DOI: 10.1016/j.jmmm.2015.03.093)

[55] Lehmann H. W., Robbins M., (1966), Electrical Transport Properties of the Insulating Ferromagnetic Spinels $CdCr_2S_4$ and $CdCr_2Se_4$, J. Appl. Phys, 37(3) 1389–1390 (DOI:10.1063/1.1708485).

[56] Lubecka M. and Maksymowicz L. J., (1991), Reentrant transition and spin-glass state in $CdCr_{2x}In_{2-2x}Se_4$ thin films, Phys. Rev. B, 44, 10106-10111 (DOI: 10.1103/PhysRevB.44.10106).

[57] Wagner V., Mitlehner, Geick H. R., (1971), Opt. Commun. 2, 429-430.

[58] Saha-Dasgupta T., Raychaudhury Molly De, Sarma D. D. (2007), Ferromagnetism in metallic chalcospinels $CuCr_2S_4$ and $CuCr_2Se_4$, Phys. Rev. B, 76, 054441 (DOI:10.1103/PhysRevB.76.054441)

[59] Brändle H., Schoenes J., Wachter P., Hulliger F., Reim W., (1991), J. Magn. Magn. Mater. 93, 207

[60] Kang J. -S., Kim S. J., Kim C. S., *et al.*, (2001), Valence-band photoemission spectroscopy of the giant magnetoresistive spinel compound $Fe_{0.5}Cu_{0.5}Cr_2S_4$ Phys. Rev. B, 63, 144412 (DOI:10.1103/PhysRevB.63.144412).

[61] Kimura A., Matsuno J., Okabayashi J., *et al*., (2001), Soft x-ray magnetic circular dichroism study of the ferromagnetic spinel-type Cr chalcogenides Phys. Rev. B, 63, 224420 (DOI: 10.1103/PhysRevB.63.224420)

[62] Deb A., Mizumaki M., Muro T., *et al.*, (2003), Soft-x-ray magnetic-circular-dichroism study of the colossal-magnetoresistance spinel $Fe_{0.5}Cu_{0.5}Cr_2S_4$ Phys. Rev. B, 68, 014427 (DOI: 10.1103/PhysRevB.68.014427)

[63] Locher P. R., (1967), Cu-NMR in paramagnetic and ferromagnetic $CuCr_2Se_4$, Solid State Commun., 5, 185 (DOI:10.1016/0038-1098(67)905157)

[64] Colominas C., (1967), Neutron-Diffraction Investigation of CuCr2Se4 and $CuCr_2Te_4$, Phys. Rev., 153, 558.26 (DOI: 10.1103/PhysRev.153.558)

[65] Yamashita O., Yamaguchi Y., Nakatani I., et al., (1979), Polarized Neutron Diffraction Study of a $CuCr_2Se_4$ Single Crystal, Phys. Soc. Jpn., 46, 1145-1152 (DOI: 10.1143/JPSJ.46.1145).

[66] Krok-Kowalski J., Gron T., Warczewski J., *et al.*, (1997), Ferrimagnetism and metamagnetism in $Cd_{1-x}Cu_xCr_2S_4$spinels, J. Magn. Magn. Mater., 168, 129-138 (DOI: 10.1016/S0304-8853(96)00663-4)

[67] Oh H.-J., Kang J.-S., Lee S.S., *et al.*, (2007), Valence values of the cations in selenospinel $Cu(Cr,Ti)_2Se_4$, Europhys. Lett., 78, 27004 (DOI: 10.1209/0295-5075/78/27004)

[68] Wang Y., Gupta A., Chshiev M., Butler W., (2008), Half-metallic electronic structures of quaternary ferromagnetic chalcospinels: $Cd_xCu_{1-x}Cr_2S_4$ and $Cd_xCu_{1-x}Cr_2Se_4$, Appl. Phys. Lett. 92, 062507 (DOI: 10.1063/1.2841848)

[69] Plumier R., (1966), J. Phys. France, 27, 213-219 (DOI: 10.1051/jphys:01966002703-4021300)

[70] Kleinberger R., Kouchkovsky R. de, (1966), CR Acad. Sci. (France) 262, 628

[71] Hidaka M., Tokiwa N., Fuji M., *et al.*, (2003), Correlation between the structural and antiferromagnetic phase transitions in $ZnCr_2Se_4$, Phys. Stat. Sol. (b), 236, 9-18 (DOI: 10.1002/pssb.200301502)

[72] Rudolf T., Kant Ch., Mayr F., *et al.*, (2007), Spin-phonon coupling in $ZnCr_2Se_4$ Phys. Rev. B 75, 052410 (DOI:10.1103/PhysRevB.75.052410).

[73] Jenkins R. (2000), X-ray Techniques: Overview. In: Meyers R.A. (Eds.), Encyclopedia of Analytical Chemistry, John Wiley & Sons Ltd, Chichester, pp.13269-13288.

[74] Cullity B. D. (1956), Elements of X-Ray Diffraction, Add1son-Wesley Publishing Company, Inc., Massachusetts, pp.1-531.

[75] Guinebretière R. (2006), X-ray Diffraction by Polycrystalline Materials, ISTE Ltd, Lavoisier, London (ISBN-13:978-1-905209-21-7).

[76] http://iiti.ac.in/sic/index.php?q=pxrd

[77] http://www.saha.ac.in/web/home-photon-factory/powder-diffraction-at-lt

[78] Rietveld H. M. (1969), A profile refinement method for nuclear and magnetic structures, J. Appl. Cryst. 2, 65-71 (DOI:10.1107/S0021889869006558).

[79] Rodríguez-Carvajal J. (2001), Recent Developments of the Program FULLPROF, in Commission on Powder Diffraction (IUCr). Newsletter, 26, 12-19.

[80] Goldstein J. I., Newbury D. E. *et al.* (2003), Scanning Electron Microscopy and X-Ray Microanalysis, Springer Science, pp.1-536 (ISBN: 978-1-4615-0215-9)

[81] http://iiti.ac.in/sic/index.php?q=eds

[82] S. Conradson (2000), XAFS: A technique to probe local structure, Los Alamos Sci. 26, 422.

[83] Rehr J. J. and Albers R. C. (2000), Theoretical approaches to x-ray absorption fine structure, Rev. Mod. Phys. 72, 621 (DOI: 10.1103/RevModPhys.72.621).

[84] Newville M. (2004), Fundamentals of XAFS. http://www.xafs.org/tutorials/.

[85] Riggs-Gelasco P. J., Stemmler T. L., *et al* (1995), XAFS of Dinuclear Metal Sites in Proteins and Model Compounds, Coord. Chem. Rev., 144, 245-286.

[86] http://iiti.ac.in/sic/index.php?q=xafs

[87] Ravel B. and Newville M. (2005), ATHENA, ARTEMIS, HEPHAESTUS: data analysis for X-ray absorption spectroscopy using IFEFFIT, J. Synchrotron Rad., 12, 537-541 (DOI: 10.1107/S0909049505012719)

[88] Newville M.(2001), IFEFFIT : interactive XAFS analysis and FEFF fitting, J. Synchrotron Rad., 8, 322-324 (DOI: 10.1107/S0909049500016964)

[89] http://www.cat.gov.in/technology/accel/srul/beamlines/mcd_pes.html

[90] Raman C.V. and Krishnan K.S. (1928), A New Type of Secondary Radiation, Nature, 121, 501-502 (DOI:10.1038/121501c0).

[91] Wartewig S. (2003), IR and Raman Spectroscopy: Fundamental Processing, Wiley-Vch Verlag & Co., Weinheim. (DOI: 10.1002/3527601635.ch8 and ISBN: 9783527601639).

[92] Ferraro J. R., Nakamoto K., *et al.*, (2003), Introductory Raman Spectroscopy, Elsevier, pp. 1-146 (ISBN: 978-0-12-254105-6).

[93] Loudon R. (1964), The Raman effect in crystals, Adv. Phys., 13, 423-480 (DOI: 10.1080/00018736400101051).

[94] http://www.linkam.co.uk/thms600-features/

[95]http://www.infim.ro/content/superconducting-quantum-interference magnetometer-squid-quantum-design

[96] https://lot-qd.de/en/products/materials-science/systems-to-measure-physical-properties/product/physical-property-measurement-system-ppms/

[97] https://www.qdusa.com/sitedocs/appNotes/ppms/1078-201.pdf

[98] Blundell S. (2001), Magnetism in Condensed Matter, Oxford Master Series in Condensed Matter Physics. Oxford University Press, Oxford; New York.

[99]https://www.mrl.ucsb.edu/sites/default/files/mrl_docs/instruments/manPPMS.pdf

[100] Quantum Design, Physical Property Measurement System: Heat Capacity Option User's Manual, January 2004, 11th edition.

[101] Quantum Design, Physical Property Measurement System: Heat Capacity Option User's Manual, January 2004, 11th edition.

[102] Groń T., Krajewski A., Kusz J., *et al.*, (2005), Thermoelectric power of $CdCr_{2-x}Ga_xSe_4$ p-type spinel semiconductors, Phys. Rev. B, 71, 035208 (DOI: 10.1103/PhysRevB.71.035208).

[103] Waśkowska A., Gerward L., Staun Olsen J., *et al.*, (2008), Temperature dependent lattice instability in single crystals of ferromagnetic $CdCr_2Se_4$

diluted with In and Sb, J. Phys: Condens. Matter 20, 425209 (DOI: 10.1088/0953-8984/20/42/425209).

[104] Malicka E., Waśkowska A., Skrzypek D., *et al.*, (2009), The effects of doping ferromagnetic spinel $CdCr_2Se_4$ with Sb^{3+} ions, J. Sol. State. Chem. 182, 3149-3154 (DOI: 10.1016/j.jssc.2009.09.002).

[105] Pinch H. L., Berger S. B., (1988), The effects of nonstocheiometry on the magnetic properties of cadmium chromium chalcogenide spinels, J. Phys. Chem. Sol. 29, 2091–2099.

[106] Iliev M., (1980), Thermoreflectance, photoconductance and Raman scattering of ferromagnetic spinels MCr_2X_4 (M = Cd, Hg; X = S, Se) near the magnetic phase transition, J. Phys., Colloq. 41, C5-23 (DOI: 10.1051/jphyscol:1980505).

[107] Iliev M., G¨untherodt G., and Pink H., (1978), Resonant Raman scattering of $CdCr_2Se_4$, Solid State Comm. 27, 863-866 (DOI: 10.1016/0038-1098(78)90193-X).

[108] Tachibana M., Taira N. and Kawaji H., (2011), Heat capacity and thermal expansion of $CdCr_2Se_4$ and $CdCr_2S_4$, Solid State Comm., 151, 1776-1779 (DOI: 10.1016/j.ssc.2011.08.029).

[109] Kundu S., Nath T. K., (2012), Suppression of a glassy magnetic state and emergence of a Griffiths-like phase on size reduction in $Nd_{0.8}Sr_{0.2}MnO_3$, J. Appl. Phys.111, 113903 (DOI: 10.1063/1.4722322).

[110] Van Stapele R. P., (1982), In: Ferromagnetic Materials, E.P. Wohlfarth (Ed.), 3, (North-Holland, Amsterdam) p. 603.

[111] Shannon R.D., (1976), Revised effective ionic radii and systematic studies of interatomic distances in halides and chalcogenides, Acta Crystallogr. A 32, 751–767 (DOI: 10.1107/S0567739476001551).

[112] Gasparov L. V., Tanner D. B., Romero D. B, *et al.*, (2000), Infrared and Raman studies of the Verwey transition in magnetite, Phys. Rev. B 62, 7939-7944 (DOI: 10.1103/PhysRevB.62.7939).

[113] Verble J. L. (1974), Temperature-dependent light-scattering studies of the Verwey transition and electronic disorder in magnetite, Phys. Rev. B, 9, 5236-5248 (DOI: 10.1103/PhysRevB.9.5236).

[114] Bruesch P. and D'Ambrogio P. (1972), Lattice dynamics and magnetic ordering in the chalcogenide spinels $CdCr_2S_4$ and $CdCr_2Se_4$, Phys. Status Solidi B 50, 513-526 (DOI: 10.1002/pssb.2220500212).

[115] Iliev M. N., Popov V. N., Litvinchuk A. P, et al. (2005), Comparative Raman studies of Sr_2RuO_4, $Sr_3Ru_2O_7$ and $Sr_4Ru_3O_{10}$, Physica B: Condens. Matter 358, 138-152 (DOI: 10.1016/j.physb.2004.12.069).

[116] Ahlawat A., Satapathy S., Sathe V. G. et al. (2013), Evidence of spin phonon coupling in magnetoelectric $NiFe_2O_4$/PMN-PT composite, Appl. Phys. Lett. 103, 252902 (DOI: 10.1063/1.4850555).

[117] Callen E. (1968), Optical Absorption Edge of Magnetic Semiconductors, Phys. Rev. Lett. 20, 1045-1048 (DOI: 10.1103/PhysRevLett.20.1045).

[118] Oliveira G. N. P., Pereira A. M., Lopes A. M. L., et al. (2012), Dynamic Off-Centering of Cr^{3+} Ions and Short-Range Magneto-Electric Clusters in $CdCr_2S_4$, Phys. Rev. B 86 (22), 224418 (DOI:10.1103/PhysRevB.86.224418).

[119] Jin S., Mccormack M., Tiefel T. H., and Ramesh R. (1994), Colossal magnetoresistance in La-Ca-Mn-O ferromagnetic thin films, *J. Appl. Phys*. **76**, 6929 (DOI: 10.1063/1.358119).

[120] Lunkenheimer P., Fichtl R., Hemberger J., *et al.* (2005), Relaxation dynamics and colossal magnetocapacitive effect in $CdCr_2S_4$, Phys. Rev. B 72 (6), 060103 (DOI:10.1103/PhysRevB.72.060103).

[121] Fritsch V., Deisenhofer J., Fichtl R., Hemberger J., (2003), Anisotropic colossal magnetoresistance effects in $Fe_{1-x}Cu_xCr_2S_4$, Phys. Rev. B 67, 144419 (DOI:10.1103/PhysRevB.67.144419).

[122] Ok H.N., Chung Yu, Kim Ju. G., (1979), Crystallographic and magnetic properties of $Fe_xCu_{1-x}Cr_2Se_4$, Phys. Rev. B, 20, 4550 (DOI: 10.1103/PhysRevB.20.4550).

[123] Maciazek E., Molak A., Goryczka T., (2007), Influence of cobalt substitution on structure and electric conduction of $CuCr_2Se_4$, J. Alloys Compd., 441, 222-230 (DOI: 10.1016/j.jallcom.2006.09.134).

[124] Jendrzejewska I., (2000), Influence of nickel substitution on the crystal structure of $CuCr_2Se_4$, J. Alloys Compd., 305, 90-92 (DOI: /10.1016/S0925-8388(00)00727-1)

[125] Wehmeier F. H., Keve E.T, S. C. Abrahams S. C., (1970), Preparation, structure, and properties of some chromium selenides. Crystal growth with selenium vapor as a novel transport agent, Inorg. Chem. 9, 2125-2131, (DOI: 10.1021/ic50091a032)

[126] Nacatani I., Nose H., Masumoto K., (1978), J. Phys. Chem. Solids 39, 743.

[127] Zhang L., Ling L., Fan J., *et al.*, (2011), 3D-Heisenberg ferromagnetic characteristics in $CuCr_2Se_4$, J. Appl. Phys. 109, 113911 (DOI: doi.org/10.1063/1.3594752).

[128] Yuzuri M., (1973), Magnetic Properties of the Compound Cr-Se System, J. Phys. Soc. Jap. 35, 1252 (DOI: 10.1143/JPSJ.35.1252).

[129] Furukawa N., Shimomura Y., Akimoto T., *et al.*, (2001), Magnon scattering processes and low-temperature resistivity in CMR manganites, J. Magn. Magn. Mater. 226-230, 782-783 (DOI: 10.1016/S0304-8853(00)00748-4).

[130] Li X.W., Gupta A., McGuire T., *et al.*, (1999), Magnetoresistance and Hall effect of chromium dioxide epitaxial thin films, J. Appl. Phys. 85, 5585 (DOI: 10.1063/1.369807)

[131] Tripathi T. S., Tewari G. C., Rastogi A. K., (2010), The study of magnon-drag effects in the thermopower of $CuCr_2X_4$ (X = S, Se and Te), J. Phys.: Conf. Ser. 200, 032060 (DOI: 10.1088/1742-6596/200/3/032060)

[132] Mills D.L., Fert A., Campbell I.A., (1971), Temperature Dependence of the Electrical Resistivity of Dilute Ferromagnetic Alloys, Phys. Rev. B, 4, 196 (DOI: 10.1103/PhysRevB.4.196).

[133] Herring C., Kittle C., (1951), On the Theory of Spin Waves in Ferromagnetic Media, Phys. Rev 81, 869, (DOI:10.1103/PhysRev.81.869).

[134] Bettinger J., Chopdekar R., Liberati M., *et al.*, (2007), Magnetism and transport of $CuCr_2Se_4$ thin films, J. Magn. Magn. Mater. 318, 65 (DOI: 10.1016/j.jmmm.2007.04.024)

[135] Antonov V., Antropov V., Harmo B., *et al.*, (1998), Fully relativistic spin-polarized LMTO calculations of the magneto-optical Kerr effect of *d* and *f* ferromagnetic materials. I. Chromium spinel chalcogenides, Phys. Rev. B, 59, 14552. (DOI: 10.1103/PhysRevB.59.14552)

[136] Dedkov Yu. S., Vinogradov A. S., Fonin M., *et al.*, (2005), Correlations in the electronic structure of half-metallic ferromagnetic CrO_2 films: An x-ray absorption and resonant photoemission spectroscopy study, Phys. Rev. B, 72 060401(R). (DOI: 10.1103/PhysRevB.72.060401)

[137] Iwata J. M., Chopdekar R. V., Wong F. J., *et al.*, (2009), Enhanced magnetization of $CuCr_2O_4$ thin films by substrate-induced strain, J. Appl. Phys. 105, 07A905 (DOI: 10.1063/1.3058612)

[138] Locher R. P., Stapele R. P. van, (1970), Super transferred hyperfine fields on tetrahedral sites in some chromium sulpho- and seleno spinels, J. Phys. Chem. Solids, 31, 2643-2652 (DOI: 10.1016/0022-3697(70)90260-X).

[139] Brydson R., Williams B. G., Engel W., *et al.*, (1987), Electron energy-loss spectroscopy (EELS) and the electronic structure of titanium dioxide, Solid State Commun. 64, 609–612 (DOI: 10.1016/0038-1098(87)90792-7).

[140] Kimura A., Matsuno J., Okabayashi J., *et al*., (2001), Soft x-ray magnetic circular dichroism study of the ferromagnetic spinel-type Cr chalcogenides, Phys. Rev. B, 63, 224420 (DOI: 10.1103/PhysRevB.63.224420).

[141] Deb A., Mizumaki M., Muro T., *et al.*, (2003), Soft-x-ray magnetic-circular-dichroism study of the colossal-magnetoresistance spinel $Fe_{0.5}Cu_{0.5}Cr_2S_4$, Phys. Rev. B, 68, 014427 (DOI: 10.1103/PhysRevB.68.014427).

[142] Deisenhofer J., Braak D., Krug von Nidda H.-A., *et al.*, (2005), Observation of a Griffiths Phase in Paramagnetic $La_{1-x}Sr_xMnO_3$, Phys. Rev. Lett. 95, 257202 (DOI: 10.1103/PhysRevLett.95.257202)

[143] Coey J. M. D., Viret M., Molna´r S. von, (1999), Mixed-valence manganites, Adv. Phys. 48, 167-293.

[144] Ramirez A. P., Cava R. J., Krajewski J., (1997), Colossal magnetoresistance in Cr-based chalcogenide spinels, Nature (London) 386, 156-159 (DOI:10.1038/386156a0).

[145] Lee W.L., Watauchi S., Miller V. L., *et al.*, (2004), Dissipationless anomalous Hall current in the ferromagnetic spinel $CuCr_2Se_{4-x}Br_x$, Science 303, 1647-9 (DOI:10.1126/science.1094383)

[146] Parker D. R., Green M. A., Bramwell S. T., *et al.*, (2004), Crossover from Positive to Negative Magnetoresistance in a Spinel, J. Am. Chem. Soc., 126, 2710-2711 (DOI: 10.1021/ja036965a).

[147] Yokaichiya F., Krimmel A., Tsurkan V., *et al.*, (2009), Spin-driven phase transitions in $ZnCr_2Se_4$ and $ZnCr_2S_4$ probed by high-resolution synchrotron x-ray and neutron powder diffraction, Phys. Rev. B, 79, 064423 (DOI: 10.1103/PhysRevB.79.064423)

[148] Mott N. F. (1990) Metal-Insulator Transitions; Taylor & Francis: London.